

Electron Dynamics in Molecular Qubits and Catalytic Films

Thesis by
Ruben Mirzoyan

In Partial Fulfillment of the Requirements for the degree of
Doctor of Philosophy



CALIFORNIA INSTITUTE OF TECHNOLOGY
Pasadena, California

2025
(Defended September 20th, 2024)

© 2024

Ruben Mirzoyan
ORCID: 0000-0002-2334-4012

ACKNOWLEDGEMENTS

It has been an amazing ride, and I will always look back at my grad school experience with fondness. I am deeply indebted to all the friends, colleagues, family, and teachers who have made this possible. To preface these words of gratitude, I wish to posthumously acknowledge Dr. Stavros Naxakis, my former high school chemistry teacher back in Vaughan, Ontario, Canada. For me to have pursued a PhD in Chemistry at Caltech was solely due to his outstanding influence as an inspiring teacher and friend.

My experience at Caltech was greatly shaped by my PhD adviser, Prof. Ryan Hadt. Thank you Ryan, for the opportunity to be one of your founding lab members and for being a formidable mentor and person. I still recall the initial sub-basement lab space, the informal brainstorming sessions, and the feeling of accomplishment when I electrodeposited my first CoPi film. It has been uniquely valuable to contribute to the growth of both the physical lab space and the research program over the years, and I am immensely grateful for the learning experience and support.

I have also been fortunate to have exceptionally supportive committee members. Prof. Harry Gray, besides encouraging me to complete Ch 213a which built my confidence in ligand field theory, has provided invaluable advice and support over the course of my graduate degree. Prof. Kimberly See welcomed me to Caltech as a rotating student and provided me with a rich learning environment and an upbeat social setting which set the momentum for the rest of my PhD. Jay Winkler has helped me with the running of laser experiments, and inspired me with his old-school custom built setups.

My friends and colleagues in the laboratory have consistently pushed me to be the best scientist I could be. My start in Ryan's lab was alongside Gautam Stroschio, Ryan Ribson, Gautam Stroschio and Jaron Tong, who upkept a welcoming and fun environment where it felt like anything could happen. David Cagan and I have seen it all since the early lab days, and it was so awesome to watch each other progress over the years as we handled different research areas in the group.

Alec Follmer was one of the most impactful postdocs that I had met and he offered substantial encouragement and advice at the most pivotal early times of my main research projects. It was fun doing science, hanging out, and hitting the gym together.

I believe I was supposed to be Nathanael's grad student mentor when he joined the group, but I feel that the roles quickly changed and I learned more from Nathanael Kazmierczak than from anyone else for the duration of my PhD. On top of being an exceptionally brilliant person to work with, he has been an exceptionally kind colleague and friend. I always felt challenged and inspired by our academic discussions, and always found it fun to chat about casual philosophical topics.

My experience in the lab was always elevated with Christian Totoiu and Katie Luedecke — Chris with an infectious positive attitude and Katie with the social glue that seems to bring everyone in the lab together. I am indebted to Brendon McNicholas for helping me learn the concepts in Ch213a and teaching me electrochemistry tricks. I enjoyed our casual conversations and workouts together. Thank you to Erica Sutcliffe for sharing your lasers and optics knowledge with me, and always having an uplifting vibe. Thank you to Hermann Klein-Hessling Barrientos for his stellar contributions to the CoPi project as a summer undergraduate student, and to Keon Ha Hwang for his positive spirit and help in carrying out electrochemical measurements. I am grateful to Erica Sutcliffe, Daniel Bim, Stefan Lohaus, Kay Xia, Stephen DiLuzio, Thais Scott, Jacob Rothbaum, Maria Blankenmeyer and Edwin Zhang for their positive energy, with lively and often productive encounters in the lab.

I am grateful for the many friends who have kept me happy throughout my time in Pasadena. Thank you to Roman Korol, who has been my best friend and workout partner since our days at UofT together. My friends and former roommates, Gavin Heim and Alex Buser, thank you for all the fun times and for being total bros. Thank you to the international students who always provide wholesome support and fun updates since the first week that we met at Caltech — Linh Le, Marta Gonzalvo and Liam Heidt.

Thank you to my undergraduate research advisers — Profs. Gilbert Walker, Doug Stephan, Al-Amin Dhirani, and Pierre Kennepohl.

It has sometimes not been easy to settle on the opposite side of the continent from where I grew up and my family resides. I am greatly indebted to those who gave me a sense of home during my time here in California. Thank you to David, Danny, and Ariella Vaystukh, who have hosted me countless times in their home. Danny has been my closest friend throughout the past 6 years, sharing wildly

fun times together, countless late night phone conversations, and providing an often much needed respite from my academic life. I am also incredibly grateful for Rabbi Hershy and Sheva Stolik of the Chabad Student Center of Pasadena, who exemplify the humility and passion for caring that makes me strive to be a better man. Their Shabbat dinners have resulted in a nice community which led to many transformative relationships in my life.

To wrap up, I owe everything to my parents, who have invested everything for me to live a happy life. Words cannot express their love and support that I constantly feel in my soul, which allows me to confidently pursue what I desire in life. I am grateful to my brother Arthur who consistently checks in on me and answers anything I ask him about.

Finally, I am grateful to the woman of my dreams, Karen — for bringing so much excitement, joy, and love to my life. I am so excited for our future together.

ABSTRACT

This thesis investigates two major themes within the realm of molecular and materials chemistry: spin-phonon coupling in molecular qubits and electrocatalysis in cobalt oxyhydroxide thin films. Across four chapters and one appendix, this work explores the intricacies of electron spin relaxation mechanisms within transition metal complexes and the catalytic properties of cobalt oxyhydroxide films through an array of spectroscopies and magnetic field effects.

Chapter 1 reviews recent advancements in molecular quantum information science, emphasizing the decoherence mechanisms in transition metal complex-based qubits. This chapter categorizes the different regimes of decoherence—spin-spin, motional, and spin-phonon—and discusses the contributions of intramolecular vibrations to the spin-phonon decoherence regime using a dynamic ligand field model. This provides a framework for designing molecular qubits tailored to various operational environments.

Chapter 2, Part 1 introduces a general ligand field theory model to quantify the spin-phonon coupling in $S = \frac{1}{2}$ transition metal complexes. The model evaluates the influence of spin-orbit coupling, ligand field energy gradients, and covalency dynamics on spin-phonon interactions. Through DFT and TDDFT calculations, the chapter correlates theoretical models with experimental quantum coherence properties in Cu(II) and V(IV)-based molecular qubits, offering a benchmark for future qubit design. Chapter 2, Part 2 enhances the model from Part 1 by adding temperature dependence and utilizing group theory selection rules. The model accurately forecasts relative experimental T_1 trends and identifies vibrational modes responsible for decoherence, enhancing understanding of room temperature coherence in these systems.

Chapter 3 employs steady-state and time-resolved spectroelectrochemical techniques to study the photoexcited states of amorphous cobalt-phosphate (CoPi) and cobalt-borate (CoBi) oxyhydroxide films used in oxygen evolution catalysis. The analysis reveals key insights into the dynamic defect states and electron transport mechanisms, differentiating the electronic properties and behaviors of CoPi and CoBi despite their structural similarities.

Chapter 4 oversees the development of a unique magneto-electrochemical setup and demonstrates a 30-40% increase in electrocatalytic current for water splitting under a 1.5 T magnetic field, independently of the cobalt-phosphate oxyhydroxide catalyst. This enhancement, attributed to the facilitated removal of O₂ gas bubbles, underscores the potential synergistic effects of magnetic fields in electrocatalysis and highlights the need for further investigation into such interactions.

Appendix A addresses the ongoing debate on the vibrational modes contributing most to electron spin relaxation in $S = \frac{1}{2}$ transition metal complexes. It uses Raman spectroscopy to experimentally identify vibrational energies and symmetries, providing critical experimental data for refining spin-vibrational coupling models.

PUBLISHED CONTENT AND CONTRIBUTIONS

Mirzoyan, R.; Hadt, R. G. The Dynamic Ligand Field of a Molecular Qubit: Decoherence through Spin–Phonon Coupling. *Phys. Chem. Chem. Phys.* **2020**, *22* (20), 11249–11265. <https://doi.org/10.1039/D0CP00852D>.

R.M. participated in the conception of the project, ran all calculations, developed theoretical expressions, and participated in the writing of the manuscript.

Mirzoyan, R.; Kazmierczak, N. P.; Hadt, R. G. Deconvolving Contributions to Decoherence in Molecular Electron Spin Qubits: A Dynamic Ligand Field Approach. *Chem. Eur. J.* **2021**, *27* (37), 9482–9494. <https://doi.org/10.1002/chem.202100845>.

R.M. designed the outline of the minireview and participated in the writing of the manuscript.

Kazmierczak, N. P.; **Mirzoyan, R.;** Hadt, R. G. The Impact of Ligand Field Symmetry on Molecular Qubit Coherence. *J. Am. Chem. Soc.* **2021**, *143* (42), 17305–17315. <https://doi.org/10.1021/jacs.1c04605>.

R.M. participated in the conception of the project, ran a portion of the calculations, and participated in the writing of the manuscript.

Mirzoyan, R.; Follmer, A. H.; Hadt, R. G. Observing Long-Lived Photogenerated Holes in Cobalt Oxyhydroxide Oxygen Evolution Catalysts. *ACS Appl. Energy Mater.* **2024**, *7* (7), 2837–2846. <https://doi.org/10.1021/acsaem.3c03269>.

R.M. participated in the conception of the project, conducted the experiments, analyzed the data, and participated in the writing of the manuscript.

Mirzoyan, R.; Barrientos, H. K.-H.; Hwang, K. H.; Hadt, R. Magnetic Field Effect on the Electrocatalytic Activity of Cobalt-Phosphate Oxyhydroxide Oxygen Evolving Thin Films. *ChemRxiv* August 23, 2024. <https://doi.org/10.26434/chemrxiv-2024-k3x2k>.

R.M. participated in the conception of the project, led the experimental design and data analysis, and participated in the writing of the manuscript.

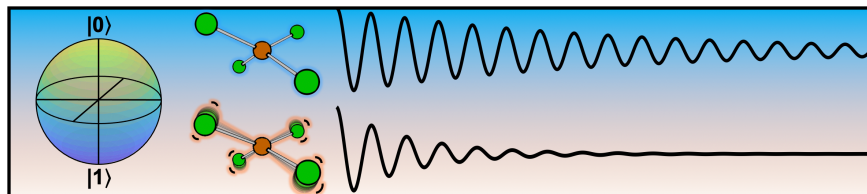
TABLE OF CONTENTS

ACKNOWLEDGEMENTS	iii
ABSTRACT	vi
PUBLISHED CONTENT AND CONTRIBUTIONS	viii
<i>A Ligand Field Based Introduction to Molecular Spin Qubits</i>	1
Abstract	2
Introduction	2
Motivation	2
Defining and Using Quantum Coherence	3
The Idea of Decoherence Regimes	6
Spin-Spin and Motional Contributions to Decoherence	9
Phonon Contributions to Decoherence	12
Temperature Scaling	12
Coupling Mechanisms	14
New Models	15
Dynamic Ligand Fields in Electron Spin Qubits	16
Summary and Outlook	24
Acknowledgments	26
References	26
<i>Chemical Design Principles Prolonging Coherence Times of $S = \frac{1}{2}$ Transition Metal Complexes</i>	35
Part 1: The Dynamic Ligand Field of a Molecular Qubit: Decoherence Through Spin–Phonon Coupling	36
Abstract	36
1-1. Introduction	36
2-1. Results	39
2-1.1. Dynamic Ligand Field Theory of Cu(II) g Values	39
2-1.2. Spin–Phonon Coupling Terms in $[\text{CuCl}_4]^{2-}$	43
2-1.2.2. D_{2d} and Comparisons to D_{4h} $[\text{CuCl}_4]^{2-}$	51
2.2.3. Cu(II) Effective Decoherence Maps and Comparisons to Ligand Field Theory	54
Supporting Information	75
Part 2: The Impact of Ligand Field Symmetry on Molecular Qubit Coherence	171
Abstract	171
2-2.1. Introduction	171
2-2.2. Ligand Field Paradigm for Electron Spin Relaxation	175
2-2.3. Discussion	188
Acknowledgments	192

References	X 193
Supporting Information	197
<i>Steady-State and Ultrafast Spectroelectrochemical Investigations of Amorphous Oxygen-Evolving Cobalt Oxide Films</i>	241
Abstract	242
Introduction	243
Supporting Information	266
<i>Magnetic Field Effects on Electrocatalytic Oxygen Evolution by Amorphous Cobalt Oxide Films</i>	301
<i>Elucidating Totally Symmetric Vibrational Mode Contributions of $S = \frac{1}{2}$ Molecular Qubit Candidates through Resonance Raman Spectroscopy</i>	303

Chapter 1

A LIGAND FIELD BASED INTRODUCTION TO MOLECULAR SPIN QUBITS



Adapted with permission from:

Mirzoyan, R.; Kazmierczak, N. P.; Hadt, R. G. Deconvolving Contributions to Decoherence in Molecular Electron Spin Qubits: A Dynamic Ligand Field Approach. *Chemistry – A European Journal* **2021**, 27 (37), 9482–9494. <https://doi.org/10.1002/chem.202100845>.

Copyright 2021 Wiley-VCH.

Abstract

In the past decade, transition metal complexes have gained momentum as electron spin-based quantum bit (qubit) candidates due to their synthetic tunability and long achievable coherence times. The decoherence of magnetic quantum states imposes a limit on the use of these qubits for quantum information technologies, such as quantum computing, sensing, and communication. With rapid recent development in the field of molecular quantum information science, a variety of chemical design principles for prolonging coherence in molecular transition metal qubits have been proposed. Here we delineate the spin-spin, motional, and spin-phonon regimes of decoherence, outlining design principles for each. We show how dynamic ligand field models can provide insights into the intramolecular vibrational contributions in the spin-phonon decoherence regime. This minireview aims to inform the development of molecular quantum technologies tailored for different environments and conditions.

Introduction

Motivation

Near the beginning of the 20th century, quantum mechanics developed new fundamental rules that describe the natural world, constituting the first quantum revolution. The second quantum revolution now endeavors to control individual quantum systems, enabling powerful applications in computing, sensing, and communication.^{1,2} The fundamental unit of quantum information science is the quantum bit (qubit), a two-level quantum system.³ Paramagnetic molecules can serve as qubit platforms due to the Zeeman effect, wherein the M_S sublevels of an unpaired electron in a magnetic field generate an effective two-level system with an energy gap in the microwave frequency range (Figure 1.1A). The quantum states of electron spins can then be initialized, manipulated, and studied using microwave pulses in electron paramagnetic resonance (EPR) spectrometers.⁴ Furthermore, paramagnetic transition metal complexes are synthetically tunable and can be attached to templated substrates and surfaces,⁵ tethered to electrodes,⁶ and integrated with superconducting resonators^{7,8} to realize quantum technological devices tunable on the molecular scale.^{9–15}

Defining and Using Quantum Coherence

An essential feature of quantum systems is the property of phase coherence (hereafter simply “coherence”), in which qubits in an ensemble retain their relative phase relations.¹⁶ Interactions between the qubits and their environment cause the ensemble to lose coherence and collapse to a classically observable state, limiting the time in which uniquely quantum behavior can be observed. This process is known as decoherence.¹⁶ Successful electron spin qubits in both sensing and computing must have long coherence times relative to their Larmor precession frequency, which governs the limiting timescale at which the electron spin qubit can change its quantum state. Using X-band EPR (~9.5 GHz), this timescale is on the order of 10 ns. To maintain phase information adequate for fault-tolerant quantum computations, the coherence time should be 10^4 – 10^5 times longer.¹⁷ Therefore, understanding the contributions to coherence times is a critical factor for the development of technologies that exploit quantum information.²

In the simplest model, decoherence of an $S = 1/2$ system can be described by two mono-exponential processes, with time constants T_1 and T_2 based on the Bloch equations.¹⁸ T_1 defines the time required for an ensemble of electron spins to relax back to thermodynamic equilibrium, a criterion satisfied when the Zeeman-split magnetic sublevels are populated according to a Boltzmann distribution. For an initial excess of excited spins, this requires dissipation of energy to a surrounding bath or lattice. T_1 is therefore often called the “spin-lattice” relaxation time, though the environment need not necessarily be a crystalline lattice. T_2 defines the time required for an ensemble of spins to lose their phase relations. This does not necessitate dissipation of energy to the lattice and arises from the differential couplings between qubit electron spins and spins in the bath. For this reason, T_2 is often called the “spin-spin” relaxation time. Both processes can be visualized by considering spin magnetization vectors projected onto a complex unit sphere known as the Bloch sphere (Figure 1.1A). A pure (coherent) state is represented by a vector extending towards a point on the surface of the sphere, while a mixed (partially or fully decohered) state is represented by a vector extending towards a point within the interior of the sphere.³ As can be seen geometrically, longitudinal electron spin relaxation (T_1) necessarily destroys transverse magnetization (Figure 1.1B). Therefore, the upper limit to T_2 (Figure 1.1C) is defined by T_1 , in which case T_2 is said to be T_1 -limited. This regime

is important to consider when seeking to increase the temperature at which coherence can be maintained and used.

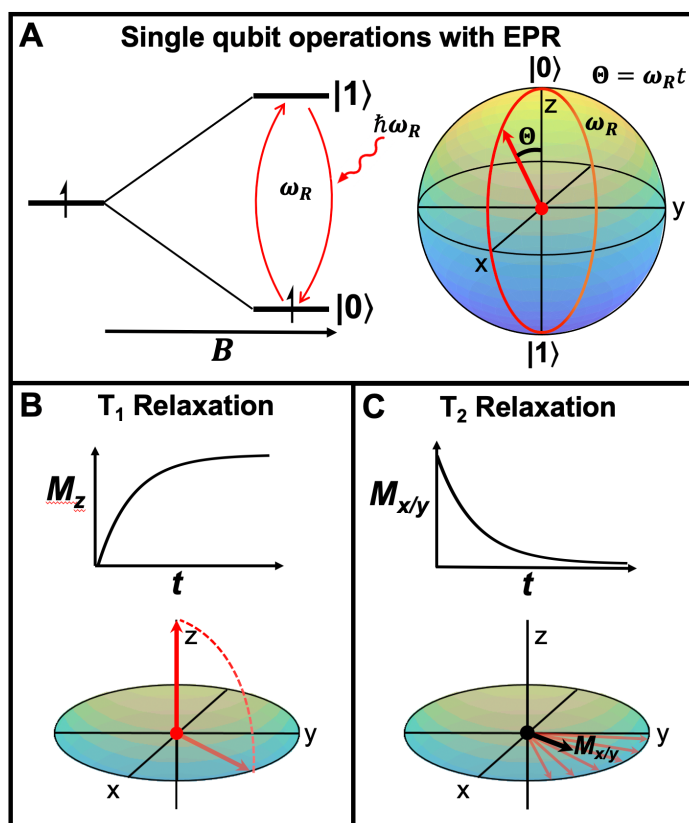


Figure 1.1 Principles of qubit measurements in EPR spectroscopy. **(A)** Magnetically split electron spin sublevels serve as the qubit platform. The quantum state can be controlled by the microwave pulse length t , which alters the wavefunction parameter θ in the Bloch sphere representation of the single qubit. **(B)** T_1 relaxation, as depicted by the recovery of net longitudinal magnetization M_z in the rotating frame representation. **(C)** T_2 relaxation, as depicted by the decrease in the net transverse magnetization vector $M_{x/y}$ (black arrow) as the ensemble of spins (red arrows) lose their phase coherence. The T_1 contribution to T_2 is not shown.

The characteristic decoherence time constants can be determined experimentally using pulsed EPR spectroscopy. An initial state is prepared by a coherent pulse, which both excites members of the spin ensemble and synchronizes their phases. Experimental coherence times are defined herein by time constants T_2^{DD} , T_M , and T_2^* ; each pertains to a time decay following a well-defined pulse sequence (Figure 1.2A). It should be noted that naming convention can differ, and

some authors refer to T_2 and T_M interchangeably. T_2^* corresponds to the free-induction decay following a single $\pi/2$ pulse and is the simplest measurement of decoherence. T_M corresponds to the decay following a Hahn-echo pulse sequence, in which a π pulse removes dephasing due to static inhomogeneities in the magnetic environment (Figure 1.2B). T_2 as defined by Bloch cannot usually be measured in EPR owing to spectral diffusion (Figure 1.2C),¹⁹ a process arising from the narrow bandwidth of the microwave radiation compared to the absorbance lineshape. In some cases, dynamic decoupling methods can more closely measure T_2 by filtering out quantum noise at the frequency corresponding to the interactions (typically hyperfine) that dominate spectral diffusion. The commonly used Carr-Purcell-Meiboom-Gill (CPMG) pulse sequence uses a train of “rephasing” π pulses, which can substantially diminish spectral diffusion effects in EPR dephasing.^{20–22} While dynamical decoupling methods are powerful, the upper limit for coherence times are set by the molecular properties of the qubit. Thus, this minireview focuses on establishing design principles for long quantum coherence times through synthetically tunable chemical properties of the qubit and its environment.

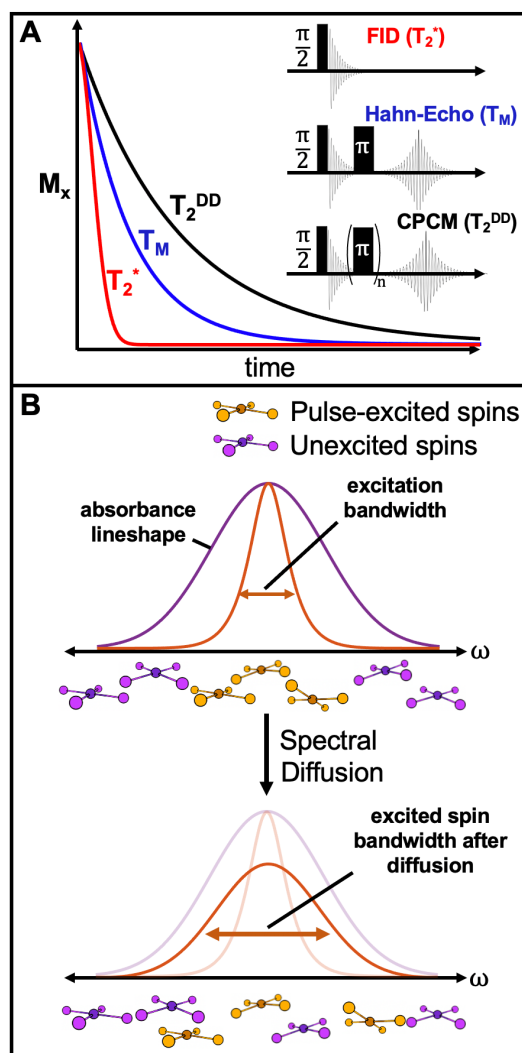


Figure 1.2. Experimental methods and considerations for spin coherence. **(A)** Overlay of FID (T_2^*), Hahn-echo (T_M), and dynamically decoupled echo (T_2^{DD}) decays, together with the corresponding pulse sequences to measure these time constants. **(B)** Schematic illustration of spectral diffusion, in which magnetic interactions modify the resonant frequency of excited spins after excitation.

The Idea of Decoherence Regimes

To understand factors leading to decoherence, it is useful to consider the terms of the spin Hamiltonian for the transition metal complex. A common model for decoherence is based on a quantum bath approach, in which the qubit and the bath are together considered as a closed quantum

system.²³ The Hamiltonian of the system is defined as $\mathbf{H} = \mathbf{H}_{\text{spin}} + \mathbf{H}_{\text{bath}} + \mathbf{H}_{\text{int}}$, where the spin Hamiltonian \mathbf{H}_{spin} for a transition metal complex is given by:

$$\mathbf{H}_{\text{spin}} = \mu_e \mathbf{g} \widehat{\mathbf{S}} \mathbf{B}_0 + \widehat{\mathbf{S}} \mathbf{A} \widehat{\mathbf{I}} + \widehat{\mathbf{S}} \mathbf{D} \widehat{\mathbf{S}} \quad (1.1)$$

In order of appearance, Equation 1 contains the electronic Zeeman, hyperfine, and zero-field splitting terms. Here the external magnetic field is \mathbf{B}_0 and the electron and nuclear spin angular momenta are $\widehat{\mathbf{S}}$ and $\widehat{\mathbf{I}}$, with hyperfine tensor \mathbf{A} and electronic g-tensor \mathbf{g} . The zero-field splitting tensor is given by \mathbf{D} and is considered for systems in which the total electron spin is $S > 1/2$. The spin-bath interaction term \mathbf{H}_{int} determines the decoherence properties of any molecular electron spin qubit.

A variety of strategies for increasing coherence times have been pursued, leading to different design principles for different goals and conditions. To prolong T_M , much emphasis has been placed on suppressing hyperfine interactions through nuclear spin dilution,²⁴⁻²⁷ elimination,²⁸ substitution with nuclei having smaller magnetic moments,^{27,29,30} and, more recently, “patterning,”³¹ in which the neighboring nuclei of a lattice or ligand framework have a mismatch in their magnetic moments. These strategies suppress dipolar and hyperfine interaction terms in \mathbf{H}_{int} . The current record for the longest T_M in a transition metal complex is 0.7 ms at 10 K, which was observed for a six-coordinate V(IV) complex having a nuclear spin-free ligand and solvent environment (CS_2).²⁸ Inspired from atomic physics, another approach uses clock transitions, in which the Zeeman energy is centered at an avoided level crossing to suppress magnetic noise.³²⁻³⁵ To prolong T_1 , several studies have chosen structurally rigid ligand frameworks that suppress the effect of molecular vibrations and their modulation of spin-orbit coupling, with specific emphasis on building around the vanadyl (VO) moiety.³⁶⁻³⁸ A recent strategy has targeted the minimization of ground state orbital angular momentum in a series of 3d and 4f metal complexes.³⁹ Despite possessing concentrated nuclear spins and a ligand framework that is structurally non-rigid, the isotropic ground state wave function enabled these qubits to reach μs coherence times at room temperature. To enable applications, molecular design is often inspired from a desired initialization or readout mechanism of the quantum state. For instance, optically addressable $S = 1$ molecular qubits, such as recently synthesized Cr(IV) complexes,⁴⁰ feature a spin-selective intersystem crossing in the excited state that enables a fluorescence-based readout of the quantum state. Such readout mechanisms were inspired⁴¹ by the

famous optically addressable solid-state electron spin qubits, such as nitrogen vacancy centers in diamond^{42,43} and the divacancies in the 4H polytype of silicon carbide.⁴⁴ Alternatively, single qubit control may be pursued through the spatial resolution offered by metal organic frameworks (MOFs).^{45,46} In accordance with the variety of experimental goals and design strategies, molecular qubit candidates display substantial structural diversity (Figure 1.3). Care must be taken to determine the dominant processes responsible for decoherence under a given set of conditions.

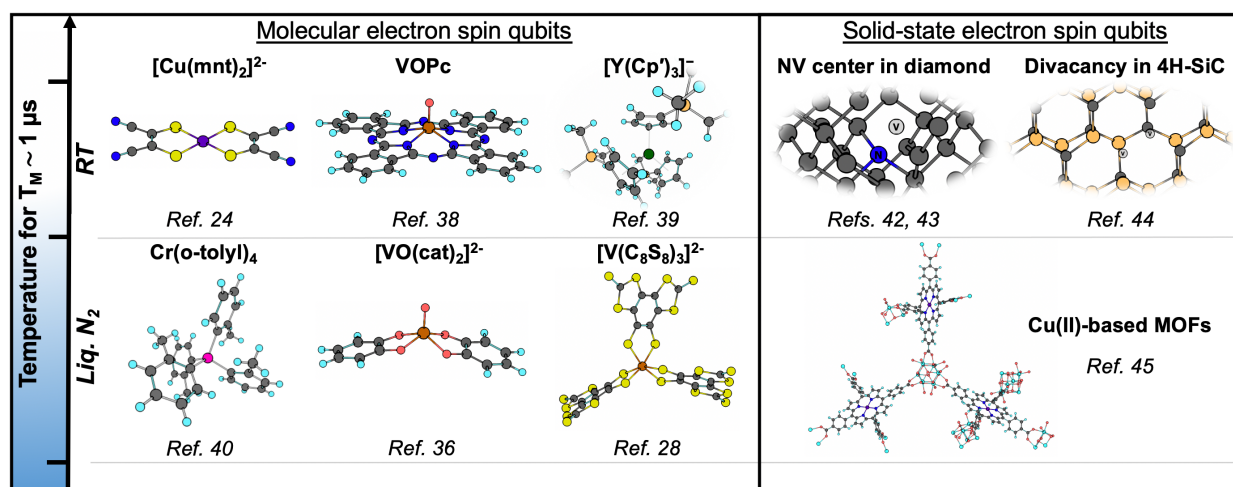


Figure 1.3. Representative electronic spin-based qubits.^{24,28,36,38–40,42,44,45} Top row: representative qubits exceeding $T_M = 1 \mu s$ at room temperature. Abbreviations: (mnt) = maleonitriledithiolate; VOPc = vanadyl phthalocyanine; $\text{Cp}' = (\text{C}_5\text{H}_4\text{SiMe}_3)$; (cat) = catecholate. Atomic Color Scheme: Cu (purple), S (yellow), C (charcoal gray), V (orange), Cr (pink), O (red), N (blue), Si (dark yellow), H (cyan), Y (dark green).

The dominant decoherence processes of molecular qubits can be categorized into three distinct regimes: the spin-spin (Figure 1.4A), motional (Figure 1.4B), and spin-phonon limits (Figure 1.4C). In the spin-spin regime, the spin bath dominates T_M through electronic and nuclear spin flip-flops. In the motional limit, T_M is dominated by molecular tumbling (solution phase) or low amplitude librations (glassy solids), which dynamically change the portion of the anisotropic Zeeman tensor aligned with the external magnetic field. In the spin-phonon limit, T_M is limited by T_1 , which is dominated by intramolecular vibrations that modulate the orbital angular momentum of the ground state. Each of the three regimes will be discussed in turn.

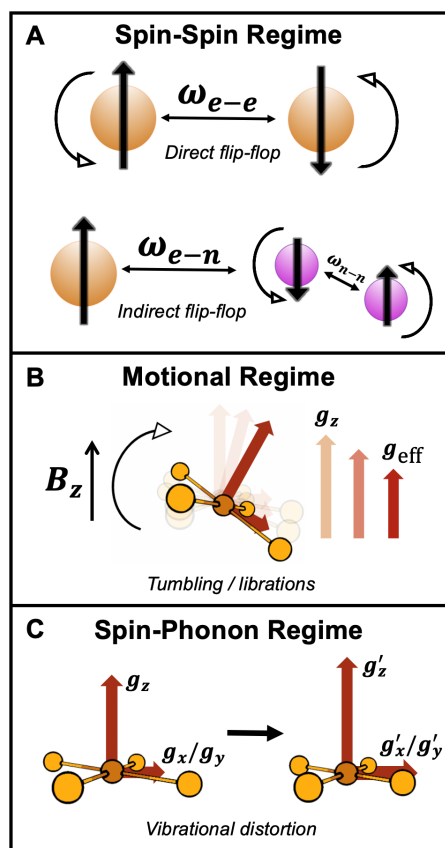


Figure 1.4. Regimes of decoherence in molecular electron spin qubits. (A) Dipolar flip-flops dominate the spin-spin decoherence regime, which occurs at low temperatures and in concentrated spin environments. Direct flip-flops occur when a pair of spins exchanges their spin angular momenta, while indirect flip-flops arise from interaction with nearby spin pairs. (B) Tumbling and librational dynamics characterize the motional decoherence regime, which occurs in liquids and glassy solids containing molecules with anisotropic Zeeman or hyperfine tensors. (C) Vibrationally-induced molecular distortions characterize the spin-phonon decoherence regime, which dominates at high temperatures in the solid phase.

Spin-Spin and Motional Contributions to Decoherence

Electron spin qubits undergo decoherence in the presence of other electronic and nuclear spins in the environment due to the coupling of spin angular momenta. Electron and nuclear spins both on the qubit molecule and within the bath can undergo thermal energy-conserving flip-flops, which perturb the magnetic dipolar coupling of the electron spin qubit and induce decoherence.⁴⁷ Direct and indirect spin-spin interactions contributing to T_M are represented in Figure 1.4A. Spin-spin

decoherence arises primarily through hyperfine coupling with nuclear spins in the solvent,^{26,28} hyperfine coupling with nuclear spins on the ligands,⁴⁸ and direct spin flip-flops between electronic spin centers.^{45,46} To minimize the latter contribution, dilution of the paramagnetic qubit in a matrix of a diamagnetic analog is a commonly employed strategy.⁴⁹ The suppression of hyperfine coupling is attained through nuclear-spin-free ligand scaffolds and spin-free solvents, such as carbon disulfide, which have shown great success.²⁸

An additional key consideration is the spin-diffusion barrier,^{50,51} in which nuclear spins that are within a 4–8 Å radius of the electron spin contribute only a small degree to decoherence.⁵² Nuclei within the barrier couple strongly to the electron spin, which detunes them to other nuclei in the bath, reducing their participation in nuclear spin flip-flops. Experimental evidence for the spin-diffusion barrier has been obtained from a series of vanadyl complexes using carbon/sulfur ligand scaffolds to systematically vary the distance between the terminal hydrogens and the electron spin center.⁵³ Molecules containing hydrogen atoms only within 6 Å were found to have a sharp increase in coherence time, owing to strengthened coupling between the hydrogen-based nuclear spins and the vanadium-based unpaired electron. Some models for fitting T_2 data have incorporated the spin diffusion barrier radius.^{26,54–56}

Additional decoherence mechanisms are possible whenever an electron spin qubit exhibits rotational and translational degrees of freedom in solutions or glasses. An ensemble of qubits with anisotropic \mathbf{g} or \mathbf{A} tensors can dephase through molecular rotations with respect to the applied magnetic field (Figure 1.4B), which alters the resonance frequency conditions and decreases T_M .⁵² Due to the characteristic anisotropy of \mathbf{g} and \mathbf{A} in transition metal complexes, the T_M of transition-metal-based qubits is often more sensitive to orientation than that of organic radicals. Orientation-dependent T_M values for paramagnetic transition metal complexes in frozen solution have been attributed to small-angle librations (hindered rotations) at temperatures well below the glass-transition temperature of the frozen glasses. Such librations are not prevalent in crystals. Experimentally, strong T_M orientation dependence was observed for a Cr(V) tetratolyl-porphyrin complex in the glassy state but not in crystals.⁵⁷ Orientation-dependent studies of T_M can therefore provide a selective diagnostic for librational decoherence processes. The role of the counterion

structure in glasses has also been investigated. Through analyses of the temperature dependent T_M times, it was proposed that methyl rotors proximal to the electron spin have a detrimental impact on T_M .⁵⁸ However, similar T_M behavior has also been observed in systems with no methyl groups present.⁴⁹

The well-studied class of V(IV) qubits contain experimental examples in each of the three decoherence regimes, providing for an instructive conceptual comparison. The electron spin relaxation of vanadyl phthalocyanine (VOPc) has been studied in a glassy frozen solution,⁵⁹ a pure crystalline solid,³⁸ and diamagnetically diluted crystalline dispersions in titanyl phthalocyanine (TiOPc) host at 1:10, 1:100, and 1:1000 concentrations.^{38,49} At 300 K in 1:10 dilution, VOPc exists in the spin-spin regime, where T_M is significantly smaller than T_1 owing to electronic dipolar contributions to decoherence. However, the 1:1000 dilution displays $T_M \sim T_1$ at 300 K, indicating T_M is T_1 limited.³⁸ The increased dilution suppresses dipolar interactions and causes phonon contributions to dominate decoherence, moving VOPc from the spin-spin regime to the spin-phonon regime through sample preparation. Finally, the V(IV) qubit $(n\text{-Bu}_3\text{NH})_2[\text{V}(\text{C}_6\text{H}_4\text{O}_2)_3]$ in a frozen glass has demonstrated 20 % variation in T_M times as a function of field position, consistent with motional contributions to decoherence.⁶⁰ It is to be expected that other V(IV) qubits will demonstrate the same behavior. These examples show how sample preparation and measurement conditions can place a qubit into any one of the three decoherence regimes. Further research is needed to ascertain how spin-phonon contributions to decoherence change when a qubit moves from a crystalline to a motional environment, an effort which may prove key for applications in quantum sensing.

Crystal packing effects can also play a significant role in magnetic decoherence properties. A study comparing two different crystal packing modes of lanthanide-based nitroxide radicals showed that the structure with proximal intermolecular nitroxide spins possessed the stronger spin-spin exchange coupling.⁶¹ Crystal packing thus modulates the strength of the spin-spin decoherence regime for magnetically undiluted crystals. Further research is required to elucidate the effect of ligand spin polarization on decoherence.

Phonon Contributions to Decoherence

In the crystalline solid phase, thermodynamic spin relaxation transfers energy to lattice phonons. At high temperatures, this relaxation process causes T_M to become T_1 -limited,⁶² defining the spin-phonon regime of decoherence. Two criteria must hold for spin-phonon mediated relaxation processes.^{63,64} First, energy conservation must be satisfied, implying that only lattice processes matching the spin-flip energy can occur. This could arise through emission of a single phonon possessing the correct spin-flip energy (direct mechanism^{16,65}), inelastic scattering of two phonons with the correct energy difference via a virtual state (Raman mechanism^{16,65}), or two phonon relaxation through a real electronic excited state (Orbach mechanism^{16,66}), as shown in Figure 1.5A. In dilute monometallic $S = 1/2$ qubits, contributions from the Orbach mechanism are often negligible owing to the lack of thermally accessible electronic excited states.⁶⁷ Second, there must be a nonzero transition probability for the energy to transfer from the spin to the lattice phonon, a criterion known as spin-phonon coupling. The theoretical underpinnings for spin-lattice relaxation in solids were developed by Van Vleck,^{65,68} Pryce,⁶⁹ Orbach,⁷⁰ and others.^{71,72}

Temperature Scaling

To diagnose the dominant phonon mechanism, early spin-phonon relaxation literature focused on deriving functional forms for how T_1 scales with temperature (T) and magnetic field (B). For example, treatment for $S = 1/2$ systems resulted in $1/T_1 \propto B^4T$ for the direct process and $1/T_1 \propto T^9$ and $1/T_1 \propto B^2T^7$ for the Raman process.¹⁶ It is crucial to note, however, that these derivations use the Debye model, which describes crystal vibrations solely as acoustic phonons (i.e., displacement waves, Figure 1.5B) carrying momentum and possessing a linear dispersion relation.⁷³ Optical phonons (Figure 1.5B), which include the intramolecular vibrations commonly analyzed in molecular vibrational spectroscopy, are not considered in the Debye model. This assumption has two key consequences for a spin-phonon coupling model:^{63,65,74} (1) relaxation takes place exclusively through scattering of acoustic phonons rather than optical phonons, and (2) the spin-phonon coupling constants for each phonon mode are equal or follow some predictable functional form, as no provision can be made for unique spin-phonon coupling for distinct intramolecular vibrations.⁶³ For

more details on spin-phonon implications of the Debye model, see the perspective by Coronado, Gaita-Ariño and coworkers.⁷⁵

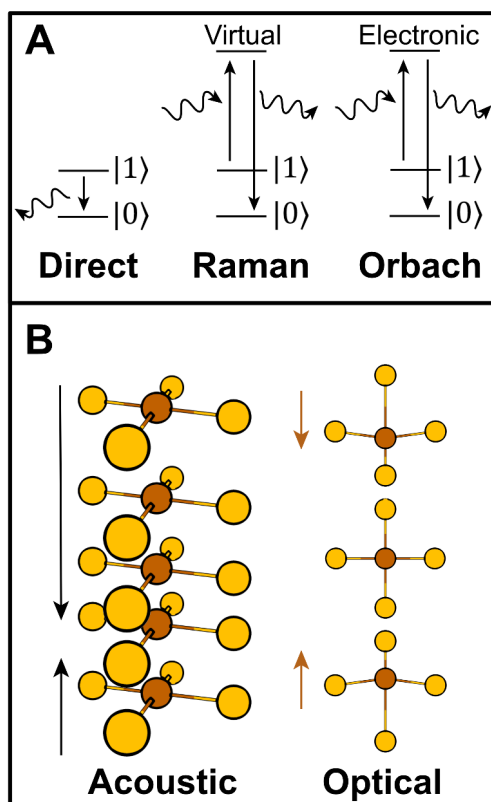


Figure 1.5. Phonon involvement in spin-lattice relaxation. **(A)** Mechanisms of phonon-induced relaxation. Zig-zag arrows represent phonon scattering. **(B)** Schematics of the two types of phonons involved in relaxation processes in molecular solids. Acoustic phonons are characterized by displacement waves, while optical phonons additionally involve intramolecular vibrations.

The temperature scaling relationships derived from the Debye model often show excellent agreement with experiment for homogeneous extended solids at low temperatures, such as Tm^{2+} in alkaline earth fluorides.⁷⁶ However, the Debye model assumptions are no longer appropriate when localized molecular vibrations become thermally activated with increasing temperature. In an extended solid, such local modes may be attributed to defects in the crystal structure.^{77,78} In a molecular solid, local modes correspond to optical phonons with large intramolecular vibrational

character (Figure 1.5B).^{73,79} Models for the temperature scaling of Raman relaxation through local modes have produced several new functional forms,^{77,78} including $1/T_1 \propto T^3$, $1/T_1 \propto T^5$, and $1/T_1 \propto \exp(T)/(\exp(T) - 1)^2$.

While useful as empirical tools for analyzing data, the proliferation of such functional forms points to the theoretical inability of the Debye model to describe the spin-phonon decoherence regime in molecular solids. In such materials, spin-lattice relaxation involves Raman processes with optical phonons, and the density of states for optical phonons is in general not homogeneous.^{80,81} Furthermore, the spin-phonon coupling terms in molecular solids may vary by orders of magnitude depending on the phonon mode under consideration.^{80,82} These effects are not captured in the Debye model temperature scaling predictions, rendering deviations from experiment unsurprising.^{79,83} Distinctly molecular models of spin-lattice relaxation are thus required to understand the spin-phonon regime and pinpoint the specific vibrational modes that contribute to decoherence.

Coupling Mechanisms

A second issue relates to the source of the spin-phonon coupling, which is a distinct consideration from the phonon mechanism (direct, Raman, Orbach). Coupling arises when phonons modulate the spin Hamiltonian; that is, $\partial \mathbf{H}_{spin} / \partial Q_i$ is nonzero for atomic displacements that take place along the vibrational coordinate Q_i of mode i .^{64,82} For an $S = 1/2$ qubit (Equation 1), both the g -tensor (\mathbf{g}) and the hyperfine tensor (\mathbf{A}) can have significant nonzero derivatives with respect to nuclear motion along Q_i . Assuming weak coupling, this yields two types of terms contributing to the spin-phonon interaction:^{64,84}

$$\frac{\partial \mathbf{H}_{spin}}{\partial Q_i} = \mu_e \mathbf{B}_0 \cdot \frac{\partial \mathbf{g}}{\partial Q_i} \cdot \hat{\mathbf{S}} + \hat{\mathbf{S}} \cdot \frac{\partial \mathbf{A}}{\partial Q_i} \cdot \hat{\mathbf{I}} \quad (1.2)$$

Equation 2 gives first-order spin-phonon coupling terms for the direct process.⁸⁴ Mixed partial derivatives relate to the Raman process, but the magnitudes of the mixed partial derivatives are expected to trend similarly to the first derivatives.⁸⁰ Each phonon mode has unique spin-phonon coupling terms, which may be either zero or non-zero. Owing to larger modulations of the first coordination sphere of the spin bearing metal ion (Figure 1.5B), optical phonons exhibit much larger

spin-phonon coupling terms than acoustic phonons.⁶⁴ Optical phonons therefore dominate spin-lattice relaxation when the temperature is high enough for their thermal population. Optical bands may be approximated by molecular vibrations at the gamma point (zero phonon momentum), enabling description of the Raman process solely through molecular quantities.⁸⁰ An active area of research seeks to understand the physical origins (i.e., molecular geometry and bonding) of the magnitudes of spin-phonon coupling coefficients under different experimental conditions.^{64,82,85,86} For example, a recent study of the $S = 1/2$ organometallic [Cp(Ti)(cot)] complex found that it possesses a surprisingly long T_M , attributed to weak spin-phonon coupling with the d_{z^2} ground state.⁸⁷

New Models

Two recent complementary approaches that go beyond the Debye model have gained new insights into relaxation in the spin-phonon regime. First, the *ab initio* spin dynamics approach of Lunghi, Sanvito, Sessoli, and coworkers seeks to computationally predict T_1 from the full phonon dispersion relation, calculating the unique spin-phonon coupling contribution from each phonon mode across the entire Brillouin zone. The predicted temperature scalings for T_1 are a good match for available experimental data.^{64,83,84} A key breakthrough in high temperature spin-lattice relaxation modeling was achieved by using machine learning to predict the \mathbf{g} and \mathbf{A} tensor values as a function of molecular geometry.^{83,84} This made second-order numerical differentiation of the \mathbf{g} and \mathbf{A} tensors computationally tractable for the first time, enabling *ab initio* prediction of the Raman relaxation processes dominating at high temperature.⁸⁴ Additionally, four-dimensional inelastic neutron scattering was recently used to map the phonon dispersion of a transition metal qubit, providing an experimental calibration of the phonon states responsible for magnetic relaxation.⁸⁸ The *ab initio* spin dynamics approach rigorously considers all spin-phonon coupling coefficients, but places less emphasis on interpreting the electronic structure origins of the \mathbf{g} and \mathbf{A} tensor derivatives.

A second approach uses ligand field theory and molecular vibrations to understand the origins of the dynamic Hamiltonian tensor values.^{82,89} This method provides a chemical explanation of the factors responsible for spin-phonon coupling, along with a mode-by-mode description of

which molecular vibrations contribute the most to decoherence across different coordination geometries and electronic structures. Such a description enables targeted molecular design focused on specific vibrational modes rather than the unspecific “rigidity” descriptor of the Debye model.⁷⁵ The ligand field method is outlined in the following section.

Dynamic Ligand Fields in Electron Spin Qubits

The ground states of free transition metal ions have intrinsic in-state orbital angular momentum, as the degenerate set of d orbitals can freely rotate into one another with no energy barrier. The g value in these cases can be predicted through the Landé formula and in general deviates strongly from the free-electron g value of 2.0023 (g_e). For example, a free Cu^{2+} ion with a ground state of $^2D_{5/2}$ has a predicted g value of 1.2. In the ligand fields encountered for molecular qubits, the ground state is orbitally nondegenerate, which quenches in-state orbital angular momentum. However, spin-orbit coupling between ground and excited states can reintroduce orbital angular momentum into the ground state (out-of-state orbital angular momentum). The impact on the g value from this orbital angular momentum can be expressed through the general perturbative expression for the g value of a given d electron ground state:⁹⁰

$$g_i = g_e - 2\lambda \sum_{e \neq g} \frac{\langle \Psi_g | \hat{L}_i | \Psi_e \rangle \langle \Psi_e | \hat{L}_i | \Psi_g \rangle}{E_e} \quad (1.3)$$

Here Ψ_g and Ψ_e represent ground and excited state wavefunctions, respectively, E_e represents the energy of Ψ_e relative to the ground state, \hat{L}_i is an orbital angular momentum operator, and λ is the many-electron spin-orbit coupling constant. Note $\lambda = \pm \zeta_{3d}/2S$, where S is the total electron spin, ζ_{3d} is the one-electron spin-orbit coupling constant, and + and – are used for less than half filled and greater than half filled d^n shells, respectively. Taking $D_{4h} [\text{CuCl}_4]^{2-}$ as an example, the g_z (g_{\parallel}) value is modified by spin-orbit coupling between the $^2B_{2g}$ (d_{xy}) excited state and the $^2B_{1g}$ ($d_{x^2-y^2}$) ground state. Table 1 gives the effect of \hat{L}_i on real d orbitals and can be used in conjunction with Equation 3 to derive a simple formula for g_z , where a factor η is used to account for the covalencies of the donor and acceptor orbitals of the ground and excited states:⁹¹

$$g_z = g_e - 2 \frac{\lambda \eta \langle x^2 - y^2 | \hat{L}_z | xy \rangle \langle xy | \hat{L}_z | x^2 - y^2 \rangle}{E_{B_{2g}}} = g_e - \frac{8\lambda\eta}{E_{B_{2g}}} \quad (1.4)$$

Table 1.1. Application of orbital angular momentum operators to the real d orbitals.

\hat{L}_x	\hat{L}_y	\hat{L}_z
$\hat{L}_x d_{xz} = -i d_{xy}$	$\hat{L}_y d_{xz} = i d_{x^2-y^2} - i\sqrt{3} d_{z^2}$	$\hat{L}_z d_{xz} = i d_{yz}$
$\hat{L}_x d_{yz} = i\sqrt{3} d_{z^2} + i d_{x^2-y^2}$	$\hat{L}_y d_{yz} = i d_{xy}$	$\hat{L}_z d_{yz} = -i d_{xz}$
$\hat{L}_x d_{xy} = i d_{xz}$	$\hat{L}_y d_{xy} = -i d_{yz}$	$\hat{L}_z d_{xy} = -2i d_{x^2-y^2}$
$\hat{L}_x d_{x^2-y^2} = -i d_{yz}$	$\hat{L}_y d_{x^2-y^2} = -i d_{xz}$	$\hat{L}_z d_{x^2-y^2} = 2i d_{xy}$
$\hat{L}_x d_{z^2} = -i\sqrt{3} d_{yz}$	$\hat{L}_y d_{z^2} = i\sqrt{3} d_{xz}$	$\hat{L}_z d_{z^2} = 0$

It should be noted that the η parameter can be derived from the spin densities of the metal ion and ligating atoms: a lower spin density on the metal center indicates a more covalent interaction, in which less spin on the metal is available to spin-orbit couple with d-d excited states. This proxy for covalency therefore takes into account the delocalization of spin density with the ligating environment. An important assumption here is that λ for the metal ion is much greater than that of the ligands, which justifies treating spin-orbit coupling only in the d-d manifold. The error in this approximation increases when heavy ligand atoms are present. However, contributions from ligand-based spin-orbit coupling may be incorporated into the model.

To minimize spin-phonon coupling, $\partial g / \partial Q$ should be as small as possible (Equation 1.2). By differentiating Equation 1.4 with respect to the i^{th} vibrational coordinate, we obtain an analytical expression for the spin-phonon coupling coefficient for g_z :⁸²

$$\frac{\partial g_z}{\partial Q_i} = 8\lambda \frac{\eta \left(\frac{\partial E_{B_{2g}}}{\partial Q_i} \right) - E_{B_{2g}} \left(\frac{\partial \eta}{\partial Q_i} \right)}{\left(E_{B_{2g}} \right)^2} \quad (1.5)$$

The logic behind the ligand field model of decoherence is summarized in Figure 1.6. As was previously shown, the spin-phonon coupling coefficients for a wide variety of molecular electron spin qubits qualitatively track with increased T_M in the spin-phonon decoherence regime.⁸² Crucially, Equation 1.5 expresses these coefficients in terms of spectroscopically observable and computationally accessible quantities: d-d ligand field transition energies ($E_{B_{2g}}$), ligand–metal covalencies (η), and the many-electron spin-orbit coupling constant of the metal ion (λ). The energies of ligand field excited states of first-row transition metal complexes can be quantified by a combination of electronic absorption⁹¹ and magnetic circular dichroism (MCD) spectroscopies.⁹² However, highly covalent ligand–metal bonds, which are often present in molecular qubit candidates, can lead to low-energy, high-intensity charge transfer transitions. These, together with intra-ligand molecular excited states with large dipole allowed intensities (e.g., Soret and Q-bands in porphyrins and phthalocyanines), can obscure ligand field transitions even when using low temperature MCD. X-ray spectroscopies provide powerful approaches to overcome these limitations by gaining metal-centric electronic structure insights in highly covalent systems. For example, the covalencies of ligand–metal bonds can be quantified using metal L-edge^{93,94} and ligand K-edge⁹⁵ X-ray absorption spectroscopies. Additionally, 2p3d resonant inelastic X-ray scattering (RIXS) can be utilized to directly measure spin-allowed and spin-forbidden ligand field excited state energies.^{96,97} 1s2p RIXS can also provide L-edge-like data using hard X-rays through constant incident energy (CIE) cuts taken within the 1s-3d K pre-edge.⁹⁸ Therefore, combining inorganic electronic spectroscopies with the dynamic ligand field model can provide a quantitative experimental basis for understanding bonding and electronic structure contributions to molecular qubit coherence times.

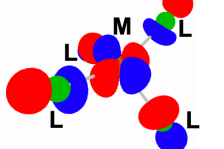
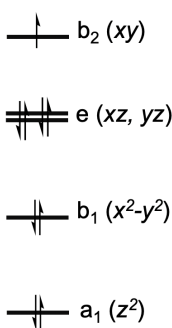
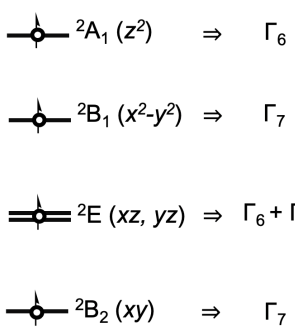

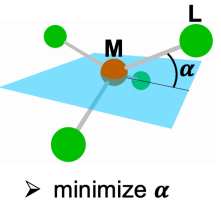
Molecular parameters	Orbital Diagram	State Diagram (hole formalism)	Spin-Orbit Symmetries	Spin-Phonon Design Principles
 Point group symmetry: D_{2d} MO coefficients on M and L SOC constant: λ Vibrational energies and symmetries, Q_i				

Figure 1.6. A general ligand field theory method for predicting decoherence in the spin-phonon regime from equilibrium molecular parameters (example: $D_{2d} d^9 ML_4$ complex). A molecular orbital diagram containing metal d -based orbitals can be mapped to a state diagram, and spin-orbit coupling contributions can be evaluated using the corresponding double group (shown in Bethe notation) to obtain molecular g values. With the aid of Equation 5, minimization of $\partial g / \partial Q$ for the lowest-energy bending mode can be achieved by obtaining a planar equilibrium geometry (see also Figure 1.7).

Equation 1.5 suggests two approaches for engineering long coherence times in molecular electron spin qubits. First, the overall ground state orbital angular momentum can be minimized, as $\partial g / \partial Q$ is lessened when g is small initially. This can occur by (1) decreasing the spin-orbit coupling constant, (2) increasing the excited state energy separation, (3) increasing the covalencies of ligand–metal bonds, or (4) engineering a ground state wave function that cannot engage in excited state spin-orbit coupling. Consideration of the d orbital rotations enables the latter strategy through direct evaluation of orbital angular momentum matrix elements for $S = 1/2$ qubits. As shown in Table 1.1, the d_{z^2} orbital cannot rotate into any other d orbital about the z -axis, so a molecule with a d_{z^2} ground state should exhibit small spin-phonon coupling with the g_z transition. Experimentally, a yttrium complex with a partially covalent $4d_{z^2}/5s$ -based ground state demonstrated a μs T_M at room temperature, despite featuring ligands with nuclear spins, unoptimized magnetic dilution, and a non-rigid ligand framework.³⁹ This example establishes minimizing ground state orbital angular momentum as a powerful design principle for engineering molecular qubits within the spin-phonon decoherence regime.

Second, the magnitude of the vibrational derivatives can be directly decreased by employing ligand frameworks with few vibrational modes that can undergo spin-phonon coupling.^{48,82} This can be accomplished by either (1) reducing the vibrational density of states at low energies,⁶² as thermal phonon occupation is required for the Raman relaxation process, or (2) tailoring the coordination geometry to reduce spin-phonon coupling by symmetry.⁴⁸ Dynamic ligand field analysis of a $[\text{CuCl}_4]^{2-}$ model compound has illuminated how vibrational symmetry can engender an optimal coordination geometry for $S = \frac{1}{2}$ Cu(II) qubits.⁸² Depending on the counterion, $[\text{CuCl}_4]^{2-}$ can adopt a square planar (D_{4h}) or distorted tetrahedral (D_{2d}) crystal geometry.⁹⁹ These two structures are directly related by a low-energy bending mode (Figure 1.7A). Analyses of the ground and excited state potential energy surfaces (PESs) along this coordinate provide insight into the electronic structure origins of spin-phonon coupling over different structures. For example, at the D_{4h} geometry, there is no excited state distortion and therefore no excited state linear coupling term (Figure 1.7B, dashed blue line). The absence of linear excited state coupling eliminates linear spin-phonon coupling in the ground state. For D_{2d} , however, the excited state PES is shifted relative to the ground state (i.e., there is an excited state distorting force), giving rise to a non-zero excited state linear coupling term for the D_{2d} structure. This provides a mechanism for the amount of orbital angular momentum mixed into the D_{2d} ground state to dynamically fluctuate along Q_i (Figure 1.7B-C). This analysis demonstrates that new vibrational modes can be activated for spin-phonon coupling upon small modifications of the coordination geometry.^{100–102}

Density functional theory (DFT) calculations confirm that the D_{4h} $[\text{CuCl}_4]^{2-}$ g_z value exhibits linear spin-phonon coupling along only the totally symmetric stretching mode (i.e., breathing mode). However, upon distorting to the D_{2d} geometry, the bending distortion mode changes in symmetry from b_{2u} (in D_{4h}) to a_1 (in D_{2d}), thus activating it for linear spin-phonon coupling (Figure 1.7F). The spin-phonon coupling (arrow size) clearly increases as the distortion angle α departs from 180° and the slope of the g_z surface (i.e., $\partial g_z / \partial Q_\alpha$) increases. At $\alpha = 180^\circ$, the surface flattens as linear spin-phonon coupling in the bending mode is removed. Examination of the covalency (Figure 1.7D) and excited state energies (Figure 1.7E) shows these quantities correlate strongly with the g_z value, as expected on the basis of Equations 4 and 5.⁸² This model explains why Cu(II) transition metal

complexes with the longest T_1 times host a square planar geometry around the metal center, while tetrahedrally distorted complexes exhibit shorter T_1 times.⁷⁹ While vibrational symmetry effects have so far been investigated in the context of discrete molecular qubits,⁴⁸ such strategies will likely also prove important in designing arrays of qubits in MOFs, where a large density of low-energy phonons leads to enhanced spin-phonon coupling.^{45,46}

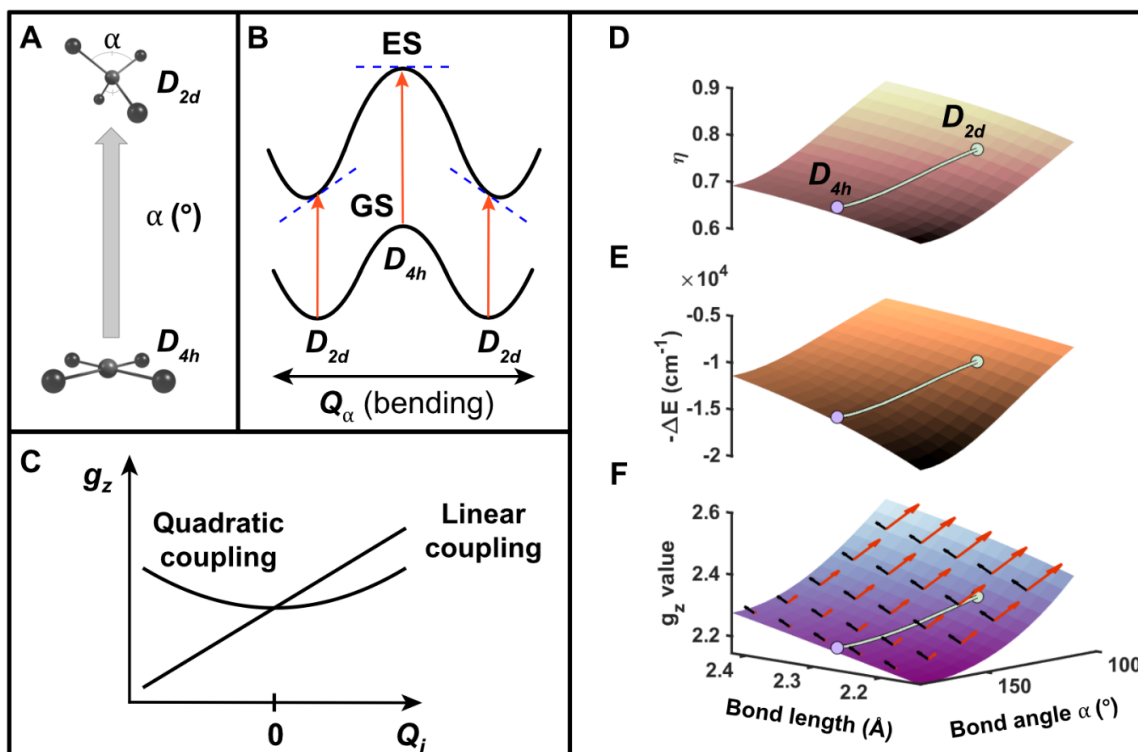


Figure 1.7. Effect of geometric distortion on spin-phonon coupling terms. (A) D_{4h} and D_{2d} $[\text{CuCl}_4]^{2-}$ are related by a distortion parametrized by bond angle α . (B) The ground and excited state equilibrium geometry mismatch at D_{2d} leads to linear excited state coupling (dashed blue lines) for the bending mode. (C) Linear versus quadratic spin-phonon coupling. (D), (E), (F) represent the variation of Cu d orbital contribution, first excited state energy, and g_z in $[\text{CuCl}_4]^{2-}$ as a function of geometry, respectively. Arrows give the spin-phonon coupling terms along the symmetric stretch (black) and bending (red) modes. Adapted from Ref. 79.

Notably, the gas phase equilibrium geometries of four-coordinate Cu(II) complexes are D_{2d} . However, ligand field strain through crystal packing effects can enforce geometries that would

otherwise be out of equilibrium, similar to the concept of the entatic state in bioinorganic chemistry.^{99,103} Cu complexes featuring symmetry- and distortion-altering intramolecular steric interactions have also been developed. These interactions can strongly influence ground state redox potentials and reorganization energies, as well as the lifetimes of metal-to-ligand charge transfer excited states for Cu(I).^{101,102,104} Similar ligand design approaches will enable systematic evaluation of how ligand field strain and secondary coordination sphere interactions contribute to coherence times Cu(II) qubit candidates.

The interplay between factors in the dynamic ligand field model can be illustrated by recent studies comparing Cu(II) and V(IV) $S = \frac{1}{2}$ qubit candidates.^{49,62} It was experimentally shown that the T_1 of vanadyl phthalocyanine (VOPc) is longer than that of copper phthalocyanine (CuPc) at higher temperatures (>25 K) where the spin-phonon regime dominates,⁴⁹ with VOPc exhibiting coherence up to room temperature.³⁸ These results can be rationalized and quantitatively understood using the spin-phonon coupling factors found in Equation 1.5: (1) the energy of the ligand field excited state that spin-orbit couples with the ground state, (2) the covalencies of the ligand–metal bonds, and (3) the spin-orbit coupling constant. To the best of our knowledge, the specific ligand field transition contributions to the g values of CuPc and VOPc are not known experimentally, likely due to the intense, dominant intra-Pc contributions to the electronic absorption spectrum. For g_z , they were calculated to be similar in energy (22,165 and 22,745 cm^{-1} , respectively⁸²), so (1) is likely not the distinguishing factor between CuPc and VOPc. Ligand–metal covalency in the ground state wave function is significantly larger in CuPc relative to VOPc, but this would suggest a longer coherence time for CuPc, so (2) is not the distinguishing factor. Thus, in the comparison between Cu(II) and V(IV)O in the same equatorial ligand set, the significantly reduced spin-orbit coupling constant of V(IV) in VOPc is of critical importance. Indeed, DFT calculations show that spin-phonon coupling coefficients between comparable vibrational modes of CuPc and VOPc differ primarily by the ratio of the spin-orbit coupling constants.⁸²

In a comparison between four-coordinate $[\text{Cu(II)(bdt)}_2]^{2-}$ (bdt=benzene-1,2-dithiolate) and six-coordinate $[\text{V(IV)(bdt)}_3]^{2-}$, the observation of longer electron spin relaxation for the former was ascribed to increased covalency of the Cu(II)–S bonds. Interestingly, this is opposite of the behavior observed for CuPc vs VOPc, where longer coherence times were observed for the more ionic ground state. While $[\text{Cu(bdt)}_2]^{2-}$ is square planar, $[\text{V(bdt)}_3]^{2-}$ adopts a pseudo-octahedral coordination geometry and was calculated to have seventeen linear spin-phonon coupling active vibrational modes below 400 cm^{-1} for g_z ; square planar $[\text{Cu(bdt)}_2]^{2-}$ has only one for g_z .⁸² Additionally, lower energy excited states in the six-coordinate V(IV) complexes, which increase ground state orbital angular momentum and thus sensitivity to spin-phonon coupling, may also be of critical importance for determining relaxation times. Thus, based on the ligand field theory model, the shorter coherence time in the six-coordinate V(IV) complex arises from increased spin-phonon coupling relative to the Cu(II) complex due to the different coordination environment, despite the lower spin-orbit coupling constant of the former. While substitution of sulfur with selenium in the ligands (forming benzene-1,2-diselenate, bds) increases the ligand–metal covalency, T_1 values were experimentally observed to decrease for both Cu(II) and V(IV). This likely arises because the heavy atom substitution decreases the frequency of the spin-phonon coupling active vibrational modes, thereby increasing the thermal population and total spin-phonon coupling, even though the spin-phonon coupling coefficient itself may decrease due to increased covalency.^{62,82} An additional factor to consider is the significantly increased spin-orbit coupling constant of selenium relative to sulfur, which will also contribute to accelerated relaxation. The considerations in this Section demonstrate the critical importance of evaluating dynamic ligand field properties when comparing coherence times between different molecular qubit candidates, especially if they feature different first coordination spheres.

The ligand field model of spin-phonon coupling as described is general for understanding couplings in any $S = \frac{1}{2}$ system. It has also been adapted for studying $S > \frac{1}{2}$ systems. Here modulation of \mathbf{D} and \mathbf{E} in the zero-field splitting Hamiltonian along vibrational coordinates enables a description of excited state intersystem crossing and single molecule magnet relaxation.¹⁰⁵ Further extensions of

the ligand field model are possible to also account for hyperfine contributions⁶⁴ ($\partial A/\partial Q$) to spin-lattice relaxation.

Summary and Outlook

The study of electron spin relaxation has a rich history and much is known. However, further understanding decoherence mechanisms at the molecular level is a key step towards the development of quantum technologies that can employ the versatility and tunability of coordination complexes. Here we have leveraged the idea of coherence regimes to highlight specific molecular contributions to decoherence. It is clear that the conditions (temperature, solid/solution phase) of the desired quantum application (computing/sensing) will define the specific design principles. In the spin-spin decoherence regime, decreasing spin-spin interactions through magnetic dilution and decreasing the concentration or gyromagnetic ratios of nuclear spins has the largest impact on prolonging T_M . In the motional regime, molecular tumbling and librational dynamics alter the resonance frequency conditions and decrease T_M . At higher temperatures in the solid state, T_M is limited by T_1 . We find this spin-phonon regime particularly exciting, as it provides a means for fundamental studies of how specific atomic motions are coupled to dynamic electronic structure changes. These considerations are also crucial for understanding time-dependent magnetization phenomena beyond quantum information science, including single-molecule magnetism, spin crossover complexes, and the kinetics of photomagnetic processes. From considering dynamic ligand fields, several strategies for minimizing spin-phonon coupling have been characterized and applied to experimental case studies. It is important to note, however, that the specific molecular vibration(s) that are responsible for decoherence in the spin-phonon regime have yet to be experimentally assigned. In the future, we anticipate that the dynamic ligand field model will provide an analytical link between molecular vibrations and temperature dependent electron spin relaxation rates. This will facilitate experimental assignment of the decoherence-inducing vibrations, allowing for a more tailored synthetic design approach to prolonging T_M .

Careful examination of the various decoherence mechanisms also provides insights into applications beyond quantum computing. These considerations extend nicely to the development of qubits as molecular quantum sensors (qusors), which provide several attractive features: (1) the

ability to target local regions of space on a molecular level, (2) novel coherence-based sensing mechanisms, and (3) a platform for fundamental studies of coherence in chemical microenvironments formed on electrode interfaces or in biological systems. In solution phases, including cases where qusors are immobilized on surfaces or bound to larger macromolecular structures (e.g., proteins), the magnitude of motional contributions to decoherence will be important to consider. By tailoring the ground state orbital angular momentum anisotropy and the molecular vibrations, it will be possible to design qusors that selectively sense rotational versus vibrational degrees of freedom and vice-versa, providing new insight into molecular dynamics in chemical microenvironments. Ligand sets with peripheral H-bond donors and acceptors may also provide a strategy to “lock-in” a specific molecular orientation and limit motional contributions. Additionally, it may be possible to sense the local electric fields in chemical microenvironments through their effects on T_1 and T_M , lending insight into the functional role of the local electrostatic environment. Previous work by Mims has shown that electron spin precession can be perturbed by an external electric field.¹⁰⁶ Electric field sensing has already been accomplished using solid state systems such as nitrogen vacancies in diamond,^{9,107} but solid state sensors have inherently limited spatial resolution and tunability. An exciting molecular engineering challenge will be to tune and enhance qusor electric field sensitivity through noncentrosymmetric perturbations manifesting in odd parity ligand field components,¹⁰⁶ while still minimizing spin-phonon coupling. This level of detailed understanding will derive from incorporating electric field effects into the dynamic ligand field model and learning to describe and control vibrational symmetry, which remains an outstanding challenge in engineering molecular electron spin qubits.

While many approaches to prolonging coherence times have sought to make qubit frameworks more rigid, there are a variety of important geometric and electronic structure factors that are not captured by this description. Detailed ligand field analyses coupled to high-resolution inorganic spectroscopies are called for to understand the role of molecular “rigidity” and symmetry by defining the precise vibrational modes that contribute to spin-phonon coupling and tuning their frequencies through synthetic design strategies. This level of new molecular insight will guide fundamental studies of spin-phonon coupling over a broad range of one-, two-, and three-

dimensional $S = \frac{1}{2}$ systems, as well as the development of electron spin qubit and qusor constructs for use in quantum technologies.

Acknowledgments

Nathanael Kazmierczak acknowledges support by the National Science Foundation Graduate Research Fellowship under Grant No. DGE-1745301. Financial support from Caltech and the Dow Next Generation Educator Fund is gratefully acknowledged.

References

- (1) Dowling, J. P.; Milburn, G. J. Quantum Technology: The Second Quantum Revolution. *Philos. Trans. Math. Phys. Eng. Sci.* **2003**, *361* (1809), 1655–1674.
- (2) Wasielewski, M. R.; Forbes, M. D. E.; Frank, N. L.; Kowalski, K.; Scholes, G. D.; Yuen-Zhou, J.; Baldo, M. A.; Freedman, D. E.; Goldsmith, R. H.; Goodson, T.; Kirk, M. L.; McCusker, J. K.; Ogilvie, J. P.; Shultz, D. A.; Stoll, S.; Whaley, K. B. Exploiting Chemistry and Molecular Systems for Quantum Information Science. *Nat. Rev. Chem.* **2020**, *4* (9), 490–504. <https://doi.org/10.1038/s41570-020-0200-5>.
- (3) Nielsen, M. A.; Chuang, I. L. *Quantum Computation and Quantum Information: 10th Anniversary Edition*; Cambridge University Press: Cambridge, 2010. <https://doi.org/10.1017/CBO9780511976667>.
- (4) Schweiger, A.; Jeschke, G. *Principles of Pulse Electron Paramagnetic Resonance*; Oxford University Press: Oxford, UK ; New York, 2001.
- (5) Cimatti, I.; Bondì, L.; Serrano, G.; Malavolti, L.; Cortigiani, B.; Velez-Fort, E.; Betto, D.; Ouerghi, A.; B. Brookes, N.; Loth, S.; Mannini, M.; Totti, F.; Sessoli, R. Vanadyl Phthalocyanines on Graphene/SiC(0001): Toward a Hybrid Architecture for Molecular Spin Qubits. *Nanoscale Horiz.* **2019**, *4* (5), 1202–1210. <https://doi.org/10.1039/C9NH00023B>.
- (6) Cardona-Serra, S.; Gaita-Ariño, A. Vanadyl Dithiolate Single Molecule Transistors: The next Spintronic Frontier? *Dalton Trans.* **2018**, *47* (16), 5533–5537. <https://doi.org/10.1039/C8DT00139A>.
- (7) Urtizberea, A.; Natividad, E.; Alonso, P. J.; Pérez-Martínez, L.; Andrés, M. A.; Gascón, I.; Gimeno, I.; Luis, F.; Roubeau, O. Vanadyl Spin Qubit 2D Arrays and Their Integration on Superconducting Resonators. *Mater. Horiz.* **2020**, *7* (3), 885–897. <https://doi.org/10.1039/C9MH01594A>.
- (8) Bonizzoni, C.; Ghirri, A.; Atzori, M.; Sorace, L.; Sessoli, R.; Affronte, M. Coherent Coupling between Vanadyl Phthalocyanine Spin Ensemble and Microwave Photons: Towards Integration of Molecular Spin Qubits into Quantum Circuits. *Sci. Rep.* **2017**, *7* (1), 13096. <https://doi.org/10.1038/s41598-017-13271-w>.

- (9) Dolde, F.; Fedder, H.; Doherty, M. W.; Nöbauer, T.; Rempp, F.; Balasubramanian, G.; Wolf, T.; Reinhard, F.; Hollenberg, L. C. L.; Jelezko, F.; Wrachtrup, J. Electric-Field Sensing Using Single Diamond Spins. *Nat. Phys.* **2011**, *7* (6), 459–463. <https://doi.org/10.1038/nphys1969>.
- (10) Kucsko, G.; Maurer, P. C.; Yao, N. Y.; Kubo, M.; Noh, H. J.; Lo, P. K.; Park, H.; Lukin, M. D. Nanometre-Scale Thermometry in a Living Cell. *Nature* **2013**, *500* (7460), 54–58. <https://doi.org/10.1038/nature12373>.
- (11) Mamin, H. J.; Kim, M.; Sherwood, M. H.; Rettner, C. T.; Ohno, K.; Awschalom, D. D.; Rugar, D. Nanoscale Nuclear Magnetic Resonance with a Nitrogen-Vacancy Spin Sensor. *Science* **2013**, *339* (6119), 557–560. <https://doi.org/10.1126/science.1231540>.
- (12) Hensen, B.; Bernien, H.; Dréau, A. E.; Reiserer, A.; Kalb, N.; Blok, M. S.; Ruitenberg, J.; Vermeulen, R. F. L.; Schouten, R. N.; Abellán, C.; Amaya, W.; Pruneri, V.; Mitchell, M. W.; Markham, M.; Twitchen, D. J.; Elkouss, D.; Wehner, S.; Taminiau, T. H.; Hanson, R. Loophole-Free Bell Inequality Violation Using Electron Spins Separated by 1.3 Kilometres. *Nature* **2015**, *526* (7575), 682–686. <https://doi.org/10.1038/nature15759>.
- (13) Yu, Y.; Ma, F.; Luo, X.-Y.; Jing, B.; Sun, P.-F.; Fang, R.-Z.; Yang, C.-W.; Liu, H.; Zheng, M.-Y.; Xie, X.-P.; Zhang, W.-J.; You, L.-X.; Wang, Z.; Chen, T.-Y.; Zhang, Q.; Bao, X.-H.; Pan, J.-W. Entanglement of Two Quantum Memories via Fibres over Dozens of Kilometres. *Nature* **2020**, *578* (7794), 240–245. <https://doi.org/10.1038/s41586-020-1976-7>.
- (14) Abobeih, M. H.; Randall, J.; Bradley, C. E.; Bartling, H. P.; Bakker, M. A.; Degen, M. J.; Markham, M.; Twitchen, D. J.; Taminiau, T. H. Atomic-Scale Imaging of a 27-Nuclear-Spin Cluster Using a Quantum Sensor. *Nature* **2019**, *576* (7787), 411–415. <https://doi.org/10.1038/s41586-019-1834-7>.
- (15) Graham, M. J.; Zadrozny, J. M.; Fataftah, M. S.; Freedman, D. E. Forging Solid-State Qubit Design Principles in a Molecular Furnace. *Chem. Mater.* **2017**, *29* (5), 1885–1897. <https://doi.org/10.1021/acs.chemmater.6b05433>.
- (16) Standley, K. J.; Vaughan, R. A. *Electron Spin Relaxation Phenomena in Solids*; Springer US: Boston, MA, 1969. <https://doi.org/10.1007/978-1-4899-6539-4>.
- (17) DiVincenzo, D. P. The Physical Implementation of Quantum Computation. *Fortschritte Phys.* **2000**, *48* (9–11), 771–783. [https://doi.org/10.1002/1521-3978\(200009\)48:9/11<771::AID-PROP771>3.0.CO;2-E](https://doi.org/10.1002/1521-3978(200009)48:9/11<771::AID-PROP771>3.0.CO;2-E).
- (18) Bloch, F. Nuclear Induction. *Phys. Rev.* **1946**, *70* (7–8), 460–474. <https://doi.org/10.1103/PhysRev.70.460>.
- (19) Kurshev, V. V.; Raitsimring, A. M. Carr-Purcell Train in the Conditions of Partial Excitation of Magnetic Resonance Spectrum. *J. Magn. Reson.* **1969** **1990**, *88* (1), 126–129. [https://doi.org/10.1016/0022-2364\(90\)90113-N](https://doi.org/10.1016/0022-2364(90)90113-N).
- (20) Witzel, W. M.; Sarma, S. D. Multiple-Pulse Coherence Enhancement of Solid State Spin Qubits. *Phys. Rev. Lett.* **2007**, *98* (7), 077601. <https://doi.org/10.1103/PhysRevLett.98.077601>.
- (21) Morton, J. J. L.; Tyryshkin, A. M.; Brown, R. M.; Shankar, S.; Lovett, B. W.; Ardavan, A.; Schenkel, T.; Haller, E. E.; Ager, J. W.; Lyon, S. A. Solid-State Quantum Memory Using

- the 31 P Nuclear Spin. *Nature* **2008**, *455* (7216), 1085–1088. <https://doi.org/10.1038/nature07295>.
- (22) Bluhm, H.; Foletti, S.; Neder, I.; Rudner, M.; Mahalu, D.; Umansky, V.; Yacoby, A. Dephasing Time of GaAs Electron-Spin Qubits Coupled to a Nuclear Bath Exceeding 200 Ms. *Nat. Phys.* **2011**, *7* (2), 109–113. <https://doi.org/10.1038/nphys1856>.
- (23) Breuer, H.-P.; Petruccione, F. *The Theory of Open Quantum Systems*; Oxford University Press: Oxford, 2007.
- (24) Bader, K.; Dengler, D.; Lenz, S.; Endeward, B.; Jiang, S.-D.; Neugebauer, P.; van Slageren, J. Room Temperature Quantum Coherence in a Potential Molecular Qubit. *Nat. Commun.* **2014**, *5*, 5304. <https://doi.org/10.1038/ncomms6304>.
- (25) Graham, M. J.; Zadrozny, J. M.; Shiddiq, M.; Anderson, J. S.; Fataftah, M. S.; Hill, S.; Freedman, D. E. Influence of Electronic Spin and Spin–Orbit Coupling on Decoherence in Mononuclear Transition Metal Complexes. *J. Am. Chem. Soc.* **2014**, *136* (21), 7623–7626. <https://doi.org/10.1021/ja5037397>.
- (26) Yu, C.-J.; Graham, M. J.; Zadrozny, J. M.; Niklas, J.; Krzyaniak, M. D.; Wasielewski, M. R.; Poluektov, O. G.; Freedman, D. E. Long Coherence Times in Nuclear Spin-Free Vanadyl Qubits. *J. Am. Chem. Soc.* **2016**, *138* (44), 14678–14685. <https://doi.org/10.1021/jacs.6b08467>.
- (27) Graham, M. J.; Krzyaniak, M. D.; Wasielewski, M. R.; Freedman, D. E. Probing Nuclear Spin Effects on Electronic Spin Coherence via EPR Measurements of Vanadium(IV) Complexes. *Inorg. Chem.* **2017**, *56* (14), 8106–8113. <https://doi.org/10.1021/acs.inorgchem.7b00794>.
- (28) Zadrozny, J. M.; Niklas, J.; Poluektov, O. G.; Freedman, D. E. Millisecond Coherence Time in a Tunable Molecular Electronic Spin Qubit. *ACS Cent. Sci.* **2015**, *1* (9), 488–492. <https://doi.org/10.1021/acscentsci.5b00338>.
- (29) Ardavan, A.; Rival, O.; Morton, J. J. L.; Blundell, S. J.; Tyryshkin, A. M.; Timco, G. A.; Winpenny, R. E. P. Will Spin-Relaxation Times in Molecular Magnets Permit Quantum Information Processing? *Phys. Rev. Lett.* **2007**, *98* (5), 057201. <https://doi.org/10.1103/PhysRevLett.98.057201>.
- (30) Bader, K.; Schlindwein, S. H.; Gudat, D.; Slageren, J. van. Molecular Qubits Based on Potentially Nuclear-Spin-Free Nickel Ions. *Phys. Chem. Chem. Phys.* **2017**, *19* (3), 2525–2529. <https://doi.org/10.1039/C6CP08161D>.
- (31) Jackson, C. E.; Lin, C.-Y.; Johnson, S. H.; Tol, J. van; Zadrozny, J. M. Nuclear-Spin-Pattern Control of Electron-Spin Dynamics in a Series of V(IV) Complexes. *Chem. Sci.* **2019**, *10* (36), 8447–8454. <https://doi.org/10.1039/C9SC02899D>.
- (32) Shiddiq, M.; Komijani, D.; Duan, Y.; Gaita-Ariño, A.; Coronado, E.; Hill, S. Enhancing Coherence in Molecular Spin Qubits via Atomic Clock Transitions. *Nature* **2016**, *531* (7594), 348–351. <https://doi.org/10.1038/nature16984>.
- (33) Ghosh, S.; Datta, S.; Friend, L.; Cardona-Serra, S.; Gaita-Ariño, A.; Coronado, E.; Hill, S. Multi-Frequency EPR Studies of a Mononuclear Holmium Single-Molecule Magnet Based on the Polyoxometalate [HoIII(W5O18)2]9–. *Dalton Trans.* **2012**, *41* (44), 13697–13704. <https://doi.org/10.1039/C2DT31674A>.

- (34) Zadrozny, J. M.; Gallagher, A. T.; Harris, T. D.; Freedman, D. E. A Porous Array of Clock Qubits. *J. Am. Chem. Soc.* **2017**, *139* (20), 7089–7094. <https://doi.org/10.1021/jacs.7b03123>.
- (35) Giménez-Santamarina, S.; Cardona-Serra, S.; Clemente-Juan, J. M.; Gaita-Ariño, A.; Coronado, E. Exploiting Clock Transitions for the Chemical Design of Resilient Molecular Spin Qubits. *Chem. Sci.* **2020**, *11* (39), 10718–10728. <https://doi.org/10.1039/D0SC01187H>.
- (36) Atzori, M.; Benci, S.; Morra, E.; Tesi, L.; Chiesa, M.; Torre, R.; Sorace, L.; Sessoli, R. Structural Effects on the Spin Dynamics of Potential Molecular Qubits. *Inorg. Chem.* **2018**, *57* (2), 731–740. <https://doi.org/10.1021/acs.inorgchem.7b02616>.
- (37) Atzori, M.; Morra, E.; Tesi, L.; Albino, A.; Chiesa, M.; Sorace, L.; Sessoli, R. Quantum Coherence Times Enhancement in Vanadium(IV)-Based Potential Molecular Qubits: The Key Role of the Vanadyl Moiety. *J. Am. Chem. Soc.* **2016**, *138* (35), 11234–11244. <https://doi.org/10.1021/jacs.6b05574>.
- (38) Atzori, M.; Tesi, L.; Morra, E.; Chiesa, M.; Sorace, L.; Sessoli, R. Room-Temperature Quantum Coherence and Rabi Oscillations in Vanadyl Phthalocyanine: Toward Multifunctional Molecular Spin Qubits. *J. Am. Chem. Soc.* **2016**, *138* (7), 2154–2157. <https://doi.org/10.1021/jacs.5b13408>.
- (39) Ariciu, A.-M.; Woen, D. H.; Huh, D. N.; Nodaraki, L. E.; Kostopoulos, A. K.; Goodwin, C. A. P.; Chilton, N. F.; McInnes, E. J. L.; Winpenny, R. E. P.; Evans, W. J.; Tuna, F. Engineering Electronic Structure to Prolong Relaxation Times in Molecular Qubits by Minimising Orbital Angular Momentum. *Nat. Commun.* **2019**, *10* (1), 1–8. <https://doi.org/10.1038/s41467-019-11309-3>.
- (40) Bayliss, S. L.; Laorenza, D. W.; Mintun, P. J.; Kovos, B. D.; Freedman, D. E.; Awschalom, D. D. Optically Addressable Molecular Spins for Quantum Information Processing. *Science* **2020**, *370* (6522), 1309–1312. <https://doi.org/10.1126/science.abb9352>.
- (41) Fataftah, M. S.; Freedman, D. E. Progress towards Creating Optically Addressable Molecular Qubits. *Chem. Commun.* **2018**, *54* (98), 13773–13781. <https://doi.org/10.1039/C8CC07939K>.
- (42) Bar-Gill, N.; Pham, L. M.; Jarmola, A.; Budker, D.; Walsworth, R. L. Solid-State Electronic Spin Coherence Time Approaching One Second. *Nat. Commun.* **2013**, *4* (1), 1743. <https://doi.org/10.1038/ncomms2771>.
- (43) Warner, M.; Din, S.; Tupitsyn, I. S.; Morley, G. W.; Stoneham, A. M.; Gardener, J. A.; Wu, Z.; Fisher, A. J.; Heutz, S.; Kay, C. W. M.; Aeppli, G. Potential for Spin-Based Information Processing in a Thin-Film Molecular Semiconductor. *Nature* **2013**, *503* (7477), 504–508. <https://doi.org/10.1038/nature12597>.
- (44) Koehl, W. F.; Buckley, B. B.; Heremans, F. J.; Calusine, G.; Awschalom, D. D. Room Temperature Coherent Control of Defect Spin Qubits in Silicon Carbide. *Nature* **2011**, *479* (7371), 84–87. <https://doi.org/10.1038/nature10562>.
- (45) Yu, C.-J.; Krzyaniak, M. D.; Fataftah, M. S.; Wasielewski, M. R.; Freedman, D. E. A Concentrated Array of Copper Porphyrin Candidate Qubits. *Chem. Sci.* **2019**, *10* (6), 1702–1708. <https://doi.org/10.1039/C8SC04435J>.

- (46) Yu, C.-J.; von Kugelgen, S.; Krzyaniak, M. D.; Ji, W.; Dichtel, W. R.; Wasielewski, M. R.; Freedman, D. E. Spin and Phonon Design in Modular Arrays of Molecular Qubits. *Chem. Mater.* **2020**, *32* (23), 10200–10206. <https://doi.org/10.1021/acs.chemmater.0c03718>.
- (47) Klauder, J. R.; Anderson, P. W. Spectral Diffusion Decay in Spin Resonance Experiments. *Phys. Rev.* **1962**, *125* (3), 912–932. <https://doi.org/10.1103/PhysRev.125.912>.
- (48) Santanni, F.; Albino, A.; Atzori, M.; Ranieri, D.; Salvadori, E.; Chiesa, M.; Lunghi, A.; Bencini, A.; Sorace, L.; Totti, F.; Sessoli, R. Probing Vibrational Symmetry Effects and Nuclear Spin Economy Principles in Molecular Spin Qubits. *Inorg. Chem.* **2021**, *60* (1), 140–151. <https://doi.org/10.1021/acs.inorgchem.0c02573>.
- (49) Follmer, A. H.; Ribson, R. D.; Oyala, P. H.; Chen, G. Y.; Hadt, R. G. Understanding Covalent versus Spin–Orbit Coupling Contributions to Temperature-Dependent Electron Spin Relaxation in Cupric and Vanadyl Phthalocyanines. *J. Phys. Chem. A* **2020**, *124* (44), 9252–9260. <https://doi.org/10.1021/acs.jpca.0c07860>.
- (50) Wald, L. L.; Hahn, E. L.; Lukac, M. Fluorine Spin Frozen Core in Pr³⁺:LaF₃ Observed by Cross Relaxation. *J. Opt. Soc. Am. B* **1992**, *9* (5), 789–793. <https://doi.org/10.1364/JOSAB.9.000789>.
- (51) Bloembergen, N. On the Interaction of Nuclear Spins in a Crystalline Lattice. *Physica* **1949**, *15* (3), 386–426. [https://doi.org/10.1016/0031-8914\(49\)90114-7](https://doi.org/10.1016/0031-8914(49)90114-7).
- (52) Eaton, S. S.; Eaton, G. R. Distance Measurements by CW and Pulsed EPR. In *Distance Measurements in Biological Systems by EPR*; Berliner, L. J., Eaton, G. R., Eaton, S. S., Eds.; Biological Magnetic Resonance; Springer US: Boston, MA, 2000; pp 1–27. https://doi.org/10.1007/0-306-47109-4_1.
- (53) Graham, M. J.; Yu, C.-J.; Krzyaniak, M. D.; Wasielewski, M. R.; Freedman, D. E. Synthetic Approach To Determine the Effect of Nuclear Spin Distance on Electronic Spin Decoherence. *J. Am. Chem. Soc.* **2017**, *139* (8), 3196–3201. <https://doi.org/10.1021/jacs.6b13030>.
- (54) Milov, A. D.; Salikhov, K. M.; Tsvetkov, Y. D. Phase relaxation of hydrogen atoms stabilized in amorphous matrices. *Fiz. Tverd. Tela* **1973**, *15* (4), 1187–1195.
- (55) Zecevic, A.; Eaton, G. R.; Eaton, S. S.; Lindgren, M. Dephasing of Electron Spin Echoes for Nitroxyl Radicals in Glassy Solvents by Non-Methyl and Methyl Protons. *Mol. Phys.* **1998**, *95* (6), 1255–1263. <https://doi.org/10.1080/00268979809483256>.
- (56) Canarie, E. R.; Jahn, S. M.; Stoll, S. Quantitative Structure-Based Prediction of Electron Spin Decoherence in Organic Radicals. *J. Phys. Chem. Lett.* **2020**, *11* (9), 3396–3400. <https://doi.org/10.1021/acs.jpcclett.0c00768>.
- (57) Konda, R.; Du, J.-L.; Eaton, S. S.; Eaton, G. R. Electron Spin Relaxation Rates for Nitridochromium(V) Tetratolylporphyrin and Nitridochromium(V) Octaethylporphyrin in Frozen Solution. *Appl. Magn. Reson.* **1994**, *7* (2), 185–193. <https://doi.org/10.1007/BF03162611>.
- (58) Lin, C.-Y.; Ngendahimana, T.; Eaton, G. R.; Eaton, S. S.; Zadrozny, J. M. Counterion Influence on Dynamic Spin Properties in a V(IV) Complex. *Chem. Sci.* **2019**, *10* (2), 548–555. <https://doi.org/10.1039/C8SC04122A>.

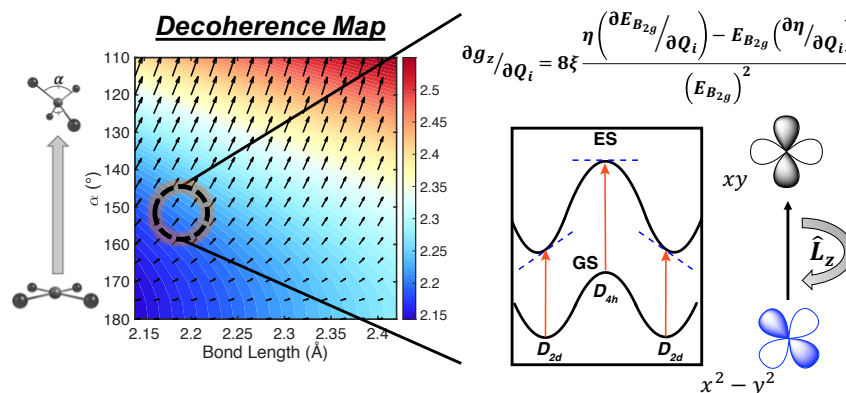
- (59) Bader, K.; Winkler, M.; van Slageren, J. Tuning of Molecular Qubits: Very Long Coherence and Spin–Lattice Relaxation Times. *Chem. Commun.* **2016**, 52 (18), 3623–3626. <https://doi.org/10.1039/C6CC00300A>.
- (60) Jackson, C. E.; Lin, C.-Y.; van Tol, J.; Zdrozny, J. M. Orientation Dependence of Phase Memory Relaxation in the V(IV) Ion at High Frequencies. *Chem. Phys. Lett.* **2020**, 739, 137034. <https://doi.org/10.1016/j.cplett.2019.137034>.
- (61) Pointillart, F.; Bernot, K.; Poneti, G.; Sessoli, R. Crystal Packing Effects on the Magnetic Slow Relaxation of Tb(III)-Nitronyl Nitroxide Radical Cyclic Dinuclear Clusters. *Inorg. Chem.* **2012**, 51 (22), 12218–12229. <https://doi.org/10.1021/ic301394x>.
- (62) Fataftah, M. S.; Krzyaniak, M. D.; Vlaisavljevich, B.; Wasielewski, M. R.; Zdrozny, J. M.; Freedman, D. E. Metal–Ligand Covalency Enables Room Temperature Molecular Qubit Candidates. *Chem. Sci.* **2019**, 10 (27), 6707–6714. <https://doi.org/10.1039/C9SC00074G>.
- (63) Gatteschi, D.; Sessoli, R.; Villain, J. *Molecular Nanomagnets*; Oxford University Press: Oxford, 2006.
- (64) Lunghi, A.; Sanvito, S. How Do Phonons Relax Molecular Spins? *Sci. Adv.* **2019**, 5 (9), eaax7163. <https://doi.org/10.1126/sciadv.aax7163>.
- (65) Van Vleck, J. H. Paramagnetic Relaxation Times for Titanium and Chrome Alum. *Phys. Rev.* **1940**, 57 (5), 426–447. <https://doi.org/10.1103/PhysRev.57.426>.
- (66) Orbach, R. Spin-Lattice Relaxation in Rare-Earth Salts. *Proc. R. Soc. Lond. A* **1961**, 264, 458–484.
- (67) Zhou, Y.; Bowler, B. E.; Eaton, G. R.; Eaton, S. S. Electron Spin Lattice Relaxation Rates for $S = 12$ Molecular Species in Glassy Matrices or Magnetically Dilute Solids at Temperatures between 10 and 300 K. *J. Magn. Reson.* **1999**, 139 (1), 165–174. <https://doi.org/10.1006/jmre.1999.1763>.
- (68) Van Vleck, J. H. Paramagnetic Relaxation and the Equilibrium of Lattice Oscillators. *Phys. Rev.* **1941**, 59 (9), 724–729. <https://doi.org/10.1103/PhysRev.59.724>.
- (69) Pryce, M. H. L.; Stevens, K. W. H. The Theory of Magnetic Resonance-Line Widths in Crystals. *Proc. Phys. Soc. Sect. A* **1950**, 63 (1), 36–51. <https://doi.org/10.1088/0370-1298/63/1/306>.
- (70) Orbach, R. On the Theory of Spin-Lattice Relaxation in Paramagnetic Salts. *Proc. Phys. Soc.* **1961**, 77 (4), 821–826. <https://doi.org/10.1088/0370-1328/77/4/301>.
- (71) Abragam, A. *The Principles of Nuclear Magnetism*; Clarendon Press: London, 1961.
- (72) Stevens, K. W. H. The Theory of Paramagnetic Relaxation. *Rep. Prog. Phys.* **1967**, 30 (1), 189–226. <https://doi.org/10.1088/0034-4885/30/1/305>.
- (73) Gu, L.; Wu, R. Origin of the Anomalously Low Raman Exponents in Single Molecule Magnets. *Phys. Rev. B* **2021**, 103 (1), 014401. <https://doi.org/10.1103/PhysRevB.103.014401>.
- (74) Casimir, H. B. G.; du Pré, F. K. Note on the Thermodynamic Interpretation of Paramagnetic Relaxation Phenomena. *Physica* **1938**, 5 (6), 507–511. [https://doi.org/10.1016/S0031-8914\(38\)80164-6](https://doi.org/10.1016/S0031-8914(38)80164-6).

- (75) Escalera-Moreno, L.; Baldoví, J. J.; Gaita-Ariño, A.; Coronado, E. Spin States, Vibrations and Spin Relaxation in Molecular Nanomagnets and Spin Qubits: A Critical Perspective. *Chem. Sci.* **2018**, *9* (13), 3265–3275. <https://doi.org/10.1039/C7SC05464E>.
- (76) Sabisky, E. S.; Anderson, C. H. Spin-Lattice Relaxation of Tm^{2+} in CaF_2 , SrF_2 , and BaF_2 . *Phys. Rev. B* **1970**, *1* (5), 2028–2040. <https://doi.org/10.1103/PhysRevB.1.2028>.
- (77) Castle, J. G.; Feldman, D. W.; Klemens, P. G.; Weeks, R. A. Electron Spin-Lattice Relaxation at Defect Sites; E' Centers in Synthetic Quartz at 3 Kilo-Oersteds. *Phys. Rev.* **1963**, *130* (2), 577–588. <https://doi.org/10.1103/PhysRev.130.577>.
- (78) Castle, J. G.; Feldman, D. W. Resonance Modes at Defects in Crystalline Quartz. *Phys. Rev.* **1965**, *137* (2A), A671–A673. <https://doi.org/10.1103/PhysRev.137.A671>.
- (79) Fielding, A. J.; Fox, S.; Millhauser, G. L.; Chattopadhyay, M.; Kroneck, P. M. H.; Fritz, G.; Eaton, G. R.; Eaton, S. S. Electron Spin Relaxation of Copper(II) Complexes in Glassy Solution between 10 and 120K. *J. Magn. Reson.* **2006**, *179* (1), 92–104. <https://doi.org/10.1016/j.jmr.2005.11.011>.
- (80) Albino, A.; Benci, S.; Tesi, L.; Atzori, M.; Torre, R.; Sanvito, S.; Sessoli, R.; Lunghi, A. First-Principles Investigation of Spin–Phonon Coupling in Vanadium-Based Molecular Spin Quantum Bits. *Inorg. Chem.* **2019**, *58* (15), 10260–10268. <https://doi.org/10.1021/acs.inorgchem.9b01407>.
- (81) Tesi, L.; Lunghi, A.; Atzori, M.; Lucaccini, E.; Sorace, L.; Totti, F.; Sessoli, R. Giant Spin–Phonon Bottleneck Effects in Evaporable Vanadyl-Based Molecules with Long Spin Coherence. *Dalton Trans.* **2016**, *45* (42), 16635–16643. <https://doi.org/10.1039/C6DT02559E>.
- (82) Mirzoyan, R.; Hadt, R. G. The Dynamic Ligand Field of a Molecular Qubit: Decoherence through Spin–Phonon Coupling. *Phys. Chem. Chem. Phys.* **2020**, *22* (20), 11249–11265. <https://doi.org/10.1039/D0CP00852D>.
- (83) Lunghi, A.; Sanvito, S. Multiple Spin–Phonon Relaxation Pathways in a Kramer Single-Ion Magnet. *J. Chem. Phys.* **2020**, *153* (17), 174113. <https://doi.org/10.1063/5.0017118>.
- (84) Lunghi, A.; Sanvito, S. The Limit of Spin Lifetime in Solid-State Electronic Spins. *J. Phys. Chem. Lett.* **2020**, *11* (15), 6273–6278. <https://doi.org/10.1021/acs.jpcllett.0c01681>.
- (85) Escalera-Moreno, L.; Suaud, N.; Gaita-Ariño, A.; Coronado, E. Determining Key Local Vibrations in the Relaxation of Molecular Spin Qubits and Single-Molecule Magnets. *J. Phys. Chem. Lett.* **2017**, *8* (7), 1695–1700. <https://doi.org/10.1021/acs.jpcllett.7b00479>.
- (86) Atzori, M.; Tesi, L.; Benci, S.; Lunghi, A.; Righini, R.; Taschin, A.; Torre, R.; Sorace, L.; Sessoli, R. Spin Dynamics and Low Energy Vibrations: Insights from Vanadyl-Based Potential Molecular Qubits. *J. Am. Chem. Soc.* **2017**, *139* (12), 4338–4341. <https://doi.org/10.1021/jacs.7b01266>.
- (87) Camargo, L. C. de; Briganti, M.; Santana, F. S.; Stinghen, D.; Ribeiro, R. R.; Nunes, G. G.; Soares, J. F.; Salvadori, E.; Chiesa, M.; Benci, S.; Torre, R.; Sorace, L.; Totti, F.; Sessoli, R. Exploring the Organometallic Route to Molecular Spin Qubits: The [CpTi(Cot)] Case. *Angew. Chem.* **2021**, *133* (5), 2620–2625. <https://doi.org/10.1002/ange.202009634>.
- (88) Garlatti, E.; Tesi, L.; Lunghi, A.; Atzori, M.; Voneshen, D. J.; Santini, P.; Sanvito, S.; Guidi, T.; Sessoli, R.; Carretta, S. Unveiling Phonons in a Molecular Qubit with Four-Dimensional

- Inelastic Neutron Scattering and Density Functional Theory. *Nat. Commun.* **2020**, *11* (1), 1751. <https://doi.org/10.1038/s41467-020-15475-7>.
- (89) Lunghi, A. Ligand-Field Contributions to Spin-Phonon Coupling in a Family of Vanadium Molecular Qubits from Multi-Reference Electronic Structure Theory. *ArXiv191204545 Cond-Mat Physicsquant-Ph* **2019**.
- (90) Ballhausen, C. J. *Introduction to Ligand Field Theory*; McGraw-Hill, 1962.
- (91) Solomon, E. I. Inorganic Spectroscopy - An Overview. *Comments Inorg. Chem.* **1984**, *3*, 227–320.
- (92) Pavel, E. G.; Solomon, E. I. Recent Advances in Magnetic Circular Dichroism Spectroscopy. In *Spectroscopic Methods in Bioinorganic Chemistry*; Solomon, E. I., Hodgson, K. O., Eds.; ACS Symposium Series; American Chemical Society: Washington, DC, 1998; Vol. 692, pp 119–135. <https://doi.org/10.1021/bk-1998-0692.ch006>.
- (93) George, S. J.; Lowery, M. D.; Solomon, E. I.; Cramer, S. P. Copper L-Edge Spectral Studies: A Direct Experimental Probe of the Ground-State Covalency in the Blue Copper Site in Plastocyanin. *J. Am. Chem. Soc.* **1993**, *115* (7), 2968–2969. <https://doi.org/10.1021/ja00060a052>.
- (94) Wasinger, E. C.; de Groot, F. M. F.; Hedman, B.; Hodgson, K. O.; Solomon, E. I. L-Edge X-Ray Absorption Spectroscopy of Non-Heme Iron Sites: Experimental Determination of Differential Orbital Covalency. *J. Am. Chem. Soc.* **2003**, *125* (42), 12894–12906. <https://doi.org/10.1021/ja034634s>.
- (95) Glaser, T.; Hedman, B.; Hodgson, K. O.; Solomon, E. I. Ligand K-Edge X-Ray Absorption Spectroscopy: A Direct Probe of Ligand–Metal Covalency. *Acc. Chem. Res.* **2000**, *33* (12), 859–868. <https://doi.org/10.1021/ar990125c>.
- (96) Van Kuiken, B. E.; Hahn, A. W.; Maganas, D.; DeBeer, S. Measuring Spin-Allowed and Spin-Forbidden d–d Excitations in Vanadium Complexes with 2p3d Resonant Inelastic X-Ray Scattering. *Inorg. Chem.* **2016**, *55* (21), 11497–11501. <https://doi.org/10.1021/acs.inorgchem.6b02053>.
- (97) van Schooneveld, M. M.; Gosselink, R. W.; Eggenhuisen, T. M.; Al Samarai, M.; Monney, C.; Zhou, K. J.; Schmitt, T.; de Groot, F. M. F. A Multispectroscopic Study of 3 d Orbitals in Cobalt Carboxylates: The High Sensitivity of 2p3d Resonant X-Ray Emission Spectroscopy to the Ligand Field. *Angew. Chem. Int. Ed.* **2013**, *52* (4), 1170–1174. <https://doi.org/10.1002/anie.201204855>.
- (98) Lundberg, M.; Kroll, T.; DeBeer, S.; Bergmann, U.; Wilson, S. A.; Glatzel, P.; Nordlund, D.; Hedman, B.; Hodgson, K. O.; Solomon, E. I. Metal–Ligand Covalency of Iron Complexes from High-Resolution Resonant Inelastic X-Ray Scattering. *J. Am. Chem. Soc.* **2013**, *135* (45), 17121–17134. <https://doi.org/10.1021/ja408072q>.
- (99) Szilagy, R. K.; Metz, M.; Solomon, E. I. Spectroscopic Calibration of Modern Density Functional Methods Using [CuCl₄]²⁻. *J. Phys. Chem. A* **2002**, *106* (12), 2994–3007. <https://doi.org/10.1021/jp014121c>.
- (100) Scaltrito, D. V.; Thompson, D. W.; O’Callaghan, J. A.; Meyer, G. J. MLCT Excited States of Cuprous Bis-Phenanthroline Coordination Compounds. *Coord. Chem. Rev.* **2000**, *208* (1), 243–266. [https://doi.org/10.1016/S0010-8545\(00\)00309-X](https://doi.org/10.1016/S0010-8545(00)00309-X).

- (101) Mara, M. W.; Fransted, K. A.; Chen, L. X. Interplays of Excited State Structures and Dynamics in Copper(I) Diimine Complexes: Implications and Perspectives. *Coord. Chem. Rev.* **2015**, 282–283, 2–18. <https://doi.org/10.1016/j.ccr.2014.06.013>.
- (102) Stroschio, G. D.; Ribson, R. D.; Hadt, R. G. Quantifying Entatic States in Photophysical Processes: Applications to Copper Photosensitizers. *Inorg. Chem.* **2019**, 58 (24), 16800–16817. <https://doi.org/10.1021/acs.inorgchem.9b02976>.
- (103) Solomon, E. I.; Hadt, R. G. Recent Advances in Understanding Blue Copper Proteins. *Coord. Chem. Rev.* **2011**, 255 (7), 774–789. <https://doi.org/10.1016/j.ccr.2010.12.008>.
- (104) Tsukuda, T.; Nakamura, A.; Arai, T.; Tsubomura, T. Luminescence of Copper(I) Dinuclear Complexes Bridged by Diphosphine Ligands. *Bull. Chem. Soc. Jpn.* **2006**, 79 (2), 288–290. <https://doi.org/10.1246/bcsj.79.288>.
- (105) Higdon, N. J.; Barth, A. T.; Kozlowski, P. T.; Hadt, R. G. Spin–Phonon Coupling and Dynamic Zero-Field Splitting Contributions to Spin Conversion Processes in Iron(II) Complexes. *J. Chem. Phys.* **2020**, 152 (20), 204306. <https://doi.org/10.1063/5.0006361>.
- (106) Mims, W. B. *The Linear Electric Field Effect in Paramagnetic Resonance*; Clarendon Press: Oxford, 1976.
- (107) Fujisaku, T.; Tanabe, R.; Onoda, S.; Kubota, R.; Segawa, T. F.; So, F. T.-K.; Ohshima, T.; Hamachi, I.; Shirakawa, M.; Igarashi, R. pH Nanosensor Using Electronic Spins in Diamond. *ACS Nano* **2019**, 13 (10), 11726–11732. <https://doi.org/10.1021/acs.nano.9b05342>.

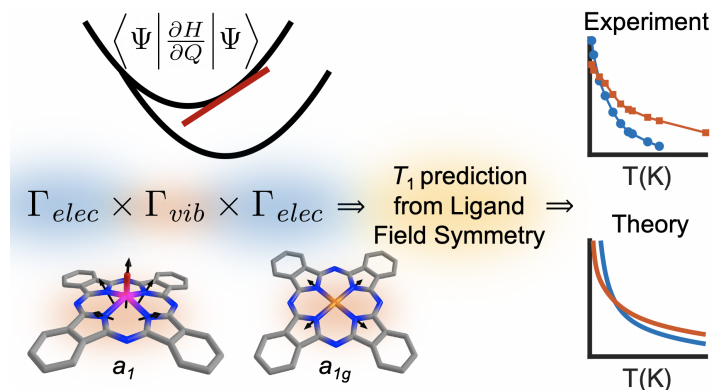
Chapter 2

CHEMICAL DESIGN PRINCIPLES PROLONGING COHERENCE TIMES OF $S = 1/2$ TRANSITION METAL COMPLEXES

Part 1 adapted with permission from:

Mirzoyan, R.; Hadt, R. G. The Dynamic Ligand Field of a Molecular Qubit: Decoherence through Spin–Phonon Coupling. *Phys. Chem. Chem. Phys.* **2020**, *22* (20), 11249–11265. <https://doi.org/10.1039/D0CP00852D>.

Copyright 2020 Royal Society of Chemistry.



Part 2 adapted with permission from:

Kazmierczak, N. P.; Mirzoyan, R.; Hadt, R. G. The Impact of Ligand Field Symmetry on Molecular Qubit Coherence. *J. Am. Chem. Soc.* **2021**, *143* (42), 17305–17315. <https://doi.org/10.1021/jacs.1c04605>.

Copyright 2021 American Chemical Society.

Part 1: The Dynamic Ligand Field of a Molecular Qubit: Decoherence Through Spin–Phonon Coupling

Abstract

Quantum coherence of $S = \frac{1}{2}$ transition metal-based quantum bits (qubits) is strongly influenced by the magnitude of spin–phonon coupling. While this coupling is recognized as deriving from dynamic distortions about the first coordination sphere of the metal, a general model for understanding and quantifying ligand field contributions has not been established. Here we derive a general ligand field theory model to describe and quantify the nature of spin–phonon coupling terms in $S = \frac{1}{2}$ transition metal complexes. We show that the coupling term for a given vibrational mode is governed by: 1) the magnitude of the metal-based spin–orbit coupling constant, 2) the magnitude and gradient in the ligand field excited state energy, which determines the magnitude of ground state orbital angular momentum, and 3) dynamic relativistic nephelauxetic contributions reflecting the magnitude and gradient in the covalency of the ligand–metal bonds. From an extensive series of density functional theory (DFT) and time-dependent DFT (TDDFT) calculations calibrated to a range of experimental data, spin–phonon coupling terms describing minimalistic D_{4h}/D_{2d} $[\text{CuCl}_4]^{2-}$ and C_{4v} $[\text{VOCl}_4]^{2-}$ complexes translate to and correlate with experimental quantum coherence properties observed for Cu(II)- and V(IV)-based molecular qubits with different ligand sets, geometries, and coordination numbers. While providing a fundamental framework and means to benchmark current qubits, the model and methodology described herein can be used to screen any $S = \frac{1}{2}$ molecular qubit candidate and guide the discovery of room temperature coherent materials for quantum information processing.

1-1. Introduction

The coupling of electron spin to phonons/vibrations plays important roles in the dynamical properties of transition metal complexes and materials. For example, spin–phonon coupling plays a major role in the photophysical and photochemical properties of transition metal complexes, including ultrafast spin state switching and intersystem crossing, wherein it provides a strong influence on nonequilibrium dynamics.^{1–5} It is also a major factor in the magnetization dynamics of single

molecule magnets⁶⁻⁹ and coherent materials for quantum information science.¹⁰⁻¹⁶ Beyond molecular systems, spin-phonon coupling also plays important roles in condensed matter (e.g., transition metal oxides) by giving rise to emergent phenomena such as colossal magnetoresistance and high T_C superconductivity,¹⁷⁻²² including vibrational or optical control of these properties.²³⁻²⁶ Thus, there are fascinating intersections between the nature of spin-phonon coupling in molecular systems (e.g., mononuclear, binuclear, and multinuclear transition metal complexes) and solids to explore.

Recent research has explored the use of $S = 1/2$ transition metal complexes as quantum bits (qubits), as the magnetic field split electron spin sublevels ($M_s = \pm 1/2$) provide a two-level system in which a coherent superposition state can be formed. This coherent superposition state, often initiated with a well-defined microwave pulse sequence in an electron paramagnetic resonance (EPR) spectrometer (~ 9 or 35 GHz for X- or Q-band, respectively), can be leveraged to satisfy DiVincenzo's criteria for the physical implementation of a quantum computer.²⁷ However, the lifetime of this state must be significantly longer than the gate operation time, and a significant challenge in molecular qubits is to understand the principles controlling coherence lifetimes. This understanding can then be leveraged for the synthetic design of new transition metal complexes with long-lived coherent states.

The quantities of measure are the longitudinal (spin-lattice) relaxation time, T_1 , the transverse (spin-spin) lattice relaxation time, T_2 , and the phase memory time, T_m , which serves as an "effective" T_2 often measured instead. Recent work has demonstrated a remarkable increase in T_2 when minimizing the quantity of nuclear spins in the environment of the complex, inclusive of both solvent and the ligand set.²⁸ In nuclear spin-free environments, T_1 has proved to be the upper bound to coherence lifetimes, which further motivates efforts to understand contributions to T_1 , including the role of the geometric and electronic structure of the transition metal complex.²⁸⁻⁴⁵ Recent works in this area by Sessoli et al.^{13,44}, Coronado et al.^{14,15}, and Freedman et al.³³ have highlighted specific ligand field contributions to spin-phonon coupling and coherence dynamics. Additionally, T_1 relaxation times will also play a major role when molecular qubits are entangled in dimers,⁴⁶⁻⁵⁰ higher order complexes, or spin-dense arrays,³⁶ which will be required for the realization of quantum computing applications.

While progress has been made experimentally in elongating T_1 and T_m relaxation times of transition metal complexes at low temperatures (< 80 K), very few complexes exhibit coherence properties up to room temperature. For example, vanadyl phthalocyanine (VOPc) diluted in a diamagnetic titanyl matrix exhibits room temperature coherence with a T_m of ~ 1 μ s at 300 K, even in the presence of a

nuclear spin containing environment.³⁷ Spin echoes have also been observed up to room temperature in the benzene-1,2-dithiolate (bdt) ligated $(\text{Ph}_4\text{P})_2[\text{Cu}(\text{C}_6\text{H}_4\text{S}_2)_2]^{33}$ ($[(\text{Cu}(\text{bdt})_2)]^{2-}$) and the maleonitriledithiolate (mnt) ligated $(\text{Ph}_4\text{P})_2[\text{Cu}(\text{mnt})_2]^{51}$ ($[(\text{Cu}(\text{mnt})_2)]^{2-}$) complexes diluted in diamagnetic Ni lattices. At lower temperatures ($\sim < 80$ K), relaxation is dominated by the direct, Raman, and Orbach mechanisms, while a mechanism involving spin–phonon coupling and the modulation of the energy gap between the $M_S = \pm \frac{1}{2}$ sublevels dominates at higher temperatures.^{52,53} Thus, in order to achieve room temperature coherent materials, spin–phonon coupling and its contribution to T_1 must be better understood. Doing so will allow for direct manipulation of geometric and electronic structure to overcome this barrier. Furthermore, while achieving room temperature coherence is of great technological interest for quantum information processing, these room temperature coherent materials will also provide exciting opportunities for the fundamental studies of spin–phonon coupling and will complement studies of single molecule magnets and photoactive transition metal complexes.

Many of the highest performing $S = \frac{1}{2}$ qubit candidates feature similar structural motifs: 1) a four coordinate square planar Cu(II), or 2) a four coordinate vanadyl moiety featuring a triple bond between the V(IV) and oxo ligand. Comparisons between 1) and 2) and six coordinate, pseudo O_h V(IV) complexes have also been made to highlight structural and electronic contributions to T_1 .^{13,33,54} As shown below, multiple contributions need to be accounted for in order to make direct comparisons between $S = \frac{1}{2}$ molecular qubits and thus to understand the origins of their coherence times at higher temperatures.

Given coherent superposition states are generated within the $M_S = \pm \frac{1}{2}$ sublevels of a metal complex, coherence properties are expected to be influenced by the same contributions governing g values. Ligand field theory (LFT) has provided expressions for understanding geometric and electronic structure contributions to the g values of Cu(II) complexes.⁵⁵ Here this model is extended more generally to a dynamic regime, which allows for the direct understanding of spin–phonon coupling contributions to the g values of $S = \frac{1}{2}$ transition metal complexes. Using the ORCA program,^{56,57} the LFT expressions are further supported by a range of spectroscopically calibrated density functional theory (DFT) and time-dependent DFT (TDDFT) calculations on the well-studied D_{4h} and D_{2d} $[\text{CuCl}_4]^{2-}$ and C_{4v} $[\text{VOCl}_4]^{2-}$.^{58,59} The correlations between experiment and LFT, DFT, and TDDFT calculations have elucidated the key factors that contribute to the nature of spin–phonon coupling terms in $S = \frac{1}{2}$ transition metal complexes, thus providing a detailed orbital and bonding

picture for the first time. The model presented here indicates spin–phonon coupling terms are governed by the magnitude of the metal-based spin–orbit coupling (SOC) constant, excited state mixing of orbital angular momentum into the ground state, and dynamic relativistic nephelauxetic contributions. The latter contribution is directly related to the covalencies of ligand–metal bonds and can modify the metal-based SOC constant from that of the free ion in a dynamic manner. Also, correlations between dynamic ground state orbital angular momentum and excited state coupling terms and their relations to spin–phonon coupling terms are drawn for the first time. Specific group theoretical correlations between high and lower symmetry point groups further provide a means to evaluate spin–phonon coupling terms across transition metal complexes and molecular qubits featuring different ligand sets, geometries, and coordination numbers. The model is in excellent agreement with a wide range of experimental quantum coherence properties of Cu(II)- and V(IV)-based molecular qubits and therefore provides a means to rapidly evaluate spin–phonon coupling terms in any $S = 1/2$ transition metal complex, including new qubit candidates.

2-1. Results

2-1.1. Dynamic Ligand Field Theory of Cu(II) g Values

D_{4h} $[\text{CuCl}_4]^{2-}$ has a ${}^2B_{1g}$ (x^2-y^2) ground state (Figure 2-1.1). In the absence of SOC, the ${}^2B_{1g}$ ground state contains no orbital angular momentum and thus would exhibit a g value of 2.0023 (e.g., g_e of the free electron) in the presence of a magnetic field. However, SOC from excited states mixes orbital angular momentum into the ${}^2B_{1g}$ ground state. This is shown in Figure 2-1.1 for D_{4h} $[\text{CuCl}_4]^{2-}$. Including SOC, the ${}^2B_{1g}$ ground state (Γ_7) can mix with both the ${}^2B_{2g}$ (Γ_7) and 2E_g ($\Gamma_6 + \Gamma_7$) excited states (Figure 2-1.1). From first order perturbation theory, the ground state reflecting the contributions of excited state SOC is:⁵⁵

$$|{}^2B'_{1g}\rangle = |x^2 - y^2\rangle - \frac{\lambda\langle x^2 - y^2 | \mathbf{L} \cdot \mathbf{S} | xy \rangle}{E_{B_{2g}}} |xy\rangle - \frac{\lambda\langle x^2 - y^2 | \mathbf{L} \cdot \mathbf{S} | xz, yz \rangle}{E_{E_g}} |xz, yz\rangle \quad (2-1.1)$$

where $\lambda = \pm\zeta/2S$ (-830 cm^{-1} for Cu(II)), \mathbf{L} and \mathbf{S} are the total orbital and spin angular momentum operators, respectively, and $E_{B_{2g}}$ and E_{E_g} are the energies of the ${}^2B_{2g}$ and 2E_g excited states,

respectively.⁵⁵ For greater or less than half-filled electron configurations, either the negative or positive components of $\pm\zeta$ are used, respectively.

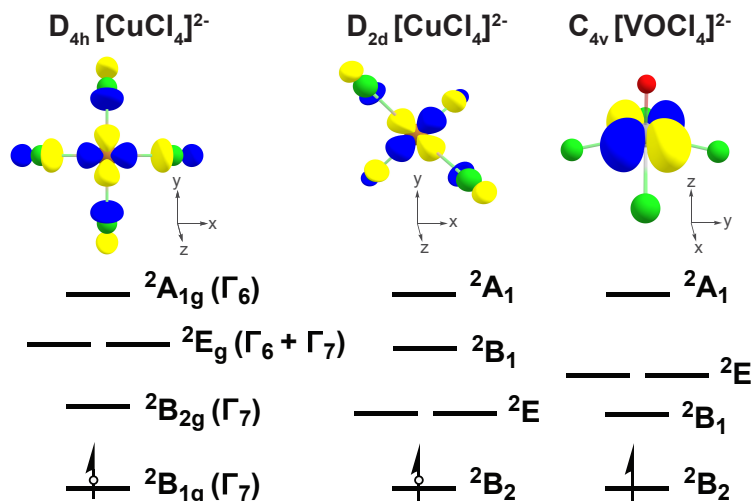


Figure 2-1.1. β -LUMOs and qualitative excited state energy diagrams for transition metal complexes considered in the Results sections. The hole formalism is used for $[\text{CuCl}_4]^{2-}$, with SOC symmetries given for D_{4h} .

An applied magnetic field will project out different components of L (e.g., $L_{x,y,z}$). Consequently, the magnitude of orbital angular momentum mixing into the ground state is anisotropic. The resulting perturbed ground state wavefunction can be modified to include covalent ligand–metal interactions. For $H \parallel z$ and taking the covalency of the b_{1g} and b_{2g} orbitals into account, the expression for g_{\parallel} (g_z) becomes:⁵⁵

$$g_{\parallel} = g_e - \frac{8\lambda\alpha_1^2\beta_1^2}{E_{B_{2g}}}, \quad (2-1.2)$$

where α_1 and β_1 are the coefficients reflecting the amount of $d(xy)$ and $d(x^2-y^2)$ character, respectively. With $H \parallel x,y$ and considering covalent interactions, equation 2-1.2 for g_{\perp} becomes:

$$g_{\perp} = g_e - \frac{2\lambda\gamma_1^2\beta_1^2}{E_{E_g}}. \quad (2-1.3)$$

where γ_1 is the coefficient reflecting the d(xz,yz) orbital contribution. From equations 2-1.2 and 2-1.3, increasing the covalency of the ligand–metal bonds will decrease the deviation from 2.0023 through a relativistic nephelauxetic effect.⁶⁰ The prefactors of 8 in g_{\parallel} and 2 in g_{\perp} come from operating on the spin orbit perturbed ground state with the orbital angular momentum operators, L_i .

The splitting between the ground state $M_s = \pm 1/2$ sublevels and the resulting coherent superposition lifetime is thus sensitive to dynamic behavior of the ligand field excited states and the covalencies of ligand–metal bonds. Fluctuations in the energy gap of a two-level system result in decoherence, and a coherence lifetime has been previously related to the variance in the energy gap by an inverse square root dependence.⁶¹ As the g_z value and the $M_s = \pm 1/2$ energy gap are directly proportional to one another, the variance in the energy gap can be monitored by proxy of the g value. Therefore, a descriptor to reflect such fluctuations is the variance in g_z (equation 2-1.5). To describe the M vibrational modes denoted by Q_i , we separate the total harmonic vibrational wave function, Ψ_{vib} , as a product of harmonic vibrational wave functions of each mode, Ψ_i , with the vibrational quantum numbers $N = \{n_1, \dots, n_R\}$.

$$\Psi_{vib}^N(Q_1, \dots, Q_R) = \prod_{i=1}^M \Psi_i^{n_i}(Q_i). \quad (2-1.4)$$

The variance in g_z can then be expressed as:

$$\text{Var}[g_z] = \langle g_z^2 \rangle - \langle g_z \rangle^2 \approx \frac{\hbar}{2\pi} \sum_{i=1}^R \left(\frac{\partial g_z}{\partial Q_i} \right)_e^2 \left(n_i + \frac{1}{2} \right) \left(\frac{1}{v_i m_i} \right) + \frac{\hbar}{4\pi} \sum_{i=1}^R \left(\frac{\partial^2 g_z}{\partial Q_i^2} \right)_e^2 \left(n_i^2 + n_i + \frac{1}{4} \right) \left(\frac{1}{v_i^2 m_i^2} \right). \quad (2-1.5)$$

In equation 2-1.5, $\left(\frac{\partial g_z}{\partial Q_i} \right)$ and $\left(\frac{\partial^2 g_z}{\partial Q_i^2} \right)$ are the equilibrium values of $\frac{\partial g_z}{\partial Q_i}$ and $\frac{\partial^2 g_z}{\partial Q_i^2}$ when $Q_i = 0$, respectively, v_i are the harmonic frequencies, and m_i are the reduced masses. To simplify the treatment of g_z , which depends on the position along a vibrational coordinate Q_i , we separate the normal modes into two types under the harmonic approximation: even modes, where $g_z(Q_{even}) = g_z(-Q_{even})$ and odd modes, where $g_z(Q_{odd}) = -g_z(-Q_{odd})$. For the former, at the equilibrium geometry, $\frac{\partial g_z}{\partial Q_{even}} = 0$ and $\frac{\partial^2 g_z}{\partial Q_{even}^2} \neq 0$. For the latter, $\frac{\partial g_z}{\partial Q_{odd}} \neq 0$ and $\frac{\partial^2 g_z}{\partial Q_{odd}^2} = 0$. The use of the terms “even” and “odd” throughout the manuscript refer only to parity of the function of g along the vibrational coordinate Q_i and is not to be confused with the parity of Hermite polynomials, which define the eigenstates of the quantum harmonic oscillator.

Under the harmonic approximation, the first term in the expansion (equation 2-1.5) is non-zero for odd modes, while the second term is non-zero for even modes. It is clear from this expression that odd modes have a larger impact on the variance of g_z and consequently the coherence lifetime. $\partial g_z / \partial Q_i$ and $\partial^2 g_z / \partial Q_i^2$ at the equilibrium geometries can be directly related to ligand field parameters in equations 2-1.2 and 2-1.3. Taking the partial derivative of equation 2 with respect to a vibration coordinate Q_i gives:

$$\partial g_z / \partial Q_i = 8\xi \frac{\eta \left(\frac{\partial E_{B_{2g}}}{\partial Q_i} \right) - E_{B_{2g}} \left(\frac{\partial \eta}{\partial Q_i} \right)}{\left(E_{B_{2g}} \right)^2} \quad (2-1.6)$$

where $\eta = \alpha_1^2 \beta_1^2$ and provides adjustments due to covalency. We make the assumption that α_1^2 and β_1^2 change linearly with one another at minimal displacements about the equilibrium position and can therefore be represented by a single ‘‘covalency’’ parameter, η . In the regime where $\eta \left(\frac{\partial E_{B_{2g}}}{\partial Q_i} \right) \gg E_{B_{2g}} \left(\frac{\partial \eta}{\partial Q_i} \right)$, $\partial g_z / \partial Q_i$ will have an inverse square dependence on $E_{B_{2g}}$. Conversely, when $\eta \left(\frac{\partial E_{B_{2g}}}{\partial Q_i} \right) \ll E_{B_{2g}} \left(\frac{\partial \eta}{\partial Q_i} \right)$, $\partial g_z / \partial Q_i$ will have an inverse dependence on $E_{B_{2g}}$ and a linear dependence with covalency, η . In both cases, the role of the transition energy is clear: The higher the energy separation from the ground state, the lower the $\partial g_z / \partial Q_i$ term by at least an inverse dependence. However, as shown below, the complexes considered here are largely in the regime corresponding to an inverse square dependence on $E_{B_{2g}}$.

For even modes under the harmonic approximation and at the equilibrium geometry, $\frac{\partial E_{B_{2g}}}{\partial Q_i} = \frac{\partial \eta}{\partial Q_i} = 0$. To describe the variance in the energy gap for even modes, a second partial derivative of g_z with respect to the vibrational coordinate is needed.

$$\partial^2 g_z / \partial Q_i^2 = 8\xi \frac{(E_{B_{2g}}) \left(-\frac{\partial^2 \eta}{\partial Q_i^2} \right) + \eta \left(\frac{\partial^2 E_{B_{2g}}}{\partial Q_i^2} \right)}{\left(E_{B_{2g}} \right)^2} \quad (2-1.7)$$

The spin–phonon coupling terms $\partial g_z / \partial Q_i$ and $\partial^2 g_z / \partial Q_i^2$ for odd and even modes, respectively, are therefore related to spectroscopic observables and quantities that are easily calculable. It should be noted that the treatment above has been generated with respect to g_z of D_{4h} Cu(II), but can be done analogously for any $S = 1/2$ system. At the very least, the equations above can be used as screening tools to estimate relative coherence lifetimes of molecular qubits by estimating parameters such as the relevant d-d transition energies and covalencies of the ligand–metal bonds, which can be obtained from quantum chemical calculations. The spin–phonon coupling terms in equations 6 and 7 have been computed for a large scope of $S = 1/2$ transition metal qubits reported in the literature to establish ligand field principles for manipulating coherence lifetimes.

Below, we utilize D_{4h} and D_{2d} $[\text{CuCl}_4]^{2-}$ as structural models to quantitatively evaluate this LFT model using DFT and TDDFT calculations and to define the nature of spin–phonon coupling terms in Cu(II) complexes. This analysis is then translated to C_{4v} $[\text{VOCl}_4]^{2-}$ and finally to a variety of Cu(II)- and V(IV)-based molecular qubits reported in the literature.

2-1.2. Spin–Phonon Coupling Terms in $[\text{CuCl}_4]^{2-}$

2-1.2.1. D_{4h} $[\text{CuCl}_4]^{2-}$

Depending on the counterion, $[\text{CuCl}_4]^{2-}$ can exist in a series of distorted T_d geometries along the D_{4h} to D_{2d} coordinate governed by the Cl–Cu–Cl angle, α . By correlating to a range of spectroscopic data on D_{4h} and D_{2d} $[\text{CuCl}_4]^{2-}$, Solomon et al.^{58,59} have developed a spectroscopically calibrated DFT-based methodology to accurately describe the bonding (e.g., covalency) by incorporating 38% Hartree-Fock (HF) exchange into the exchange correlation functional.^{58,59} This methodology has been used for calculations presented in this section. A calibrated amount of HF exchange is determined independently for each case considered in subsequent sections.

The DFT calculated g values and excited state energies for an idealized D_{4h} $[\text{CuCl}_4]^{2-}$ structure are compared to experiment in Tables 2-1.1 and 2-1.2, respectively. Idealized structures of D_{2d} and D_{4h} $[\text{CuCl}_4]^{2-}$ give nearly identical results to those from crystal structures⁶²; for a direct comparison to group theory, only results from idealized structures are presented here (see Methods in Supporting Information and Table S1a/b for bond distances and angles). Experimentally, the D_{4h}

g_z and $g_{x,y}$ values are 2.221 and 2.040, respectively.^{63,64} The calculated values for an idealized geometry based on the X-ray crystallographic structure are 2.204 and 2.056, respectively, in agreement with experiment. The HF dependence of the g_z value for this structure is given in Figure 2-1.S1.

In D_{4h} , the irreducible representations for the vibrational modes are $\Gamma_{vib} = a_{1g} + b_{1g} + b_{2g} + a_{2u} + b_{2u} + 2e_u$. The energies, symmetry labels, and scaled vector displacements for all nine normal modes of vibration using the idealized D_{4h} $[\text{CuCl}_4]^{2-}$ structure are given in Table S2a. Spin-phonon analyses using the calculated g values were carried out as described in the Methods section. Briefly, the coupling term for a given g value and vibrational mode is determined by calculating the g value along positive and negative distortions about a given normal mode, and the magnitude of the coupling term can be qualitatively estimated by the magnitude of the slope (for odd modes) or curvature (for even modes). The spin-phonon coupling term calculations for the g_z value of idealized D_{4h} $[\text{CuCl}_4]^{2-}$ are given in Figure 2-1.2A, and their frequencies and fits are given in Table 2-1.S3a. Note that the fits are reported for the scaled vibrational displacements and are converted for comparison purposes when possible to \AA^{-1} or $^\circ^{-1}$. The largest coupling term is observed for the totally symmetric a_{1g} breathing mode (mode 7, 296 cm^{-1}), which shows a strong linear dependence between the g_z value and the vibrational coordinate. Note the calculated frequency for the a_{1g} mode is in fairly good agreement with experimental vibrational energy (276 cm^{-1}).⁵⁹ For the a_{1g} mode, a linear fit along the vibrational mode, Q_i , provides a slope of $-0.241 \text{ g}_z/Q_i$ ($0.482 \text{ g}_z/\text{\AA}$). Interestingly, the spin-phonon coupling terms for the totally symmetric stretch exhibit insightful trends when compared to D_{2d} $[\text{CuCl}_4]^{2-}$ and C_{4v} $[\text{VOCl}_4]^{2-}$, while also correlating with experimental coherence properties as discussed below.

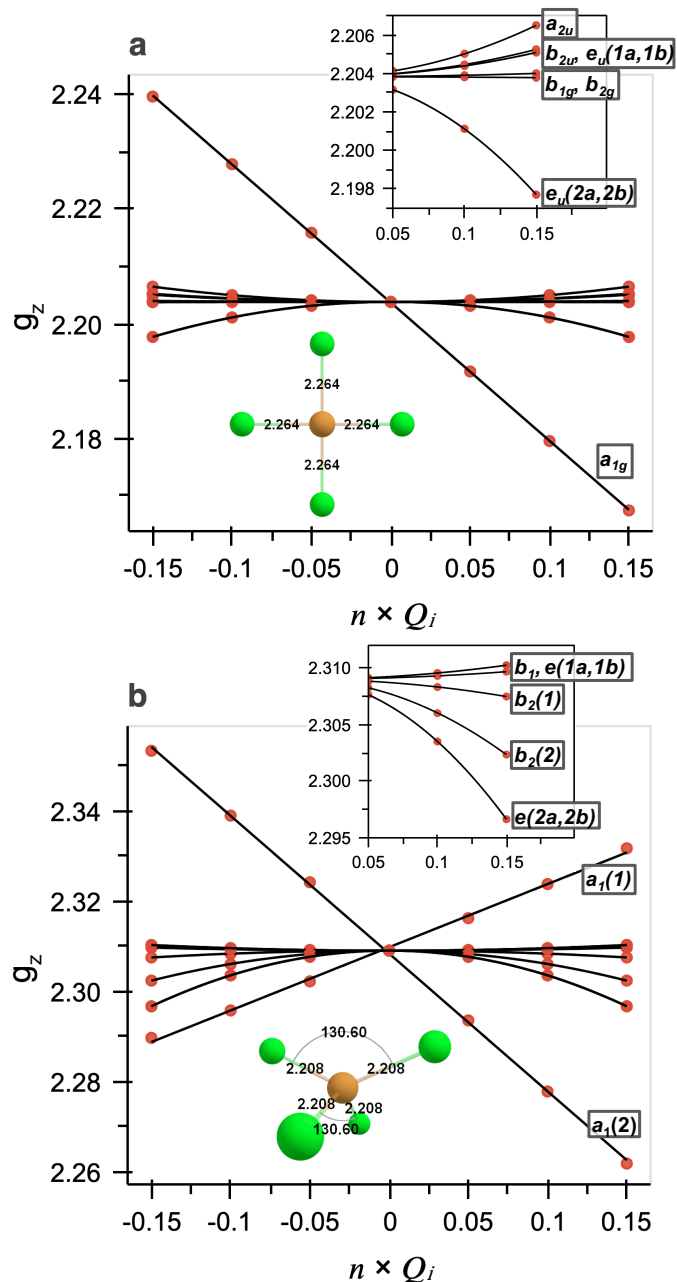


Figure 2-1.2. Evolution of the g_z values along each normal mode of vibration for idealized structures of (a) D_{4h} and (b) D_{2d} $[\text{CuCl}_4]^{2-}$. Insets provide zoomed in views for positive distortion and pictorial representations of the respective molecules.

Of the other vibrational modes comprising 1 (b_{2u} , -86 cm^{-1}), 2 (a_{2u} , 140 cm^{-1}), 3/4 ($e_u(1a, 1b)$, 172 cm^{-1}), and 8/9 ($e_u(2a, 2b)$, 342 cm^{-1}) are even modes with quadratic coupling terms. The a_{2u} and $e_u(2a, 2b)$ modes exhibit the largest coupling terms (0.119 and $-0.272 \text{ g}_z/Q_i$, respectively) and involve motion of the metal out-of-plane and in-plane, respectively (Table 2-1.S2a). For the a_{2u}

mode, the slope can be better quantified by using the amount of metal displacement and gives $0.216 \text{ g}_z/\text{\AA}$. The coefficients for the b_{2u} and e_u ($1a$, $1b$) modes are -0.063 and $-0.056 \text{ g}_z/Q_i$, respectively. While the quadratic spin–phonon coupling terms of the e_u ($2a$, $2b$) modes are the largest, they also have the highest calculated frequencies (342 cm^{-1}) and are therefore not considered in detail here, as these modes will not be as thermally populated past their zero-point energies at practical temperatures. Finally, modes 5 (b_{2g} , 183 cm^{-1}) and 6 (b_{1g} , 198 cm^{-1}) exhibit negligible spin–phonon coupling terms with the g_z value (Table 2-1.S3a). Note, however, the corresponding coupling terms are substantially smaller when the magnetic field is oriented along L_x or L_y (i.e., for $g_{x,y}$ values). Also, the spin–phonon coupling term for the b_{2u} mode is increased substantially in the D_{2d} structure. These observations are discussed further below. It should be noted that the imaginary frequency of the b_{2u} mode is a result of the D_{4h} structure not being an equilibrium structure in the gas phase, as computed by DFT. However, the nature and symmetry of the mode tracks with group theoretical predictions and the energy of the mode is not consequential for the magnitude of the spin–phonon coupling term.

Table 2-1.1. Comparisons between a variety of experimental and calculated g values for D_{4h} and D_{2d} $[\text{CuCl}_4]^{2-}$ and other Cu(II) complexes.

Molecule	g_z		g_y		g_x	
	Exp.	Calc.	Exp.	Calc.	Exp.	Calc.
$D_{4h} [\text{CuCl}_4]^{2-}$ ^a	2.221	2.204	2.040	2.057	2.040	2.054
$D_{4h} [\text{CuCl}_4]^{2-}$ ^b	2.221	2.204	2.040	2.056	2.040	2.056
$D_{2d} [\text{CuCl}_4]^{2-}$ ^{a,c}	2.435	2.304	2.079	2.123	2.079	2.065
$D_{2d} [\text{CuCl}_4]^{2-}$ ^b	2.435	2.309	2.079	2.095	2.079	2.095
$[\text{Cu}(\text{mnt})_2]^{2-}$ ^d	2.091	2.085	-	2.039	-	2.036
CuPc ^e	2.199	2.163	2.052	2.026	2.052	2.026
CuN_4 (H) ^f	2.19	2.196	-	2.055	-	2.063
CuN_4 (Me) ^f	2.205	2.218	-	2.053	-	2.078
CuN_4 (t-Bu) ^f	2.28	2.273	-	2.049	-	2.141
$[\text{Cu}(\text{bdt})_2]^{2-}$ ^g	2.085	2.047	2.019	2.015	2.019	2.016
$[\text{Cu}(\text{bds})_2]^{2-}$ ^h	2.082	2.089	2.018	2.053	2.018	2.031

^a Crystal structure from ref. 62, g values from ref. 63.

^b Idealized structure from crystal structure.

^c g values from ref. 64.

^d Crystal structure and g values from ref. 14.

^e DFT optimized structure, g values from ref. 73.

^f DFT optimized structure, experimental g values from ref. 70.

^g Crystal structure from ref. 74, g values from ref. 33.

^h Crystal structure and g values from ref. 33.

Table 2-1.2. Comparisons between experimental and calculated ligand field transitions for D_{4h} and D_{2d} $[\text{CuCl}_4]^{2-}$.

Exp. (cm^{-1}) ^c	Assignment	Calc. (cm^{-1}) ^a	Calc. (cm^{-1}) ^b	Exp. (cm^{-1}) ^c	Assignment	Calc. (cm^{-1}) ^a	Calc. (cm^{-1}) ^b
D_{4h}				D_{2d}			
12000	${}^2\text{B}_{1g} \rightarrow {}^2\text{B}_{2g}$	14470	14475	5500	${}^2\text{B}_2 \rightarrow {}^2\text{E}$	6470	6825
13500	${}^2\text{B}_{1g} \rightarrow {}^2\text{E}_g$	14525	14610			7360	6825
		14685	14610	8000	${}^2\text{B}_2 \rightarrow {}^2\text{B}_1$	10465	10440
16500	${}^2\text{B}_{1g} \rightarrow {}^2\text{A}_{1g}$	15485	15485	9400	${}^2\text{B}_2 \rightarrow {}^2\text{A}_1$	9130	9005

^a X-ray crystal structure from ref. 62.

^b Idealized structure from crystal structure.

^c Experimental d-d transitions from ref. 65.

Given the ligand field origin of the SOC induced mixing of orbital angular momentum into the ${}^2\text{B}_{1g}$ ground state (Figure 2-1.1), an analysis of the excited state energies was also carried out. Comparisons between experimental and calculated ligand field transitions are given in Table 2-1.2. Experimentally, the ${}^2\text{B}_{2g}$, ${}^2\text{E}_g$, and ${}^2\text{A}_{1g}$ ligand field transitions of D_{4h} $[\text{CuCl}_4]^{2-}$ are observed at 12000, 13500, and 16500 cm^{-1} , respectively.⁶⁵ From equation 2-1.2, the ${}^2\text{B}_{2g}$ excited state can introduce ground state orbital angular momentum through SOC, and the g_z value is inversely dependent on the ligand field energy. A TDDFT calculation gives an energy of 14470 cm^{-1} , in fairly good agreement.

The vibrational analysis of the ${}^2\text{B}_{2g}$ ligand field energy is given in Figure 2-1.3a, with corresponding fits given in Table 2-1.S3a. The calculation of the ligand field energy along a given vibrational mode provides the excited state linear coupling term, which takes into account the displacement between the ground and excited state potential energy surfaces (Figure 2-1.4a). The degree of distortion can be estimated by evaluating the effect of electron-nuclear coupling on the total energy of the excited state, E_{ES} :⁵⁵

$$E_{elec-nuc}^e = \left\langle \psi_e^{elec} \left| \frac{\partial \mathbf{H}_{ES}}{\partial Q_i} \right| \psi_e^{elec} \right\rangle Q_i \quad (2-1.8)$$

For non-zero values of this integral, the excited state will distort along Q_i by a value ΔQ_i ; the excited state coupling term is determined by calculating the energy change in the electronic transition to the excited state ψ_e with a change along the coordinate Q_i . This is shown qualitatively for D_{4h} and D_{2d} structures in Figure 2-1.4a. The partial derivative ($\partial E/\partial Q_i$) reflects the relative curvature of the

excited state potential energy surface near the ground state equilibrium geometry (i.e., in the vicinity of the Franck-Condon region). The excited state coupling term therefore provides a means to quantify the change in excited state orbital angular momentum that can SOC into the ground state along a given vibrational coordinate.

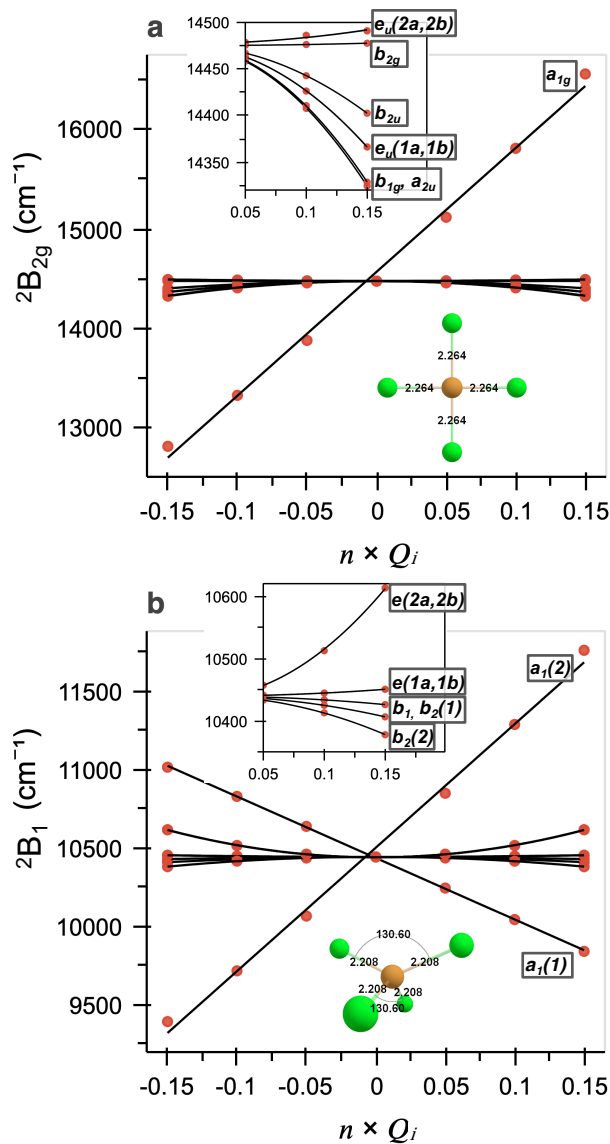


Figure 2-1.3. Evolution of $d(x^2-y^2) \rightarrow d(xy)$ transition energies for (a) D_{4h} and (b) D_{2d} $[\text{CuCl}_4]^{2-}$.

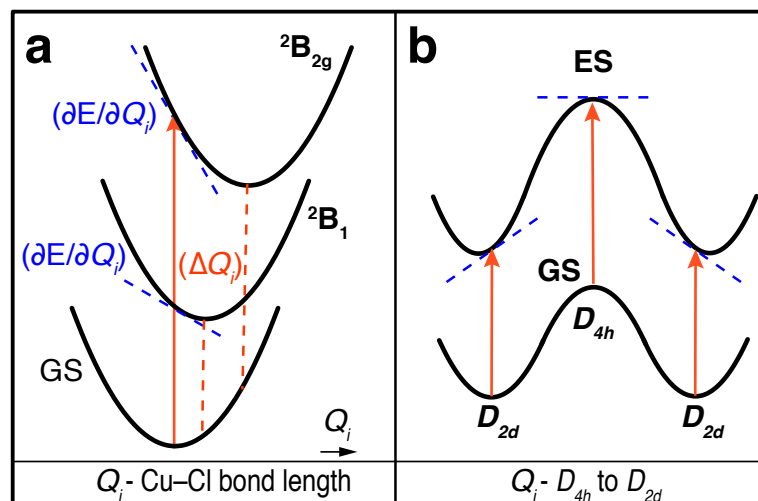


Figure 2-1.4. Qualitative potential energy surfaces of $[\text{CuCl}_4]^{2-}$. (a) Excited state linear coupling terms for the totally symmetric Cu–Cl stretch, and (b) change in the excited state linear coupling term upon distorting from D_{4h} to D_{2d} . To simplify (a), the ground state potential energy surfaces of D_{4h} and D_{2d} are overlaid even though their Cu–Cl bonds do not have the same equilibrium distance.

As with the g_z value analysis, the totally symmetric a_{1g} mode exhibits the largest coupling term for the ${}^2B_{1g}$ excited state (Figure 2-1.3a), namely $12405 \text{ cm}^{-1}/Q_i$ or $-24940 \text{ cm}^{-1}/\text{\AA}$. The quadratic terms for the a_{2u} mode are $-6700 \text{ cm}^{-1}/Q_i$ and $-12230 \text{ cm}^{-1}/\text{\AA}$. Note the slopes and curvatures of the ${}^2B_{2g}$ energy are inverted relative to those for the g_z value slope (Figure 2-1.2a). This behavior is consistent with equation 2-1.2 and the inverse energy dependence on SOC. The other modes discussed above that exhibit spin–phonon coupling terms with the g_z value also exhibit inverted behavior. For example, the a_{2u} and b_{2u} modes exhibit positive quadratic behaviors in Figure 2-1.2a and negative ones in Figure 2-1.3a. Note the b_{1g} mode does not exhibit a substantial coupling term for the g_z value but does with the ${}^2B_{2g}$ energy. This is due to the nature of the b_{1g} vibrational distortion (see Table 2.S2a), which lowers the symmetry from D_{4h} to D_{2h} by making two of the Cu(II)–Cl bonds, and thus the x- and y-axes, inequivalent. This turns on a small mixing between a forbidden (in D_{4h}) ${}^2A_{2g}$ charge transfer state and the ${}^2B_{2g}$ ligand field state. Both of these states transform as ${}^2B_{1g}$ upon lowering symmetry to D_{2h} . The energy of the forbidden ${}^2A_{2g}$ state exhibits a strong dependence on the b_{1g} mode distortion. Thus, we ascribe the energy shift of the ${}^2B_{2g}$ state observed in Figure 2-1.3a to this mixing. Also, other than e_u ($2a$, $2b$) modes, no other modes exhibit this distortion induced mixing, and they maintain their original ligand field compositions observed for the D_{4h} structure. Thus, the excited state coupling term (equation 2-1.8) for the ${}^2B_{1g} \rightarrow {}^2B_{2g}$

excitation provides a means to evaluate the vibrationally induced change in ground state orbital angular momentum and its effect on the g_z value.

In addition to excited state SOC, equation 2-1.2 indicates covalency contributions are important determinants of molecular g values. Experimentally, the Cu(d) character for D_{4h} $[\text{CuCl}_4]^{2-}$ is 0.62 ± 0.02 .^{58,59} The β -LUMO of the model considered here is given in Figure 2-1.1 and reflects a total Cu(d) character and spin density of 65 % and 0.668 from Löwdin population analysis and spin density, respectively. As shown below, the measure of covalency at the equilibrium geometry, by proxy of the spin density, is a key determinant to understanding its role in spin–phonon coupling terms. Thus, the 38 % HF method applied to a complex with known Cu(d) character provides an excellent starting point. Fits for the spin-phonon coupling term analyses using Cu spin densities are given in Table 2-1.S3e. The fits for the a_{1g} mode give values of $-0.157 \text{ SD}/Q_i$ and $0.221 \text{ SD}/\text{Å}$. As observed above for g_z values and the ${}^2B_{2g}$ energies, the largest coupling term for Cu spin density is observed for the totally symmetric a_{1g} mode. For this mode, the change in covalency along the a_{1g} coordinate contributes in the same direction/sign to the change in g_z value as the ${}^2B_{2g}$ ligand field energy. This is also the case for the b_{2u} mode. The concerted contribution from ligand field energies and covalency is not observed for all modes, however (Figure 2-1.S3-8). From example, the Cu spin density contribution for the a_{2u} mode opposes the contribution to the g_z value from the ${}^2B_{1g}$ excited state and illustrates an important interplay between excited state SOC and covalency to the resulting spin–phonon coupling term for the g_z value. See Figure 2-1.S9 and accompanying text for further analyses of the qualitative decomposition of the spin–phonon coupling term into contributions from ground state covalency and orbital angular momentum from excited state SOC.

The spin–phonon coupling terms for the $g_{x,y}$ values for the D_{4h} structure are given in Figure 2-1.S10, with the corresponding fits given in Table 2-1.S3b and 2-1.S3c. The coupling terms for the g_x - and g_y values are very similar except for the inversion of the e_u modes (e.g., the $1a/2a$ components switch with the $2a/2b$ components). As with the g_z value, the largest coupling term for the $g_{x,y}$ values is observed for the a_{1g} mode ($-0.072 \text{ } g_z/Q_i$). However, the coupling term for the $g_{x,y}$ values is significantly less than that observed for g_z values ($-0.241 \text{ } g_z/Q_i$) by a factor of ~ 3.3 . This difference reflects the ratio of the prefactors given in equations 2-1.2 and 2-1.3, as well as contributions from anisotropic covalency. The other modes show a similar behavior between g_x - and g_z values and therefore are not discussed here. However, while the b_{1g} mode exhibited a negligible spin–phonon coupling term for the g_z value (Figure 2-1.2a), it exhibits a larger coupling term for the $g_{x,y}$ values

(Figures 2-1.S8a/b). Thus, the main differences between the g_z and $g_{x,y}$ regions is the magnitude and anisotropy of the spin–phonon coupling terms, with different vibrational modes (e.g., b_{1g} mode) being selectively activated in the g_{\perp} region.

The corresponding spin–phonon coupling terms of the two components of the 2E_g excited state are given in Figure 2-1.S11. The correlation between the $g_{x,y}$ values and the excited state SOC is similar to that laid out for the g_z value and is therefore not addressed further here.

In summary for D_{4h} $[\text{CuCl}_4]^{2-}$, up to the totally symmetric stretch, the vibrational modes that exhibit the largest spin–phonon coupling terms are the a_{2u} and a_{1g} modes, with the b_{2u} and e_u ($1a$, $1b$) modes having smaller coupling terms. Excited state SOC and covalent contributions are both important quantifiers and determinants of spin–phonon coupling terms, and they can either work cooperatively or oppose one another (Figure 2-1.5). Lastly, the spin–phonon coupling terms are anisotropic between the g_{\parallel} and g_{\perp} regions, with a general decrease in coupling terms in the g_{\perp} region and an activation of different vibrational modes. This anisotropy may be an interesting way to experimentally probe and explore spin–phonon coupling terms in transition metal complexes and qubits.

2-1.2.2. D_{2d} and Comparisons to D_{4h} $[\text{CuCl}_4]^{2-}$

Going from D_{4h} to D_{2d} $[\text{CuCl}_4]^{2-}$, the g values shift from 2.221 and 2.040 to 2.435 and 2.079, respectively (Table 2.1). The experimental increase in g values is reproduced by the DFT calculated g values (2.309 and 2.095, respectively). In addition, the ligand field strength decreases significantly upon distorting to D_{2d} , which results in a decrease in the ligand field transition energies to 5500, 8000, and 9400 cm^{-1} . The transition at 8000 cm^{-1} is the ${}^2B_2 \rightarrow {}^2B_1$ transition, which is predicted at 10440 cm^{-1} using TDDFT. The irreducible representations of the normal modes of vibration in D_{2d} are $\Gamma_{vib} = 2a_1 + b_1 + 2b_2 + 2e$. Note in going from D_{4h} to D_{2d} group theory requires the ground state to transform as 2B_2 (Figure 2-1.1).⁶⁵ While this formally leads to a switch of the ground state from x^2-y^2 to xy , the overall orientation of the orbital with respect to the ligand–metal bonds does not change upon lowering symmetry from D_{4h} to D_{2d} , and we therefore retain the x^2-y^2 labeling as done previously.⁵⁵ Translating to the D_{2d} structure decreases the overlap between the Cu $d(x^2-y^2)$ orbital and the ligand p orbitals, which results in a decrease in the covalency of the Cu–Cl bonds and thus a larger Cu spin density. As done above for D_{4h} , using the DFT calculated spin density, the 2B_1

ligand field energy, and equation 2-1.2 predicts a g_z value of 2.361, which is in the range of that predicted from the DFT calculation (2.309).

The spin–phonon analysis for the g_z value of D_{2d} $[\text{CuCl}_4]^{2-}$ is given in Figure 2-1.2b (fits given in Table 2-1.S4a). Group theory provides a means to directly correlate the D_{4h} and D_{2d} vibrational modes. These correlations are applied here and are reflected in the labels of the D_{2d} figures and tables throughout. As observed for the D_{4h} , the largest coupling term for the D_{2d} structure is observed for the totally symmetric breathing mode, $a_{1g}(2)$ (mode 7, Table 2.S3) (a_{1g} in D_{4h}). For the $a_{1g}(2)$ mode, a linear fit along the vibrational mode, Q_i , provides a slope of $-0.306 \text{ g}_z/Q_i$ ($0.612 \text{ g}_z/\text{\AA}$). These slopes are larger than those observed for the a_{1g} mode in the D_{4h} structure ($-0.241 \text{ g}_z/Q_i$ and $0.482 \text{ g}_z/\text{\AA}$). Furthermore, while no other modes exhibited substantial linear coupling terms in the D_{4h} structure, from the spin–phonon analyses in Figure 2-1.2b, the $a_{1g}(1)$ mode (mode 1 in both D_{4h} and D_{2d} ; b_{2u} in D_{4h}) becomes activated and linear in the D_{2d} structure. For the $a_{1g}(1)$ mode, the linear fit along the vibrational mode, Q_i , provides a slope of $0.140 \text{ g}_z/Q_i$. The activation of the $a_{1g}(1)$ mode and the observation of linear coupling term behavior upon going to the D_{2d} structure is especially important for local mode contributions to decoherence, as the $a_{1g}(1)$ mode is the lowest energy mode in these structures and thus can become populated at relatively low temperatures. This is discussed further in the following section.

The quadratic coefficient of the $b_{2g}(1)$ mode of the D_{2d} structure ($-0.068 \text{ g}_z/Q_i$) is reduced relative to the D_{4h} structure ($0.119 \text{ g}_z/Q_i$) (a_{2u} in D_{4h}). Of the modes with frequencies less than the $a_{1g}(2)$ totally symmetric stretch, the $b_{2g}(2)$ mode has a quadratic coefficient of $-0.295 \text{ g}_z/Q_i$, which is activated relative to the D_{4h} structure in which a very small coupling term was observed (b_{1g} in D_{4h}).

The spin–phonon analysis for the 2B_1 excited state of D_{2d} $[\text{CuCl}_4]^{2-}$ is given in Figure 2-1.3b. Both $a_{1g}(2)$ and $a_{1g}(1)$ modes exhibit oppositely signed slopes between Figure 2-1.2b and 2-1.3b, indicating appreciable contributions to the spin–phonon coupling term from excited state SOC. For the $a_{1g}(2)$ mode, the linear fit along the vibrational mode, Q_i , provides a slope of $7885 \text{ cm}^{-1}/Q_i$ ($-15770 \text{ cm}^{-1}/\text{\AA}$). These slopes are smaller than those observed for the a_{1g} mode in the D_{4h} structure ($12405 \text{ cm}^{-1}/Q_i$ and $-24940 \text{ cm}^{-1}/\text{\AA}$). The larger slope for the D_{4h} structure might suggest it would have a larger spin–phonon coupling term. However, equation 2-1.2 and its differentiated forms predict important behavior in this regard when comparing the D_{4h} and D_{2d} structures. This behavior is addressed below.

The slope of the $a_1(1)$ mode for the D_{2d} structure is $-3925 \text{ cm}^{-1}/Q_i$, roughly half that observed for the $a_1(2)$ mode ($7885 \text{ cm}^{-1}/Q_i$). The activation of this mode is a direct consequence of the symmetry about the Cu complex and its effect on the excited state coupling term (equation 2-1.8). This is shown pictorially in Figure 2-1.4b. For the D_{4h} structure, the b_{2u} mode is imaginary, representing a saddle point on the ground state potential energy surface. It has also been stressed that the $D_{4h} [\text{CuCl}_4]^{2-}$ structure arises due to crystal packing forces, and the D_{2d} structure represents the energetic minimum on the ground state potential energy surface.⁵⁸ However, the symmetry of the complex has important consequence for the excited state coupling term and thus the spin–phonon coupling terms. In D_{4h} , the excited state that can SOC with the ground state is at an energetic maximum along the b_{2u} (in D_{4h}) mode connecting the D_{4h} and D_{2d} structures. Upon distorting along this mode, both the ground and excited state energies are reduced. At the ground state minimum the excited state potential energy surface is shifted relative to the ground state surface. This offset gives rise to a non-zero excited state coupling term for the D_{2d} structure and provides a mechanism for the amount of orbital angular momentum mixed into the D_{2d} ground state to change along the vibrational mode. This mixing is prohibited in the D_{4h} ground state. In some ways, this qualitatively resembles atomic clock transitions that have also been utilized in the development of qubits.^{35,66–69}

The spin density as a function of the vibrational coordinate for the D_{2d} structure is given in Figure 2-1.S2b. The slopes for the $a_1(2)$ mode are $-0.157 \text{ SD}/Q_i$ and $0.315 \text{ SD}/\text{Å}$. These are larger than the values for the a_{1g} mode in the D_{4h} structure ($-0.111 \text{ SD}/Q_i$ and $0.221 \text{ SD}/\text{Å}$). As done for the D_{4h} structure, the individual contributions to the g_z value from the ${}^2\text{B}_{1g}$ energy and Cu spin density can be estimated using equation 2-1.1. These results are given in Figures 2-1.S6-2-1.S8.

The spin–phonon analyses were extended to the $g_{x,y}$ values of $D_{2d} [\text{CuCl}_4]^{2-}$. These results are given in Figure 2-1.S11 and Tables 2-1.S4b and 2-1.S4c. The corresponding vibrational analyses are for the ${}^2\text{E}$ excited state of $D_{2d} [\text{CuCl}_4]^{2-}$ are given in Figure 2-1.S12 and Tables 2-1.S4b and 2-1.S4b. Similar to D_{4h} , there are new modes that are activated for the $g_{x,y}$ values. For the D_{2d} structure, these include the $b_2(1)$ and $b_2(2)$ modes.

In summary, for D_{2d} , in addition to the $a_1(2)$ mode, a linear spin–phonon coupling term in the $a_1(1)$ mode (i.e., the b_{2u} parent mode in D_{4h}) becomes activated. This is anticipated to be especially important for local mode contributions to decoherence, as the $a_1(1)$ mode is the lowest energy mode in these structures and thus can become populated at relatively low temperatures. Indeed, all Cu(II)-based qubits in the literature are roughly square planar, D_{4h} . Insightful and

quantitative comparisons can be drawn between the vibrational analyses of the total symmetric breathing modes of the D_{4h} and D_{2d} structures, with the latter exhibiting a larger spin–phonon coupling term. This larger coupling term occurs even though the excited state coupling term (Figure 2-1.4a) is larger than the D_{2d} structure. The activation of the $a_1(1)$ mode for the D_{2d} structure and its excited state coupling behavior can be understood via the qualitative potential energy surfaces in Figure 2-1.4b. Given the ground state structure of $[\text{CuCl}_4]^{2-}$ in the absence of any structural constraints is D_{2d} , going to the D_{4h} structure on the ground state surfaces results in a scenario where there is a relatively small gradient in the excited state potential energy surfaces. Thus, for the D_{4h} structure, there is little change in the ground state orbital angular momentum upon fluctuations in the b_{2u} mode that provides a coordinate between the D_{4h} and D_{2d} structures. However, the excited state potential energy surface is offset from the ground state surface near the equilibrium position of the D_{2d} geometry, which allows for larger changes in ground state orbital angular momentum for the $a_1(1)$ mode.

2.2.3. Cu(II) Effective Decoherence Maps and Comparisons to Ligand Field Theory

For D_{2d} $[\text{CuCl}_4]^{2-}$, the vibrational modes with by far the largest spin–phonon coupling terms were those of $a_1(1)$ and $a_1(2)$ symmetry and thus have the greatest impact on the quantum decoherence of Cu(II) complexes. The $a_1(1)$ mode can be described by the Cl–Cu–Cl bond angle, α , while the $a_1(2)$ mode can be described by the Cu–Cl bond distance. Effective decoherence maps have been generated spanning this space of $[\text{CuCl}_4]^{2-}$ geometries (Figure 2-1.5). In Figure 2-1.5, the magnitude and direction of g_z value gradients (i.e., effective linear spin–phonon coupling terms in this space) are represented by the size and directions of the arrows. The horizontal and vertical components of the arrows reflect the relative contributions to the $a_1(2)$ and $a_1(1)$ modes, respectively. For the D_{4h} structure, the gradient in g_z value is small for any linear combination of these two structural coordinates. However, upon increasing the angle, α , the gradient in g_z increases, reflecting the larger slope of the g_z value vs. Cu–Cl bond length observed for D_{2d} (0.612 $g_z/\text{\AA}$) vs. D_{4h} (0.482 $g_z/\text{\AA}$) $[\text{CuCl}_4]^{2-}$. This map can be translated to any four coordinate Cu(II) complex. Indeed, previous EPR experiments on a large scope of Cu(II) complexes have concluded that spin relaxation rates are faster for tetrahedrally-distorted geometries vs. square planar geometries.⁷⁰ This observation is fully supported by extension of the model derived here (see Figure 2-1.S20). The 2D maps are also

presented for spin density and the ${}^2B_{2g}/{}^2B_1$ ligand field transition energies, wherein the trends in both cases track with expressions in Section 2-1.1. This extension further demonstrates that the model can be applied to complexes with asymmetric ligand sets where the treatment of even vs. odd vibrations may break down.

Individual ligand field contributions from the ligand field transition energy and spin density are given in Figures 2-1.5b and 2-1.5c, respectively. Even though the excited state linear coupling term of the ${}^2B_{2g}$ excited state (in D_{4h}) is larger than the 2B_1 state (in D_{2d}) (also compare blue lines in Figure 2-1.4a), the resultant effect on the gradient in g_z value is smaller because the initial ${}^2B_{2g}$ state is higher in energy than the 2B_1 state. Furthermore, the effective decoherence map generated using the Cu spin density (Figure 2-1.5c) shows that the gradient of the change in absolute value of the spin density increases with increasing angle, α . This behavior is similar to Figure 2-1.5a for g_z . While it is clear that the D_{2d} structure has a larger spin–phonon coupling term in the g_z -plot alone, the different behaviors for the individual contributions from ligand field transition energy (Figure 2-1.5b) and spin density (Figure 2-1.5c) are insightful and in line with the expressions derived in Section 2-1.1.

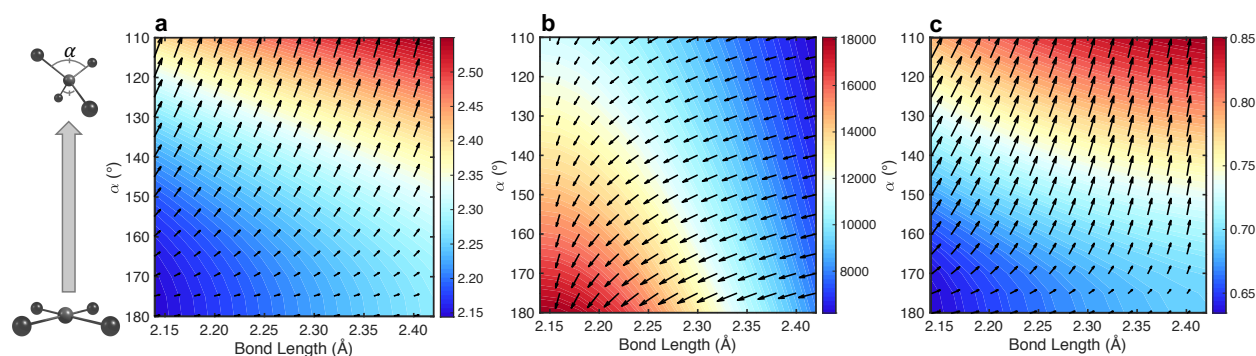


Figure 2-1.5. Effective decoherence maps generated using 225 geometries of $[\text{CuCl}_4]^{2-}$ spanning different bond lengths and angles, α , and the corresponding gradients (denoted by the size and magnitude of the arrows) in the 2D space. (a) g_z value, (b) ${}^2B_{2g}/{}^2B_1$ ligand field energy (cm^{-1}), and (c) Loewdin spin density on Cu.

2-1.3. Spin–Phonon Coupling Terms in C_{4v} $[\text{VOCl}_4]^{2-}$ and Comparisons to D_{4h} $[\text{CuCl}_4]^{2-}$

The bond metrics of the X-ray crystal structure and an idealized C_{4v} $[\text{VOCl}_4]^{2-}$ model structure are given in Table 2-1.S5. As for $[\text{CuCl}_4]^{2-}$, the X-ray structure and idealized structure gave essentially identical results and only the idealized structure is considered. The DFT calculated g values and ligand field excited state energies for C_{4v} $[\text{VOCl}_4]^{2-}$ are compared to experiment in Tables 2-1.3 and

2-1.4, respectively. Experimentally, the g_z and $g_{x,y}$ values of $[\text{VOCl}_4]^{2-}$ are 1.948 and 1.979, respectively.⁷¹ The calculated values are 1.963 and 1.973, respectively, in fair agreement with experiment. The HF dependence of the g_z value for this structure is given in Figure 2-1.S14. For overall consistency and accuracy, calculations reported here for V(IV) complexes utilize 60 % HF exchange, as this value provides better overall agreement across a variety of other V(IV)-based complexes.

Table 2-1.3. Comparisons between a variety of experimental and calculated g values for C_{4v} $[\text{VOCl}_4]^{2-}$ and other V(IV) complexes.

Molecule	g_x		g_y		g_z	
	Exp.	Calc.	Exp.	Calc.	Exp.	Calc.
$C_{4v}[\text{VOCl}_4]^{2-}$ ^a	1.979	1.973	1.979	1.973	1.948	1.962
$C_{4v}[\text{VOCl}_4]^{2-}$ ^b	1.979	1.973	1.979	1.973	1.948	1.963
VOPc ^c	1.989	1.973	1.989	1.973	1.966	1.963
$\text{VO}(\text{acac})_2$ ^d	1.975	1.978	1.979	1.980	1.949	1.945
$[\text{VO}(\text{cat})_2]^{2-}$ ^e	1.980	1.976	1.988	1.982	1.956	1.951
$[\text{VO}(\text{dmit})_2]^{2-}$ ^f	1.986	1.979	1.988	1.977	1.970	1.963
$[\text{V}(\text{bdt})_3]^{2-}$ ^g	1.970	1.947	1.970	1.949	1.988	1.962
$[\text{V}(\text{bds})_3]^{2-}$ ^g	1.960	1.872	1.955	1.871	1.950	1.849

^a Crystal structure from ref. 77, g values from ref. 71.

^b Idealized structure from crystal structure.

^c DFT-Optimized structure. g values from ref. 76.

^d DFT-Optimized structure. g values from ref. 78.

^e DFT-Optimized structure. g values from ref. 43.

^f $\text{VO}(\text{dmit})_2$: xtal structure and g values from ref. 54.

^g g values and xtal structures from ref. 33.

Table 2-1.4. Comparisons between experimental and calculated ligand field transitions for C_{4v} $[\text{VOCl}_4]^{2-}$.

Exp. ^a (cm^{-1})	Assignment	Calc. (cm^{-1}) ^b	Calc. (cm^{-1}) ^c
~12000	${}^2\text{B}_2 \rightarrow {}^2\text{B}_1$	15080	15230
13700	${}^2\text{B}_2 \rightarrow {}^2\text{E}$	15925	16325
		16825	16325
22000	${}^2\text{B}_2 \rightarrow {}^2\text{A}_1$	29270	19190

^a Ref. 72.

^b X-ray crystal structure from ref. 77.

^c Idealized structure from crystal structure.

The energies, symmetry labels, and scaled vector displacements for all 12 normal modes of vibration for the idealized C_{4v} $[\text{VOCl}_4]^{2-}$ are given in Table 2-1.S6 ($\Gamma_{vib} = 3a_1 + 2b_1 + b_2 + 3e$). Spin–phonon calculations for the g_z value of C_{4v} $[\text{VOCl}_4]^{2-}$ are given in Figure 2-1.6A, and their fits are given in Table 2-1.S7a. A strong coupling term for the g_z value is observed for the totally symmetric $a_1(2)$ V(IV)–Cl breathing mode (mode 9, 323 cm^{-1}). The linear fits provide slopes of 0.068 g_z/Q_i and $-0.130 g_z/\text{\AA}$. These slopes are significantly smaller than those observed for $a_{1g}/a_1(2)$ modes of either D_{4h} ($-0.241 g_z/Q_i$ and $0.482 g_z/\text{\AA}$) or D_{2d} ($-0.306 g_z/Q_i$ and $0.612 g_z/\text{\AA}$) $[\text{CuCl}_4]^{2-}$. The ratios of the C_{4v} $[\text{VOCl}_4]^{2-}$ and D_{4h} $[\text{CuCl}_4]^{2-}$ slopes are ~ 0.27 . This is very similar to the relative magnitudes of the V(IV) (250 cm^{-1}) and Cu(II) (-830 cm^{-1}) SOC constants (0.3), showing that spin–phonon coupling terms of V(IV) are systematically decreased by a factor of ~ 3.3 , largely due to the reduced SOC constant of V(IV) relative to Cu(II).

For C_{4v} $[\text{VOCl}_4]^{2-}$, of the other vibrations with energies less than $a_1(2)$, modes 1 ($b_1(1)$, -51 cm^{-1}), 2/3 ($e(1a, 1b)$, 160 cm^{-1}), 4 ($a_1(1)$, 166 cm^{-1}), 5 (b_2 , 187 cm^{-1}), 6 ($b_1(2)$, 233 cm^{-1}), 7/8 ($e(2a, 2b)$, 267 cm^{-1}) all exhibit quadratic coupling terms. From low to high energy, the largest quadratic coupling terms are observed for modes $b_1(1)$ ($-0.016 g_z/Q_i$), $e(1a, 1b)$ ($-0.020 g_z/Q_i$), $a_1(1)$ ($-0.018 g_z/Q_i$), $b_1(2)$ ($-0.016 g_z/Q_i$), and $e(2a, 2b)$ ($0.017 g_z/Q_i$). These quadratic coefficients are significantly less than the important low-energy quadratic modes in D_{4h} $[\text{CuCl}_4]^{2-}$, which ranged from 0.056 to 0.118 g_z/Q_i . When scaled for the different SOC constant of V(IV), the quadratic coefficients for $[\text{VOCl}_4]^{2-}$ range from 0.054 to 0.067 g_z/Q_i , which are much closer to the those for D_{4h} $[\text{CuCl}_4]^{2-}$. For more direct comparison, the coefficient of the b_{2u} mode of D_{4h} $[\text{CuCl}_4]^{2-}$ is 0.063 g_z/Q_i , while for the $b_1(1)$ mode of $[\text{VOCl}_4]^{2-}$ is $-0.016 g_z/Q_i$. Also, the coefficient of the a_{2u} mode of D_{4h} $[\text{CuCl}_4]^{2-}$ is 0.119 g_z/Q_i , while for the $a_1(1)$ mode of $[\text{VOCl}_4]^{2-}$ is $-0.018 g_z/Q_i$. From group theory, these modes correlate between the D_{4h} and C_{4v} point groups. For example, the a_{2u} mode involves out-of-plane Cu motion, while the $a_1(1)$ mode involves movement of the vanadyl unit out-of-plane with respect to the chloride ligands. Thus, the spin–phonon coupling terms of both linear and quadratic modes are significantly less for the vanadyl complex relative to the Cu(II) complexes. Scaled for angle change, the absolute values of the b_{2u} and $b_1(1)$ slopes are $0.98 \times 10^{-4} (g_z/^\circ)$ and $0.28 \times 10^{-4} (g_z/^\circ)$, respectively, with the b_{2u} mode being larger by a factor of 3.5. Scaled for metal displacement, the absolute values of the a_{2u} and $a_1(1)$ slopes are 0.216 and 0.077 ($g_z/\text{\AA}$), respectively, with the a_{2u} mode being larger by a factor of ~ 2.8 . In both cases, the difference in slope is strongly influenced by the ratio of the SOC constant.

Vibrational analyses of the 2B_1 excited state energies were carried out for C_{4v} $[\text{VOCl}_4]^{2-}$. Comparisons between experimental and calculated ligand field transitions are given in Table 2-1.4. Experimentally, the 2B_1 , 2E , and 2A_1 ligand field transitions of C_{4v} $[\text{VOCl}_4]^{2-}$ are observed at ~ 12000 , 13700 , and 22000 cm^{-1} , respectively.⁷² The ${}^2B_2 \rightarrow {}^2B_1$ transition provides the SOC of orbital angular momentum for g_z , while the ${}^2B_2 \rightarrow {}^2E$ transition provides SOC for $g_{x,y}$ (Figure 2-1.1). A TDDFT calculation gives the energies of these transitions at 15080 and 16325 cm^{-1} , respectively, in fairly good agreement.

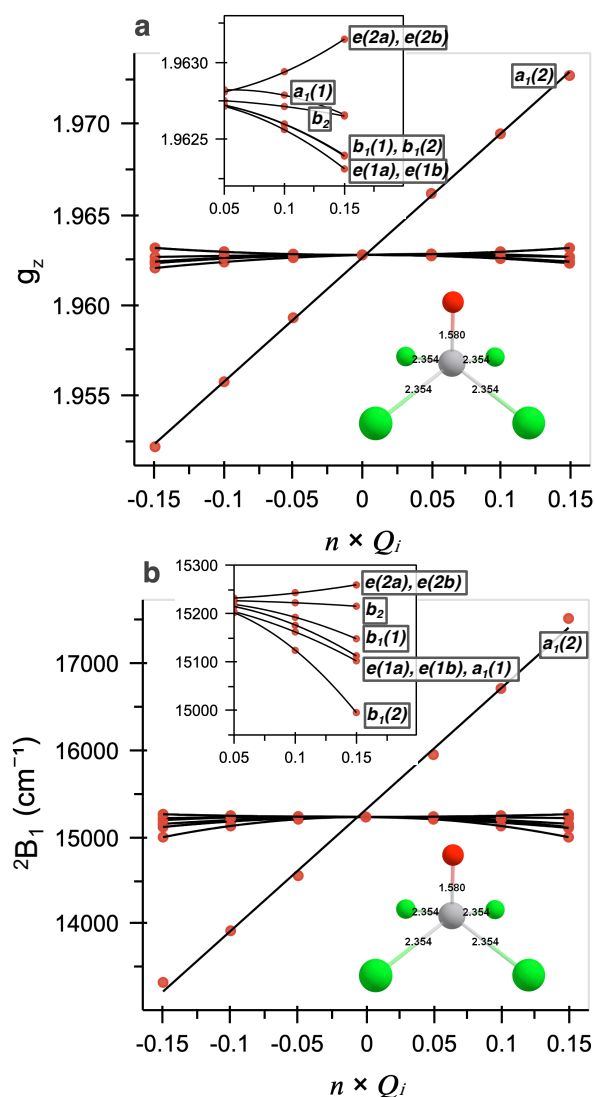


Figure 2-1.6. LFT parameters along the vibrational coordinates of the first nine vibrational modes of $[\text{VOCl}_4]^{2-}$. (a) g_z value, (b) ligand field excited state transition energy.

The vibrational analysis of the 2B_1 ligand field excited state is given in Figure 2-1.6b, with fits given in Table 2-1.S7a. As with the g_z value analysis, the totally symmetric $a_1(2)$ mode exhibits the largest coupling term. The slope of the $a_1(2)$ mode is $13945 \text{ cm}^{-1}/Q_i$ ($-26450 \text{ cm}^{-1}/\text{\AA}$). These values are similar to those of D_{4h} $[\text{CuCl}_4]^{2-}$ ($12405 \text{ cm}^{-1}/Q_i$ or $-24940 \text{ cm}^{-1}/\text{\AA}$). However, despite having similar ligand field excited state energies (14475 vs. 15080 cm^{-1}) and slopes (-26450 and $-24940 \text{ cm}^{-1}/\text{\AA}$) for the totally symmetric stretch, the corresponding slopes for the change in g_z value are significantly lower for $[\text{VOCl}_4]^{2-}$ vs. $[\text{CuCl}_4]^{2-}$ ($-0.130 \text{ g}_z/\text{\AA}$ vs. $0.482 \text{ g}_z/\text{\AA}$, respectively). This difference is due to the different ratio of SOC constants for V(IV) and Cu(II).

The total Loewdin unoccupied V(IV) d(xy) character and V(IV) spin density for $[\text{VOCl}_4]^{2-}$ are 88 % and 0.98, respectively. As expected, the covalency of the V(IV)–Cl bonds are significantly lower than those of D_{4h} $[\text{CuCl}_4]^{2-}$ (e.g., 88 % vs. 65 % unoccupied metal d character). The spin density vibrational analysis for C_{4v} $[\text{VOCl}_4]^{2-}$ is given in Figure 2-1.S15, with fits given in Table 2.S7e. The fits for the $a_1(2)$ mode give values of $-0.102 \text{ SD}/Q_i$ and $0.194 \text{ SD}/\text{\AA}$. These values are smaller than those observed for D_{4h} $[\text{CuCl}_4]^{2-}$ ($-0.157 \text{ SD}/Q_i$ and $0.221 \text{ SD}/\text{\AA}$), consistent with the σ overlap in $[\text{CuCl}_4]^{2-}$ (Figure 2-1.1). The spin density change for $[\text{VOCl}_4]^{2-}$ is due to the π -type interaction between the out-of-plane Cl p orbitals and the V d(xy) orbital.

The spin–phonon coupling terms for the $g_{x,y}$ values for the C_{4v} structure are given in Figure 2-1.S16, with the corresponding fits given in Table 2-1.S7b and 2-1.S7c. Both g_x and g_y give similar results, and only g_x is considered. As observed for D_{4h} $[\text{CuCl}_4]^{2-}$, the spin–phonon coupling terms are different in the g_{\perp} region relative to g_{\parallel} . For the most part, the magnitudes of the spin–phonon coupling terms are decreased going from g_{\parallel} to g_{\perp} . For instance, the slope of the $a_1(2)$ mode decreases from 0.068 to $0.005 \text{ g}_z/Q_i$, and the slopes of the $b_1(1)$ and $a_1(1)$ modes go from -0.016 and $-0.018 \text{ g}_z/Q_i$ to -0.002 and $-0.007 \text{ g}_z/Q_i$, respectively. The b_2 and $e(2a, 2b)$ modes exhibit an increase in coupling term (0.017 to $-0.032 \text{ g}_z/Q_i$). These changes in spin–phonon coupling terms are correlated to the changes in the slopes of the ligand field transitions. The vibrational analyses of the 2E ligand field excited state energies are given in Figure 2-1.S17. For instance, for the b_2 mode, the excited state slope changes from -565 to $3775 \text{ cm}^{-1}/Q_i$. For the $e(2a, 2b)$ modes, the slopes go from 1370 to $-5945/-9620 \text{ cm}^{-1}/Q_i$.

In summary, the totally symmetric $a_1(2)$ mode exhibits a strong spin–phonon coupling term for C_{4v} $[\text{VOCl}_4]^{2-}$, making for an insightful comparison to the a_{1g} mode of D_{4h} $[\text{CuCl}_4]^{2-}$. The

magnitude of the spin–phonon coupling term is significantly less for $[\text{VOCl}_4]^{2-}$. This difference in spin–phonon coupling terms could be quantified to a factor of ~ 0.27 , which is ascribed here to the difference in SOC constants for V(IV) vs. Cu(II). Importantly, the reduction in spin–phonon coupling in $[\text{VOCl}_4]^{2-}$ relative to $[\text{CuCl}_4]^{2-}$ occurs even though the complexes have similar ligand field excited state energies and similar excited state coupling terms. These observations further support that the reduced SOC constant reduces the spin–phonon coupling terms. Also, as observed for $[\text{CuCl}_4]^{2-}$, the spin–phonon coupling terms in $[\text{VOCl}_4]^{2-}$ are anisotropic, with different modes being activated in the g_{\parallel} and g_{\perp} regions. Nonetheless, the spin–phonon coupling terms of $[\text{VOCl}_4]^{2-}$, even when scaled for degree of distortion, are significantly reduced relative to $[\text{CuCl}_4]^{2-}$ in either g_{\parallel} and g_{\perp} directions. The reduced spin–phonon coupling terms will play a major role in the room temperature coherence properties of vanadyl complexes relative to Cu(II) complexes.

2-1.3. Discussion

Transition metal complexes are being explored as qubits for quantum computing. In addition to significant hurdles related to the eventual quantum entanglement of molecular qubits, spin–phonon coupling in transition metal complexes often prohibits the observation of room temperature coherence properties. This has inspired recent research efforts to better understand the nature of spin–phonon coupling in transition metal complexes and how it might be tuned and controlled by variations in the ligand set and thus the ligand field environment.^{13–15,33,44} As highlighted in the Introduction, spin–phonon couplings also play important roles in single molecule magnets and photophysics, and studies directed at fundamental understanding will have broad impact.

Above, we have outlined a general LFT model of spin–phonon coupling terms in $S = \frac{1}{2}$ transition metal complexes. This model is derived from the first and second derivatives of the LFT expressions of g values given in Section 2-1.1.⁵⁵ While these expressions define the zero temperature magnitudes of spin–phonon coupling terms in $S = \frac{1}{2}$ complexes, they can be expanded to consider additional dynamic effects through the variance of g_z , $\langle g_z^2 \rangle$, which highlights the importance of the first derivative, $\frac{\partial g_z}{\partial Q_i}$, and therefore its role in the coherence lifetimes of $S = \frac{1}{2}$ transition metal complexes. This suggests that, without considering thermal population, odd modes such as totally symmetric stretches will have a more substantial effect on spin-phonon coupling terms and

decoherence compared to even modes, in which their value of relevance, $\frac{\partial^2 g_z}{\partial Q_i^2}$, only appears in the second order term of the Taylor expansion (equation 2-1.5). The fundamental behavior of these expressions were borne out by an extensive range of DFT and TD-DFT calculations on minimalistic $S = \frac{1}{2}$ models, D_{4h}/D_{2d} $[\text{CuCl}_4]^{2-}$ and C_{4v} $[\text{VOCl}_4]^{2-}$. Together, the results above provide a general description of the roles of transition metal geometric and electronic structure in spin–phonon coupling. For instance, the magnitudes of spin–phonon coupling terms are strongly influenced by excited state SOC of orbital angular momentum into the ground state and are predicted to be strongly influenced by the energy of the particular ligand field excited state mixing with the ground state (equations 2-1.6 and 2-1.7) (e.g., ${}^2B_{2g}$ for a ${}^2B_{1g}$ ground state in D_{4h} $[\text{CuCl}_4]^{2-}$). This excited state SOC contribution is governed by the ligand field geometry about the metal complex. For example, going from D_{4h} to D_{2d} $[\text{CuCl}_4]^{2-}$ turns on additional mode coupling terms due to the enhancement of excited state coupling terms (Figure 2-1.4). Furthermore, the magnitude of spin–phonon coupling terms are strongly influenced by the covalency of ligand–metal bonds. This dynamic effect largely reflects a relativistic nephelauxetic effect, which effectively modulates the SOC constant of the metal from that of the free ion. In short, the more covalent the ligand–metal bond, the smaller the spin–phonon coupling terms become. Relatedly, a significant overall reduction in SOC constant can of course be achieved through the use of different transition metal complexes (e.g., V(IV) vs. Cu(II) vs. Cr(V)). As shown below, V(IV), which has a significantly lower SOC constant than Cu(II), can still maintain favorable spin–phonon coupling terms despite having significantly more ionic ligand-metal bonds than Cu(II) complexes. Complications can also arise from trying to quantify spin–phonon coupling terms in different ligand field environments, as the nature of the modes can change. However, this can be facilitated to some degree by leveraging specific group theoretical correlations as demonstrated here for D_{4h} , D_{2d} , and C_{4v} transition metal complexes. The spin–phonon analyses presented above for $[\text{CuCl}_4]^{2-}$ and $[\text{VOCl}_4]^{2-}$ are now extended to a range of $S = \frac{1}{2}$ Cu(II) and V(IV) molecular qubit candidates.

2-3.1 Extension to Cu(II)- and V(IV)-Based Qubits

The spin–phonon analyses of the Cu(II) qubit complexes and their g_z values are given in Figures 2-1.S18 and Tables 2-1.S8(a-d). The spin-phonon analyses of the V(IV) complexes and their g_z values for all modes up to at least 400 cm^{-1} in energy are given in Figures 2-1.S19(a-f) and Tables 2-1.S9(a-

f). Comparisons between all geometry optimized and crystal structures are given in Tables 2-1.S10(a,b) and 2-1.S11(a-c) for Cu(II) and V(IV) complexes, respectively. Providing quantitative comparisons between the spin–phonon analyses for different complexes is a complicated task. This is largely because the nature and amount of atomic motions are not necessarily conserved over all vibrations. However, as discussed here, the modes identified above for D_{4h} $[\text{CuCl}_4]^{2-}$ and C_{4v} $[\text{VOCl}_4]^{2-}$ that exhibited particularly large spin–phonon coupling terms are also those that exhibit spin–phonon coupling terms in qubits. Thus, the parent vibrational modes provide a means to make quantitative comparisons across Cu(II) and V(IV) complexes.

Table 2-1.5. Spin–vibrational coupling terms, excited state energies, and covalencies across a variety of Cu(II) complexes/qubits.

Complex	a_{1g} (cm^{-1})	($\text{g}/\text{\AA}$)	a_{2u} (cm^{-1})	($\text{g}/\text{\AA}$)	ES ^a	M(d) ^b	M SD
D_{4h} $[\text{CuCl}_4]^{2-}$	296.3	0.482	140.5	0.216	14475	65 %	0.670
D_{2d} $[\text{CuCl}_4]^{2-}$	316.7	0.612	66.9	0.529	10440	70 %	0.760
CuPc	259.4	0.464	151.7	0.151	22165	72 %	0.734
$[\text{Cu}(\text{mnt})_2]^{2-}$	303.4	0.384	141.2	0.102	22305	42 %	0.434
$[\text{Cu}(\text{bdt})_2]^{2-}$	387.4	0.232	85.1	0.103	29700	41 %	0.424
$[\text{Cu}(\text{bds})_2]^{2-}$	199.3	0.165	97.8	0.039	24390	37 %	0.377

^a Excited state which spin orbit couples into the ground state for g_z .

^b M(d) character in unoccupied component orbital from Loewdin population analyses.

^c Loewdin metal spin density.

The experimental and calculated g values of Cu(II) qubits are given in Table 1,^{14,33,73,74} while spin–phonon linear coupling terms and additional computational results are given in Table 2-1.5. Note X-ray crystal structures were utilized for $[\text{Cu}(\text{mnt})_2]^{2-}$, $[\text{Cu}(\text{bdt})_2]^{2-}$, and $[\text{Cu}(\text{bds})_2]^{2-}$ (bds = benzene-1,2-diselenate) complexes, as their structures were not well reproduced using DFT geometry optimization. However, CuPc provided a good agreement and thus the optimized structure was used. As outlined above, the totally symmetric stretch (a_{1g} in D_{4h} $[\text{CuCl}_4]^{2-}$) and the out-of-plane motion of the metal/vanadyl moiety (a_{2u} in D_{4h} $[\text{CuCl}_4]^{2-}$ and $a_1(1)$ in C_{4v} $[\text{VOCl}_4]^{2-}$) were the main modes to consider. The nature of these modes are well conserved over the complexes considered here allow for the spin–phonon coupling terms to be compared on a \AA^{-1} scale. As elucidated above, the linear coupling terms for the totally symmetric modes of D_{4h} and D_{2d} $[\text{CuCl}_4]^{2-}$ were determined to be 0.482 and 0.612 $\text{g}_z/\text{\AA}$. These modes for qubit candidates CuPc,⁷⁵ $[\text{Cu}(\text{mnt})_2]^{2-}$,⁵¹ $[\text{Cu}(\text{bdt})_2]^{2-}$,³³ and $[\text{Cu}(\text{bds})_2]^{2-}$ ³³ are 0.464, 0.384, 0.232, and 0.165 $\text{g}_z/\text{\AA}$, respectively. Interestingly, of these qubits,

$[\text{Cu}(\text{bdt})_2]^{2-}$ exhibited spin echoes that persist to room temperature, and it has one of the lowest spin–phonon coupling terms of the Cu(II) complexes, with only $[\text{Cu}(\text{bds})_2]^{2-}$ being lower. Note the lack of spin echoes for $[\text{Cu}(\text{bds})_2]^{2-}$ and its comparison to $[\text{Cu}(\text{bdt})_2]^{2-}$ is discussed further below. For the a_{2u} parent mode, the quadratic coefficients for D_{4h} and D_{2d} $[\text{CuCl}_4]^{2-}$ were determined to be 0.216 and 0.529 $\text{g}_z/\text{\AA}$, respectively. In a similar fashion to the a_{1g} parent mode, the quadratic coefficients of the a_{2u} parent mode decrease to 0.151, 0.102, 0.103, and 0.039 $\text{g}_z/\text{\AA}$ for CuPc, $[\text{Cu}(\text{mnt})_2]^{2-}$, $[\text{Cu}(\text{bdt})_2]^{2-}$, and $[\text{Cu}(\text{bds})_2]^{2-}$, respectively. Thus, there is a systematic decrease in the spin–phonon coupling terms across these Cu(II) complexes. These observations can be understood utilizing the LFT model outlined above. For example, $[\text{Cu}(\text{bdt})_2]^{2-}$ exhibits the highest calculated ligand field excited state energy (29700 cm^{-1}) and has highly covalent ligand–metal bonds (41 % Cu(d)). The decreased slope of $[\text{Cu}(\text{bds})_2]^{2-}$ is due to the increased covalency of the Cu–Se vs. Cu–S bonds (Table 2-1.5). Furthermore, the slopes and quadratic coefficients of $[\text{Cu}(\text{mnt})_2]^{2-}$ are larger than those $[\text{Cu}(\text{bdt})_2]^{2-}$ and $[\text{Cu}(\text{bds})_2]^{2-}$. From Table 2-1.5, this is largely reflected by the lower excited state energy (22305 cm^{-1}) (and thus the higher amount of ground state orbital angular momentum) and, to a smaller extent, the lower covalency (42 % Cu(d)). The slopes and coefficients for CuPc are increased further relative to the other Cu(II) complexes, as the Cu–N bonds are significantly more ionic than the Cu–S bonds of $[\text{Cu}(\text{mnt})_2]^{2-}$, $[\text{Cu}(\text{bdt})_2]^{2-}$ and $[\text{Cu}(\text{bds})_2]^{2-}$.

These electronic differences between $[\text{Cu}(\text{bdt})_2]^{2-}$ and $[\text{Cu}(\text{mnt})_2]^{2-}$ can be understood from their X-ray crystal structures. For example, the Cu–S bond lengths of $[\text{Cu}(\text{mnt})_2]^{2-}$ are ~ 2.33 \AA , which are longer than those for the $[\text{Cu}(\text{bdt})_2]^{2-}$ complex (~ 2.15 \AA). For $[\text{Cu}(\text{bdt})_2]^{2-}$, the contraction of the ligand–metal bonds destabilizes the Cu $d(x^2-y^2)$ β -LUMO orbital, which increases the energy of the ${}^2\text{B}_{2g}$ ligand field transition and increases the orbital overlap (covalency) of the ligand–metal bonds (Figure 2-1.1). Thus, the ligand set and $[\text{Cu}(\text{bdt})_2]^{2-}$ complex exhibits the ideal characteristics for a Cu(II)-based qubit. Also, while the slopes of the $[\text{Cu}(\text{bds})_2]^{2-}$ complex would suggest longer coherence times relative to $[\text{Cu}(\text{bdt})_2]^{2-}$, the lack of spin echoes at higher temperatures can be attributed to the significant decrease in the vibrational frequency of the a_{1g} parent mode due to the mass effect of the S to Se conversion (e.g., 387 vs. 199 cm^{-1} , respectively). Interestingly, the fits to the temperature dependence of the T_1 for these complexes suggest local mode contributions of 488 ± 72 and 344 ± 80 cm^{-1} .³³ Combined with the computational results here, these frequencies and their differences provide strong evidence that the totally symmetric a_{1g} parent mode contributes to the coherence times of Cu(II) complexes. Thus, we propose that the rapidly accessible data in Table 2-

1.5 can be computed to qualitatively and semi-quantitatively evaluate and screen potential Cu(II)-based qubits.

Recent work by Sessoli et al.^{13,54} has highlighted the important role of the vanadyl moiety in V(IV)-based qubits. The calculated and experimental g values of a variety of vanadyl and V(IV) qubits are given in Table 2-1.3,^{43,54,71,76–78} with the corresponding spin–phonon analyses given in Figures 2-1.S19(a-f) and Tables 2-1.S9(a-f) and specific spin–phonon slopes and additional computational results given in Table 2-1.S12. Note, of the vanadyl complexes considered here, VOPc, VO(acac)₂, and [VO(cat)₂]²⁻ were geometry optimized. Similarly to the Cu complexes considered above, X-ray crystal structures were used for structures where geometry optimizations resulted in significantly different structures (e.g., [VO(dmit)₂]²⁻, [V(bdt)₃]²⁻, and [V(bds)₃]²⁻). Experimentally, long coherence times have been observed for a variety of vanadyl complexes. However, only VOPc has been directly studied in a solid diamagnetic matrix, which has thus far prohibited further investigation of vanadyl complexes up to room temperature. From the data given in Table 2-1.S12, there are currently no clear defining characteristics to be observed across the vanadyl complexes. Thus, other vanadyl complexes, when isolated in similar solid diamagnetic matrices, will likely exhibit long relaxation times, with the potential for room temperature coherence.

The spin–phonon model presents a stark difference for vanadyl vs. six coordinate V(IV) complexes. As shown in Sessoli et al.,^{13,54} six coordinate V(IV) complexes do not exhibit long T_1 s at elevated temperatures. Very recently, Albino et al.¹³ pointed to the role of increased excited state SOC in six coordinate complexes relative to vanadyl complexes. Furthermore, Fataftah et al.³³ compared six coordinate V(IV) complexes to Cu(II) complexes to suggest the role of increased covalency in elongating T_1 relaxation lifetimes. Here we have extended our LFT model to the [V(bdt)₃]²⁻ and [V(bds)₃]²⁻ complexes studied by Fataftah et al.³³ (Table 2-1.S12). Interestingly, as pointed out by Albino et al.¹³ for other six coordinate V(IV) complexes, the [V(bdt)₃]²⁻ and [V(bds)₃]²⁻ complexes exhibit very low energy calculated ligand field transitions (7935 cm⁻¹ and 6785 cm⁻¹, respectively). Furthermore, the totally symmetric stretches of these complexes were computed at 351.7 and 209.8 cm⁻¹, respectively. These modes allow for a quantitative comparison between the linear spin–phonon coupling term of Cu(II) complexes on a Å⁻¹ scale. The linear coupling terms for [V(bds)₃]²⁻ in the g_{\parallel} and g_{\perp} regions are -0.420 and -0.357 g/Å, respectively. For comparison, the linear coupling term of the totally symmetric a_{1g} parent mode of [Cu(bdt)₂]²⁻ is

smaller (0.232 g/Å). Also, the calculated vibrational frequency decreases and the linear coupling terms increase going from $[\text{V}(\text{bdt})_3]^{2-}$ to $[\text{V}(\text{bds})_3]^{2-}$. Thus, the longer spin–lattice relaxation time at higher temperatures for $[\text{Cu}(\text{bdt})_2]^{2-}$ vs. $[\text{V}(\text{bdt})_3]^{2-}$ is not due to differences in ligand–metal covalency, but rather stems from efficient excited state SOC as a result of the relatively low energy ligand field transition energies for $[\text{V}(\text{bdt})_3]^{2-}$. This is further supported by the observation of room temperature coherence in vanadyl complexes,³⁷ despite ionic ligand metal bonding. More generally, the amount of excited state SOC has proven to be critical with the recent discovery of room temperature coherence in $S = 1/2$ transition metal complexes with well energetically isolated $d(z^2)$ ground states.⁴⁵ Together, these DFT/TDDFT calculations are consistent with the LFT model derived here and further highlight the importance of considering both excited state SOC and ligand–metal covalency when comparing different complexes with different metals and/or coordination environments.

2-1.3.2 Ligand Field Strain in Qubits

As previously highlighted for D_{4h}/D_{2d} $[\text{CuCl}_4]^{2-}$, the planar D_{4h} Cu(II) structure represents a saddle point on the ground state potential energy surface that can only be stabilized in the presence of crystal packing forces.^{58,59} The formation of this structure in $[\text{CuCl}_4]^{2-}$ was likened to the entatic/rack state in bioinorganic chemistry, where the protein architecture (inclusive of first and second sphere contributions, as well as long range H-bonding and electrostatics) can place a metal ion in a strained ligand field.^{79–82} This ligand field strain can generate unique properties. The entatic/rack state and ligand field strain is therefore of relevance to molecular qubits. For example, Cu(II)-based complexes with the longest coherence times are square planar Cu(II) sites stabilized in diamagnetic lattices (e.g., $[\text{Cu}(\text{mnt})_2]^{2-51}$ and $[\text{Cu}(\text{bdt})_2]^{2-33}$). The geometric dependence to T_1 was also noted in an EPR study of a variety of Cu(II) complexes.⁷⁰ Here we have shown that the origin of this dependence for the square planar Cu(II) geometry derives from the significant minimization of excited state coupling terms, which reduces dynamic SOC of orbital angular momentum into the ground state (Figure 2-1.4).

In addition to crystal packing forces, variations in the ligand set can effectively control the deviation from planarity in Cu(II) complexes. This can be observed directly in the dependence of the electronic energy as a function of the b_{2u} parent mode (in D_{4h}) distortion. For instance, as noted above, distortion along this mode will decrease the energy for the square planar Cu(II) complexes studied here, which

results in the b_{2u} mode being imaginary. However, this is not the case for CuPc. Thus, linking the four N-based ligands into the aromatic planar structure of the Pc ligand provides an entatic state that can oppose distortions along the b_{2u} parent mode. However, the drawback of the Pc ligand arises also from its N-based coordination, which gives rise to fairly ionic ligand–metal bonds and opposes the effects provided by the rigid and constrained ligand field (i.e., entatic state).

In relation, significant efforts have been guided toward better identifying, understanding, and quantifying entatic states,^{83–85} which have traditionally been used to rationalize electron transfer properties. However, given the general nature of this description, it is being extended to other scenarios, including photochemistry and catalysis.^{86–90} Strain effects have also been discussed in the context of both ground and excited states and their contributions to the coherence properties in solid state qubits (e.g, vacancies in diamond).^{10–12,91} Thus, engineering ligand field strain and rigidity into covalent environments will be useful for advancing the geometric and electronic structural contributions to the quantum coherence of transition metal complexes, and the model outlined here can guide these future investigations.

2-1.4. Conclusion

The spin–phonon coupling terms of minimalized D_{4h}/D_{2d} $[\text{CuCl}_4]^{2-}$ and C_{4v} $[\text{VOCl}_4]^{2-}$ complexes translate onto Cu(II)- and V(IV)-based molecular qubits and are dominated by three major factors: 1) the magnitude of the metal-based SOC constant, 2) the initial magnitude and gradient of change in ground state orbital angular momentum, which is governed by the ligand field excited state energies, and 3) dynamic relativistic nephelauxetic contributions, including the initial magnitude and gradient in the covalency of the ligand–metal bonds. Factors 1) and 3) are directly related, as covalency further reduces the SOC constant of a metal in a complex relative to that of the free ion. LFT expressions derived here predict spin–phonon coupling terms in both odd and even modes are important to consider for decoherence times (equation 2-1.5). However, odd modes such as the totally symmetric stretch play a key role for decoherence times. We have further shown how the LFT expressions and thus spin–phonon coupling terms (equations 2-1.6 and 2-1.7) can be directly related to spectroscopic observables and calculable quantities. For Cu(II), key geometric and symmetry factors, including ligand field strain, significantly lower excited state coupling terms while simultaneously increasing orbital overlap and ligand–metal covalency. Importantly, all factors relating to excited state SOC and covalency need to be evaluated when comparing spin–phonon

coupling terms, including local mode contributions to T_l and T_m relaxation times, of various metal complexes. The model outlined here provides a means to quantify spin–phonon coupling terms for given vibrational modes for any $S = \frac{1}{2}$ molecule, providing a powerful means to benchmark current and future qubit candidates. The further discovery of room temperature coherent materials will provide exciting opportunities to develop fundamental structure–function correlations for spin–phonon coupling in transition metal complexes.

References

- (1) Penfold, T. J.; Gindensperger, E.; Daniel, C.; Marian, C. M. Spin-Vibronic Mechanism for Intersystem Crossing. *Chem. Rev.* **2018**, *118* (15), 6975–7025. <https://doi.org/10.1021/acs.chemrev.7b00617>.
- (2) Kjær, K. S.; Driel, T. B. V.; Harlang, T. C. B.; Kunnus, K.; Biasin, E.; Ledbetter, K.; Hartsock, R. W.; Reinhard, M. E.; Koroidov, S.; Li, L.; Laursen, M. G.; Hansen, F. B.; Vester, P.; Christensen, M.; Haldrup, K.; Nielsen, M. M.; Dohn, A. O.; Pápai, M. I.; Møller, K. B.; Chabera, P.; Liu, Y.; Tatsuno, H.; Timm, C.; Jarenmark, M.; Uhlig, J.; Sundstöm, V.; Wärnmark, K.; Persson, P.; Németh, Z.; Szemes, D. S.; Bajnóczi, É.; Vankó, G.; Alonso-Mori, R.; Glowonia, J. M.; Nelson, S.; Sikorski, M.; Sokaras, D.; Canton, S. E.; Lemke, H. T.; Gaffney, K. J. Finding Intersections between Electronic Excited State Potential Energy Surfaces with Simultaneous Ultrafast X-Ray Scattering and Spectroscopy. *Chem. Sci.* **2019**, *10* (22), 5749–5760. <https://doi.org/10.1039/C8SC04023K>.
- (3) Lemke, H. T.; Kjær, K. S.; Hartsock, R.; van Driel, T. B.; Chollet, M.; Glowonia, J. M.; Song, S.; Zhu, D.; Pace, E.; Matar, S. F.; Nielsen, M. M.; Benfatto, M.; Gaffney, K. J.; Collet, E.; Cammarata, M. Coherent Structural Trapping through Wave Packet Dispersion during Photoinduced Spin State Switching. *Nat. Commun.* **2017**, *8*, 15342. <https://doi.org/10.1038/ncomms15342>.
- (4) Monni, R.; Auböck, G.; Kinschel, D.; Aziz-Lange, K. M.; Gray, H. B.; Vlček, A.; Chergui, M. Conservation of Vibrational Coherence in Ultrafast Electronic Relaxation: The Case of Diplatinum Complexes in Solution. *Chem. Phys. Lett.* **2017**, *683*, 112–120. <https://doi.org/10.1016/j.cplett.2017.02.071>.
- (5) Pižl, M.; Hunter, B. M.; Greetham, G. M.; Towrie, M.; Záliš, S.; Gray, H. B.; Vlček, A. Ultrafast Wiggling and Jiggling: Ir₂(1,8-Diisocyanomenthane)₄²⁺. *J. Phys. Chem. A* **2017**, *121* (48), 9275–9283. <https://doi.org/10.1021/acs.jpca.7b10215>.
- (6) Lunghi, A.; Totti, F.; Sanvito, S.; Sessoli, R. Intra-Molecular Origin of the Spin-Phonon Coupling in Slow-Relaxing Molecular Magnets. *Chem. Sci.* **2017**, *8* (9), 6051–6059. <https://doi.org/10.1039/C7SC02832F>.
- (7) Lunghi, A.; Totti, F.; Sessoli, R.; Sanvito, S. The Role of Anharmonic Phonons in Under-Barrier Spin Relaxation of Single Molecule Magnets. *Nat. Commun.* **2017**, *8*, 14620. <https://doi.org/10.1038/ncomms14620>.
- (8) Moseley, D. H.; Stavretis, S. E.; Thirunavukkuarasu, K.; Ozerov, M.; Cheng, Y.; Daemen, L. L.; Ludwig, J.; Lu, Z.; Smirnov, D.; Brown, C. M.; Pandey, A.; Ramirez-Cuesta, A. J.; Lamb, A. C.; Atanasov, M.; Bill, E.; Neese, F.; Xue, Z.-L. Spin–Phonon Couplings in

- Transition Metal Complexes with Slow Magnetic Relaxation. *Nat. Commun.* **2018**, *9* (1), 2572. <https://doi.org/10.1038/s41467-018-04896-0>.
- (9) Atanasov, M.; Neese, F. Computational Studies on Vibronic Coupling in Single Molecule Magnets: Impact on the Mechanism of Magnetic Relaxation. *J. Phys. Conf. Ser.* **2018**, *1148* (1), 012006. <https://doi.org/10.1088/1742-6596/1148/1/012006>.
- (10) Udvarhelyi, P.; Shkolnikov, V. O.; Gali, A.; Burkard, G.; Pályi, A. Spin-Strain Interaction in Nitrogen-Vacancy Centers in Diamond. *Phys. Rev. B* **2018**, *98* (7), 075201. <https://doi.org/10.1103/PhysRevB.98.075201>.
- (11) Goldman, M. L.; Sipahigil, A.; Doherty, M. W.; Yao, N. Y.; Bennett, S. D.; Markham, M.; Twitchen, D. J.; Manson, N. B.; Kubanek, A.; Lukin, M. D. Phonon-Induced Population Dynamics and Intersystem Crossing in Nitrogen-Vacancy Centers. *Phys. Rev. Lett.* **2015**, *114* (14), 145502. <https://doi.org/10.1103/PhysRevLett.114.145502>.
- (12) Goldman, M. L.; Doherty, M. W.; Sipahigil, A.; Yao, N. Y.; Bennett, S. D.; Manson, N. B.; Kubanek, A.; Lukin, M. D. State-Selective Intersystem Crossing in Nitrogen-Vacancy Centers. *Phys. Rev. B* **2015**, *91* (16), 165201. <https://doi.org/10.1103/PhysRevB.91.165201>.
- (13) Albino, A.; Benci, S.; Tesi, L.; Atzori, M.; Torre, R.; Sanvito, S.; Sessoli, R.; Lunghi, A. First-Principles Investigation of Spin-Phonon Coupling in Vanadium-Based Molecular Spin Quantum Bits. *Inorg. Chem.* **2019**, *58* (15), 10260–10268. <https://doi.org/10.1021/acs.inorgchem.9b01407>.
- (14) Escalera-Moreno, L.; Suaud, N.; Gaita-Ariño, A.; Coronado, E. Determining Key Local Vibrations in the Relaxation of Molecular Spin Qubits and Single-Molecule Magnets. *J. Phys. Chem. Lett.* **2017**, *8* (7), 1695–1700. <https://doi.org/10.1021/acs.jpcclett.7b00479>.
- (15) Escalera-Moreno, L.; Baldoví, J. J.; Gaita-Ariño, A.; Coronado, E. Spin States, Vibrations and Spin Relaxation in Molecular Nanomagnets and Spin Qubits: A Critical Perspective. *Chem. Sci.* **2018**, *9* (13), 3265–3275. <https://doi.org/10.1039/C7SC05464E>.
- (16) Dobrovitski, V. v.; Fuchs, G. d.; Falk, A. l.; Santori, C.; Awschalom, D. d. Quantum Control over Single Spins in Diamond. *Annu. Rev. Condens. Matter Phys.* **2013**, *4* (1), 23–50. <https://doi.org/10.1146/annurev-conmatphys-030212-184238>.
- (17) Khomskii, D. I.; Sawatzky, G. A. Interplay between Spin, Charge and Orbital Degrees of Freedom in Magnetic Oxides. *Solid State Commun.* **1997**, *102* (2), 87–99. [https://doi.org/10.1016/S0038-1098\(96\)00717-X](https://doi.org/10.1016/S0038-1098(96)00717-X).
- (18) Orenstein, J.; Millis, A. J. Advances in the Physics of High-Temperature Superconductivity. *Science* **2000**, *288* (5465), 468–474. <https://doi.org/10.1126/science.288.5465.468>.
- (19) Lanzara, A.; Bogdanov, P. V.; Zhou, X. J.; Kellar, S. A.; Feng, D. L.; Lu, E. D.; Yoshida, T.; Eisaki, H.; Fujimori, A.; Kishio, K.; Shimoyama, J.-I.; Noda, T.; Uchida, S.; Hussain, Z.; Shen, Z.-X. Evidence for Ubiquitous Strong Electron-Phonon Coupling in High-Temperature Superconductors. *Nature* **2001**, *412* (6846), 510–514. <https://doi.org/10.1038/35087518>.
- (20) Tokura, Y.; Nagaosa, N. Orbital Physics in Transition-Metal Oxides. *Science* **2000**, *288* (5465), 462–468. <https://doi.org/10.1126/science.288.5465.462>.
- (21) Mochizuki, M.; Furukawa, N.; Nagaosa, N. Theory of Spin-Phonon Coupling in Multiferroic Manganese Perovskites RMnO_3 . *Phys. Rev. B* **2011**, *84* (14), 144409. <https://doi.org/10.1103/PhysRevB.84.144409>.
- (22) Brinzari, T. V.; Haraldsen, J. T.; Chen, P.; Sun, Q.-C.; Kim, Y.; Tung, L.-C.; Litvinchuk, A. P.; Schlueter, J. A.; Smirnov, D.; Manson, J. L.; Singleton, J.; Musfeldt, J. L. Electron-Phonon and Magnetoelastic Interactions in Ferromagnetic

- $\text{Co}^{\text{II}}\text{N}^{\text{III}}\text{CN}^{\text{I}}$. *Phys. Rev. Lett.* **2013**, *111* (4), 047202. <https://doi.org/10.1103/PhysRevLett.111.047202>.
- (23) Rini, M.; Tobey, R.; Dean, N.; Itatani, J.; Tomioka, Y.; Tokura, Y.; Schoenlein, R. W.; Cavalleri, A. Control of the Electronic Phase of a Manganite by Mode-Selective Vibrational Excitation. *Nature* **2007**, *449* (7158), 72–74. <https://doi.org/10.1038/nature06119>.
- (24) Fausti, D.; Tobey, R. I.; Dean, N.; Kaiser, S.; Dienst, A.; Hoffmann, M. C.; Pyon, S.; Takayama, T.; Takagi, H.; Cavalleri, A. Light-Induced Superconductivity in a Stripe-Ordered Cuprate. *Science* **2011**, *331* (6014), 189–191. <https://doi.org/10.1126/science.1197294>.
- (25) Först, M.; Manzoni, C.; Kaiser, S.; Tomioka, Y.; Tokura, Y.; Merlin, R.; Cavalleri, A. Nonlinear Phononics as an Ultrafast Route to Lattice Control. *Nat. Phys.* **2011**, *7* (11), 854–856. <https://doi.org/10.1038/nphys2055>.
- (26) Maehrlein, S. F.; Radu, I.; Maldonado, P.; Paarmann, A.; Gensch, M.; Kalashnikova, A. M.; Pisarev, R. V.; Wolf, M.; Oppeneer, P. M.; Barker, J.; Kampfrath, T. Dissecting Spin-Phonon Equilibration in Ferrimagnetic Insulators by Ultrafast Lattice Excitation. *Sci. Adv.* **2018**, *4* (7), eaar5164. <https://doi.org/10.1126/sciadv.aar5164>.
- (27) DiVincenzo, D. P. The Physical Implementation of Quantum Computation. *Fortschritte Phys.* **2000**, *48* (9–11), 771–783. [https://doi.org/10.1002/1521-3978\(200009\)48:9:11<771::AID-PROP771>3.0.CO;2-E](https://doi.org/10.1002/1521-3978(200009)48:9:11<771::AID-PROP771>3.0.CO;2-E).
- (28) Zadrozny, J. M.; Niklas, J.; Poluektov, O. G.; Freedman, D. E. Millisecond Coherence Time in a Tunable Molecular Electronic Spin Qubit. *ACS Cent. Sci.* **2015**, *1* (9), 488–492. <https://doi.org/10.1021/acscentsci.5b00338>.
- (29) Zadrozny, J. M.; Niklas, J.; Poluektov, O. G.; Freedman, D. E. Multiple Quantum Coherences from Hyperfine Transitions in a Vanadium(IV) Complex. *J. Am. Chem. Soc.* **2014**, *136* (45), 15841–15844. <https://doi.org/10.1021/ja507846k>.
- (30) Fataftah, M. S.; Zadrozny, J. M.; Coste, S. C.; Graham, M. J.; Rogers, D. M.; Freedman, D. E. Employing Forbidden Transitions as Qubits in a Nuclear Spin-Free Chromium Complex. *J. Am. Chem. Soc.* **2016**, *138* (4), 1344–1348. <https://doi.org/10.1021/jacs.5b11802>.
- (31) Fataftah, M. S.; Coste, S. C.; Vlaisavljevich, B.; Zadrozny, J. M.; Freedman, D. E. Transformation of the Coordination Complex $[\text{Co}(\text{C}_3\text{S}_5)_2]^{2-}$ from a Molecular Magnet to a Potential Qubit. *Chem. Sci.* **2016**, *7* (9), 6160–6166. <https://doi.org/10.1039/C6SC02170K>.
- (32) Graham, M. J.; Zadrozny, J. M.; Shiddiq, M.; Anderson, J. S.; Fataftah, M. S.; Hill, S.; Freedman, D. E. Influence of Electronic Spin and Spin–Orbit Coupling on Decoherence in Mononuclear Transition Metal Complexes. *J. Am. Chem. Soc.* **2014**, *136* (21), 7623–7626. <https://doi.org/10.1021/ja5037397>.
- (33) S. Fataftah, M.; D. Krzyaniak, M.; Vlaisavljevich, B.; R. Wasielewski, M.; M. Zadrozny, J.; E. Freedman, D. Metal–Ligand Covalency Enables Room Temperature Molecular Qubit Candidates. *Chem. Sci.* **2019**. <https://doi.org/10.1039/C9SC00074G>.
- (34) J. Pearson, T.; W. Laorenza, D.; D. Krzyaniak, M.; R. Wasielewski, M.; E. Freedman, D. Octacyanometallate Qubit Candidates. *Dalton Trans.* **2018**, *47* (34), 11744–11748. <https://doi.org/10.1039/C8DT02312C>.
- (35) Zadrozny, J. M.; Gallagher, A. T.; Harris, T. D.; Freedman, D. E. A Porous Array of Clock Qubits. *J. Am. Chem. Soc.* **2017**, *139* (20), 7089–7094. <https://doi.org/10.1021/jacs.7b03123>.

- (36) Yu, C.-J.; Krzyaniak, M. D.; Fataftah, M. S.; Wasielewski, M. R.; Freedman, D. E. A Concentrated Array of Copper Porphyrin Candidate Qubits. *Chem. Sci.* **2018**. <https://doi.org/10.1039/C8SC04435J>.
- (37) Atzori, M.; Tesi, L.; Morra, E.; Chiesa, M.; Sorace, L.; Sessoli, R. Room-Temperature Quantum Coherence and Rabi Oscillations in Vanadyl Phthalocyanine: Toward Multifunctional Molecular Spin Qubits. *J. Am. Chem. Soc.* **2016**, *138* (7), 2154–2157. <https://doi.org/10.1021/jacs.5b13408>.
- (38) Yamabayashi, T.; Atzori, M.; Tesi, L.; Cosquer, G.; Santanni, F.; Boulon, M.-E.; Morra, E.; Benci, S.; Torre, R.; Chiesa, M.; Sorace, L.; Sessoli, R.; Yamashita, M. Scaling Up Electronic Spin Qubits into a Three-Dimensional Metal–Organic Framework. *J. Am. Chem. Soc.* **2018**, *140* (38), 12090–12101. <https://doi.org/10.1021/jacs.8b06733>.
- (39) Tesi, L.; Lucaccini, E.; Cimatti, I.; Perfetti, M.; Mannini, M.; Atzori, M.; Morra, E.; Chiesa, M.; Caneschi, A.; Sorace, L.; Sessoli, R. Quantum Coherence in a Processable Vanadyl Complex: New Tools for the Search of Molecular Spin Qubits. *Chem. Sci.* **2016**, *7* (3), 2074–2083. <https://doi.org/10.1039/C5SC04295J>.
- (40) Tesi, L.; Lunghi, A.; Atzori, M.; Lucaccini, E.; Sorace, L.; Totti, F.; Sessoli, R. Giant Spin–Phonon Bottleneck Effects in Evaporable Vanadyl-Based Molecules with Long Spin Coherence. *Dalton Trans.* **2016**, *45* (42), 16635–16643. <https://doi.org/10.1039/C6DT02559E>.
- (41) Stinghen, D.; Atzori, M.; Fernandes, C. M.; Ribeiro, R. R.; de Sá, E. L.; Back, D. F.; Giese, S. O. K.; Hughes, D. L.; Nunes, G. G.; Morra, E.; Chiesa, M.; Sessoli, R.; Soares, J. F. A Rare Example of Four-Coordinate Nonoxido Vanadium(IV) Alkoxide in the Solid State: Structure, Spectroscopy, and Magnetization Dynamics. *Inorg. Chem.* **2018**, *57* (18), 11393–11403. <https://doi.org/10.1021/acs.inorgchem.8b01117>.
- (42) Atzori, M.; Chiesa, A.; Morra, E.; Chiesa, M.; Sorace, L.; Carretta, S.; Sessoli, R. A Two-Qubit Molecular Architecture for Electron-Mediated Nuclear Quantum Simulation. *Chem. Sci.* **2018**, *9* (29), 6183–6192. <https://doi.org/10.1039/C8SC01695J>.
- (43) Atzori, M.; Benci, S.; Morra, E.; Tesi, L.; Chiesa, M.; Torre, R.; Sorace, L.; Sessoli, R. Structural Effects on the Spin Dynamics of Potential Molecular Qubits. *Inorg. Chem.* **2018**, *57* (2), 731–740. <https://doi.org/10.1021/acs.inorgchem.7b02616>.
- (44) Atzori, M.; Tesi, L.; Benci, S.; Lunghi, A.; Righini, R.; Taschin, A.; Torre, R.; Sorace, L.; Sessoli, R. Spin Dynamics and Low Energy Vibrations: Insights from Vanadyl-Based Potential Molecular Qubits. *J. Am. Chem. Soc.* **2017**, *139* (12), 4338–4341. <https://doi.org/10.1021/jacs.7b01266>.
- (45) Ariciu, A.-M.; Woen, D. H.; Huh, D. N.; Nodaraki, L. E.; Kostopoulos, A. K.; Goodwin, C. A. P.; Chilton, N. F.; McInnes, E. J. L.; Winpenny, R. E. P.; Evans, W. J.; Tuna, F. Engineering Electronic Structure to Prolong Relaxation Times in Molecular Qubits by Minimising Orbital Angular Momentum. *Nat. Commun.* **2019**, *10* (1), 1–8. <https://doi.org/10.1038/s41467-019-11309-3>.
- (46) Ardavan, A.; Bowen, A. M.; Fernandez, A.; Fielding, A. J.; Kaminski, D.; Moro, F.; Murny, C. A.; Wise, M. D.; Ruggi, A.; McInnes, E. J. L.; Severin, K.; Timco, G. A.; Timmel, C. R.; Tuna, F.; Whitehead, G. F. S.; Winpenny, R. E. P. Engineering Coherent Interactions in Molecular Nanomagnet Dimers. *Npj Quantum Inf.* **2015**, *1*, 15012. <https://doi.org/10.1038/npjqi.2015.12>.
- (47) Garlatti, E.; Guidi, T.; Ansbro, S.; Santini, P.; Amoretti, G.; Ollivier, J.; Mutka, H.; Timco, G.; Vitorica-Yrezabal, I. J.; Whitehead, G. F. S.; Winpenny, R. E. P.; Carretta, S. Portraying

- Entanglement between Molecular Qubits with Four-Dimensional Inelastic Neutron Scattering. *Nat. Commun.* **2017**, *8*, 14543. <https://doi.org/10.1038/ncomms14543>.
- (48) Timco, G. A.; Carretta, S.; Troiani, F.; Tuna, F.; Pritchard, R. J.; Muryn, C. A.; McInnes, E. J. L.; Ghirri, A.; Candini, A.; Santini, P.; Amoretti, G.; Affronte, M.; Winpenny, R. E. P. Engineering the Coupling between Molecular Spin Qubits by Coordination Chemistry. *Nat. Nanotechnol.* **2009**, *4* (3), 173–178. <https://doi.org/10.1038/nnano.2008.404>.
- (49) Ferrando-Soria, J.; Magee, S. A.; Chiesa, A.; Carretta, S.; Santini, P.; Vitorica-Yrezabal, I. J.; Tuna, F.; Whitehead, G. F. S.; Sproules, S.; Lancaster, K. M.; Barra, A.-L.; Timco, G. A.; McInnes, E. J. L.; Winpenny, R. E. P. Switchable Interaction in Molecular Double Qubits. *Chem* **2016**, *1* (5), 727–752. <https://doi.org/10.1016/j.chempr.2016.10.001>.
- (50) McGuire, J.; Miras, H. N.; Donahue, J. P.; Richards, E.; Sproules, S. Ligand Radicals as Modular Organic Electron Spin Qubits. *Chem. – Eur. J.* **2018**, *24* (66), 17598–17605. <https://doi.org/10.1002/chem.201804165>.
- (51) Bader, K.; Dengler, D.; Lenz, S.; Endeward, B.; Jiang, S.-D.; Neugebauer, P.; van Slageren, J. Room Temperature Quantum Coherence in a Potential Molecular Qubit. *Nat. Commun.* **2014**, *5*, 5304. <https://doi.org/10.1038/ncomms6304>.
- (52) Shrivastava, K. N. Theory of Spin–Lattice Relaxation. *Phys. Status Solidi B* **1983**, *117* (2), 437–458. <https://doi.org/10.1002/pssb.2221170202>.
- (53) Shrivastava, K. N. Lattice-Dynamical Contributions to g-Values. *J. Phys. C Solid State Phys.* **1982**, *15* (18), 3869–3876. <https://doi.org/10.1088/0022-3719/15/18/005>.
- (54) Atzori, M.; Morra, E.; Tesi, L.; Albino, A.; Chiesa, M.; Sorace, L.; Sessoli, R. Quantum Coherence Times Enhancement in Vanadium(IV)-Based Potential Molecular Qubits: The Key Role of the Vanadyl Moiety. *J. Am. Chem. Soc.* **2016**, *138* (35), 11234–11244. <https://doi.org/10.1021/jacs.6b05574>.
- (55) Solomon, E. I. Introduction. *Comments Inorg. Chem.* **1984**, *3* (5), 227–229. <https://doi.org/10.1080/02603598408080072>.
- (56) Neese, F. The ORCA Program System. *Wiley Interdiscip. Rev. Comput. Mol. Sci.* **2012**, *2* (1), 73–78. <https://doi.org/10.1002/wcms.81>.
- (57) Neese, F. Software Update: The ORCA Program System, Version 4.0. *Wiley Interdiscip. Rev. Comput. Mol. Sci.* **2018**, *8* (1), e1327. <https://doi.org/10.1002/wcms.1327>.
- (58) Szilagy, R. K.; Metz, M.; Solomon, E. I. Spectroscopic Calibration of Modern Density Functional Methods Using [CuCl₄]²⁻. *J. Phys. Chem. A* **2002**, *106* (12), 2994–3007. <https://doi.org/10.1021/jp014121c>.
- (59) Solomon, E. I.; Szilagy, R. K.; DeBeer George, S.; Basumallick, L. Electronic Structures of Metal Sites in Proteins and Models: Contributions to Function in Blue Copper Proteins. *Chem. Rev.* **2004**, *104* (2), 419–458. <https://doi.org/10.1021/cr0206317>.
- (60) Neese, F.; Solomon, E. I. Calculation of Zero-Field Splittings, g-Values, and the Relativistic Nephelauxetic Effect in Transition Metal Complexes. Application to High-Spin Ferric Complexes. *Inorg. Chem.* **1998**, *37* (26), 6568–6582. <https://doi.org/10.1021/ic980948i>.
- (61) Gu, B.; Franco, I. Generalized Theory for the Timescale of Molecular Electronic Decoherence in the Condensed Phase. *J. Phys. Chem. Lett.* **2018**, *9* (4), 773–778. <https://doi.org/10.1021/acs.jpcllett.7b03322>.
- (62) Harlow, R. L.; Wells, W. J.; Watt, G. W.; Simonsen, S. H. Crystal Structures of the Green and Yellow Thermochromic Modifications of Bis(N-Methylphenethylammonium) Tetrachlorocuprate (II). Discrete Square-Planar and Flattened Tetrahedral

- Tetrachlorocuprate(2-)Anions. *Inorg. Chem.* **1974**, *13* (9), 2106–2111. <https://doi.org/10.1021/ic50139a012>.
- (63) Cassidy, P.; Hitchman, M. A. Molecular g Values of the Planar Tetrachlorocuprate(2-) Ion. *Inorg. Chem.* **1977**, *16* (6), 1568–1570. <https://doi.org/10.1021/ic50172a067>.
- (64) Gewirth, A. A.; Cohen, S. L.; Schugar, H. J.; Solomon, E. I. Spectroscopic and Theoretical Studies of the Unusual EPR Parameters of Distorted Tetrahedral Cupric Sites: Correlations to x-Ray Spectral Features of Core Levels. *Inorg. Chem.* **1987**, *26* (7), 1133–1146. <https://doi.org/10.1021/ic00254a032>.
- (65) Ferguson, J. Electronic Absorption Spectrum and Structure of CuCl_4^- . *J. Chem. Phys.* **1964**, *40* (11), 3406–3410. <https://doi.org/10.1063/1.1725014>.
- (66) Shiddiq, M.; Komijani, D.; Duan, Y.; Gaita-Ariño, A.; Coronado, E.; Hill, S. Enhancing Coherence in Molecular Spin Qubits via Atomic Clock Transitions. *Nature* **2016**, *531* (7594), 348–351. <https://doi.org/10.1038/nature16984>.
- (67) Wolfowicz, G.; Tyryshkin, A. M.; George, R. E.; Riemann, H.; Abrosimov, N. V.; Becker, P.; Pohl, H.-J.; Thewalt, M. L. W.; Lyon, S. A.; Morton, J. J. L. Atomic Clock Transitions in Silicon-Based Spin Qubits. *Nat. Nanotechnol.* **2013**, *8* (8), 561–564. <https://doi.org/10.1038/nnano.2013.117>.
- (68) Wolfowicz, G.; Simmons, S.; Tyryshkin, A. M.; George, R. E.; Riemann, H.; Abrosimov, N. V.; Becker, P.; Pohl, H.-J.; Lyon, S. A.; Thewalt, M. L. W.; Morton, J. J. L. Decoherence Mechanisms of ^{209}Bi Donor Electron Spins in Isotopically Pure ^{28}Si . *Phys. Rev. B* **2012**, *86* (24), 245301. <https://doi.org/10.1103/PhysRevB.86.245301>.
- (69) Ghosh, S.; Datta, S.; Friend, L.; Cardona-Serra, S.; Gaita-Ariño, A.; Coronado, E.; Hill, S. Multi-Frequency EPR Studies of a Mononuclear Holmium Single-Molecule Magnet Based on the Polyoxometalate $[\text{HoIII}(\text{W}_5\text{O}_{18})_2]^{9-}$. *Dalton Trans.* **2012**, *41* (44), 13697–13704. <https://doi.org/10.1039/C2DT31674A>.
- (70) Fielding, A. J.; Fox, S.; Millhauser, G. L.; Chattopadhyay, M.; Kroneck, P. M. H.; Fritz, G.; Eaton, G. R.; Eaton, S. S. Electron Spin Relaxation of Copper(II) Complexes in Glassy Solution between 10 and 120K. *J. Magn. Reson.* **2006**, *179* (1), 92–104. <https://doi.org/10.1016/j.jmr.2005.11.011>.
- (71) Flowers, J. M.; Hempel, J. C.; Hatfield, W. E.; Dearman, H. H. An EPR Study of VO_2^+ and Cr^{3+} in $(\text{NH}_4)_2\text{SbCl}_5$. *J. Chem. Phys.* **1973**, *58* (4), 1479–1486. <https://doi.org/10.1063/1.1679383>.
- (72) Collison, D.; Gahan, B.; Garner, C. D.; Mabbs, F. E. Electronic Absorption Spectra of Some Oxovanadium(IV) Compounds. *J. Chem. Soc. Dalton Trans.* **1980**, No. 4, 667–674. <https://doi.org/10.1039/DT9800000667>.
- (73) Finazzo, C.; Calle, C.; Stoll, S.; Doorslaer, S. V.; Schweiger, A. Matrix Effects on Copper(II)Phthalocyanine Complexes. A Combined Continuous Wave and Pulse EPR and DFT Study. *Phys. Chem. Chem. Phys.* **2006**, *8* (16), 1942–1953. <https://doi.org/10.1039/B516184C>.
- (74) Mrkvová, K.; Kameníček, J.; Šindelář, Z.; Kvítek, L.; Mrozinski, J.; Nahorska, M.; Žák, Z. Synthesis, Properties and Crystal Structures of $\text{R}[\text{MIII}(\text{Bdt})_2]$ Complexes (M = Ni, Co, Cu). *Transit. Met. Chem.* **2004**, *29* (3), 238–244. <https://doi.org/10.1023/B:TMCH.0000020349.69302.37>.
- (75) Warner, M.; Din, S.; Tupitsyn, I. S.; Morley, G. W.; Stoneham, A. M.; Gardener, J. A.; Wu, Z.; Fisher, A. J.; Heutz, S.; Kay, C. W. M.; Aeppli, G. Potential for Spin-Based Information

- Processing in a Thin-Film Molecular Semiconductor. *Nature* **2013**, *503* (7477), 504–508. <https://doi.org/10.1038/nature12597>.
- (76) Assour, J. M.; Goldmacher, J.; Harrison, S. E. Electron Spin Resonance of Vanadyl Phthalocyanine. *J. Chem. Phys.* **1965**, *43* (1), 159–165. <https://doi.org/10.1063/1.1696446>.
- (77) Noll, A.; Rabe, S.; Müller, U. Die Oxochlorovanadate $\text{PPh}_4[\text{VOCl}_3\text{OH}]$, $\text{PPh}_4[\text{VOCl}_4]$, $(\text{PPh}_4)_2[\text{VOCl}_4] \cdot 2\text{CH}_3\text{CN}$ Und $(\text{PPh}_4)_2[\text{VOCl}_4] \cdot \text{CH}_3\text{CN}$ Mit Auffälligen Abweichungen von Der Quadratisch-Pyramidalen Anionenstruktur / The Oxochlorovanadates $\text{PPh}_4[\text{VOCl}_3\text{OH}]$, $\text{PPh}_4[\text{VOCl}_4]$, $(\text{PPh}_4)_2[\text{VOCl}_4] \cdot 2\text{CH}_3\text{CN}$ and $(\text{PPh}_4)_2[\text{VOCl}_4] \cdot \text{CH}_3\text{CN}$ with Remarkable Deviations from the Square-Pyramidal Anion Structure. *Z. Für Naturforschung B* **2014**, *54* (5), 591–596. <https://doi.org/10.1515/znb-1999-0504>.
- (78) Nagarajan, V.; Müller, B.; Storcheva, O.; Köhler, K.; Pöpl, A. Coordination of Solvent Molecules to $\text{VO}(\text{Acac})_2$ Complexes in Solution Studied by Hyperfine Sublevel Correlation Spectroscopy and Pulsed Electron Nuclear Double Resonance. *Res. Chem. Intermed.* **2007**, *33* (8), 705–724. <https://doi.org/10.1163/156856707782169408>.
- (79) Vallee, B. L.; Williams, R. J. Metalloenzymes: The Entatic Nature of Their Active Sites. *Proc. Natl. Acad. Sci.* **1968**, *59* (2), 498–505. <https://doi.org/10.1073/pnas.59.2.498>.
- (80) Malmström, B. G. Rack-Induced Bonding in Blue-Copper Proteins. *Eur. J. Biochem.* **1994**, *223* (3), 711–718. <https://doi.org/10.1111/j.1432-1033.1994.tb19044.x>.
- (81) Williams, R. J. P. Energised (Entatic) States of Groups and of Secondary Structures in Proteins and Metalloproteins. *Eur. J. Biochem.* **1995**, *234* (2), 363–381. https://doi.org/10.1111/j.1432-1033.1995.363_b.x.
- (82) Gray, H. B.; Malmström, B. G.; Williams, R. J. P. Copper Coordination in Blue Proteins. *JBIC J. Biol. Inorg. Chem.* **2000**, *5* (5), 551–559. <https://doi.org/10.1007/s007750000146>.
- (83) Ghosh, S.; Xie, X.; Dey, A.; Sun, Y.; Scholes, C. P.; Solomon, E. I. Thermodynamic Equilibrium between Blue and Green Copper Sites and the Role of the Protein in Controlling Function. *Proc. Natl. Acad. Sci.* **2009**, *106* (13), 4969–4974. <https://doi.org/10.1073/pnas.0900995106>.
- (84) Tsai, M.-L.; Hadt, R. G.; Marshall, N. M.; Wilson, T. D.; Lu, Y.; Solomon, E. I. Axial Interactions in the Mixed-Valent Cu^{A} Active Site and Role of the Axial Methionine in Electron Transfer. *Proc. Natl. Acad. Sci.* **2013**, *110* (36), 14658–14663. <https://doi.org/10.1073/pnas.1314242110>.
- (85) Mara, M. W.; Hadt, R. G.; Reinhard, M. E.; Kroll, T.; Lim, H.; Hartsock, R. W.; Alonso-Mori, R.; Chollet, M.; Glowina, J. M.; Nelson, S.; Sokaras, D.; Kunnus, K.; Hodgson, K. O.; Hedman, B.; Bergmann, U.; Gaffney, K. J.; Solomon, E. I. Metalloprotein Entatic Control of Ligand-Metal Bonds Quantified by Ultrafast x-Ray Spectroscopy. *Science* **2017**, *356* (6344), 1276–1280. <https://doi.org/10.1126/science.aam6203>.
- (86) Kohler, L.; Hadt, R. G.; Hayes, D.; Chen, L. X.; Mulfort, K. L. Synthesis, Structure, and Excited State Kinetics of Heteroleptic $\text{Cu}(\text{I})$ Complexes with a New Sterically Demanding Phenanthroline Ligand. *Dalton Trans.* **2017**, *46* (38), 13088–13100. <https://doi.org/10.1039/C7DT02476B>.
- (87) Dicke, B.; Hoffmann, A.; Stanek, J.; Rampp, M. S.; Grimm-Lebsanft, B.; Biebl, F.; Rukser, D.; Maerz, B.; Göries, D.; Naumova, M.; Biednov, M.; Neuber, G.; Wetzel, A.; Hofmann, S. M.; Roedig, P.; Meents, A.; Bielecki, J.; Andreasson, J.; Beyerlein, K. R.; Chapman, H. N.; Bressler, C.; Zinth, W.; Rübhausen, M.; Herres-Pawlis, S. Transferring the Entatic-State

- Principle to Copper Photochemistry. *Nat. Chem.* **2018**, *10* (3), 355–362. <https://doi.org/10.1038/nchem.2916>.
- (88) Stanek, J.; Hoffmann, A.; Herres-Pawlis, S. Renaissance of the Entatic State Principle. *Coord. Chem. Rev.* **2018**, *365*, 103–121. <https://doi.org/10.1016/j.ccr.2018.03.009>.
- (89) Snyder, B. E. R.; Vanelderen, P.; Bols, M. L.; Hallaert, S. D.; Böttger, L. H.; Ungur, L.; Pierloot, K.; Schoonheydt, R. A.; Sels, B. F.; Solomon, E. I. The Active Site of Low-Temperature Methane Hydroxylation in Iron-Containing Zeolites. *Nature* **2016**, *536* (7616), 317–321. <https://doi.org/10.1038/nature19059>.
- (90) Comba, P.; Fukuzumi, S.; Koke, C.; Martin, B.; Löhr, A.-M.; Straub, J. A Bispidine Iron(IV)–Oxo Complex in the Entatic State. *Angew. Chem. Int. Ed.* **2016**, *55* (37), 11129–11133. <https://doi.org/10.1002/anie.201605099>.
- (91) Sohn, Y.-I.; Meesala, S.; Pingault, B.; Atikian, H. A.; Holzgrafe, J.; Gündoğan, M.; Stavrakas, C.; Stanley, M. J.; Sipahigil, A.; Choi, J.; Zhang, M.; Pacheco, J. L.; Abraham, J.; Bielejec, E.; Lukin, M. D.; Atatüre, M.; Lončar, M. Controlling the Coherence of a Diamond Spin Qubit through Its Strain Environment. *Nat. Commun.* **2018**, *9* (1), 1–6. <https://doi.org/10.1038/s41467-018-04340-3>.

Supporting Information

Computational Methods

All DFT calculations were carried out using ORCA¹, version 4.0.1.2 on the High Performance Computing Cluster at Caltech. For the special case of vanadyl phthalocyanine (VOPc) frequency calculations, the version used was 4.1.2 to resolve a glitch involving jobs running on multiple nodes. Representative input parameters for optimization, frequency and single point calculations are provided in the “Representative Orca Input Files” section of this document. For Cu(II) complexes, the Hartree-Fock exchange in the B3LYP functional²⁻⁵ was modified to 38%, except in the cases of thiolate and selenate ligands for which it was left at 20%. For all V(IV) complexes, the Hartree-Fock exchange was modified to 60%. As shown previously,⁶ for values of Hartree-Fock exchange must be determined independently for complexes that exhibit strongly variable covalencies of their respective ligand–metal bonds. All calculations were carried out using the def2-TZVP basis set⁷ with auxiliary basis set def2/J on all atoms.⁸ DFT grid 7 and tight SCF convergence criteria corresponding to a convergence tolerance of 10^{-8} Hartrees were used for all calculations.

The calculated normal modes q_k are presented in ORCA as cartesian displacements weighted by the diagonal matrix $M(i, i) = \frac{1}{\sqrt{m[i]}}$, where $m[i]$ is the mass of the displaced atom.

$$Q = \sum_i c_i q_i$$

$$q_i = \sqrt{m_i} x_i$$

If Q is normalized to 1, then the reduced mass is related by the following:

$$\mu = \frac{1}{\sum_i \frac{c_i^2}{m_i}}$$

Which is then related to the harmonic angular frequency ω and harmonic force constant k through $\omega^2 = k/\mu$.

Displacement along normal modes is done by multiplying the displacement vector q_i by a distortion scaling factor n , such that the displaced vector is defined by $(1+n)q_i$. All calculations presented here were performed between $n = -0.15$ and $n = 0.15$ in 0.05 increments to obtain coupling terms that reflective of the equilibrium geometry. For simplicity, the axes titles specify n relative to 0 and not 1, such that 0 corresponds to the equilibrium geometry.

Tables

Table 2-1.S1a. Bond distances and angles for X-ray crystallographic and idealized D_{4h} $[\text{CuCl}_4]^{2-}$ structures.

Bond	Length (Å) ^a	Length (Å) ^b	Angle	Angle (°) ^a	Angle (°) ^b
Cu-Cl _a	2.281	2.264	Cl _a -Cu-Cl _b	89.9	90.0
Cu-Cl _b	2.247	2.264	Cl _b -Cu-Cl _c	90.2	90.0
Cu-Cl _c	2.281	2.264	Cl _c -Cu-Cl _d	89.9	90.0
Cu-Cl _d	2.247	2.264	Cl _d -Cu-Cl _a	90.2	90.0
			Cl _a -Cu-Cl _c	180.0	180.0
			Cl _b -Cu-Cl _d	180.0	180.0

^a X-ray crystal structure.⁹

^b Idealized structure from X-ray crystal structure.

Table 2-1.S1b. Bond distances and angles for X-ray crystallographic and idealized D_{2d} $[\text{CuCl}_4]^{2-}$ structures. This structure was used for analysis in the main text.

Bond	Length (Å) ^a	Length (Å) ^b	Angle	Angle (°) ^a	Angle (°) ^b
Cu-Cl _a	2.189	2.208	Cl _a -Cu-Cl _b	101.3	100.1
Cu-Cl _b	2.228	2.208	Cl _b -Cu-Cl _c	98.3	100.1
Cu-Cl _c	2.189	2.208	Cl _c -Cu-Cl _d	101.3	100.1
Cu-Cl _d	2.228	2.208	Cl _d -Cu-Cl _a	98.3	100.1
			Cl _a -Cu-Cl _c	138.1	130.6
			Cl _b -Cu-Cl _d	123.1	130.6

^a X-ray crystal structure.⁹

^b Idealized structure from X-ray crystal structure.

Table 2-1.S1c. Bond distances and angles for a different X-ray crystallographic and idealized D_{2d} $[\text{CuCl}_4]^{2-}$ structure. g values and d-d transitions are shown for the idealized structure to emphasize similarity of values with ones used in the main text.

Bond	Length (Å) ^a	Length (Å) ^b	Angle	Angle (°) ^a	Angle (°) ^b
Cu-Cl _a	2.244	2.230	Cl _a -Cu-Cl _b	101.9	100.6

Cu-Cl _b	2.235	2.230	Cl _b -Cu-Cl _c	99.6	100.6
Cu-Cl _c	2.220	2.230	Cl _c -Cu-Cl _d	101.9	100.6
Cu-Cl _d	2.220	2.230	Cl _d -Cu-Cl _a	99.6	100.6
			Cl _a -Cu-Cl _c	131.2	129.1
			Cl _b -Cu-Cl _d	127.1	129.1
	g_x^b	g_y^b	g_z^b	Assignment	Energy (cm ⁻¹) ^b
	2.107	2.107	2.331	² B ₂ → ² E	6220
					6220
				² B ₂ → ² B ₁	8310
				² B ₂ → ² A ₁	9890

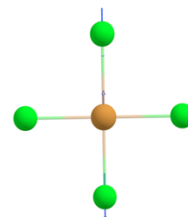
^a X-ray crystal structure.¹⁰

^b Idealized structure from X-ray crystal structure.

Table 2-1.S2a. Calculated vibrational modes for idealized D_{4h} $[\text{CuCl}_4]^{2-}$, including their energies, symmetry labels, and scaled vector displacements (arrows point towards the direction of positive displacement, where $n > 0$). $\Gamma_{vib} = a_{1g} + b_{1g} + b_{2g} + a_{2u} + b_{2u} + 2e_u$

Mode #	Energy (cm ⁻¹)	Symmetry	Scaled Vector Displacements
1	-85.8	b_{2u}	
2	140.5	a_{2u}	
3	172.2	$e_u(1a)$	
4	172.2	$e_u(1b)$	
5	182.7	b_{2g}	
6	198.5	b_{1g}	
7	296.3	a_{1g}	

8 341.4 $e_u(2a)$



9 341.5 $e_u(2b)$

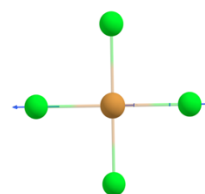
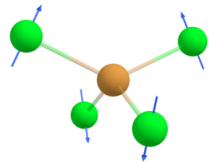
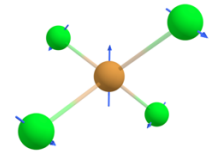
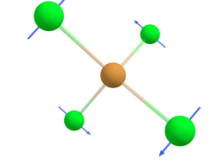
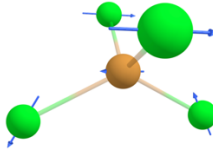
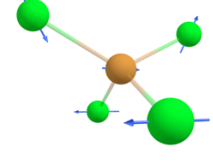
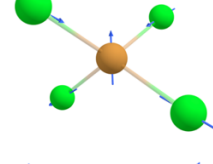
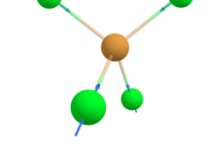
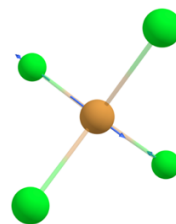


Table 2-1.S2b. Calculated vibrational modes for D_{2d} $[\text{CuCl}_4]^{2-}$, including their energies, symmetry labels, and scaled vector displacements (arrows point towards the direction of positive displacement, where $n > 0$). $\Gamma_{vib} = 2a_1 + b_1 + 2b_2 + 2e$

Mode #	Energy (cm^{-1})	Symmetry	Scaled Vector Displacements
1	-35.5	$a_1(1)$	
2	66.9	$b_2(1)$	
3	118.3	b_1	
4	128.6	$e(1a)$	
5	128.6	$e(1b)$	
6	290.2	$b_2(2)$	
7	316.7	$a_1(2)$	

8 348.7 $e(2a)$



9 348.8 $e(2b)$

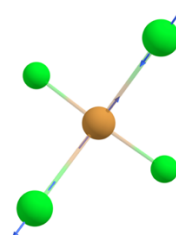


Table 2-1.S3a. Spin–phonon analyses (g_z values and ligand field energies) for idealized D_{4h} $[\text{CuCl}_4]^{2-}$.

Mode #	Energy (cm^{-1})	Symm.	Best-Fit* (g_z)*	r^2 (g_z)	Best-Fit (${}^2\text{B}_{2g}$)*	r^2 (${}^2\text{B}_{2g}$)
1	-85.78	b_{2u}	$y = 0.0630x^2 + 2.2038$	1.000	$y = -3230.5x^2 + 14475.2$	1.000
2	140.47	a_{2u}	$y = 0.1185x^2 + 2.2038$	1.000	$y = -6698.1x^2 + 14475.0$	1.000
3	172.17	$e_u(1a)$	$y = -0.0559x^2 + 2.2038$	1.000	$y = -4832.4x^2 - 0.1x + 14475.0$	1.000
4	172.2	$e_u(1b)$	$y = 0.0559x^2 + 2.2038$	1.000	$y = -4839.1x^2 + 14475.0$	1.000
5	182.65	b_{2g}	$y = -0.0020x^2 + 2.2038$	0.995	$y = 112.9x^2 - 0.2x + 14475.2$	0.999
6	198.49	b_{1g}	$y = 0.0077x^2 + 2.2038$	1.000	$y = -6530.5x^2 - 0.1x + 14475.6$	1.000
7	296.29	a_{1g}	$y = -0.2411x + 2.2037$	1.000	$y = 12470.3x + 14569.2$	0.996
8	341.38	$e_u(2a)$	$y = -0.2720x^2 + 2.2038$	1.000	$y = 651.4x^2 - 0.4x + 14477.3$	0.924
9	341.51	$e_u(2b)$	$y = -0.2720x^2 + 2.2038$	1.000	$y = 660.0x^2 + 14477.3$	0.926

Quadratic equations used to fit “even” modes where $g_z(-n) = g_z(n)$. Linear equations used for fitting “odd” modes $g_z(-n) = -g_z(n)$.

Table 2-1.S3b. Spin–phonon analyses (g_x values and ligand field energies) for idealized D_{4h} $[\text{CuCl}_4]^{2-}$.

Mode #	Energy (cm^{-1})	Symm.	Best-Fit Equation* (g_x)	$r^2(g_x)$	Best-Fit Equation* (${}^2E_g(1)$)	$r^2({}^2E_g(1))$
1	-85.8	b_{2u}	$y = 0.0174x^2 + 2.0555$	1.000	$y = -4393.8x^2 + 0.1x + 14608.5$	1.000
2	140.5	a_{2u}	$y = 0.0423x^2 + 2.0555$	1.000	$y = -10065.7x^2 + 14608.0$	1.000
3	172.2	$e_u(1a)$	$y = 0.0199x^2 + 2.0555$	1.000	$y = -2262.9x^2 - 0.1x + 14608.6$	1.000
4	172.2	$e_u(1b)$	$y = 0.0030x^2 + 2.0555$	0.999	$y = -3246.7x^2 + 14608.5$	1.000
5	182.7	b_{2g}	$y = 0.0049x^2 + 2.0555$	0.926	$y = -2174.3x^2 + 14600.3$	0.957
6	198.5	b_{1g}	$y = -0.0325x + 2.0555$	0.999	$y = -2409.4x - 14576.8$	0.991
7	296.3	a_{1g}	$y = -0.0724x + 2.0556$	1.000	$y = 12414.1x^2 + 14692.2$	0.997
8	341.4	$e_u(2a)$	$y = -0.0475x^2 + 2.0556$	0.999	$y = 13480.0x^2 - 0.1x + 14608.1$	1.000
9	341.5	$e_u(2b)$	$y = -0.1364x^2 + 2.0555$	1.000	$y = 3716.2x^2 + 14609.6$	0.999

Note mode 5 (b_{2g}) is V-shaped, but fitted as a quadratic function.

Table 2-1.S3c. Spin-phonon analyses (g_y values and ligand field energies) for idealized D_{4h} $[\text{CuCl}_4]^{2-}$.

Mode #	Energy (cm^{-1})	Symm.	Best-Fit Equation* (g_y)	r^2	Best-Fit Equation* (${}^2E_g(2)$)	r^2
1	-85.8	b_{2u}	$y = 0.0174x^2 + 2.0555$	1.000	$y = -4397.1x^2 + 14608.6$	1.000
2	140.5	a_{2u}	$y = 0.0423x^2 + 2.0555$	1.000	$y = -10070.5x^2 + 14608.1$	1.000
3	172.3	$e_u(1a)$	$y = 0.0199x^2 + 2.0555$	0.999	$y = -3240.0x^2 + 14608.6$	1.000
4	172.2	$e_u(1b)$	$y = 0.0030x^2 + 2.0555$	1.000	$y = -2268.1x^2 - 0.2x + 14608.7$	1.000
5	182.7	b_{2g}	$y = -0.0050x^2 + 2.0555$	0.928	$y = 1052.4x^2 + 14616.7$	0.830
6	198.5	b_{1g}	$y = 0.0325x + 2.0555$	0.999	$y = 1986.9x + 14610.8$	0.996
7	296.3	a_{1g}	$y = -0.0724x + 2.0556$	1.000	$y = 12414.1x^2 + 14692.3$	0.997
8	341.4	$e_u(2a)$	$y = -0.1364x^2 + 2.0555$	1.000	$y = 3715.7x^2 - 0.2x + 14609.6$	0.999
9	341.5	$e_u(2b)$	$y = -0.0475x^2 + 2.0556$	0.999	$y = 13481.9x^2 + 14608.2$	1.000

Note mode 5 (b_{2g}) is V-shaped, but fitted as a quadratic function.

Table 2-1.S3d. Spin-phonon analyses ($y = g_x - g_y$) for idealized D_{4h} $[\text{CuCl}_4]^{2-}$.

Mode #	Energy (cm^{-1})	Symm.	Best-Fit Equation*	r^2
1	-85.8	b_{2u}	$y = 0$	–
2	140.5	a_{2u}	$y = 0$	–
3	172.3	$e_u(1a)$	$y = 0.0169x^2$	1.000
4	172.2	$e_u(1b)$	$y = -0.0169x^2$	1.000
5	182.7	b_{2g}	$y = -0.0099x^2$	0.927
6	198.5	b_{1g}	$y = -0.0650x$	1.000
7	296.3	a_{1g}	$y = 0$	0.286
8	341.4	$e_u(2a)$	$y = 0.0889x^2$	0.999
9	341.5	$e_u(2b)$	$y = -0.0889x^2$	0.999

Note mode 5 (b_{2g}) is V-shaped, but fitted as a quadratic function.

Table 2-1.S3e. Spin–phonon analyses (spin densities and $y = {}^2E_g(1) - {}^2E_g(2)$) for idealized D_{4h} $[\text{CuCl}_4]^{2-}$.

Mode #	Energy (cm ⁻¹)	Symm.	Best-Fit Equation	r ²	Best-Fit Equation ${}^2E_g(1) - {}^2E_g(2)$	r ²
1	-85.8	b_{2u}	$y = 0.0484x^2 + 0.6681$	1.000	$y = 3.3x^2 + 0.1x - 0.1$	0.361
2	140.5	a_{2u}	$y = -0.0265x^2 + 0.6681$	1.000	$y = 4.8x^2 - 0.1$	0.833
3	172.3	$e_u(1a)$	$y = -0.0669x^2 + 0.6681$	1.000	$y = 977.1x^2 - 0.1x$	1.000
4	172.2	$e_u(1b)$	$y = -0.0669x^2 + 0.6681$	1.000	$y = -978.6x^2 + 0.2x - 0.2$	1.000
5	182.7	b_{2g}	$y = -0.0531x^2 + 0.6681$	1.000	$y = -3226.7x^2 - 16.4$	0.922
6	198.5	b_{1g}	$y = 0.0591x^2 + 0.6681$	1.000	$y = -4396.3x - 34.0$	0.995
7	296.3	a_{1g}	$y = -0.1107x + 0.6670$	0.993	$y = -0.1$	-
8	341.4	$e_u(2a)$	$y = -0.1704x^2 + 0.6681$	0.999	$y = 9764.3x^2 + 0.1x - 1.5$	1.000
9	341.5	$e_u(2b)$	$y = -0.1704x^2 + 0.6681$	0.999	$y = -9765.7x^2 + 1.4$	1.000

Note mode 5 (b_{2g}) is V-shaped, but fitted as a quadratic function.

Table 2-1.S4a. Spin-phonon analyses (g_z values and ligand field energies) for idealized D_{2d} $[\text{CuCl}_4]^{2-}$.

Mode #	Energy (cm^{-1})	Symm.	Best-Fit (g_z)	$r^2(g_z)$	Best-Fit (2B_1)	$r^2({}^2B_1)$
1	-35.5	$a_1(1)$	$y = 0.1403x + 2.3098$	0.998	$y = -3923.2x + 10432.9$	1.000
2	66.9	$b_2(1)$	$y = -0.0678x^2 + 2.3090$	1.000	$y = -1477.1x^2 + 0.1x + 10439.4$	1.000
3	118.3	b_1	$y = 0.0297x^2 + 2.3090$	1.000	$y = -604.8x^2 + 10439.4$	1.000
4	128.6	$e(1a)$	$y = 0.0554x^2 + 2.3090$	1.000	$y = 481.0x^2 + 10439.6$	1.000
5	128.6	$e(1b)$	$y = 0.0554x^2 + 2.3090$	1.000	$y = 481.0x^2 + 10439.6$	1.000
6	290.2	$b_2(2)$	$y = -0.2954x^2 + 2.3090$	1.000	$y = -2764.8x^2 - 0.3x + 10439.9$	1.000
7	316.7	$a_1(2)$	$y = -0.3058x + 2.3083$	1.000	$y = 7884.4x + 10498.9$	0.996
8	348.7	$e(2a)$	$y = -0.5498x^2 + 2.3090$	1.000	$y = 7766.7x^2 + 10437.2$	0.999
9	348.7	$e(2b)$	$y = -0.5498x^2 + 2.3090$	1.000	$y = 7768.1x^2 + 0.1x + 10437.2$	0.999

Table 2-1.S4b. Spin-phonon analyses (g_x values and ligand field energies) for idealized D_{2d} $[\text{CuCl}_4]^{2-}$.

Mode #	Energy (cm^{-1})	Symm.	Best-Fit Equation (g_x)	r^2	Best-Fit Equation (${}^2E(1)$)	r^2
1	-35.5	$a_1(1)$	$y = 0.0811x + 2.0957$	0.990	$y = -6942.4x + 6823.4$	1.000
2	66.9	$b_2(1)$	$y = -0.1697x + 2.0948$	1.000	$y = 2873.8x + 6843.1$	0.998
3	118.3	b_1	$y = -0.0735x^2 + 2.0942$	0.863	$y = -2418.0x + 6830.6$ for $x < 0$ $y = 2418.0x + 6830.6$ for $x > 0$	0.999 0.999
4	128.6	$e(1a)$	$y = -0.0424x^2 + 2.0948$	1.000	$y = -1371.4x^2 - 0.4x + 6827.5$	1.000
5	128.6	$e(1b)$	$y = 0.0628x^2 + 2.0947$	1.000	$y = -1953.3x^2 + 6827.4$	1.000
6	290.2	$b_2(2)$	$y = -0.2172x + 2.0943$	0.999	$y = 3053.1x + 6862.0$	0.991
7	316.7	$a_1(2)$	$y = -0.1519x + 2.0949$	1.000	$y = 5323.8x + 6861.9$	0.997
8	348.7	$e(2a)$	$y = -0.6174x^2 + 2.0945$	0.999	$y = 13733.3x^2 - 1.6x + 6827.1$	1.000
9	348.7	$e(2b)$	$y = 0.1079x^2 + 2.0949$	0.982	$y = 9170.5x^2 + 6830.5$	0.999

Note mode 3 (b_1) is V-shaped, but fitted as a quadratic function for $y = g_x$.

Table 2-1.S4c. Spin-phonon analyses (g_y values and ligand field energies) for idealized D_{2d} $[\text{CuCl}_4]^{2-}$.

Mode #	Energy (cm^{-1})	Symm.	Best-Fit Equation* (g_y)	r^2	Best-Fit Equation* (${}^2E(2)$)	r^2
1	-35.5	$a_1(1)$	$y = 0.0811x + 2.0957$	0.990	$y = -6942.0x + 6823.4$	1.000
2	66.9	$b_2(1)$	$y = 0.1697x + 2.0948$	1.000	$y = -2873.1x + 6843.1$	0.998
3	118.3	b_1	$y = 0.1356x^2 + 2.0953$	0.955	$y = 2786.2x + 6830.3$ for $x < 0$ $y = -2785.4x + 6412.5$ for $x > 0$	1.000 1.000
4	128.6	$e(1a)$	$y = 0.0629x^2 + 2.0952$	1.000	$y = -1959.1x^2 + 6827.5$	1.000
5	128.6	$e(1b)$	$y = -0.0424x^2 + 2.0948$	1.000	$y = -1369.5x^2 + 6827.4$	1.000
6	290.2	$b_2(2)$	$y = 0.2172x + 2.0943$	0.999	$y = -3053.4x + 6862.0$	0.991
7	316.7	$a_1(2)$	$y = -0.1519x + 2.0949$	1.000	$y = 5323.5x + 6861.9$	0.997
8	348.7	$e(2a)$	$y = 0.1079x^2 + 2.0949$	0.982	$y = 9170.5x^2 + 6830.5$	0.999
9	348.7	$e(2b)$	$y = -0.6175x^2 + 2.0945$	0.999	$y = 13740.5x^2 + 0.8x + 6827.1$	1.000

Note mode 3 (b_1) is V-shaped, but fitted as a quadratic for $y = g_y$.

Table 2-1.S4d. Spin-phonon analyses (g_x - g_y values) for idealized D_{2d} $[\text{CuCl}_4]^{2-}$.

Mode #	Energy (cm^{-1})	Symm.	Best-Fit Equation*	r^2	Best-Fit Equation* ${}^2E(1) - {}^2E(2)$	r^2
1	-35.5	$a_1(1)$	$y = -0.0000x - 0.0000$	0.0671	$y = -0.3571x - 0.0714$	0.625
2	66.9	$b_2(1)$	$y = -0.3393x + 0.0000$	1.000	$y = 5746.9x - 0.0142$	1.000
3	118.3	b_1	$y = -0.2091x^2 - 0.0010$	0.927	$y = -5203.4x + 0.2700$ for $x < 0$ $y = 5203.4x + 0.2700$ for $x > 0$	1.000 1.000
4	128.6	$e(1a)$	$y = -0.1053x^2 + 0.0000$	1.000	$y = 587.6x^2 - 0.4x + 0.0095$	1.000
5	128.6	$e(1b)$	$y = 0.1053x^2 - 0.0000$	1.000	$y = -583.8x^2 - 0.0619$	1.000
6	290.2	$b_2(2)$	$y = -0.4343x - 0.0000$	1.000	$y = 6106.4x + 0.0143$	1.000
7	316.7	$a_1(2)$	$y = 0.0000x - 0.0000$	0.197	$y = 0.2857x$	0.143
8	348.7	$e(2a)$	$y = -0.7254x^2 - 0.0004$	0.998	$y = 4562.9x^2 - 1.6x - 3.4142$	0.996
9	348.7	$e(2b)$	$y = 0.7254x^2 + 0.0004$	0.998	$y = -4570.0x^2 - 0.8x + 3.4571$	0.996

Note mode 3 (b_1) is V-shaped, but fitted as a quadratic function for $y = g_x - g_y$.

Table 2-1.S4e. Spin-phonon analyses (Loewdin spin densities) for idealized D_{2d} $[\text{CuCl}_4]^{2-}$.

Mode #	Energy (cm^{-1})	Symm.	Best-Fit Equation*	r^2
1	-35.5	$a_1(1)$	$y = 0.0759x + 0.7527$	1.000
2	66.9	$b_2(1)$	$y = -0.0038x^2 + 0.7525$	0.996
3	118.3	b_1	$y = -0.074x^2 + 0.7525$	1.000
4	128.6	$e(1a)$	$y = -0.0524x^2 + 0.7525$	1.000
5	128.6	$e(1b)$	$y = -0.0523x^2 + 0.7525$	1.000
6	290.2	$b_2(2)$	$y = -0.3264x^2 + 0.7525$	1.000
7	316.7	$a_1(2)$	$y = -0.1573x + 0.7510$	0.994
8	348.7	$e(2a)$	$y = -0.2429x^2 + 0.7526$	0.999
9	348.7	$e(2b)$	$y = -0.2429x^2 + 0.7526$	0.999

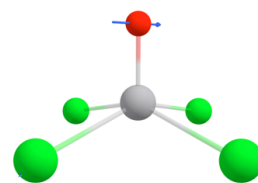
Table 2-1.S5. Bond distances and angles for X-ray crystallographic and idealized C_{4v} $[\text{VOCl}_4]^{2-}$ structures.

	Crystal Structure¹¹	Idealized Structure
V–O bond length (Å)	1.580	1.580
V–Cl _a bond length (Å)	2.362	2.354
V–Cl _b bond length (Å)	2.370	2.354
V–Cl _c bond length (Å)	2.327	2.354
V–Cl _d bond length (Å)	2.358	2.354
O–V–Cl _a bond angle (°)	106.7	104.3
O–V–Cl _b bond angle (°)	101.7	104.3
O–V–Cl _c bond angle (°)	107.4	104.3
O–V–Cl _d bond angle (°)	101.5	104.3
Cl _a –V–Cl _b bond angle (°)	85.6	86.5
Cl _a –V–Cl _c bond angle (°)	145.9	151.4
Cl _a –V–Cl _d bond angle (°)	87.7	86.5
Cl _b –V–Cl _c bond angle (°)	86.3	86.5
Cl _b –V–Cl _d bond angle (°)	156.9	151.4
Cl _c –V–Cl _d bond angle (°)	87.0	86.5

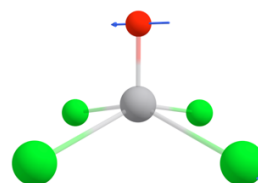
Table 2-1.S6. Calculated vibrational modes for idealized C_{4v} $[\text{VOCl}_4]^{2-}$, including their energies, symmetry labels, and scaled vector displacements (arrows point towards the direction of positive displacement, where $n > 0$). $\Gamma_{vib} = 3a_1 + 2b_1 + b_2 + 3e$

Mode #	Energy (cm^{-1})	Symmetry	Scaled Vector Displacements
1	-51.3	$b_1(1)$	
2	160.3	$e(1a)$	
3	160.3	$e(1b)$	
4	166.4	$a_1(1)$	
5	186.8	b_2	
6	233.2	$b_1(2)$	

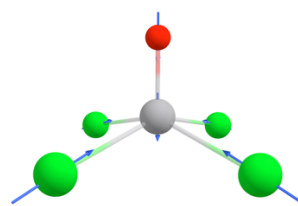
7 267.1 $e(2a)$



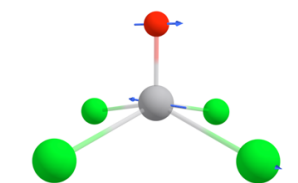
8 267.1 $e(2b)$



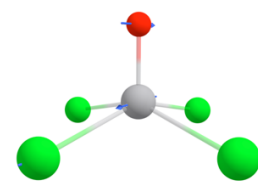
9 323.5 $a_1(2)$



10 394.9 $e(3a)$



11 394.9 $e(3b)$



12 1050.4 $a_1(3)$

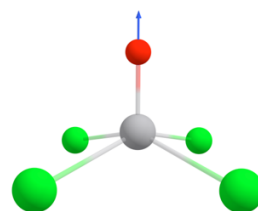


Table 2-1.S7a. Spin–phonon analyses (g_z values and ligand field energies) for idealized C_{4v} $[\text{VOCl}_4]^{2-}$.

Mode #	Energy (cm^{-1})	Symm.	Best-Fit (g_z)	$r^2(g_z)$	Best-Fit (2B_1)	$r^2({}^2B_1)$
1	-51.3	$b_1(1)$	$y = -0.0162x^2 + 1.9628$	1.000	$y = -3545.7x^2 + 15227.9$	1.000
2	160.3	$e(1a)$	$y = -0.0202x^2 + 1.9628$	1.000	$y = -5094.3x^2 + 15227.5$	1.000
3	160.3	$e(1b)$	$y = -0.0202x^2 + 1.9628$	1.000	$y = -5094.3x^2 + 15227.5$	1.000
4	166.4	$a_1(1)$	$y = -0.0183x^2 + 0.0020x + 1.9628$	1.000	$y = -3576.2x^2 - 298.857x + 15227.9$	1.000
5	186.8	b_2	$y = -0.0049x^2 + 1.9628$	1.000	$y = -564.8x^2 + 15228.0$	1.000
6	233.1	$b_1(2)$	$y = -0.0164x^2 + 1.9628$	1.000	$y = -10295.2x^2 + 15227.7$	1.000
7	267.1	$e(2a)$	$y = 0.0171x^2 + 1.9628$	1.000	$y = 1369.5x^2 + 15228.6$	0.998
8	267.1	$e(2b)$	$y = 0.0171x^2 + 1.9628$	1.000	$y = 1369.5x^2 + 15228.6$	0.998
9	323.5	$a_1(2)$	$y = 0.0684x + 1.9626$	1.000	$y = 13943.1x + 15312.6$	0.997
10	394.9	$e(3a)$	$y = -0.3125x^2 + 1.9626$	0.998	$y = -91921.0x^2 + 15002.2$	0.974
11	394.9	$e(3b)$	$y = -0.3125x^2 + 1.9626$	0.997	$y = -91921.0x^2 - 0.1x + 15002.2$	0.974
12	1050.4	$a_1(3)$	$y = 0.0302x + 1.9628$	0.999	-	-

Table 2-1.S7b. Spin-phonon analyses (g_x values and ligand field energies) for idealized C_{4v} $[\text{VOCl}_4]^{2-}$.

Mode #	Energy (cm^{-1})	Symm.	Best-Fit (g_x)	$r^2(g_x)$	Best-Fit (${}^2E(1)$)	$r^2({}^2E(1))$
1	-51.3	$b_1(1)$	$y = -0.0022x + 1.9730$	1.000	$y = -1951.0x + 16333.9$	0.998
2	160.3	$e(1a)$	$y = -0.0044x^2 + 1.9730$	1.000	$y = 1278.1x^2 + 16325.1$	0.999
3	160.3	$e(1b)$	$y = 0.0029x^2 + 1.9730$	1.000	$y = -844.8x^2 + 16324.6$	1.000
4	166.4	$a_1(1)$	$y = -0.0069x + 1.9730$	1.000	$y = -2118.9x + 16341.0$	0.996
5	186.8	b_2	$y = -0.0030x + 1.9730$ for $x < 0$ $y = 0.0030x + 1.9730$ for $x > 0$	1.000 1.000	$y = -648.2x + 16232.4$ for $x < 0$ $y = 648.2x + 16323.4$ for $x > 0$	0.999 0.999
6	233.1	$b_1(2)$	$y = -0.0017x + 1.9730$	0.993	$y = -3227.6x^2 + 16287.6$	0.990
7	267.1	$e(2a)$	$y = -0.0313x^2 + 1.9730$	1.000	$y = -5947.6x^2 + 16324.5$	1.000
8	267.1	$e(2b)$	$y = -0.0331x^2 + 1.9730$	1.000	$y = -9620.0x^2 + 16323.7$	1.000
9	323.5	$a_1(2)$	$y = 0.0047x + 1.9729$	0.988	$y = -3539.1x + 16312.5$	0.999
10	394.9	$e(3a)$	$y = 0.1276x^2 + 1.9732$	0.983	$y = 70592.4x^2 + 16551.2$	0.957
11	394.9	$e(3b)$	$y = -0.0533x^2 + 1.9730$	0.999	$y = -20075.2x^2 - 0.1x + 16323.1$	0.957
12	1050.4	$a_1(3)$	$y = -0.1014x + 1.9739$	0.979		0.998

Table 2-1.S7c. Spin-phonon analyses (g_y values and ligand field energies) for idealized C_{4v} $[\text{VOCl}_4]^{2-}$.

Mode #	Energy (cm^{-1})	Symm.	Best-Fit Equation (g_y)	$r^2(g_y)$	Best-Fit Equation (${}^2E(2)$)	$r^2({}^2E(2))$
1	-51.3	$b_1(1)$	$y = 0.0022x + 1.9730$	1.000	$y = 1951.0x + 16333.9$	0.998
2	160.3	$e(1a)$	$y = 0.0029x^2 + 1.9730$	1.000	$y = -844.8x^2 + 16324.6$	1.000
3	160.3	$e(1b)$	$y = -0.0044x^2 + 1.9730$	1.000	$y = 1278.1x^2 + 16325.1$	0.999
4	166.4	$a_1(1)$	$y = -0.0069x + 1.9730$	1.000	$y = 1633.8x^2 - 2119.1x + 16324.6$	1.000
5	186.8	b_2	$y = 0.0031x + 1.9730$ for $x < 0$	1.000	$y = 488.6x + 16323.2$ for $x < 0$,	0.997
			$y = -0.0031x + 1.9730$ for $x > 0$	1.000	$y = -488.6x + 16323.2$ for $x > 0$	0.997
6	233.1	$b_1(2)$	$y = 0.0017x + 1.9730$	0.993	$y = 3227.6x + 16287.6$	0.990
7	267.1	$e(2a)$	$y = -0.0331x^2 + 1.9730$	1.000	$y = -9620.0x^2 + 16323.7$	1.000
8	267.1	$e(2b)$	$y = -0.0313x^2 + 1.9730$	1.000	$y = -5947.6x^2 + 16324.5$	1.000
9	323.5	$a_1(2)$	$y = 0.0047x + 1.9729$	0.988	$y = -3539.1x + 16312.5$	0.999
10	394.9	$e(3a)$	$y = -0.0533x^2 + 1.9730$	0.999	$y = -20075.2x^2 + 16323.2$	0.999
11	394.9	$e(3b)$	$y = 0.1276x^2 + 1.9732$	0.983	$y = 70592.4x^2 + 16551.2$	0.957
12	1050.4	$a_1(3)$				

Table 2-1.S7d. Spin-phonon analyses ($y = g_x - g_y$ and $y = {}^2E(1) - {}^2E(2)$) for idealized C_{4v} $[\text{VOCl}_4]^{2-}$

Mode #	Energy (cm^{-1})	Symm.	Best-Fit Equation ($g_x - g_y$)	$r^2(g_x - g_y)$	Best-Fit Equation (${}^2E(1) - {}^2E(2)$)	r^2 (${}^2E(1) - {}^2E(2)$)
1	-51.3	$b_1(1)$	$y = -0.0044x^2$	1.000	$y = -3902.0x^2$	1.000
2	160.3	$e(1a)$	$y = -0.0073x^2$	1.000	$y = 2122.9x^2 - 0.5$	1.000
3	160.3	$e(1b)$	$y = 0.0073x^2$	1.000	$y = -2122.9x^2 - 0.4$	1.000
4	166.4	$a_1(1)$	$y = 0$	-	$y = 0.1x$	0.167
5	186.8	b_2	$y = -0.0060x +$ 0.0000 for $x < 0,$	1.000	$y = -1136.8x + 0.1$ for $x < 0,$	1.000
			$y = 0.0060 +$ 0.0000 for $x < 0$	1.000	$y = 1136.8x + 0.1$ for $x > 0$	1.000
6	233.1	$b_1(2)$	$y = -0.003x$	1.000	$y = -6455.3x^2$	1.000
7	267.1	$e(2a)$	$y = 0.0018x^2$	1.000	$y = 3672.4x^2 + 0.8$	1.000
8	267.1	$e(2b)$	$y = -0.0018x^2$	1.000	$y = -3672.4x^2 - 0.8$	1.000
9	323.5	$a_1(2)$	$y = 0$	-	$y = 0$	-
10	394.9	$e(3a)$	$y = 0.1809x^2 +$ 0.0002	0.992	$y = 90667.6x^2 + 228.0$	0.973
11	394.9	$e(3b)$	$y = -0.1809x^2 -$ 0.0002	0.992	$y = -90667.6x^2 - 0.1x$ -228.0	0.973
12	1050.4	$a_1(3)$	$y = 0$	-		

Table 2-1.S7e. Spin–phonon analyses (Loewdin spin densities) for idealized C_{4v} $[\text{VOCl}_4]^{2-}$.

Mode #	Energy (cm^{-1})	Symm.	Best-Fit Equation	r^2
1	-51.3	$b_1(1)$	$y = 0.0055x^2 + 0.9828$	1.000
2	160.3	$e(1a)$	$y = 0.0114x^2 + 0.9828$	1.000
3	160.3	$e(1b)$	$y = 0.0114^2 - 0.0131x + 0.9828$	1.000
4	166.4	$a_1(1)$	$y = 0.0349x^2 - 0.0131x + 0.9828$	1.000
5	186.8	b_2	$y = 0.0236x^2 + 0.9828$	1.000
6	233.1	$b_1(2)$	$y = -0.1498x^2 + 0.9828$	1.000
7	267.1	$e(2a)$	$y = -0.0112x^2 + 0.9828$	1.000
8	267.1	$e(2b)$	$y = -0.0112x^2 + 0.9828$	1.000
9	323.5	$a_1(2)$	$y = -0.1024x + 0.9823$	0.999
10	394.9	$e(3a)$	$y = -0.2412x^2 + 0.9828$	0.999
11	394.9	$e(3b)$	$y = -0.2412x^2 + 0.9828$	0.999
12	1050.4	$a_1(3)$	-	-

Table 2-1.S8a. Spin–phonon analysis for CuPc.

Mode #	Energy (cm ⁻¹)	Best-Fit Equation*	r ²
1	21.3*	$y = 0.0001x^2 + 2.1634$	0.995
2	36.9	$y = 0.0005x^2 + 2.1634$	>0.999
3	57.6	$y = 0.000006x^2 + 2.1634$	0.462
4	65.5	$y = 0.0014x^2 + 2.1634$	>0.999
5	65.6	$y = 0.0014x^2 + 2.1634$	>0.999
6	114.6	$y = 0.0002x^2 + 2.1634$	0.988
7	122.4	$y = -0.0000x^2 + 2.1634$	0.955
8	122.4	$y = -0.0000x^2 + 2.1634$	0.910
9	124.7	$y = 0.0000x^2 + 2.1634$	0.858
10	128.5	$y = 0.0010x^2 + 2.1634$	>0.999
11	128.5	$y = 0.0010x^2 + 2.1634$	>0.999
12	143.1*	$y = 0.0039x^2 + 2.1634$	>0.999
13	151.7	$y = 0.0158x^2 + 2.1634$	>0.999
14	173.8	$y = -0.0017x^2 + 2.1634$	>0.999
15	219.3	$y = 0.0015x^2 + 2.1634$	>0.999
16	230.3	$y = -0.0000x^2 + 2.1634$	0.953
17	239.4	$y = 0.0039x^2 + 2.1634$	>0.999
18	256.6	$y = 0.0076x^2 + 2.1634$	>0.999
19	256.7	$y = 0.0076x^2 + 2.1634$	>0.999
20	259.4**	$y = 0.0404x + 2.1634$	>0.999
21	282.2*	$y = 0.0173x^2 + 2.1634$	>0.999
22	288.2	$y = 0.0196x^2 + 2.1634$	>0.999
23	292.4	$y = 0.0299x^2 + 2.1634$	>0.999
24	292.9	$y = 0.0297x^2 + 2.1634$	>0.999
25	298.5	$y = 0.0069x^2 + 2.1634$	>0.999
26	298.6	$y = 0.0069x^2 + 2.1634$	>0.999
27	308.5	$y = -0.0134x^2 + 2.1634$	>0.999
28	308.8	$y = -0.0142x^2 + 2.1634$	>0.999

29 367.9

$$y = 0.0101x^2 + 2.1634$$

>0.999

* B_{2u} parent mode

** A_{1g} parent mode

Table 2-1.S8b. Spin-phonon analyses for $[\text{Cu}(\text{mnt})_2]^{2-}$.

Mode #	Energy (cm^{-1})	Best-Fit Equation*	r^2
1*	43.1	$y = 0.0036x^2 + 2.0849$	>0.999
2	45.5	$y = 0.0004x^2 + 0.0003x + 2.0849$	>0.999
3	53.8	$y = 0.0016x^2 - 0.0007x + 2.0849$	>0.999
4	57.7	$y = 0.0023x^2 + 2.0849$	>0.999
5	63.5	$y = 0.0009x^2 + 2.0849$	>0.999
6	72.0	$y = 0.0156x^2 - 0.0025x + 2.0849$	>0.999
7*	93.8	$y = -0.0024x^2 + 2.0849$	>0.999
8	99.2	$y = 0.0008x^2 + 0.0007x + 2.0849$	>0.999
9	120.1	$y = -0.0010x^2 + 0.0141x + 2.0849$	>0.999
10	131.7	$y = -0.0001x^2 + 2.0849$	0.991
11	134.4	$y = -0.0043x^2 - 0.0050x + 2.0849$	>0.999
12	141.2	$y = 0.0379x^2 + 2.0849$	>0.999
13	154.3	$y = -0.0028x^2 + 0.0147x + 2.0849$	>0.999
14	188.4	$y = 0.0035x^2 + 2.0849$	>0.999
15	215.4	$y = 0.0090x^2 + 2.0849$	>0.999
16	218.0	$y = -0.0013x^2 + 0.0009x + 2.0849$	>0.999
17	222.9	$y = -0.0151x^2 + 0.0041x + 2.0849$	>0.999
18	226.7	$y = -0.0011x^2 + 2.0849$	>0.999
19	287.8	$y = -0.0932x^2 - 0.0001x + 2.0849$	>0.999
20**	303.4	$y = -0.1118x + 2.0848$	>0.999
21	306.2	$y = -0.1261x^2 + 0.0014x + 2.0849$	>0.999
22	398.1	$y = -0.0002x^2 + 0.0019x + 2.0849$	>0.999
23	405.5	$y = -0.0177x^2 + 2.0849$	>0.999
24	409.1	$y = -0.0286x^2 + 0.0009x + 2.0849$	>0.999
25	412.3	$y = -0.0157x^2 + 2.0849$	>0.999

Note modes 2 and 3 are rotational motions, and not intramolecular vibrations.

* B_{2u} parent mode

** A_{1g} parent mode

Table 2-1.S8c. Spin-phonon analyses for $[\text{Cu}(\text{bdt})_2]^{2-}$.

Mode #	Energy (cm^{-1})	Best-Fit Equation*	r^2
1*	-104.1	$y = 0.0068x^2 + 2.0467$	>0.999
2	-87.2	$y = 0.0081x^2 - 0.0017x + 2.0467$	>0.999
3	-49.4	$y = 0.0001x^2 + 2.0467$	0.969
4	51.3	$y = 0.0009x^2 + 2.0467$	>0.999
5	85.1	$y = 0.0465x^2 + 2.0467$	>0.999
6*	108.0	$y = -0.0016x^2 + 2.0467$	>0.999
7	115.1	$y = -0.0017x^2 + 2.0467$	>0.999
8	179.8	$y = -0.0001x^2 - 0.0107x + 2.0467$	>0.999
9	206.2	$y = 0.0008x^2 + 2.0467$	>0.999
10	219.1	$y = 0.0024x^2 - 0.0015x + 2.0467$	>0.999
11	233.6	$y = 0.0004x^2 + 2.0467$	>0.999
12	246.6	$y = 0.0321x^2 + 2.0467$	>0.999
13	298.3	$y = 0.0017x^2 + 2.0467$	>0.999
14	382.2	$y = -0.0074x^2 + 0.0076x + 2.0467$	>0.999
15**	387.4	$y = -0.0920x + 2.0468$	>0.999

* B_{2u} parent mode** A_{1g} parent mode

Table 2-1.S8d. Spin–phonon analyses for [Cu(bds)₂]²⁻. (g_z)

Mode #	Energy (cm ⁻¹)	Best-Fit Equation*	r ²
1*	-61.7	$y = 0.0005x^2 + 2.0893$	0.997
2	-35.0	$y = 0.0003x^2 - 0.0004x + 2.0893$	>0.999
3	-29.6	$y = -0.0000x^2 + 2.0893$	0.941
4	31.6	$y = 0.0011x^2 + 2.0893$	>0.999
5	58.0	$y = 0.0000x^2 - 0.0003x + 2.0893$	>0.999
6*	58.4	$y = 0.0013x^2 + 2.0893$	>0.999
7	97.8	$y = 0.0312x^2 + 2.0893$	>0.999
8	103.5	$y = -0.0004x^2 - 0.0080x + 2.0893$	>0.999
9	107.4	$y = -0.0006x^2 - 0.0051x + 2.0893$	>0.999
10	156.8	$0.0033x^2 + 2.0893$	0.998
11	187.1	$0.0036x^2 - 0.0027x + 2.0893$	>0.999
12	197.7	$0.0007x^2 + 0.0001x + 2.0893$	>0.999
13**	199.3	$y = -0.0615x + 2.0893$	>0.999
14	222.1	$y = 0.0046x^2 + 2.0893$	>0.999
15	244.7	$y = 0.0026x^2 - 0.0015x + 2.0893$	>0.999
16	253.8	$y = -0.0791x^2 + 2.0893$	>0.999
17	281.8	$y = -0.0329x^2 + 2.0893$	>0.999
18	363.5	$y = -0.0207x^2 + 0.0020x + 2.0893$	>0.999
19	373.4	$y = -0.0146x^2 + 2.0893$	>0.999
20	373.7	$y = 0.0054x^2 + 0.0032x + 2.0893$	>0.999
21	375.7	$y = -0.0073x^2 + 2.0893$	>0.999

* B_{2u} parent mode** A_{1g} parent mode

Table 2-1.S9a. Spin-phonon analyses for VOPc. (g_z)

Mode #	Energy (cm ⁻¹)	Best-Fit Equation*	r ²
1	21.5	$y = -0.0000x^2 + 1.9609$	0.702
2	41.5	$y = -0.0007x + 1.9609$	>0.999
3	58.8	$y = -0.0000x + 1.9609$	0.931
4	64.6	$y = -0.0004x^2 + 1.9609$	0.998
5	64.7	$y = -0.0004x^2 + 1.9609$	>0.999
6	117.9	$y = -0.00008x^2 + 1.9609$	0.927
7	121.3	$y = -0.0001x^2 + 1.9609$	0.957
8	121.3	$y = -0.0001x^2 + 1.9609$	0.960
9	127.5	$y = 0.0000x^2 + 1.9609$	0.866
10	130.2	$y = -0.0003x^2 + 1.9609$	0.981
11	130.2	$y = -0.0003x^2 + 1.9609$	0.993
12	148.5	$y = -0.0011x^2 + 1.9609$	>0.999
13*	177.3	$y = -0.0088x + 1.9609$	>0.999
14	180.9	$y = -0.0013x^2 + 1.9609$	>0.999
15	180.9	$y = -0.0013x^2 + 1.9609$	>0.999
16	186.6	$y = -0.0003x^2 + 1.9609$	0.991
17	226.5	$y = -0.0003x^2 + 1.9609$	>0.999
18	232.2	$y = -0.0003x^2 + 1.9609$	0.995
19	248.1	$y = -0.0012x^2 + 1.9609$	0.997
20**	260.0	$y = -0.0062x + 1.9609$	>0.999
21	277.1	$y = -0.0006x^2 + 1.9609$	0.989
22	277.1	$y = -0.0005x^2 + 1.9609$	0.996
23	306.4	$y = -0.0018x^2 + 0.0001x + 1.9609$	0.924
24	306.4	$y = -0.0018x^2 - 0.0001x + 1.9609$	0.932
25	314.1	$y = -0.0039x^2 + 1.9609$	>0.999
26*	317.3	$y = -0.0143x + 1.9608$	>0.999
27	332.4	$y = -0.0003x^2 + 1.9609$	0.996
28	332.5	$y = 0.0002x + 1.9609$	0.987

29***	384.2	$y = -0.0632x^2 - 0.0001x + 1.9609$	>0.999
30***	384.2	$y = -0.0593x^2 + 1.9609$	>0.999
31*	393.9	$y = -0.0173x + 1.9608$	>0.999

* Significant pyramidal bending character

** Significant M-L stretching character (with ligands other than oxo)

*** Significant V movement in the equatorial ligand plane

Table 2-1.S9b. Spin–phonon analyses for VO(acac)₂. (g_z)

Mode #	Energy (cm ⁻¹)	Best-Fit Equation*	r ²
1	30.1	$y = -0.0005x^2 + 1.9454$	>0.999
2	42.0	$y = -0.0003x^2 + 0.0008x - 1.9454$	>0.999
3	76.1	$y = -0.0006x^2 + 1.9454$	>0.999
4	82.1	$y = -0.0004x^2 + 1.9454$	>0.999
5	90.7	$y = 0.0000x^2 + 1.9454$	0.998
6	97.0	$y = -0.0006x^2 + 1.9454$	>0.999
7	101.8	$y = 0.0000x^2 + 1.9454$	0.203
8	103.3	$y = -0.0000x^2 + 1.9454$	0.997
9	138.1	$y = -0.0009x^2 + 1.9454$	>0.999
10	143.9	$y = -0.0028x^2 + 1.9454$	>0.999
11	168.7	$y = -0.0000x^2 - 0.0001x + 1.9454$	>0.999
12	169.3	$y = -0.0004x + 1.9454$	>0.999
13*	192.3	$y = 0.0060x + 1.9454$	>0.999
14	231.0	$y = -0.0023x^2 + 0.0002x + 1.9454$	>0.999
15	243.0	$y = -0.0010x^2 + 1.9454$	>0.999
16	253.3	$y = -0.0034x^2 + 1.9454$	>0.999
17	267.1	$y = -0.0010x^2 - 0.0001x + 1.9454$	>0.999
18	277.6	$y = -0.0020x^2 + 0.0057x + 1.9454$	>0.999
19**	295.6	$y = -0.0089x^2 - 0.0214x + 1.9454$	>0.999
20***	374.5	$y = -0.0286x^2 - 0.0001x + 1.9454$	>0.999
21***	391.0	$y = -0.0299x^2 - 0.0002x + 1.9454$	>0.999

* Significant pyramidal bending character.

** Significant M-L stretching character (with ligands other than oxo).

*** Significant V movement in the equatorial ligand plane.

Table 2-1.S9c. Spin–phonon analyses for $[\text{VO}(\text{cat})_2]^{2-}$. (g_z)

Mode #	Energy (cm^{-1})	Best-Fit Equation*	r^2
1	32.6	$y = -0.0004x + 1.9613$	0.999
2	53.7	$y = -0.0016x^2 - 1.9513$	>0.999
3	82.7	$y = -0.0035x^2 + 1.9513$	>0.999
4	84.6	$y = -0.0010x^2 + 1.9513$	>0.999
5	179.3	$y = 0.0002x^2 + 1.9513$	0.988
6**	186.1	$y = -0.0042x + 1.9512$	0.996
7	197.8	$y = -0.0015x^2 - 0.0001x + 1.9513$	>0.999
8	228.3	$y = -0.0012x^2 + 1.9513$	0.999
9	254.0	$y = -0.0014x^2 - 0.0003x + 1.9513$	>0.999
10	269.0	$y = -0.0011x^2 + 1.9513$	0.998
11*	280.1	$y = -0.0168x + 1.9512$	>0.999
12	340.9	$y = -0.0011x^2 + 1.9513$	>0.999
13*	366.3	$y = -0.0115x + 1.9512$	0.998
14***	388.4	$y = -0.0387x^2 + 1.9513$	>0.999
15***	437.4	$y = -0.0655x^2 + 1.9513$	0.999

* Significant pyramidal bending character

** Significant M-L stretching character (with ligands other than oxo)

*** Significant V movement in the equatorial ligand plane

Table 2-1.S9d. Spin–phonon analyses for $[\text{VO}(\text{dmit})_2]^{2-}$.

Mode #	Energy (cm^{-1})	Best-Fit Equation*	r^2
1	-42.0	$y = -0.0076x^2 + 1.9634$	>0.999
2	-22.7	$y = -0.0024x^2 + 0.0003x - 1.9634$	>0.999
3	9.3	$y = -0.0036x^2 - 0.0010x + 1.9634$	>0.999
4	51.6	$y = -0.0017x^2 + 1.9634$	>0.999
5	87.2	$y = -0.0020x^2 + 1.9634$	>0.999
6	92.6	$y = -0.0002x^2 - 0.0001x + 1.9634$	>0.999
7	116.8	$y = -0.0024x^2 - 0.0030x + 1.9634$	>0.999
8	120.7	$y = 0.0003x^2 + 0.0014x + 1.9634$	>0.999
9	127.2	$y = 0.0004x^2 + 1.9634$	>0.999
10	144.6	$y = -0.0002x^2 - 0.0006x + 1.9634$	>0.999
11	175.8	$y = -0.0010x^2 + 1.9634$	>0.999
12	178.6	$y = -0.0160x + 1.9632$	0.993
13	189.0	$y = -0.0049x^2 + 1.9634$	>0.999
14	256.5	$y = -0.0005x^2 + 1.9634$	0.998
15	261.5	$y = 0.0017x^2 + 1.9634$	>0.999
16	261.9	$y = -0.0110x^2 + 0.0006x + 1.9634$	>0.999
17*	276.9	$y = 0.00481x + 1.9634$	>0.999
18	302.6	$y = -0.0024x^2 + 1.9634$	>0.999
19	330.2	$y = -0.0128x^2 + 1.9634$	>0.999
20	349.0	$y = -0.0134x^2 + 1.9634$	>0.999
21**	350.7	$y = -0.0430x + 1.9633$	>0.999
22	356.7	$y = -0.0045x^2 + 0.0017x + 1.9634$	>0.999
23**	378.5	$y = 0.0313x + 1.9633$	>0.999
24	414.0	$y = -0.0222x^2 + 1.9634$	>0.999
25	415.9	$y = -0.0078x^2 - 0.0009x + 1.9634$	>0.999
26***	426.6	$y = -0.0580x^2 + 1.9634$	>0.999
27***	442.7	$y = -0.0267x^2 + 1.9634$	>0.999

* Significant pyramidal bending character

** Significant M-L stretching character (with ligands other than oxo)

*** Significant V movement in the equatorial ligand plane

Table 2-1.S9e. Spin–phonon analyses for $[\text{V}(\text{bdt})_3]^{2-}$.

Mode #	Energy (cm^{-1})	Best-Fit Equation*	r^2
1	16.5	$y = -0.0003x + 1.9629$	0.990
2	24.7	$y = 0.0014x^2 + 0.0001x + 1.9628$	0.721
3	39.3	$y = -0.0003x + 1.9628$	0.941
4	59.9	$y = -0.0015x^2 + 1.9629$	0.978
5	66.7	$y = -0.0014x + 1.9628$	0.987
6	74.3	$y = 0.0013x + 1.9628$	0.994
7	115.6	$y = -0.0006x^2 - 0.0001x + 1.9629$	0.969
8	123.6	$y = -0.0021x + 1.9629$	0.981
9	136.5	$y = 0.0020x + 1.9628$	>0.999
10	150.1	$y = -0.0045x + 1.9624$	>0.999
11	152.4	$y = -0.0008x + 1.9628$	0.998
12	156.2	$y = -0.0042x + 1.9628$	0.992
13	181.2	$y = 0.0013x + 1.9628$	0.992
14	192.4	$y = 0.0017x + 1.9629$	0.971
15	195.6	$y = -0.0011x + 1.9629$	0.918
16	251.6	$y = 0.0075x^2 - 0.0005x + 1.9629$	>0.999
17	255.2	$y = 0.0064x^2 + 0.0015x + 1.9628$	>0.999
18	264.6	$y = 0.0012x + 1.9629$	0.925
19	284.5	$y = 0.0091x + 1.9630$	0.969
20	289.3	$y = 0.0270x^2 - 0.0064x + 1.9629$	>0.999
21	301.3	$y = 0.0102x^2 + 0.0009x + 1.9629$	>0.999
22*	351.7	$y = -0.1165x + 1.9610$	0.987
23	355.0	$y = -0.0425x + 1.9627$	>0.999
24	368.0	$y = -0.0308x + 1.9628$	>0.999
25	391.9	$y = 0.0228x^2 - 0.0046x + 1.9628$	0.997
26	393.6	$y = 0.0107x^2 + 0.0021x + 1.9628$	>0.999

* Symmetric M-L stretching mode

Table 2-1.S9f. Spin–phonon analyses for $[\text{V}(\text{bds})_3]^{2-}$.

Mode #	Energy (cm ⁻¹)	Best-Fit Equation*	r ²
1	12.1	$y = -0.0051x^2 + 0.0001x + 1.8512$	0.984
2	17.4	$y = -0.0102x + 1.8512$	0.997
3	32.2	$y = -0.0025x^2 - 0.0001x + 1.8512$	0.982
4	48.0	$y = -0.0042x^2 - 0.0002x + 1.8512$	0.991
5	51.5	$y = -0.0117x + 1.8511$	0.996
6	61.9	$y = 0.0137x + 1.8511$	0.996
7	81.3	$y = -0.0668x^2 - 0.0059x + 1.8514$	0.910
8	84.6	$y = -0.0283x^2 + 1.8512$	0.999
9	95.7	$y = -0.0156x^2 + 0.0001x + 1.8512$	0.999
10	124.1	$y = -0.0244x + 1.8510$	0.995
11	138.5	$y = -0.0096x^2 - 0.0006x + 1.8512$	0.999
12	138.8	$y = 0.0079x + 1.8512$	0.999
13	142.5	$y = -0.0282x^2 + 0.0017x + 1.8512$	0.997
14	144.1	$y = -0.0172x^2 + 0.0001x + 1.8512$	0.999
15	147.5	$y = -0.0174x + 1.8512$	0.999
16	180.9	$y = -0.2711x^2 - 0.0102 + 1.8509$	0.987
17	182.8	$y = -0.2562x^2 - 0.0001x + 1.8510$	0.996
18*	209.8	$y = 0.6262x + 1.8310$	0.919
19	227.2	$y = -0.0095x^2 + 1.8512$	0.998
20	238.5	$y = -0.0137x + 1.8511$	0.987
21	242.2	$y = -0.0031x^2 - 0.0001x + 1.8512$	0.995
22	251.0	$y = -0.0154x^2 + 1.8512$	0.999
23	261.2	$y = -0.0332x^2 - 0.0057x + 1.8512$	0.999
24	263.1	$y = 0.0003x^2 - 0.0001x + 1.8517$	0.924
25	302.8	$y = -1.2173x^2 + 0.0741x + 1.8503$	0.987
26	319.8	$y = -0.5816x^2 - 0.0001x + 1.8517$	0.996
27	325.4	$y = 0.0418x^2 + 1.8513$	0.942

28	380.8	$y = 0.0914x + 1.8506$	0.997
29	381.8	$y = -0.0346x + 1.8510$	0.996
30	382.6	$y = -0.0176x^2 - 0.0001x + 1.8512$	0.999
31	397.1	$y = -0.0200x^2 + 1.8512$	0.999
32	399.8	$y = -0.0237x^2 - 0.0040x + 1.8512$	0.999

* Symmetric M-L stretching mode

Table 2-1.S10a. Comparisons between optimized and X-ray crystal structure of CuPc.

	Cu-N ₁ (Å)	Cu-N ₂ (Å)	Cu-N ₃ (Å)	Cu-N ₄ (Å)
Experimental ¹²	1.960	1.965	1.960	1.965
Computed (optimized)	1.968	1.970	1.968	1.970
Difference	0.008	0.005	0.002	0.005

Table 2-1.S10b. Comparisons between optimized and X-ray crystal structure of CuN₄ complexes.

R = H	Dihedral Angle (°) ^a	Cu-N ₁ (Å)	Cu-N ₁ (Å)	Cu-N ₁ (Å)	Cu-N ₁ (Å)
Experimental ¹³	0	1.950	1.950	1.971	1.971
Computed (optimized)	6.5	1.994	1.994	2.043	2.043
R = Me	Dihedral Angle (°)	Cu-N ₁ (Å)	Cu-N ₁ (Å)	Cu-N ₁ (Å)	Cu-N ₁ (Å)
Experimental ¹³	32-33	1.938	1.938	2.016	2.016
Computed (optimized)	30.5	1.983	1.984	2.081	2.082
R = <i>tert</i>-Bu	Dihedral Angle (°)	Cu-N ₁ (Å)	Cu-N ₁ (Å)	Cu-N ₁ (Å)	Cu-N ₁ (Å)
Experimental ¹³	61	1.937	1.937	2.057	2.057
Computed (optimized)	55.6	1.966	1.966	2.136	2.136

^a Dihedral angle defined as the dihedral angle between the two chelating N(imine)–Cu–N(pyrrolate) planes.

Table 2-1.S11a. Comparisons between optimized and X-ray crystal structure of VOPc.

	Crystal structure ¹²	DFT optimized structure
V-N ₁ (Å)	2.023	2.058
V-N ₂ (Å)	2.019	2.058
V-N ₃ (Å)	2.033	2.058
V-N ₄ (Å)	2.032	2.058
V-O (Å)	1.599	1.554
O-V-N ₁ (°)	106.2	108.0
O-V-N ₂ (°)	104.6	108.1
O-V-N ₃ (°)	106.0	108.0
O-V-N ₄ (°)	106.3	107.9

Table 2-1.S11b. Comparisons between optimized and X-ray crystal structure of [VO(cat)₂]²⁻.

	Crystal structure ¹⁴	DFT optimized structure
V-O ₁ (Å)	1.960	1.996
V-O ₂ (Å)	1.978	1.999
V-O ₃ (Å)	1.973	1.996
V-O ₄ (Å)	1.980	1.999
V=O (Å)	1.614	1.584
O-V-N ₁ (°)	110.4	109.0
O-V-N ₂ (°)	108.0	108.9
O-V-N ₃ (°)	109.2	109.0
O-V-N ₄ (°)	105.6	108.9

Table 2-1.S11c. Comparisons between optimized and X-ray crystal structure of VO(acac)₂.

	Crystal Structure ¹⁵	DFT optimized structure
V-O ₁ (Å)	1.957	1.996

V-O ₂ (Å)	1.973	1.996
V-O ₃ (Å)	1.978	1.997
V-O ₄ (Å)	1.960	1.997
V=O (Å)	1.558	1.549
O-V-N ₁ (°)	106.3	107.7
O-V-N ₂ (°)	104.5	107.8
O-V-N ₃ (°)	108.2	107.7
O-V-N ₄ (°)	105.6	107.9

Table 2-1.S12. Spin–phonon coupling terms across a variety of V(IV) complexes.

Complex	Mode (cm⁻¹)	(g_z/Q_i)	ES^a	M(d)^b	M SD
<i>C</i> _{4v} [VOCl ₄] ²⁻	166.4	-0.018	15230	88 %	0.983
	323.5	0.068			
	394.9	-0.313			
	394.9	-0.322			
VOPc	177.3	-0.009	22745	85 %	0.985
	260.0	-0.006			
	317.3	-0.014			
	384.2	-0.063			
	384.2	-0.059			
	393.9	-0.017			
VO(acac) ₂	192.3	0.006	17955	84 %	0.972
	277.6	0.006			
	295.6	-0.021			
	374.5	-0.029			
	391.0	-0.030			
	475.4	0.022			
[VO(cat) ₂] ²⁻	186.1	-0.004	19335	65 %	0.987
	280.9	-0.017			
	366.3	-0.012			
	388.4	-0.039			
	437.4	-0.066			

[VO(dmit) ₂] ²⁻	116.8	-0.003	20120	50 %	0.999
	178.6	-0.016			
	350.7	-0.053			
	378.5	0.031			
	414.0	-0.022			
	426.6	-0.058			

Complex	Mode (cm ⁻¹)	(g /Å)	(g _⊥ /Å)	ES
[V(bdt) ₃] ²⁻	351.7	-0.420	-0.357	7935
[V(bds) ₃] ²⁻	209.8	-1.744	-0.766	6785

^a Excited state which spin orbit coupling into the ground state.

^b M(d) character in unoccupied component orbital from Loewdin population analyses.

^c Loewdin metal spin density.

C. Figures

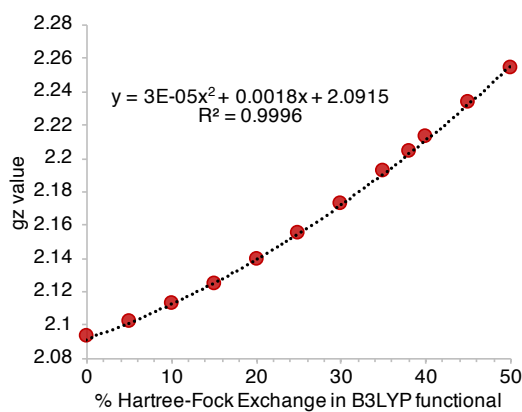


Figure 2-1.S1. Hartree-Fock dependence of the calculated value of g_z for D_{4h} Cu(II)Cl₄ using the crystal structure.⁹ The experimental value is 2.221.¹⁶ Acceptable agreement between theory and experiment is obtained near the value of 38% used in the main text.

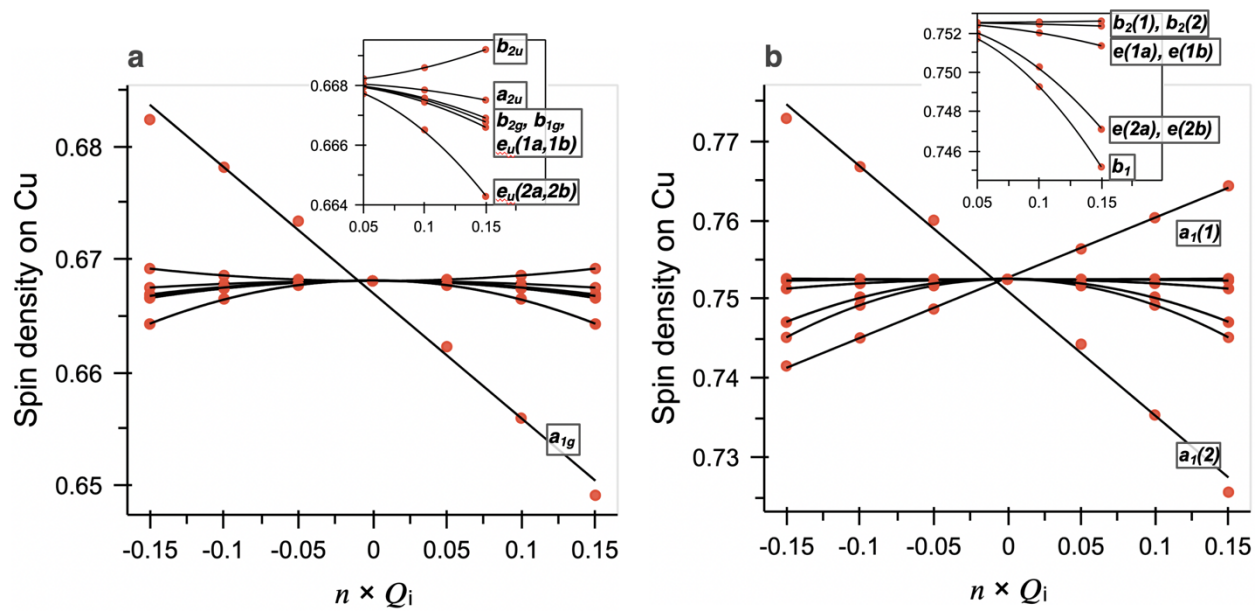


Figure 2-1.S2. Spin-phonon analyses (spin density) for idealized structures of (A) D_{4h} and (B) D_{2d} $[CuCl_4]^{2-}$.

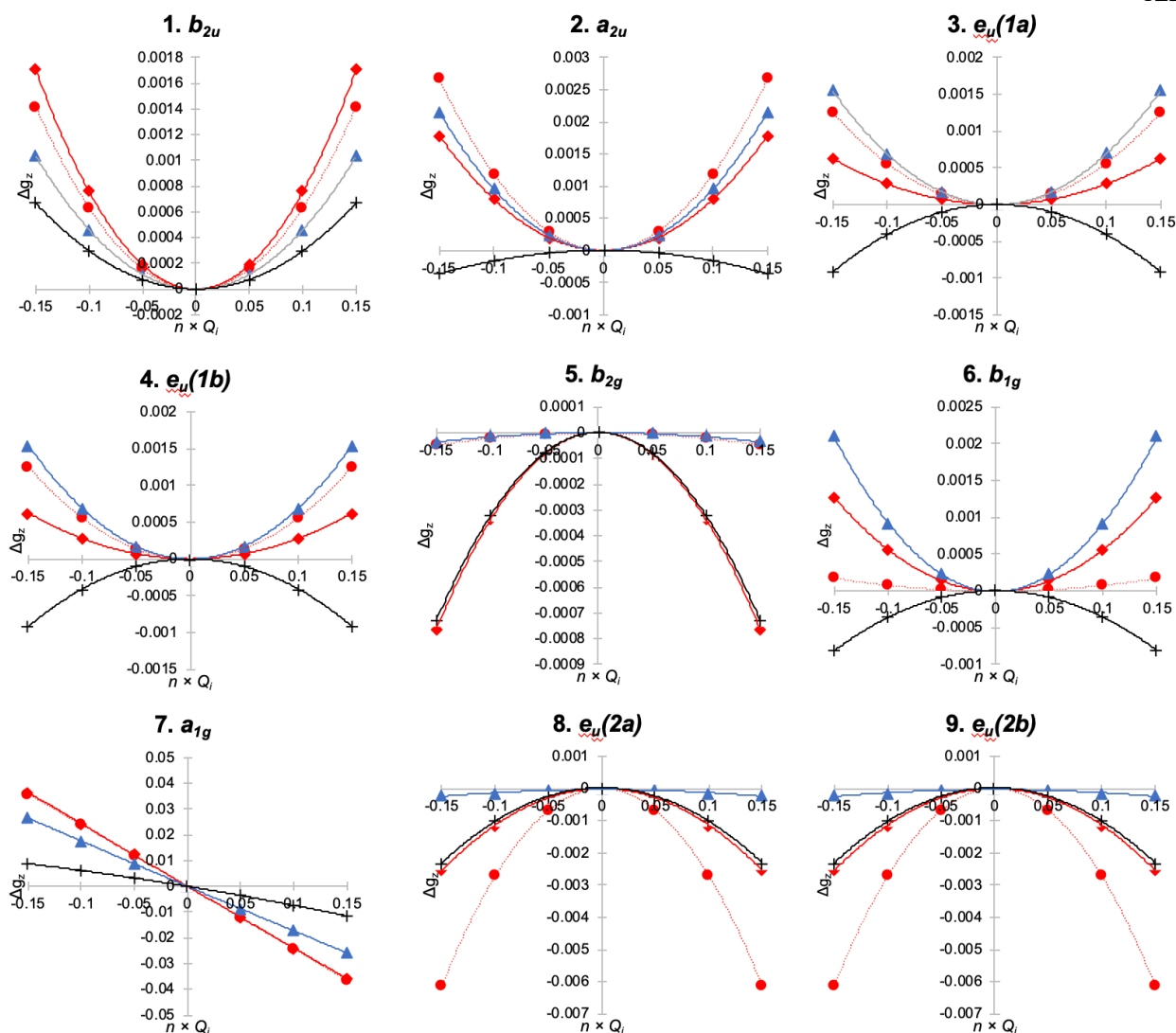


Figure 2-1.S3. Spin-phonon analyses (g_z) and comparisons to equation 1 from the main text for idealized D_{4h} $[\text{CuCl}_4]^{2-}$. Blue: changes in relevant excited state energy only. Black: changes in spin density only. Solid red: changes in both spin density and excited state energy according to the LFT equation. Dotted red: DFT-computed change in g value.

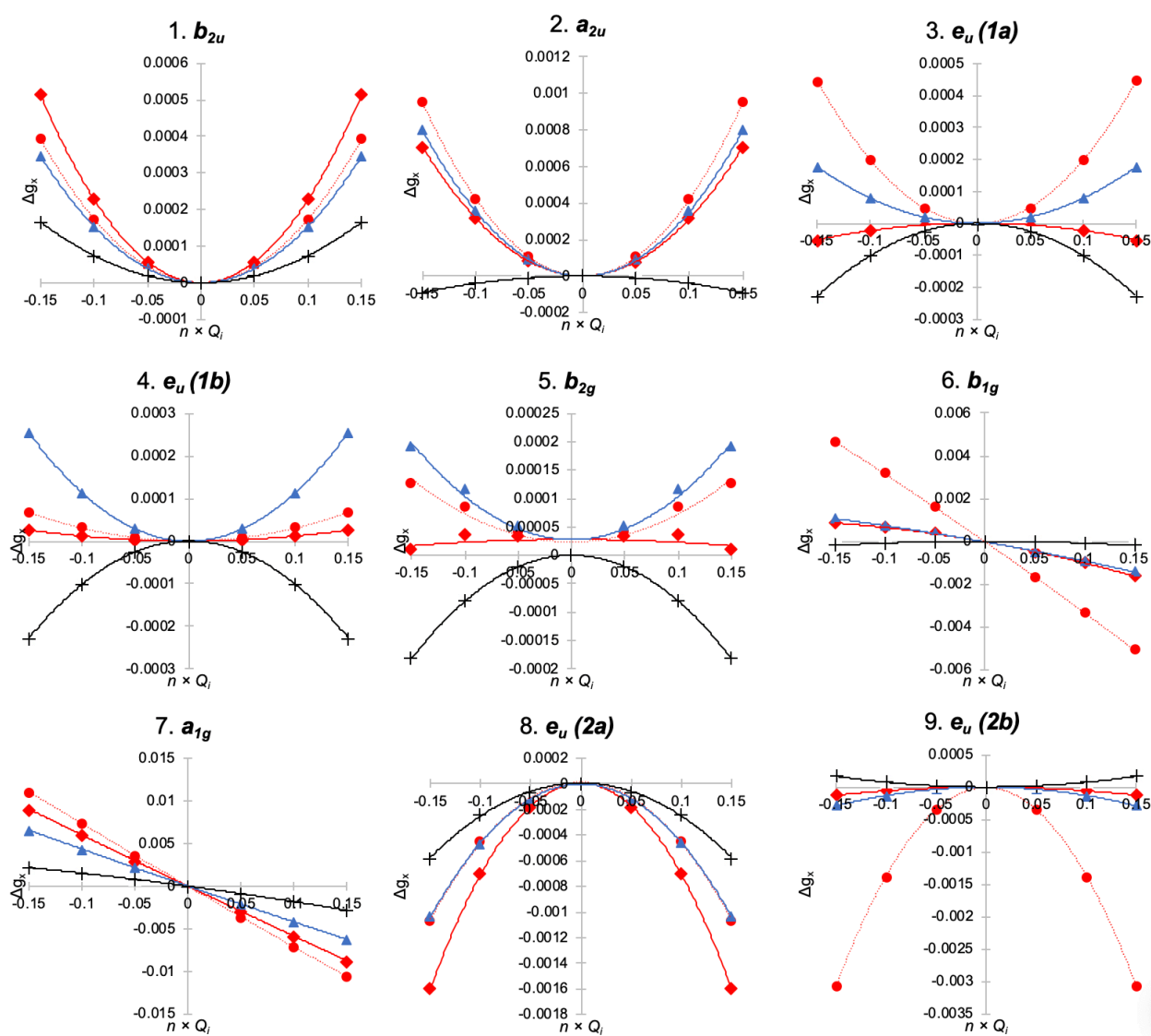


Figure 2-1.S4. Spin-phonon analyses (g_x) and comparisons to equation 2 from the main text for idealized D_{4h} $[\text{CuCl}_4]^{2-}$. Blue: changes in relevant excited state energy only. Black: changes in spin density only. Solid red: changes in both spin density and excited state energy according to the LFT equation. Dotted red: DFT-computed change in g value.

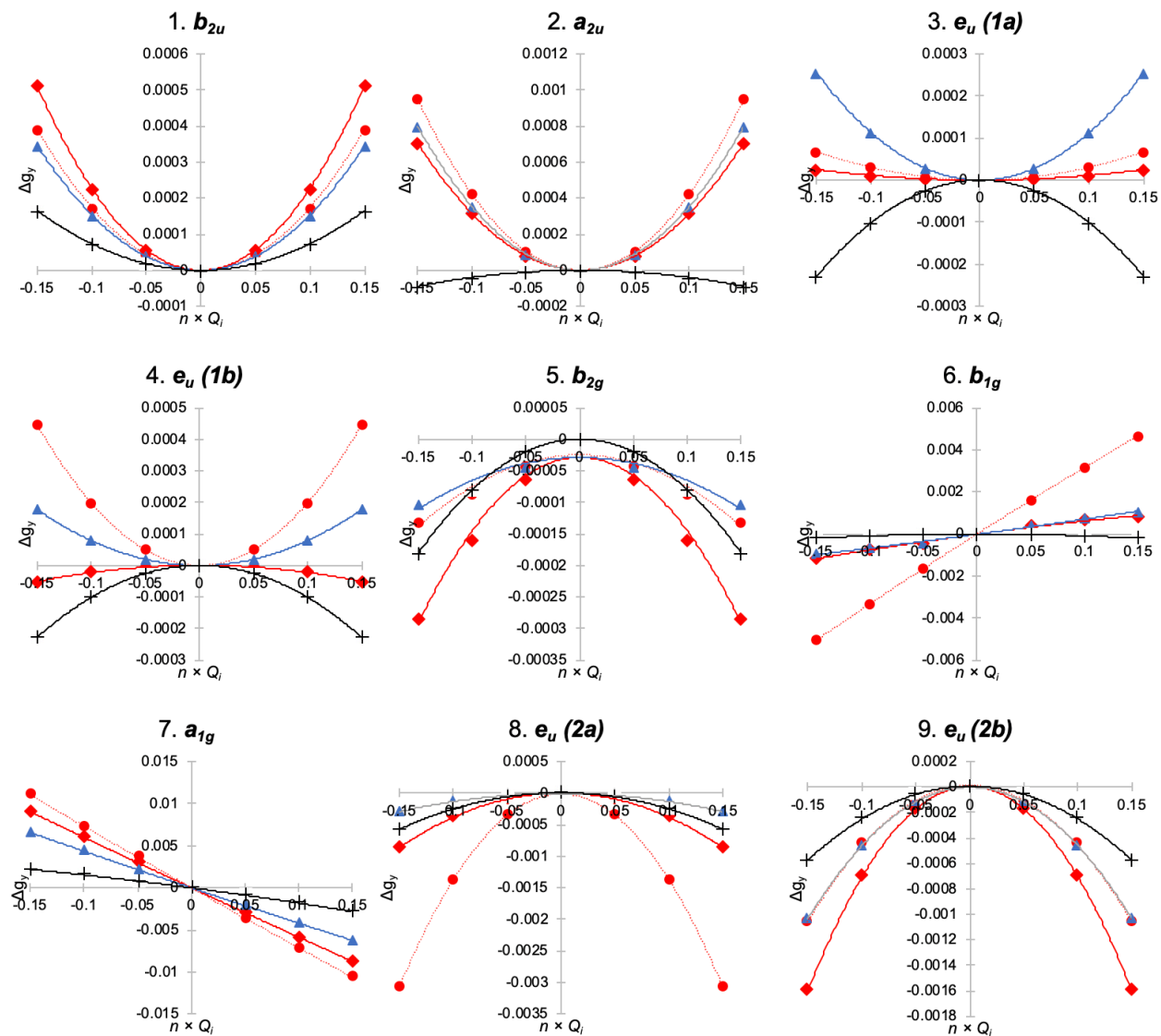


Figure 2-1.S5. Spin-phonon analyses (g_y) and comparisons to equation 2 from the main text for idealized D_{4h} $[\text{CuCl}_4]^{2-}$. Blue: changes in relevant excited state energy only. Black: changes in spin density only. Solid red: changes in both spin density and excited state energy according to the LFT equation. Dotted red: DFT-computed change in g value.

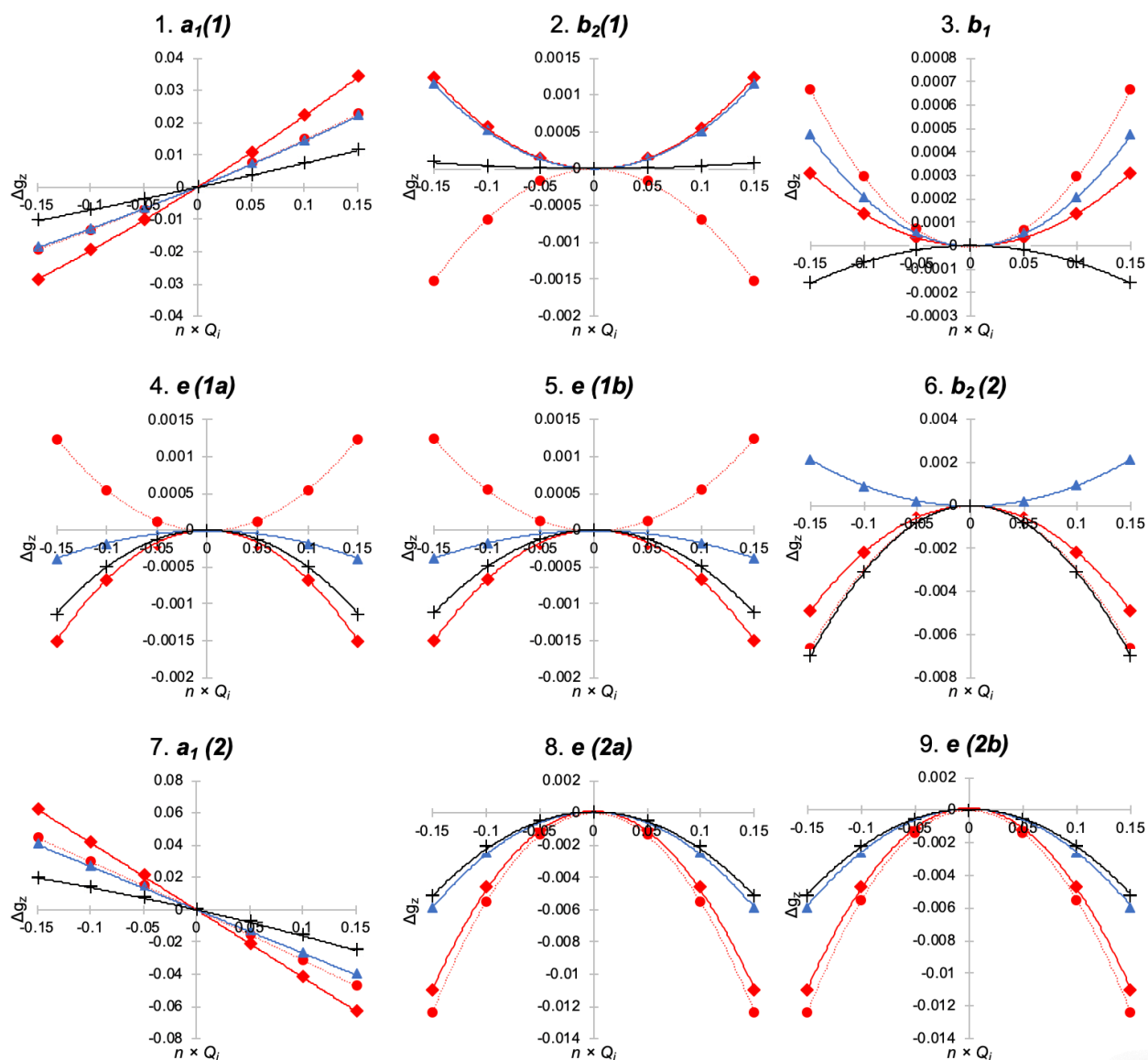


Figure 2-1.S6. Spin-phonon analyses (g_z) and comparisons to equation 2 from the main text for idealized D_{2d} $[\text{CuCl}_4]^{2-}$. Blue: changes in relevant excited state energy only. Black: changes in spin density only. Solid red: changes in both spin density and excited state energy according to the LFT equation. Dotted red: DFT-computed change in g value.

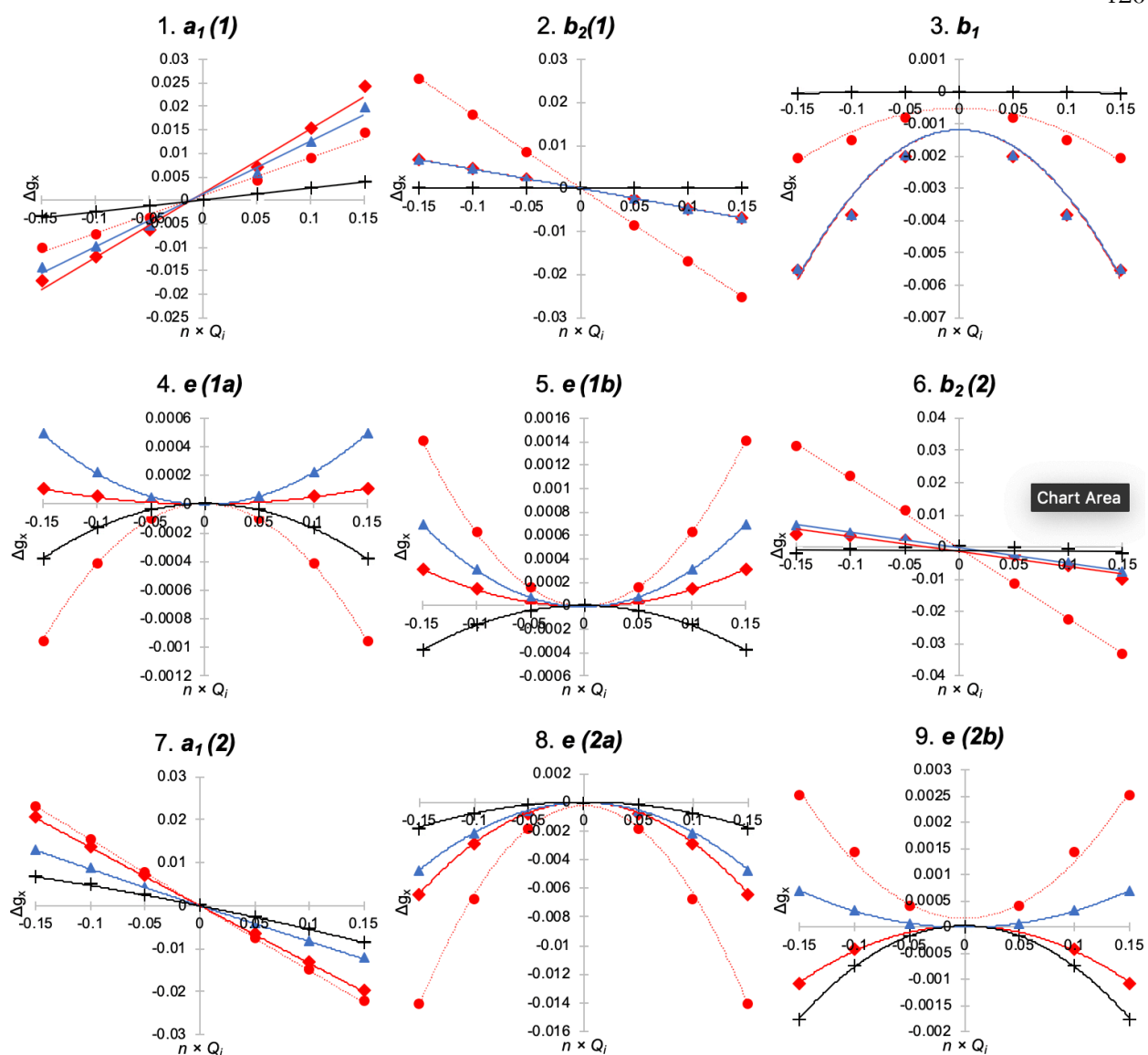


Figure 2-1.S7. Spin-phonon analyses (g_x) and comparisons to equation 2 from the main text for idealized $D_{2d} [CuCl_4]^{2-}$. Blue: changes in relevant excited state energy only. Black: changes in spin density only. Solid red: changes in both spin density and excited state energy according to the LFT equation. Dotted red: DFT-computed change in g value.

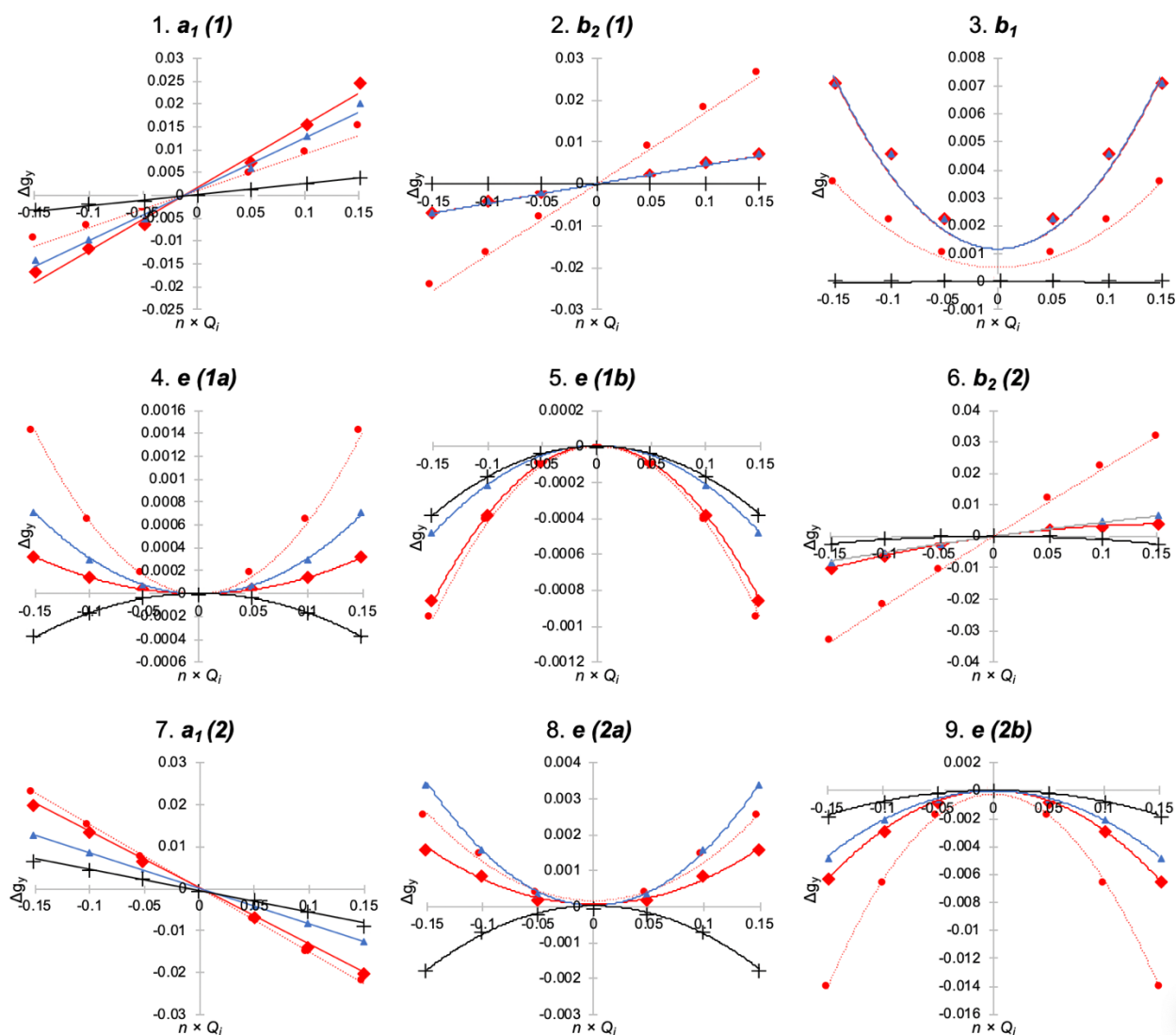


Figure 2-1.S8. Spin-phonon analyses (g_y) and comparisons to equation 2 from the main text for idealized $D_{2d} [CuCl_4]^{2-}$. Blue: changes in relevant excited state energy only. Black: changes in spin density only. Solid red: changes in both spin density and excited state energy according to the LFT equation. Dotted red: DFT-computed change in g value.

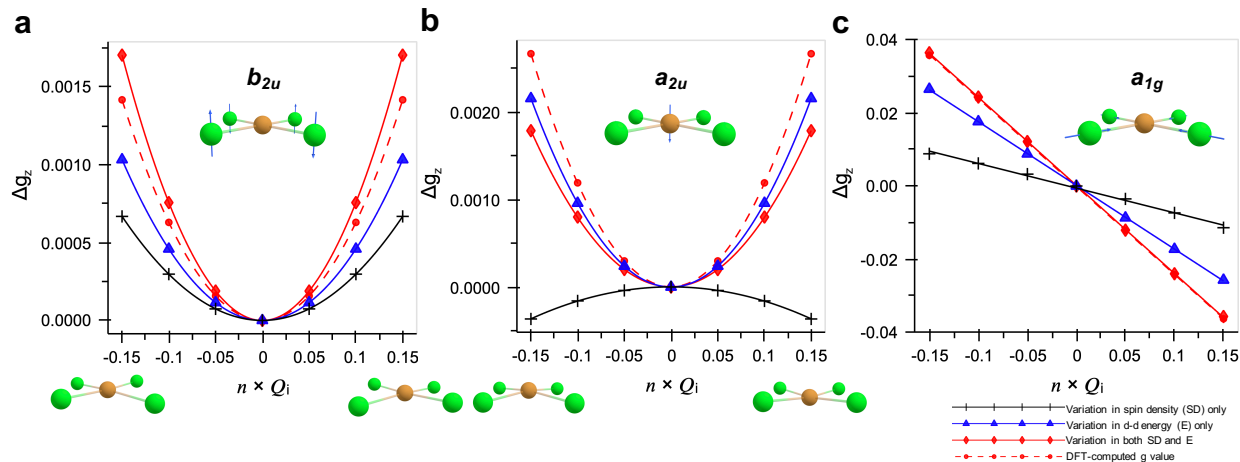


Figure 2-1.S9. Independent contributions from d-d transition energy and ligand–metal covalency to the change in g_z for D_{4h} $[\text{CuCl}_4]^{2-}$. Comparisons are made between the Δg_z as calculated from the LFT expression and as computed using ORCA for modes (a) b_{2u} , (b) a_{2u} , and (c) a_{1g} . For these plots, the square of the spin density on Cu was used as a proxy for the covalency. Vector displacements are provided for each vibrational distortion.

The individual contributions to the g_z value from the ${}^2\text{B}_{1g}$ energy and Cu spin density can be estimated using equation 2 in combination with the DFT and TDDFT calculations. For example, for D_{4h} $[\text{CuCl}_4]^{2-}$, using the calculated Cu spin density of 0.668 and the ${}^2\text{B}_{1g}$ energy of 14475 cm^{-1} , equation 2 predicts a g_z value of 2.205. This is similar to the DFT calculated g_z value (2.204). For each mode, the relative change in spin density and/or ${}^2\text{B}_{1g}$ energy can be used to estimate a change in g_z value. The g_z value estimated from equation 2 can thus be compared directly to the DFT calculated change in g_z value along each vibrational coordinate. These plots for all normal modes and each g value are given in Figures 2-1.S3-S5; the results for the b_{2u} , a_{2u} , and a_{1g} modes are given in Figures 2-1.S9 (a-c), respectively. From these comparisons for the b_{2u} mode (Figure S9a), the Cu spin density and ${}^2\text{B}_{2g}$ energy both contribute appreciably to the change in g_z value. Furthermore, for the a_{2u} mode (Figure 2-1.S9b), the change in g_z value is largely due to the change in the ${}^2\text{B}_{2g}$ energy; as mentioned above, a small component from the Cu spin density component actually opposes the

change in g_z value determined by the ${}^2B_{2g}$ energy alone. Lastly, for the a_{1g} mode, the change in the g_z value is largely due to the change in ${}^2B_{2g}$ energy, but the spin density component contributes to a small extent. This analysis (Figure 2-1.S9 and Figures 2-1.S3-S5) provides a means to qualitatively decompose the spin–phonon coupling term contributions from ground state covalency and orbital angular momentum from excited state SOC.

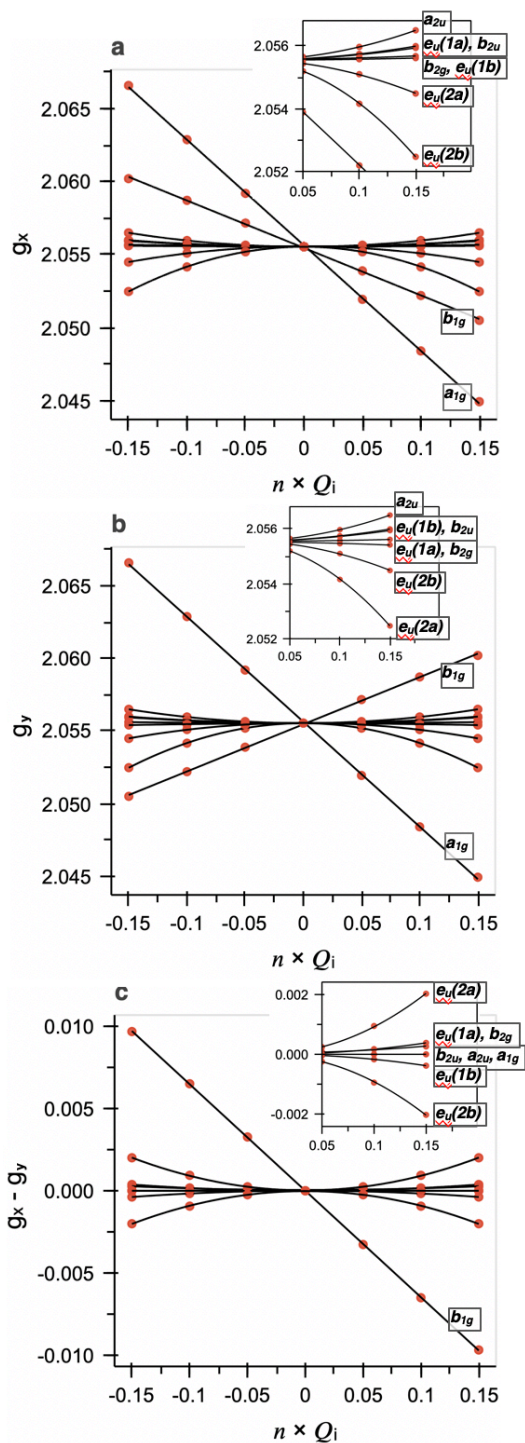


Figure 2-1.S10. Spin-phonon analyses (g_x , g_y , and $g_x - g_y$) for idealized D_{4h} $[\text{CuCl}_4]^{2-}$.

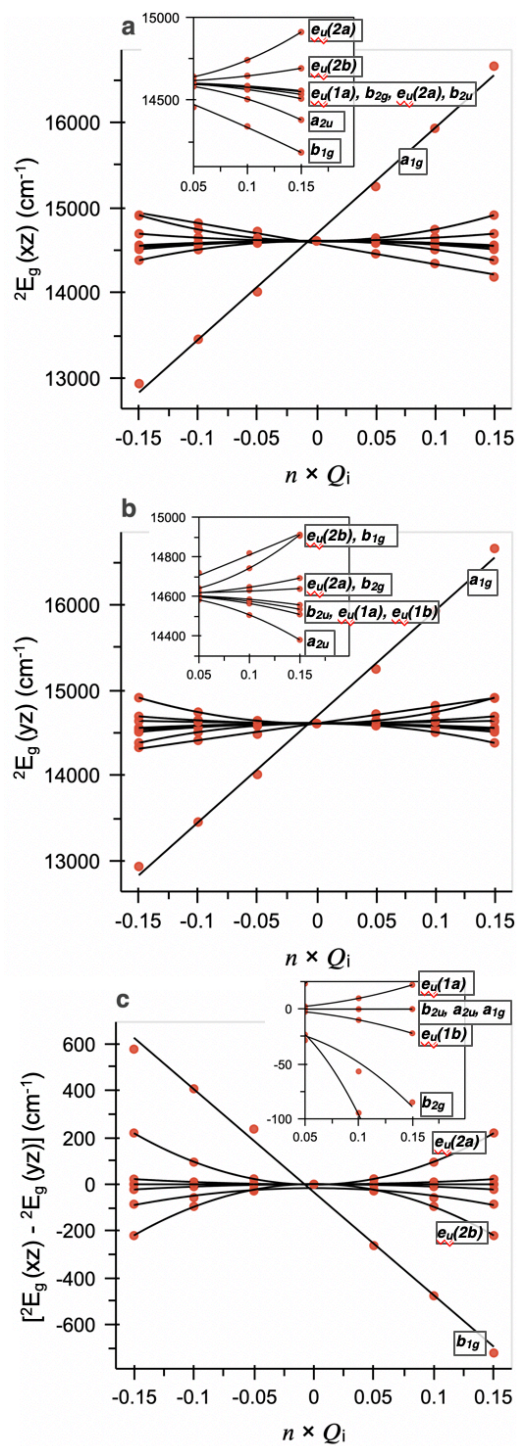


Figure 2-1.S11. Spin-phonon analyses (2E_g) for idealized D_{4h} $[\text{CuCl}_4]^{2-}$.

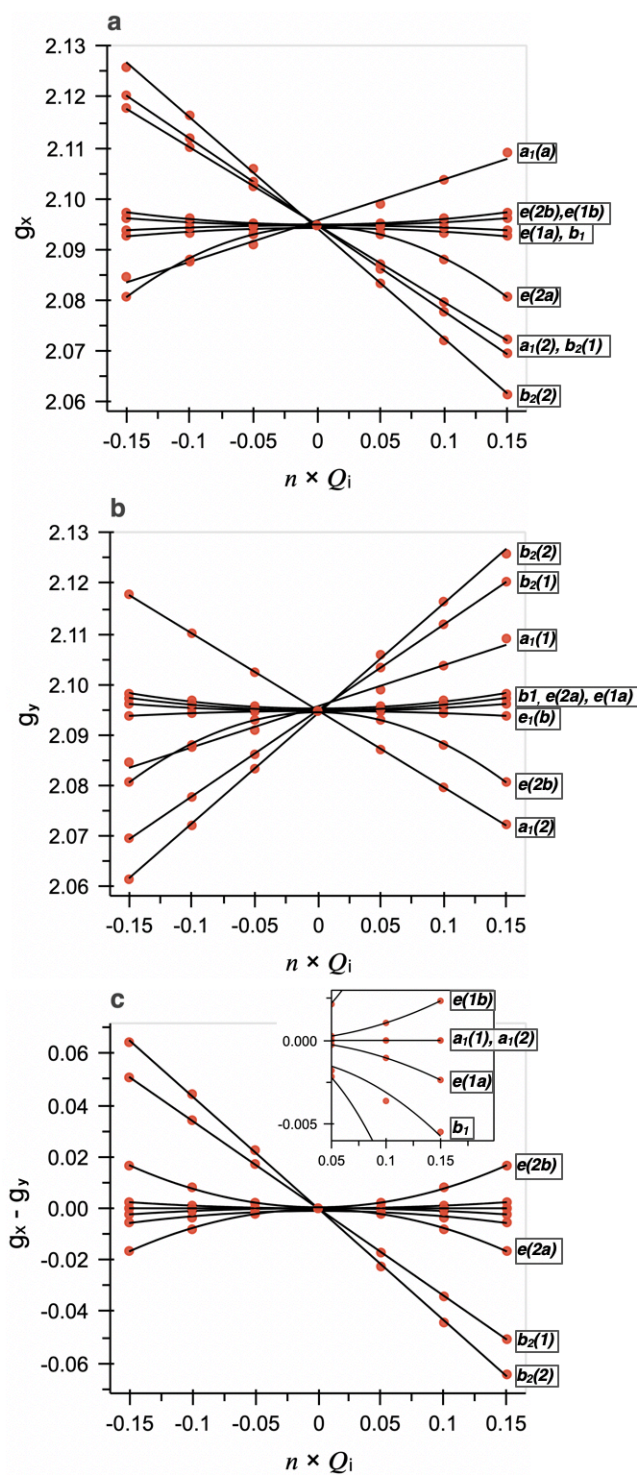


Figure 2-1.S12. Spin-phonon analyses (g_x , g_y , and $g_x - g_y$) and for idealized $D_{2d} [\text{CuCl}_4]^{2-}$.

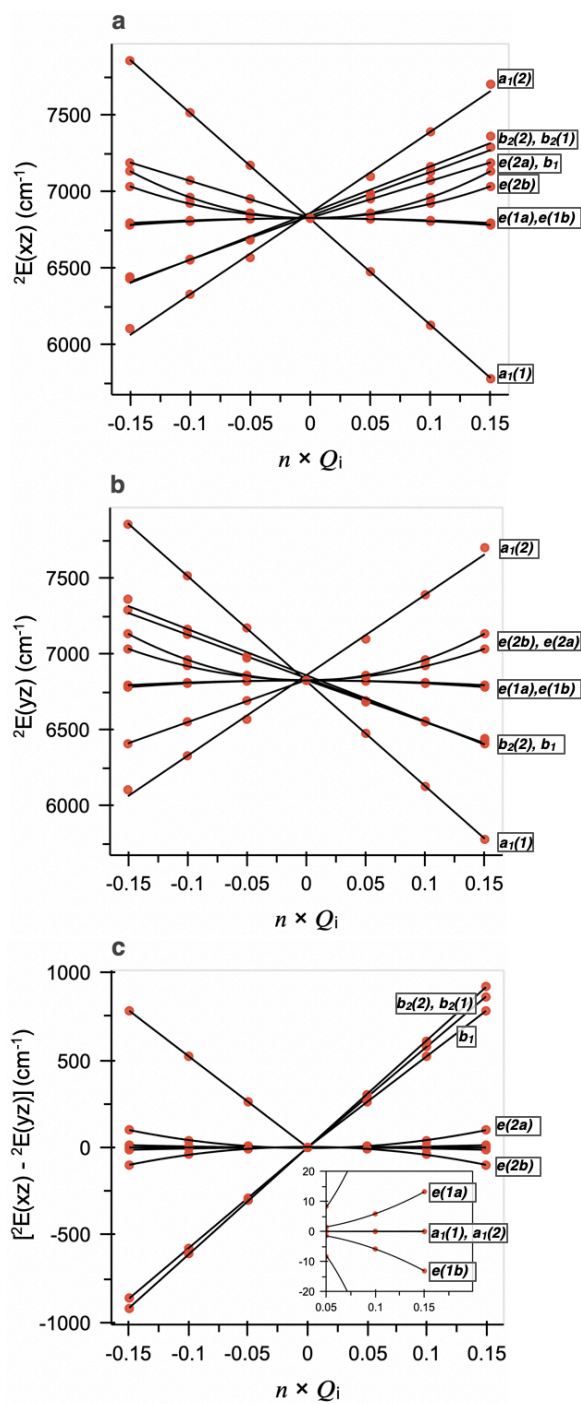


Figure 2-1.S13. Spin-phonon analyses (2E) for idealized D_{2d} $[\text{CuCl}_4]^{2-}$.

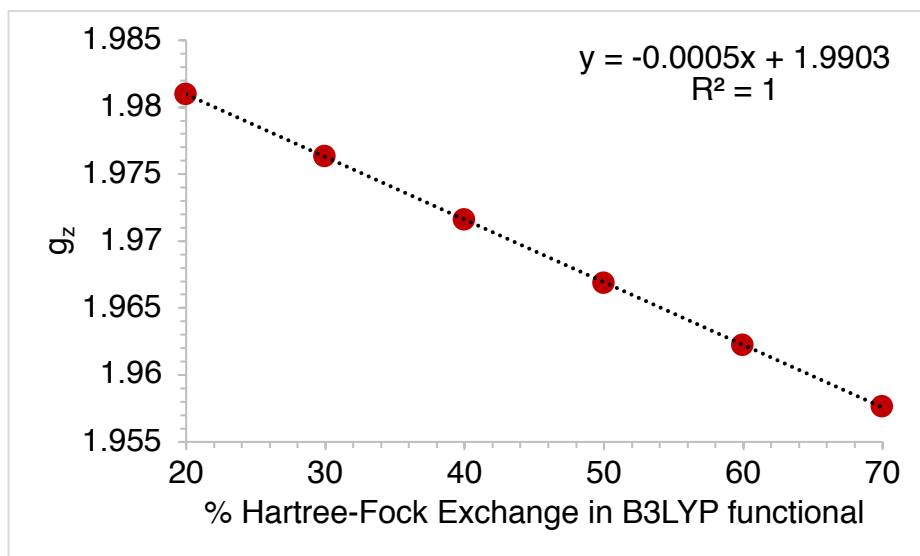


Figure 2-1.S14. Hartree-Fock dependence of the calculated value of g_z for C_{4v} $[\text{VOCl}_4]^{2-}$ using the crystal structure experimental value is 1.948. Better agreement between theory and experiment is obtained using values $>50\%$. 60% has been used here, as it provides acceptable agreement for $[\text{VOCl}_4]_2$ - and the other V(IV) complexes considered here.

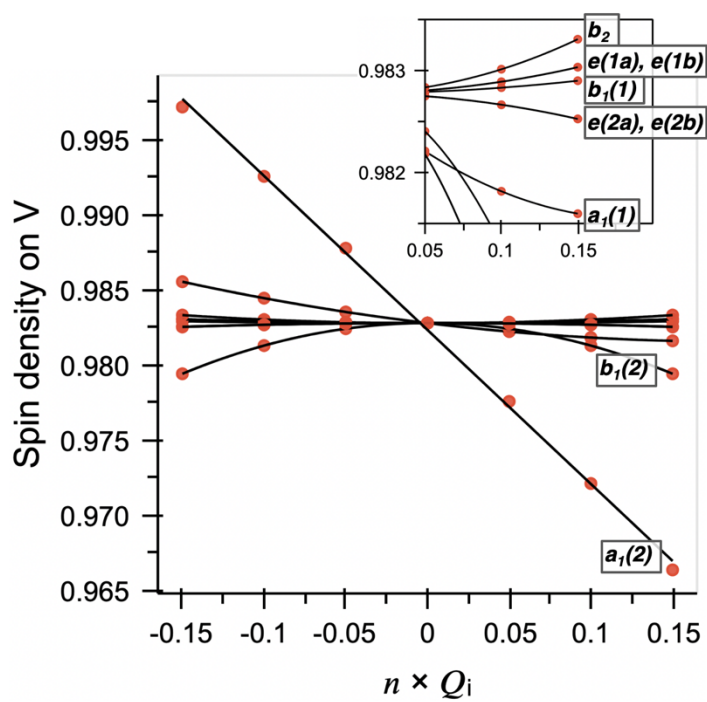


Figure 2-1.S15. Spin-phonon analyses (spin density) for the idealized structure of C_{4v} $[\text{VOCl}_4]^{2-}$. The first 9 out of 12 modes are displayed.

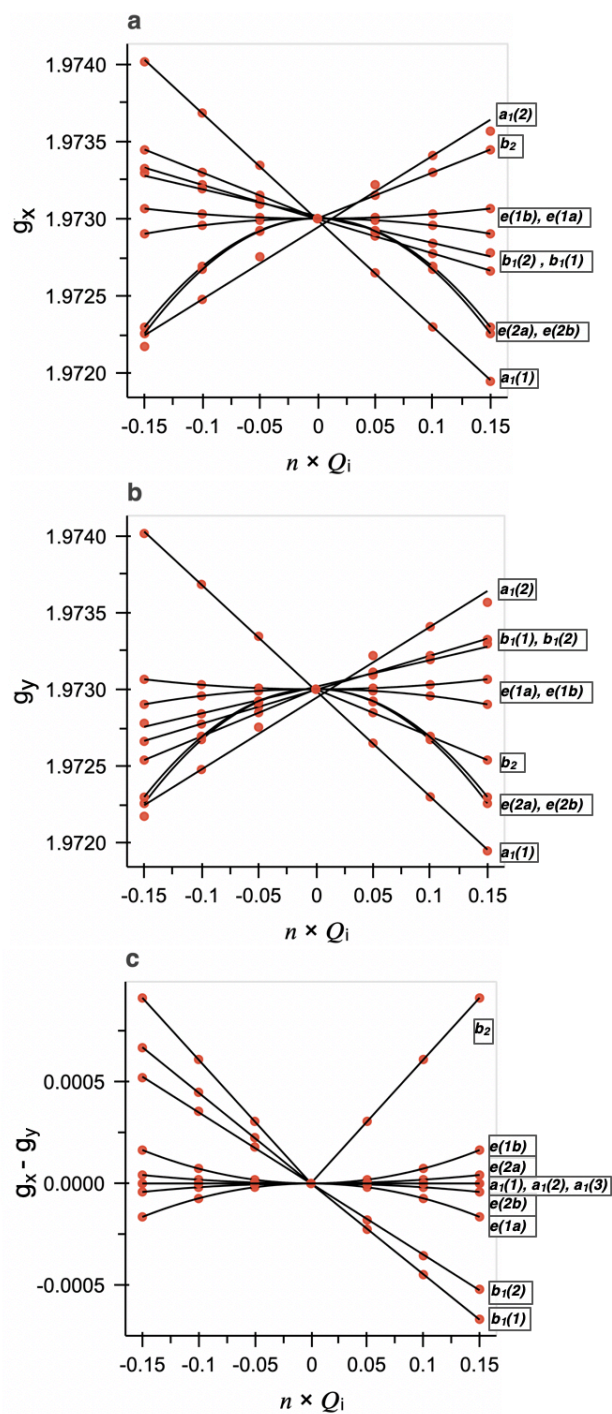


Figure 2-1.S16. Spin-phonon analyses, a) g_x b) g_y , c) $g_x - g_y$ for idealized C_{4v} $[\text{VOCl}_4]^{2-}$. The first 9 out of 12 modes are displayed.

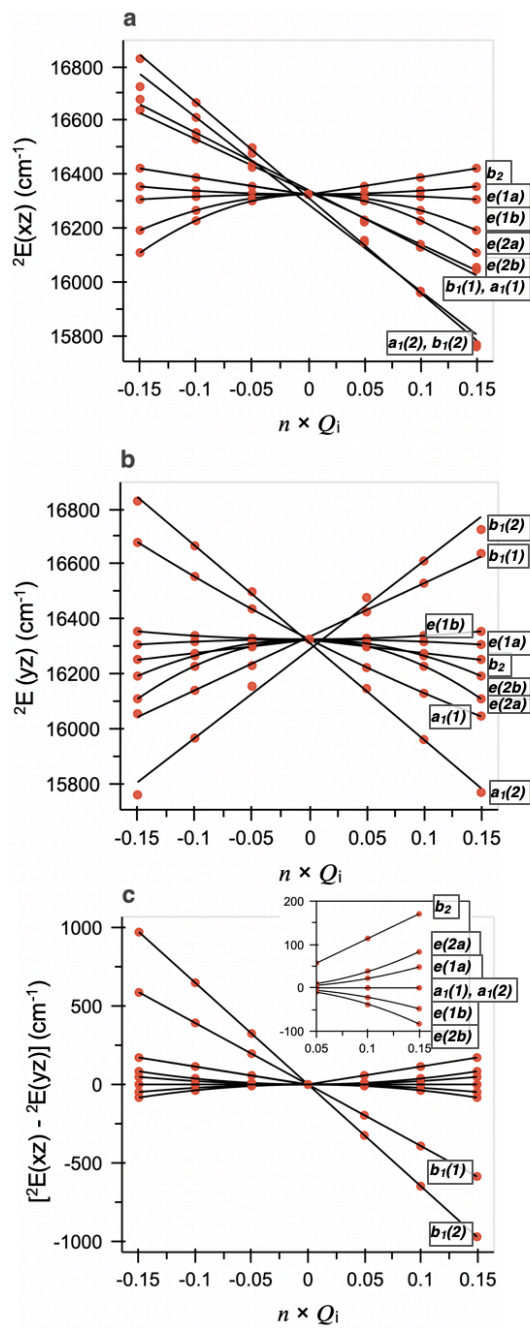


Figure 2-1.S17. Spin-phonon analyses for idealized C_{4v} $[\text{VOCl}_4]^{2-}$. a) ${}^2E(xz)$, b) ${}^2E(yz)$, c) ${}^2E(xz) - {}^2E(yz)$. The first 9 out of 12 modes are displayed.

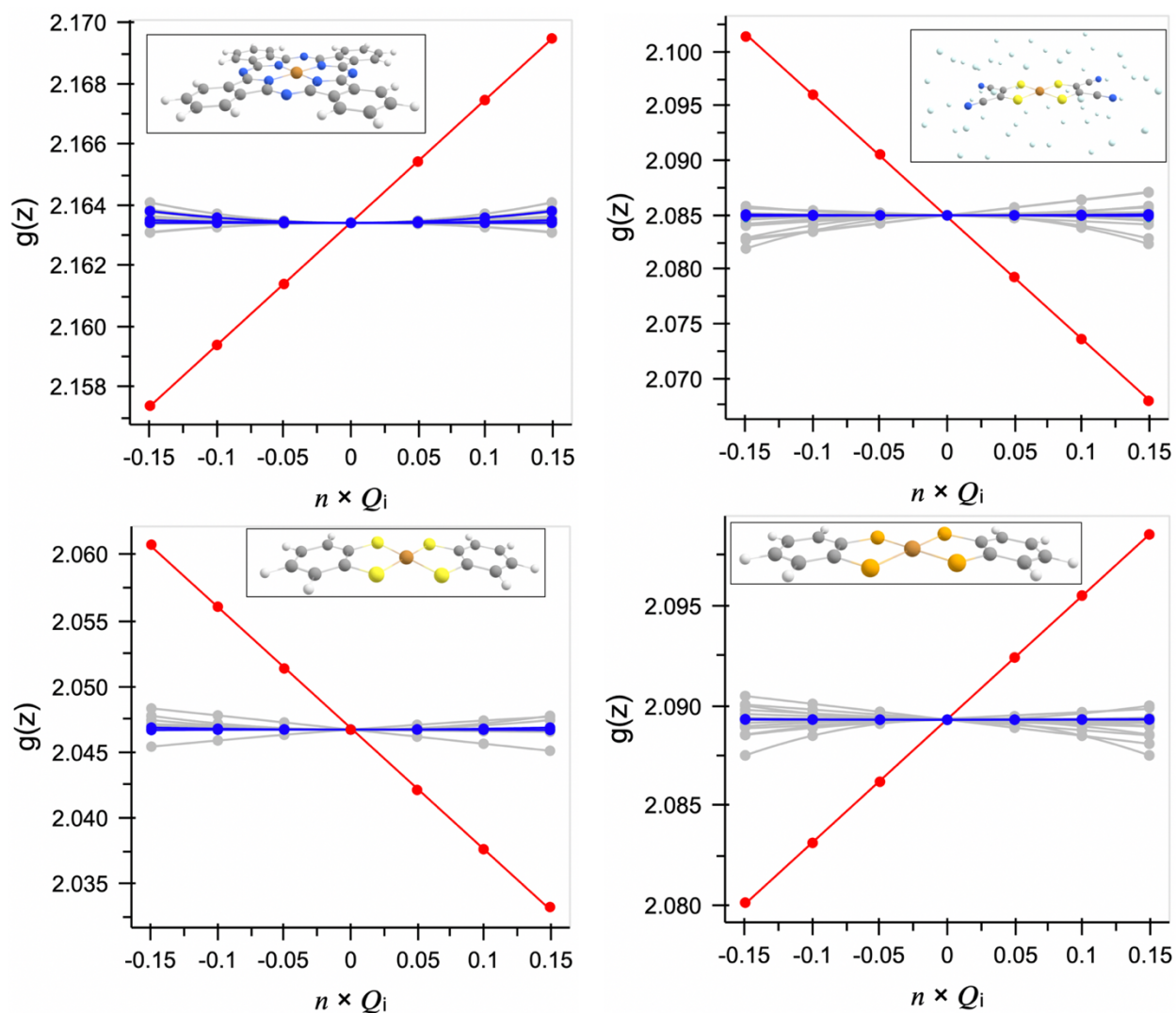


Figure 2-1.S18. Spin-phonon analyses (g_z) for Cu(II) qubits. (top left) CuPc, (top right) $[\text{Cu}(\text{mnt})_2]^{2-}$, (bottom left) $[\text{Cu}(\text{bdt})_2]^{2-}$, and (bottom right) $[\text{Cu}(\text{bds})_2]^{2-}$. Red: vibrational mode with substantial M-L stretching character. Blue: vibrational mode with substantial dihedral bending character (large change in α).

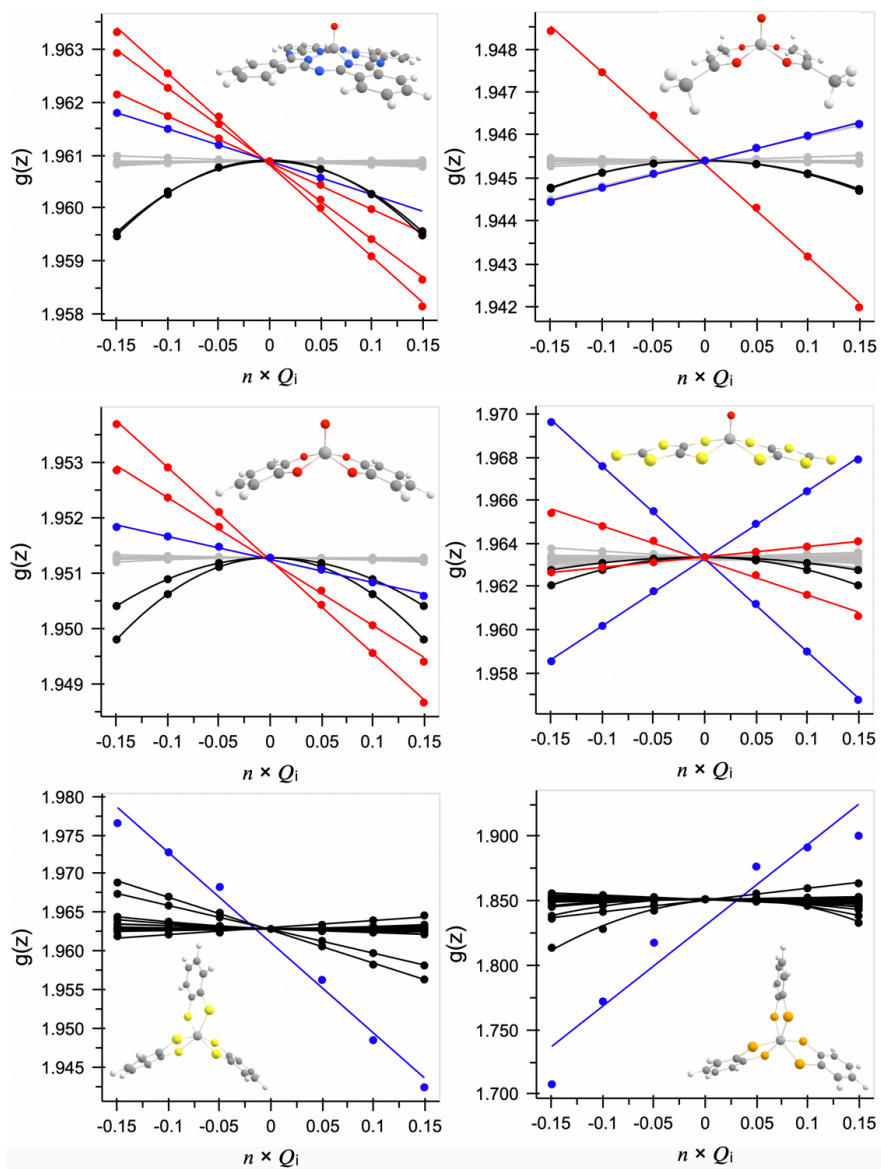


Figure 2-1.S19. Spin-phonon analyses (g_z) for V(IV) qubits. (A) VOPc, (B) VO(acac)₂, (C) [VO(cat)₂]²⁻, (D) [VO(dmit)₂]²⁻, (E) [V(bdt)₃]²⁻, and (F) [V(bds)₃]²⁻. Red: vibrational mode with substantial pyramidal bending character. Blue: vibrational mode with substantial M-L stretching character (excluding M-oxo stretch). Note, due to nonlinearity of the blue slopes for [V(bdt)₃]²⁻ and [V(bds)₃]²⁻ (totally symmetric stretches), only the first two data +/- 0.05 points were used to obtain slopes.

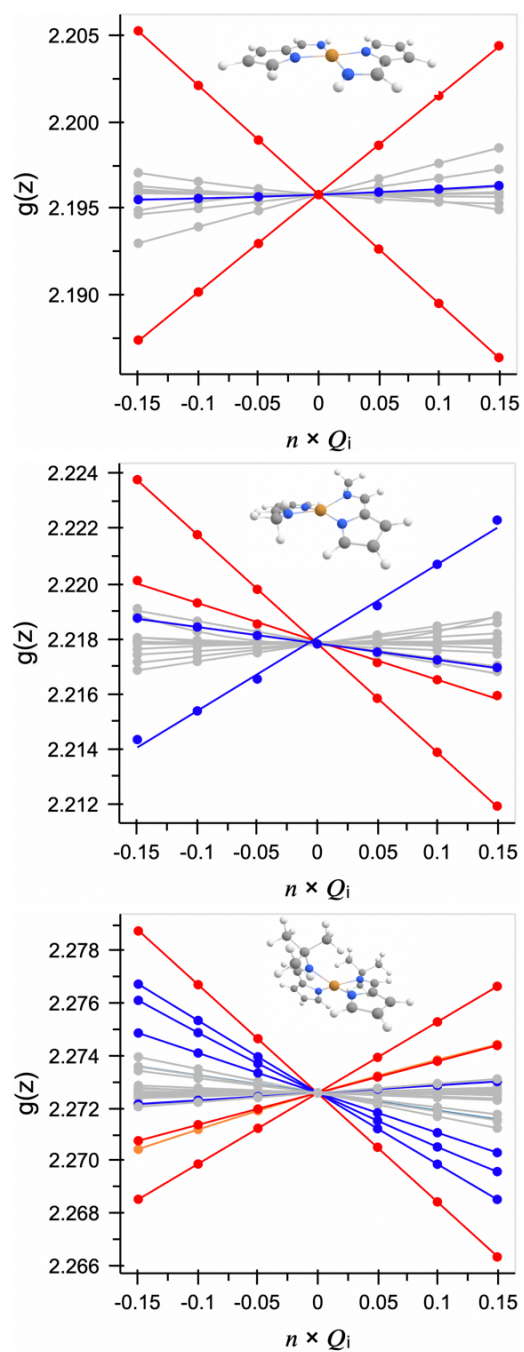


Figure 2-1.S20. DFT-optimized CuN_4 complexes (R = H (top), R = Me (middle), R = *tert*-Bu (bottom)). Red: vibrational modes with substantial M-L stretching character. Blue: vibrational mode with substantial dihedral bending character (large change in α).

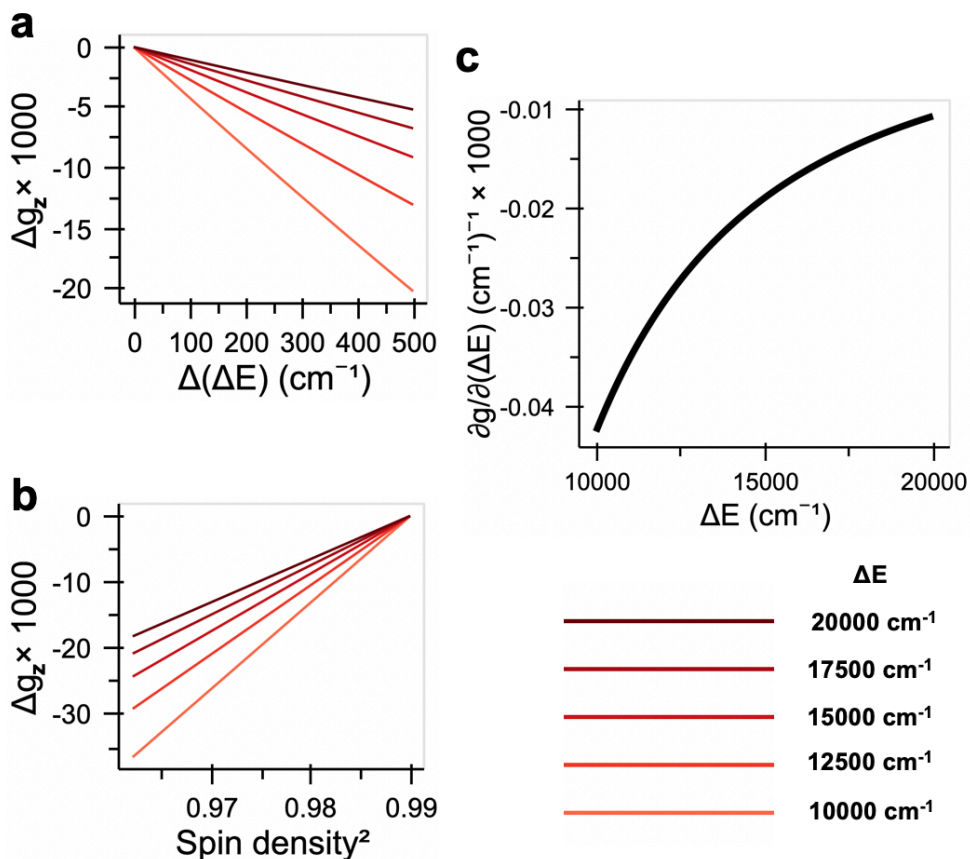


Figure 2-1.S21. LFT calculations utilizing expressions from Section 2.1 in the manuscript text. (A) Variation in the g_z value as a function of ${}^2B_{2g}$ energy, (B) Variation in the g_z value as a function of spin density squared, and (C) Inverse pseudo-quadratic dependence of spin–phonon coupling term on the initial ${}^2B_{2g}$ excited state energy.

The behavior predicted in Section 2.1 and analyzed above can further demonstrated using a series of LFT calculations. These are presented in Figure 2-1.S20 for a range of initial ${}^2B_{2g}$ energies ($\Delta E = 10000 - 20000 \text{ cm}^{-1}$) and a set value of covalency (80 % Cu(d) character). The slopes of the lines in Figure 2-1.S20A (i.e., the gradient in g_z value) increase with decreasing energy of the initial ${}^2B_{2g}$ excited state. Thus, for a given value of covalency, the LFT prediction indicates spin–phonon

coupling terms for the g_z value are smallest for complexes that have higher energy ligand field excited states energies. This is observed for both the LFT expressions and the DFT/TDDFT data in Figures 2-1.6A and 2-1.6B. Even though the excited state coupling term of the ${}^2B_{2g}$ state (in D_{4h}) is larger than the 2B_1 state (in D_{2d}) (also compare blue lines in Figure 2-1.4A), the resultant effect on the gradient in g_z value is smaller because the initial energy of ${}^2B_{2g}$ state is higher in energy than the 2B_1 state. Lastly, the slopes of the g_z value vs. ${}^2B_{2g}$ energy shown in Figure 2-1.S20A exhibit an inverse pseudo-quadratic dependence on the initial energy of the ${}^2B_{2g}$ excited state (Figure 2-1.S20C). The covalency contributions to the spin–phonon coupling terms can also be evaluated. For a given ${}^2B_{2g}$ energy (e.g., 10000 cm^{-1}), the gradient in the g_z value for a change in covalency can be calculated for a series of initial covalency values (Figure 2-1.S20B). The slopes of these lines increase with decreasing covalency. Thus, the spin–phonon coupling term for the g_z value is smaller for more covalent ligand–metal bonds, and this coupling term is linearly dependent on the covalency of a given ligand–metal bond. Again, this behavior predicted by LFT and is also observed for DFT calculations presented in Figures 2-1.6A and 2-1.6C.

D. DFT Structures and Input Coordinates**[CuCl₄]²⁻ crystal structure**

Cl	-0.002786	-2.280699	0.000000
Cl	-2.247278	-0.003002	0.000000
Cu	0.000000	0.000000	0.000000
Cl	0.002786	2.280699	0.000000
Cl	2.247278	0.003002	0.000000

[CuCl₄]²⁻ idealized structure

Cl	0.000000	-2.264000	0.000000
Cl	-2.264000	0.000000	0.000000
Cu	0.000000	0.000000	0.000000
Cl	0.000000	2.264000	0.000000
Cl	2.264000	0.000000	0.000000

[Cu(mnt)₂]²⁻ crystal structure He cage¹⁷

Cu	0.001242	0.000571	0.000099
N	5.350804	-1.883487	0.221212
N	-5.346332	1.888441	-0.221762
N	5.258176	2.173372	-0.015008
N	-5.255549	-2.172419	0.015367
S	1.692644	-1.584810	0.034526
S	-1.689934	1.586102	-0.033510
S	1.619168	1.690587	-0.126304
S	-1.617007	-1.689183	0.125983
C	3.122068	-0.596224	0.082898
C	-3.119663	0.597899	-0.081575
C	4.359048	-1.288467	0.163586
C	-4.356045	1.291124	-0.162608
C	3.091239	0.778285	0.020976
C	-3.089067	-0.776603	-0.020200
C	4.295102	1.531016	0.014252
C	-4.292806	-1.529546	-0.013695
He	6.188799	-0.937495	-3.096306
He	-6.189224	0.938056	3.096285
He	7.719578	-2.226888	-1.917291
He	-7.719989	2.227491	1.917301
He	2.268341	5.208778	1.258576
He	-2.268754	-5.208190	-1.258570
He	0.832704	-3.221674	-2.847842
He	-0.833106	3.222253	2.847850
He	1.378397	2.593504	2.995096
He	-1.378809	-2.592926	-2.995089
He	5.519905	2.227175	3.165540
He	-5.520312	-2.226597	-3.165555

He	6.773620	3.621984	1.838571
He	-0.528791	-1.914067	3.874611
He	0.528378	1.914655	-3.874611
He	-6.774018	-3.621400	-1.838565
He	6.330228	5.869329	1.772994
He	5.903450	-3.601739	-4.093076
He	0.734151	-3.465172	2.756368
He	-0.734562	3.465750	-2.756372
He	-5.903862	3.602317	4.093084
He	-6.330644	-5.868751	-1.772984
He	4.172094	-2.725347	-2.872268
He	-4.172504	2.725921	2.872274
He	2.887551	-4.099351	-1.539883
He	-2.887955	4.099942	1.539884
He	4.643875	-4.899196	0.435124
He	-4.644286	4.899720	-0.435148
He	6.908665	-1.219852	2.567387
He	5.446667	-4.587814	2.571021
He	-5.447067	4.588413	-2.571031
He	-6.909076	1.220433	-2.567391
He	7.587035	0.143413	0.860741
He	-7.587428	-0.142837	-0.860738
He	1.980676	-0.562458	-3.210510
He	-1.981065	0.563019	3.210511
He	3.816109	0.691256	-2.609753
He	-3.816476	-0.690641	2.609766
He	3.603320	3.115971	-3.882709
He	-3.603739	-3.115394	3.882705
He	6.904520	-4.226074	-0.563357
He	-6.904959	4.226712	0.563409
He	3.956188	6.048382	-1.228601

He	8.137040	-3.106397	0.983741
He	4.218233	-2.701279	4.154707
He	-4.218646	2.701867	-4.154700
He	-8.137470	3.106985	-0.983726
He	-3.956599	-6.047805	1.228598
He	6.134159	5.471991	-0.864728
He	2.650999	-1.606071	2.908682
He	-2.651410	1.606648	-2.908686
He	-6.134570	-5.471404	0.864734
He	7.054786	3.662271	-1.970599
He	2.245377	0.641117	3.270731
He	-2.245780	-0.640530	-3.270723
He	-7.055198	-3.661694	1.970606

CuPc optimized structure

Cu	1.929292	-0.000001	-0.000075
C	-0.816622	-1.133209	-0.047251
C	2.662694	-4.145743	-0.018180
C	3.389802	-5.327906	-0.015873
C	2.683996	-6.517341	-0.034066
C	1.284308	-6.528964	-0.054295
C	0.558518	-5.351405	-0.056627
C	1.265695	-4.157327	-0.038326
C	0.842295	-2.765786	-0.034679
C	-2.214832	-0.732876	-0.065020
C	-3.396860	-1.459978	-0.087676
C	-4.586241	-0.753945	-0.100581
C	-4.598029	0.645896	-0.091101
C	-3.420701	1.371474	-0.068500
C	-2.226580	0.664090	-0.055594
C	-0.835472	1.087821	-0.032306
C	3.062952	-2.747521	-0.002689
H	4.464599	-5.313798	-0.000407
H	3.216475	-7.452508	-0.032793
H	0.767555	-7.472814	-0.068156
H	-3.382884	-2.534854	-0.094865
H	-5.521234	-1.286444	-0.118247
H	-5.541833	1.162810	-0.101667
H	-3.424706	2.446437	-0.061215
N	-0.418924	-2.388251	-0.050220
N	-0.038656	-0.016058	-0.028118
N	-0.459287	2.349516	-0.018312
N	1.912461	1.969569	0.013234
N	3.897240	0.016061	0.028031
N	1.946125	-1.969570	-0.013321

N	4.317871	-2.349515	0.018258
C	0.795633	2.747519	0.002627
C	3.016288	2.765787	0.034621
C	4.675206	1.133213	0.047201
C	4.694055	-1.087818	0.032248
C	1.195887	4.145741	0.018147
C	2.592885	4.157328	0.038294
N	4.277508	2.388255	0.050174
C	6.073418	0.732880	0.065005
C	6.085164	-0.664086	0.055576
C	0.468774	5.327899	0.015871
C	3.300058	5.351407	0.056633
C	7.255446	1.459980	0.087706
C	7.279283	-1.371472	0.068524
C	1.174577	6.517336	0.034100
H	-0.606022	5.313787	0.000404
C	2.574264	6.528963	0.054331
C	8.444826	0.753944	0.100654
H	7.241471	2.534856	0.094898
C	8.456612	-0.645896	0.091172
H	7.283287	-2.446435	0.061237
H	0.642096	7.452502	0.032852
H	3.091015	7.472814	0.068223
H	9.379819	1.286442	0.118356
H	9.400415	-1.162812	0.101771
H	-0.516354	-5.355312	-0.072228
H	4.374930	5.355317	0.072236

[Cu(bdt)₂]²⁻ crystal structure (H-optimized)

Cu	-0.246333	4.840524	0.988186
S	-0.297451	7.010976	0.973118
S	1.922436	4.810648	1.000521
C	2.367678	6.499871	1.080609
C	3.698797	6.876472	1.137466
H	4.462439	6.116629	1.147774
C	4.035157	8.205599	1.189637
H	5.079044	8.487390	1.231583
C	3.061918	9.202347	1.160317
H	3.337319	10.245155	1.193239
C	1.736583	8.815746	1.112850
H	0.954494	9.558068	1.093694
C	1.378850	7.481657	1.071483
S	-0.195214	2.670072	1.003254
C	-1.871516	2.199391	0.904890
C	-2.860344	3.181176	0.895764
S	-2.415101	4.870399	0.975851
C	-4.191462	2.804575	0.838906
H	-4.955105	3.564419	0.828596
C	-4.527823	1.475448	0.786736
H	-5.571709	1.193657	0.744782
C	-3.554583	0.478701	0.816055
H	-3.829986	-0.564107	0.783138
C	-2.229249	0.865302	0.863523
H	-1.447160	0.122979	0.882678

[Cu(bds)₂]²⁻ crystal structure (H-optimized)

Se	2.413500	0.000148	-0.002234
Se	-0.002019	2.377198	0.001096
Cu	0.000006	0.000004	0.000006
C	1.828800	2.827746	0.141805
C	2.828824	1.853727	0.131995
C	2.192605	4.178527	0.280461
H	1.415755	4.924644	0.300541
C	3.518228	4.551426	0.392536
H	3.775844	5.595216	0.497960
C	4.504059	3.592788	0.359040
H	5.543168	3.877358	0.439563
C	4.168573	2.251722	0.233388
H	4.939919	1.500051	0.218160
Se	-2.413541	-0.000012	0.002216
Se	0.001902	-2.377104	-0.001162
C	-1.828840	-2.827610	-0.141824
C	-2.828865	-1.853590	-0.132013
C	-2.192722	-4.178433	-0.280528
H	-1.415864	-4.924545	-0.300632
C	-3.518268	-4.551290	-0.392554
H	-3.775907	-5.595075	-0.497978
C	-4.504100	-3.592651	-0.359058
H	-5.543201	-3.877258	-0.439582
C	-4.168690	-2.251628	-0.233454
H	-4.940029	-1.499952	-0.218244

CuN₄ (R = H) optimized structure

Cu	0.000452	0.000420	-0.032815
C	2.523472	1.222653	-0.069467
C	1.621652	2.301182	0.034792
C	1.772180	3.687526	0.114715
C	0.485159	4.209757	0.206111
C	-0.387969	3.116559	0.176993
N	2.041251	0.022674	-0.117011
N	0.288530	1.970138	0.073689
N	-2.040268	-0.017550	-0.117144
N	-0.288142	-1.972122	-0.011491
C	-2.522873	-1.218304	-0.121172
C	-1.621416	-2.300673	-0.064089
C	0.388027	-3.122140	0.041299
C	-1.772371	-3.689143	-0.044675
C	-0.485468	-4.215276	0.023130
H	3.588720	1.407793	-0.107420
H	2.696894	4.230936	0.107163
H	0.205657	5.241397	0.284455
H	-1.460023	3.133733	0.229846
H	-3.588211	-1.401245	-0.166516
H	1.460108	-3.141934	0.092722
H	-2.697282	-4.231392	-0.075393
H	-0.206268	-5.249435	0.056234
H	-2.713241	0.724694	-0.161990
H	2.714467	-0.716670	-0.194338

CuN₄ (R = Me) optimized structure

Cu	0.000095	-0.000371	-0.001644
N	0.162667	1.968189	0.178463
C	-0.537149	3.055567	0.531942
H	-1.567796	2.989866	0.820929
N	2.010380	0.172067	-0.511367
C	0.257616	4.200087	0.465966
H	-0.051485	5.200001	0.696784
C	1.520289	3.780514	0.045240
H	2.389237	4.388257	-0.115990
C	1.431118	2.399799	-0.119954
C	2.368518	1.408296	-0.493338
H	3.378397	1.698414	-0.760391
C	2.958383	-0.853529	-0.895609
H	3.872060	-0.422078	-1.298491
H	2.521105	-1.505098	-1.644424
H	3.219913	-1.469590	-0.040383
N	-0.146129	-1.942106	0.376902
C	0.576613	-2.992284	0.791386
H	1.622812	-2.902333	1.009248
C	-0.217978	-4.134925	0.885849
H	0.106967	-5.108599	1.194099
C	-1.504946	-3.753857	0.503842
H	-2.380595	-4.371377	0.455877
C	-1.429333	-2.396111	0.199622
C	-2.389890	-1.442145	-0.211096
N	-2.036446	-0.214701	-0.370462
C	-3.007899	0.771922	-0.795828
H	-3.943896	0.306704	-1.097056
H	-2.618481	1.343958	-1.631076
H	-3.217305	1.471005	0.008361

H -3.413324 -1.753147 -0.387669

CuN₄ (R = t-Bu) optimized structure

Cu	-0.002134	-0.001526	-0.007537
N	0.232946	1.902783	0.423070
C	-0.382564	2.923503	1.041897
H	-1.383534	2.829989	1.415686
C	0.454211	4.034933	1.108857
H	0.215371	4.981625	1.550847
C	1.652660	3.665911	0.493002
H	2.531428	4.267408	0.364751
C	1.487108	2.343865	0.087837
C	2.365631	1.420057	-0.535367
H	3.336152	1.780236	-0.844029
N	2.000955	0.200508	-0.722002
C	2.881979	-0.789080	-1.383967
C	4.001032	-0.145493	-2.214721
H	4.727104	0.376376	-1.600251
H	3.603539	0.550779	-2.946784
H	4.536132	-0.921916	-2.750205
C	3.508080	-1.679463	-0.300887
H	2.742743	-2.184431	0.273148
H	4.113604	-1.087349	0.378258
H	4.143516	-2.434866	-0.753185
C	2.003355	-1.636662	-2.312581
H	1.207124	-2.119627	-1.759405
H	2.596815	-2.408226	-2.792610
H	1.559754	-1.020108	-3.088240
N	-0.305981	-1.848700	0.593032
C	0.216311	-2.791226	1.394631
H	1.160601	-2.650111	1.883369
C	-0.629772	-3.894819	1.472565
H	-0.457343	-4.785855	2.042639

C	-1.734828	-3.604035	0.668720
H	-2.593334	-4.222610	0.493187
C	-1.508496	-2.332975	0.146677
C	-2.289877	-1.489612	-0.685345
H	-3.213259	-1.888429	-1.079345
N	-1.894128	-0.295461	-0.954206
C	-2.665825	0.609167	-1.836756
C	-3.682453	-0.125984	-2.721340
H	-4.488500	-0.570220	-2.146819
H	-3.208533	-0.904812	-3.310850
H	-4.132950	0.582795	-3.407283
C	-3.406579	1.627142	-0.957518
H	-2.710198	2.196567	-0.356836
H	-4.103345	1.124769	-0.293769
H	-3.966457	2.323054	-1.574885
C	-1.659499	1.334377	-2.739443
H	-0.931180	1.877905	-2.149959
H	-2.171230	2.044385	-3.381261
H	-1.132557	0.626201	-3.371455

[VOCl₄]²⁻ crystal structure

V	0.000000	0.000000	0.000000
O	0.000000	0.000000	1.580262
Cl	0.046471	2.261335	-0.680124
Cl	2.320584	0.000000	-0.478765
Cl	0.009075	-2.220921	-0.693804
Cl	-2.310796	0.005495	-0.469030

[VOCl₄]²⁻ idealized structure

V	0.000000	0.000000	0.000000
O	0.000000	0.000000	1.580260
Cl	0.000000	2.281063	-0.581436
Cl	2.281063	0.000000	-0.581436
Cl	0.000000	-2.281063	-0.581436
Cl	-2.281063	0.000000	-0.581436

VOPc optimized structure

V	0.001035	1.963761	0.670096
O	0.013536	1.990117	2.223772
N	-2.363133	-0.405430	-0.002134
N	-0.003900	3.909584	-0.001001
N	-0.005040	-0.004750	0.070561
N	1.953075	1.951164	0.017611
N	-2.361792	4.308073	-0.091161
N	-1.961757	1.953021	0.051595
N	2.352410	4.305873	-0.133225
N	2.351007	-0.407660	-0.044669
C	-4.132573	1.255777	-0.117610
C	-0.702048	-2.176858	-0.082853
C	-1.111829	-0.790634	0.010793
C	-1.110256	4.692984	-0.092603
C	1.099815	-0.791716	-0.009031
C	-2.747125	3.057546	-0.047031
C	-4.132232	2.644712	-0.143690
C	-5.313816	0.536887	-0.208089
H	-5.309608	-0.529761	-0.190798
C	-2.747704	0.846170	-0.005495
C	1.101435	4.691974	-0.112146
C	2.737394	3.054987	-0.096047
C	2.736709	0.843588	-0.054852
C	-0.699652	6.074090	-0.241555
C	0.689516	6.073473	-0.253796
C	-1.417614	7.251880	-0.374597
H	-2.484383	7.247887	-0.368043
C	4.120011	2.640887	-0.219231
C	6.469019	1.242060	-0.439532
H	7.397208	0.720324	-0.525273

C	0.687062	-2.177554	-0.095308
C	4.119550	1.251921	-0.193417
C	-6.486340	1.248062	-0.318008
H	-7.416532	0.727207	-0.385479
C	5.299224	3.355203	-0.359416
H	5.295239	4.421756	-0.382028
C	5.298160	0.531980	-0.307038
H	5.293317	-0.534673	-0.290034
C	1.406010	7.250672	-0.399422
H	2.472728	7.245814	-0.411641
C	-6.486029	2.645764	-0.344287
H	-7.415994	3.164124	-0.431327
C	0.692479	8.420258	-0.524708
H	1.211699	9.347333	-0.634462
C	-0.709228	-4.532569	-0.258316
H	-1.230021	-5.463134	-0.320990
C	1.402914	-3.360049	-0.193105
H	2.469630	-3.356319	-0.205403
C	-5.313248	3.360128	-0.261097
H	-5.308709	4.426674	-0.283896
C	-1.420778	-3.358580	-0.167825
H	-2.487538	-3.353724	-0.161014
C	0.688625	-4.533289	-0.270846
H	1.207246	-5.464394	-0.342827
C	-0.705402	8.420863	-0.512418
H	-1.225650	9.348400	-0.613022
C	6.469518	2.639776	-0.465477
H	7.398104	3.157272	-0.570515

VO(acac)₂ optimized structure

V	-0.018195	0.010755	0.121557
O	0.005209	1.915790	-0.476822
O	1.893968	0.007354	-0.449106
O	-0.007813	-1.888934	-0.493419
O	-1.904506	0.018473	-0.533481
O	-0.050859	0.005127	1.670571
C	0.606481	4.139376	-0.871912
H	-0.092762	4.219741	-1.688151
H	1.463367	4.756905	-1.069173
H	0.107442	4.489596	0.016682
C	0.971280	2.694904	-0.683473
C	2.301788	2.295314	-0.757315
H	3.048367	3.031374	-0.939755
C	2.686579	0.962509	-0.656227
C	4.130237	0.580226	-0.813593
H	4.459353	0.090496	0.088534
H	4.760367	1.427495	-1.012434
H	4.217905	-0.131653	-1.618117
C	-0.579070	-4.103402	-0.971475
H	0.162389	-4.165780	-1.751292
H	-1.421828	-4.719309	-1.225976
H	-0.125722	-4.469511	-0.064815
C	-0.958099	-2.663603	-0.775153
C	-2.282303	-2.263159	-0.922857
H	-3.013820	-2.995976	-1.168345
C	-2.677762	-0.933951	-0.813415
C	-4.109898	-0.551458	-1.053659
H	-4.493439	-0.068545	-0.169622
H	-4.725779	-1.397302	-1.297662
H	-4.148744	0.166358	-1.856479

[VO(cat)₂]²⁻ optimized structure

V	1.895061	-0.000028	0.674427
O	1.774403	1.883734	0.024685
O	0.003568	0.040555	0.028336
O	1.895060	-0.000024	2.258811
C	0.566157	2.261253	-0.305902
C	-0.422647	1.231640	-0.303999
C	-1.723449	1.545441	-0.653205
H	-2.457947	0.765471	-0.650309
C	-2.074052	2.854767	-1.004666
H	-3.088336	3.078440	-1.271946
C	-1.122074	3.845718	-1.006398
H	-1.386487	4.849776	-1.275015
C	0.200769	3.547847	-0.656756
H	0.951247	4.312456	-0.656301
O	2.015715	-1.883795	0.024688
O	3.786551	-0.040619	0.028347
C	3.223961	-2.261315	-0.305899
C	4.212767	-1.231703	-0.303990
C	5.513567	-1.545502	-0.653200
H	6.248065	-0.765531	-0.650300
C	5.864170	-2.854827	-1.004665
H	6.878454	-3.078499	-1.271949
C	4.912192	-3.845776	-1.006403
H	5.176605	-4.849833	-1.275023
C	3.589349	-3.547908	-0.656758
H	2.838871	-4.312517	-0.656309

[VO(dmit)₂]²⁻ crystal structure

V	0.000000	0.000000	0.000000
S	2.262021	-0.056228	-0.759300
S	-0.014794	2.309492	-0.600700
S	4.231492	2.190239	-1.253500
S	2.233469	4.234192	-1.120200
S	5.044606	5.036901	-1.672400
O	0.000000	0.000000	1.593900
C	2.615920	1.635520	-0.925000
C	3.899295	3.886335	-1.378100
C	1.675843	2.604849	-0.851200
S	-2.262021	0.056228	-0.759300
S	0.014794	-2.309492	-0.600700
S	-4.231492	-2.190239	-1.253500
S	-2.233469	-4.234192	-1.120200
S	-5.044606	-5.036901	-1.672400
C	-2.615900	-1.635618	-0.925000
C	-3.899274	-3.886432	-1.378100
C	-1.675843	-2.604849	-0.851200

[V(bdt)₃]²⁻ crystal structure (H-optimized)

V	-0.107511	-0.026186	0.032267
S	-0.546563	-1.945633	-1.264193
S	-0.298407	2.004904	1.248317
S	-1.161104	1.260697	-1.678541
S	1.817730	0.034480	-1.340450
S	1.467973	-0.558606	1.733511
S	-1.792951	-0.933506	1.423530
C	-1.259884	2.922434	-1.139102
C	-2.322194	-2.458880	0.745734
C	-0.929790	3.238584	0.187999
C	-3.279656	-3.258608	1.377865
H	-3.693057	-2.932876	2.308629
C	-1.679043	3.949125	-1.992480
H	-1.918214	3.717964	-3.008513
C	3.217989	-0.312264	-0.355835
C	-1.052748	4.565194	0.638591
H	-0.793146	4.792873	1.650207
C	-3.701829	-4.449352	0.808372
H	-4.437618	-5.047751	1.305545
C	-1.777183	-2.886671	-0.470229
C	-2.209421	-4.103561	-1.034574
H	-1.787877	-4.420764	-1.964161
C	3.076040	-0.488422	1.028088
C	4.497174	-0.374282	-0.925996
H	4.596615	-0.256536	-1.983869
C	-1.801662	5.261358	-1.526687
H	-2.128110	6.030793	-2.196697
C	-1.486524	5.565226	-0.217117
H	-1.579162	6.570871	0.140439
C	5.610827	-0.575317	-0.138722

H	6.579998	-0.626496	-0.592984
C	4.222528	-0.641692	1.813037
H	4.113395	-0.751303	2.871191
C	-3.154721	-4.871902	-0.395429
H	-3.476984	-5.794347	-0.835516
C	5.483014	-0.694786	1.233204
H	6.348847	-0.826682	1.849461

[V(bds)₃]²⁻ crystal structure (H-optimized)

Se	-0.796476	-1.684988	1.522772
Se	1.756761	0.274502	1.746334
Se	1.584431	1.498826	-1.354509
V	0.006380	0.103548	-0.000151
C	3.177236	1.693532	-0.319571
C	-0.424266	-3.338051	0.659263
C	3.229502	1.205867	0.990272
C	-0.677815	-4.546355	1.331841
H	-1.002722	-4.522354	2.358112
C	4.400926	1.334215	1.735563
H	4.430788	0.942208	2.738545
C	4.304237	2.314421	-0.853775
H	4.272242	2.693058	-1.861872
C	-0.525425	-5.750243	0.667172
H	-0.728327	-6.675341	1.185324
C	5.464084	2.458579	-0.093638
H	6.325811	2.944630	-0.524889
C	5.519743	1.952871	1.195814
H	6.418720	2.054646	1.783705
Se	0.596286	-1.768326	-1.520292
C	0.034960	-3.365765	-0.654413
C	0.146624	-4.596337	-1.325138
H	0.471586	-4.611647	-2.351500
C	-0.144283	-5.773423	-0.658660
H	-0.056251	-6.716407	-1.176594
Se	-1.712523	0.473678	-1.747046
Se	-1.399123	1.674454	1.351856
C	-2.958696	2.050982	0.316483
C	-3.067275	1.570684	-0.992624
C	-4.215964	1.832875	-1.738113

H	-4.291952	1.444160	-2.739806
C	-4.006049	2.799178	0.849648
H	-3.931579	3.172963	1.857495
C	-5.141422	3.075708	0.089191
H	-5.943000	3.655311	0.521005
C	-5.255447	2.577913	-1.199400
H	-6.139252	2.777354	-1.785337

E. Representative ORCA Input Files

Representative ORCA input file for an optimization calculation

```
! UKS B3LYP OPT RIJCOSX ZORA ZORA-def2-TZVP def2/J TIGHTSCF GRID7 NOFINALGRID
GRIDX9 NOFINALGRIDX
! LargePrint PrintBasis
%method
ScalHFX = 0.38
end
%scf
MaxIter 500
end
%pal nprocs 1
end
%maxcore 4500
%eprnmr
    gtensor 1
    ori -3
    printlevel 3
end
%tddft
nroots 15
maxdim 5
end
* xyzfile -2 2 /path/input.xyz
```


Representative ORCA input file for single point EPR & TDDFT calculation:

```
! UKS B3LYP SP RIJCOSX ZORA ZORA-def2-TZVP def2/J TIGHTSCF GRID7 NOFINALGRID
GRIDX9 NOFINALGRIDX
! LargePrint PrintBasis
%method
ScalHFX = 0.38
end
%scf
MaxIter 500
end
%pal nprocs 1
end
%maxcore 4500
%eprnmr
    gtensor 1
    ori -3
    printlevel 3
end
%tddft
nroots 15
maxdim 5
end
* xyzfile -2 2 /path/input.xyz
```

Representative ORCA input file for frequency calculation:

```
! UKS B3LYP RIJCOSX FREQ def2-TZVP def2/J TIGHTSCF GRID7 NOFINALGRID GRIDX9
NOFINALGRIDX
! SlowConv
%method
ScalHFX = 0.38
Z_solver DIIS
Z_MaxIter 200
Z_shift 0.3
end
%scf
MaxIter 500
end
%pal nprocs 1
end
%maxcore 9000

*xyzfile -2 2 /path/input.xyz
```

References

- (1) Neese, F. The ORCA Program System. *Wiley Interdisciplinary Reviews: Computational Molecular Science* **2012**, 2 (1), 73–78. <https://doi.org/10.1002/wcms.81>.
- (2) Becke, A. D. A New Mixing of Hartree–Fock and Local Density-functional Theories. *J. Chem. Phys.* **1993**, 98 (2), 1372–1377. <https://doi.org/10.1063/1.464304>.
- (3) Lee, C.; Yang, W.; Parr, R. G. Development of the Colle-Salvetti Correlation-Energy Formula into a Functional of the Electron Density. *Phys. Rev. B* **1988**, 37 (2), 785–789. <https://doi.org/10.1103/PhysRevB.37.785>.
- (4) Vosko, S. H.; Wilk, L.; Nusair, M. Accurate Spin-Dependent Electron Liquid Correlation Energies for Local Spin Density Calculations: A Critical Analysis. *Can. J. Phys.* **1980**, 58 (8), 1200–1211. <https://doi.org/10.1139/p80-159>.
- (5) Stephens, P. J.; Devlin, F. J.; Chabalowski, C. F.; Frisch, M. J. Ab Initio Calculation of Vibrational Absorption and Circular Dichroism Spectra Using Density Functional Force Fields. *J. Phys. Chem.* **1994**, 98 (45), 11623–11627. <https://doi.org/10.1021/j100096a001>.
- (6) Szilagy, R. K.; Metz, M.; Solomon, E. I. Spectroscopic Calibration of Modern Density Functional Methods Using $[\text{CuCl}_4]^{2-}$. *J. Phys. Chem. A* **2002**, 106 (12), 2994–3007. <https://doi.org/10.1021/jp014121c>.
- (7) Weigend, F.; Furche, F.; Ahlrichs, R. Gaussian Basis Sets of Quadruple Zeta Valence Quality for Atoms H–Kr. *J. Chem. Phys.* **2003**, 119 (24), 12753–12762. <https://doi.org/10.1063/1.1627293>.
- (8) Weigend, F. Accurate Coulomb-Fitting Basis Sets for H to Rn. *Phys. Chem. Chem. Phys.* **2006**, 8 (9), 1057–1065. <https://doi.org/10.1039/B515623H>.
- (9) Harlow, R. L.; Wells, W. J.; Watt, G. W.; Simonsen, S. H. Crystal Structures of the Green and Yellow Thermochromic Modifications of Bis(N-Methylphenethylammonium) Tetrachlorocuprate (II). Discrete Square-Planar and Flattened Tetrahedral Tetrachlorocuprate(2-)Anions. *Inorg. Chem.* **1974**, 13 (9), 2106–2111. <https://doi.org/10.1021/ic50139a012>.
- (10) McGinney, J. A. Cesium Tetrachlorocuprate. Structure, Crystal Forces, and Charge Distribution. *J. Am. Chem. Soc.* **1972**, 94 (24), 8406–8413. <https://doi.org/10.1021/ja00779a020>.
- (11) Noll, A.; Rabe, S.; Müller, U. Die Oxochlorovanadate $\text{PPh}_4[\text{VOCl}_3\text{OH}]$, $\text{PPh}_4[\text{VOCl}_4]$, $(\text{PPh}_4)_2[\text{VOCl}_4]\cdot 2\text{CH}_3\text{CN}$ Und $(\text{PPh}_4)_2[\text{VOCl}_4]\cdot \text{CH}_3\text{CN}$ Mit Auffälligen Abweichungen von Der Quadratisch-Pyramidalen Anionenstruktur / The Oxochlorovanadates $\text{PPh}_4[\text{VOCl}_3\text{OH}]$, $\text{PPh}_4[\text{VOCl}_4]$, $(\text{PPh}_4)_2[\text{VOCl}_4]\cdot 2\text{CH}_3\text{CN}$ and $(\text{PPh}_4)_2[\text{VOCl}_4]\cdot \text{CH}_3\text{CN}$ with Remarkable Deviations from the Square-Pyramidal Anion Structure. *Zeitschrift für Naturforschung B* **1999**, 54 (5), 591–596. <https://doi.org/10.1515/znb-1999-0504>.
- (12) Konarev, D. V.; Kuzmin, A. V.; Faraonov, M. A.; Ishikawa, M.; Khasanov, S. S.; Nakano, Y.; Otsuka, A.; Yamochi, H.; Saito, G.; Lyubovskaya, R. N. Synthesis, Structures, and Properties of Crystalline Salts with Radical Anions of Metal-Containing and Metal-Free Phthalocyanines. *Chemistry – A European Journal* **2015**, 21 (3), 1014–1028. <https://doi.org/10.1002/chem.201404925>.

- (13) Wansapura, C. M.; Juyoung, C.; Simpson, J. L.; Szymanski, D.; Eaton, G. R.; Eaton, S. S.; Fox, S. From Planar Toward Tetrahedral Copper(II) Complexes: Structural and Electron Paramagnetic Resonance Studies of Substituent Steric Effects in an Extended Class of Pyrrolate-Imine Ligands. *Journal of Coordination Chemistry* **2003**, *56* (11), 975–993. <https://doi.org/10.1080/00958970310001607752>.
- (14) Atzori, M.; Benci, S.; Morra, E.; Tesi, L.; Chiesa, M.; Torre, R.; Sorace, L.; Sessoli, R. Structural Effects on the Spin Dynamics of Potential Molecular Qubits. *Inorg. Chem.* **2018**, *57* (2), 731–740. <https://doi.org/10.1021/acs.inorgchem.7b02616>.
- (15) Dodge, R. P.; Templeton, D. H.; Zalkin, A. Crystal Structure of Vanadyl Bisacetylacetonate. Geometry of Vanadium in Fivefold Coordination. *J. Chem. Phys.* **1961**, *35* (1), 55–67. <https://doi.org/10.1063/1.1731933>.
- (16) Cassidy, P.; Hitchman, M. A. Molecular g Values of the Planar Tetrachlorocuprate(2-) Ion. *Inorg. Chem.* **1977**, *16* (6), 1568–1570. <https://doi.org/10.1021/ic50172a067>.
- (17) Escalera-Moreno, L.; Suaud, N.; Gaita-Ariño, A.; Coronado, E. Determining Key Local Vibrations in the Relaxation of Molecular Spin Qubits and Single-Molecule Magnets. *J. Phys. Chem. Lett.* **2017**, *8* (7), 1695–1700. <https://doi.org/10.1021/acs.jpcclett.7b00479>.

Part 2: The Impact of Ligand Field Symmetry on Molecular Qubit Coherence

Abstract

Developing quantum bits (qubits) exhibiting room temperature electron spin coherence is a key goal of molecular quantum information science. At high temperatures, coherence is often limited by electron spin relaxation, measured by T_1 . Here we develop a simple and powerful model for predicting relative T_1 relaxation times in transition metal complexes from dynamic ligand field principles. By considering the excited state origins of ground state spin-phonon coupling, we derive group theory selection rules governing which vibrational symmetries can induce decoherence. Thermal weighting of the coupling terms produces surprisingly good predictions of experimental T_1 trends as a function of temperature and explains previously confounding features in spin-lattice relaxation data. We use this model to evaluate experimental relaxation rates across $S = \frac{1}{2}$ transition metal qubit candidates with diverse structures, gaining new insights into the interplay between spin-phonon coupling and molecular symmetry. This methodology elucidates the specific vibrational modes giving rise to decoherence, providing insight into the origin of room temperature coherence in transition metal complexes. We discuss the outlook of symmetry-based modeling and design strategies for understanding molecular coherence.

2-2.1. Introduction

The use of paramagnetic transition metal complexes as molecular electron spin quantum bits (qubits) has generated considerable interest over the past decade (Figure 2-2.1A).¹⁻⁶ When placed into a magnetic field, the Zeeman effect splits the energies of the M_S sublevels into a quantum two-level system that can be leveraged for applications in computing, sensing, and communication (Figure 2-2.1B).^{2,7} Among these, molecular quantum sensing constitutes a particularly exciting application,² as molecular electron spin qubits can be synthetically tuned and located in a targeted fashion within chemical microenvironments and interfaces to read out properties of relevance in areas such as catalysis and medicine. The microenvironments of interest often exist under ambient conditions.

Thus, developing molecular qubits that operate at room temperature remains a key goal in the field.^{1,8,9}

The utility of molecular electron spin qubits is limited by the phase memory time T_M , which describes how long phase relations are retained between members of the ensemble.¹⁰ As temperature increases in spin-dilute environments, T_M becomes limited by T_1 , the spin-lattice relaxation time. T_1 describes how quickly spin energy is transferred to the vibrational bath.¹¹ In solid lattices, this process is controlled by spin-phonon coupling.¹² Three mechanisms for spin-phonon coupling deteriorate the performance of molecular qubits at room temperature, known as the direct, Raman, and Orbach processes (Figure 2-2.1B).^{10,13,14} The direct process dissipates spin energy through acoustic phonon emission and exerts the greatest contribution at low temperatures (e.g., < 10 K).¹⁵ The Raman process dissipates spin energy through inelastic scattering of phonons from a virtual state, with acoustic phonons contributing at intermediate temperatures and optical phonons (i.e., local modes⁶) dominating at elevated temperatures near ambient conditions.^{12,16} In $S = 1/2$ systems, the Orbach mechanism generally does not contribute strongly.¹⁶ Room temperature coherence lifetimes of molecular electron spin qubits are controlled by spin-phonon coupling with the molecular vibrational modes.^{4,17}

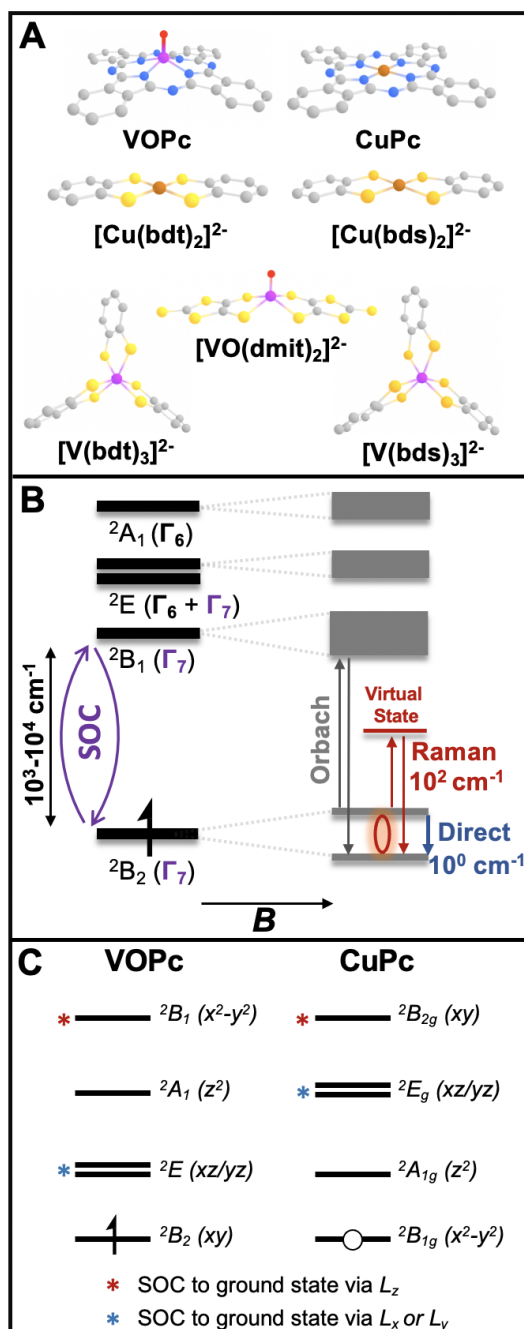


Figure 2-2.1. Overview of molecular electron spin qubits. (A) V(IV) and Cu(II) qubits considered in this study.^{8,9,18,19} VOPc = vanadyl phthalocyanine; CuPc = copper phthalocyanine; $[\text{Cu}(\text{bdt})_2]^{2-}$ = copper bis(1,2-benzenedithiolate); $[\text{Cu}(\text{bds})_2]^{2-}$ = copper bis(1,2-benzenediselenate); $[\text{VO}(\text{dmit})_2]^{2-}$ = vanadyl bis(1,3-dithiole-2-thione-4,5-dithiolate); $[\text{V}(\text{bdt})_3]^{2-}$ = vanadium tris(1,2-benzenedithiolate); $[\text{V}(\text{bds})_3]^{2-}$ = vanadium tris(1,2-benzenediselenate); (B) Electronic structure and

relaxation mechanisms of molecular qubits. (Left) Electronic states (example: VOPc) in single-valued point groups and double groups (Bethe notation) inclusive of spin-orbit coupling. Charge-transfer states not shown. (Right) T_1 relaxation mechanisms. Atomic color scheme: C (grey), N (blue), O (red), S (yellow), Se (orange), Cu (brown), V (pink). H atoms not shown for clarity. (C) Qualitative crystal field state diagrams for VOPc and CuPc (hole formalism). Excited states with red (blue) asterisks spin-orbit couple to the corresponding ground states through L_z (L_x or L_y) angular momentum operators.

A natural question arises: which vibrational modes exhibit the strongest spin-phonon coupling? Vibrational modes higher in energy than about 400 cm^{-1} are not expected to contribute significantly to spin-lattice relaxation, as the Raman process requires thermal population of an existing phonon mode (see Supporting Information, Section 4).¹⁰ While the phonon density of states and dispersion relation below 400 cm^{-1} can be probed using terahertz spectroscopy²⁰ and four-dimensional inelastic neutron scattering,²¹ ascertaining the spin-phonon coupling of those modes remains an outstanding experimental challenge. In lieu of experimental evidence, several studies have sought to assign the most impactful spin-phonon coupling modes through computational studies.^{17,22–24} There exists an emerging recognition of the importance of the symmetry of the vibrational mode, with recent studies empirically concluding that *gerade* modes exhibit heightened spin-phonon coupling over *ungerade* modes for square planar compounds.^{22,24} However, no general theory yet exists for predicting which vibrational symmetries exert the greatest spin-phonon coupling and modeling the implications for temperature-dependent T_1 . This hinders rational molecular design and constitutes an important challenge in the field.⁶

Here we derive group theory selection rules for determining vibrational modes that are active for spin-phonon coupling. We show that the coupling modes are those that are group theoretically allowed to undergo ligand field excited state distortions. These vibrational modes dynamically change the amount of ground state orbital angular momentum. We then show that a simple thermal weighting of molecular spin-phonon coupling coefficients furnishes very good agreement with relative trends in experimental spin-lattice relaxation rates, thus describing how different vibrations dominate T_1 over different temperature regimes. The resulting model predicts relative spin relaxation times (T_1), or phonon-limited coherence times (T_M) at high temperatures.

2-2.2. Ligand Field Paradigm for Electron Spin Relaxation

2-2.2.1. Symmetry effects on spin-phonon coupling. Spin-phonon coupling arises when some portion of the spin Hamiltonian is modulated by a vibrational mode.^{6,25} The g tensor, \mathbf{g} , describing the Zeeman effect has been implicated as a major source of spin-phonon coupling in molecular qubits.^{15,24} Therefore, to understand the impact of symmetry on spin-phonon coupling, we first turn to the molecular origins of the g values in a transition metal complex.

A free electron has an isotropic g value of $g_e = 2.0023$ owing to its intrinsic spin angular momentum; deviations from this value arise when the electron additionally possesses ground state orbital angular momentum, as quantified by the Landé formula. While the presence of a ligand field quenches orbital angular momentum in tetragonal transition metal complexes, spin-orbit coupling with ligand field excited states reintroduces orbital angular momentum into the ground state. Thus, changes in the g value arise from changes in spin-orbit coupling. In order for the i_{th} vibrational mode to have a nonzero first-order spin-phonon coupling coefficient, $\partial \mathbf{g} / \partial Q_i$, the magnitude of spin-orbit coupling must therefore change as a function of the vibrational mode coordinate Q_i . The expression for the g value of a transition metal complex due to the spin-orbit perturbation is given by²⁶

$$g_i = g_e - 2\lambda \sum_{e \neq g} \frac{\langle \Psi_g | \hat{L}_i | \Psi_e \rangle \langle \Psi_e | \hat{L}_i | \Psi_g \rangle}{E_e - E_g} \quad (2.2-1)$$

where λ is the many-electron spin-orbit coupling constant, Ψ_g and Ψ_e are the ground and excited states with energies E_g and E_e , respectively, \hat{L}_i is an orbital angular momentum operator, and $i = x, y, z$ refer to the g tensor principal axes and the molecular quantization frame, which are aligned for the tetragonal qubits considered in this work. Equation 1 shows that the g values have a sensitive dependence on the energy gap between the ground and excited states involved in the spin-orbit coupling. (The precise excited states involved can be determined from double groups (Figure 2-2.1B) using Tables 2-2.S13 and 2-2.S14 and tables of d orbital rotations.^{6,27}) If the ground and excited state potential energy surfaces reach a minimum at the same value of the vibrational coordinate Q_i ,

then the energy gap $E_e - E_g$ can at most vary quadratically as a function of Q_i , implying $\partial g / \partial Q_i = 0$ at equilibrium (Figure 2-2.2A). However, if the equilibrium geometry of the excited state is different than that of the ground state equilibrium geometry along Q_i , the energy gap $E_e - E_g$ can vary linearly as a function of Q_i and give rise to $(\partial g / \partial Q_i)_0 \neq 0$ (Figure 2-2.2B). We refer to such modes as the distorting modes.²⁷ The first-order coupling coefficient at equilibrium, $(\partial g / \partial Q_i)_0$ (hereafter simply $\partial g / \partial Q_i$), is predicted to exert the leading influence on spin-lattice relaxation times.^{15,24} Therefore, the most important vibrational modes for spin-phonon coupling are precisely these distorting modes.²²

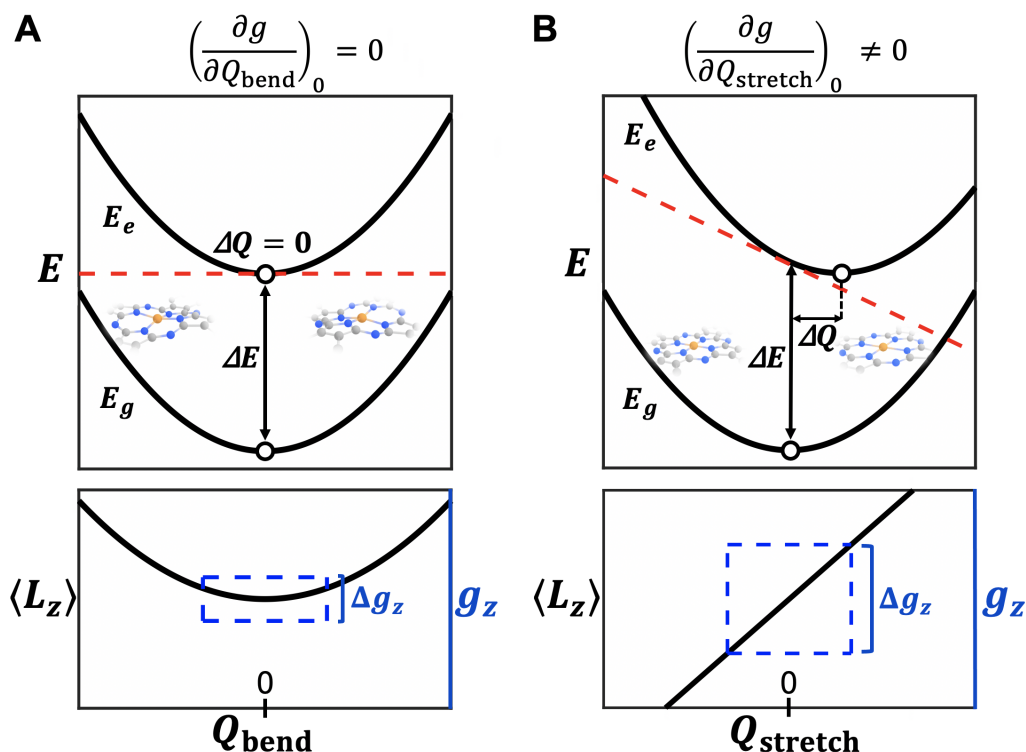


Figure 2-2.2. The excited state origins of ground state spin-phonon coupling. (A) Schematic potential energy surfaces for the b_{2u} bending mode in CuPc. The ground and excited state potential energy minima coincide, implying no excited state distortion and thus no linear spin-phonon coupling. (B) Schematic potential energy surfaces for the a_{1g} symmetric stretch in CuPc. The ground and excited state minima are offset, implying excited state distortion and linear ground state spin-phonon coupling.

Crucially, the excited state distortion can be expressed through a matrix element²⁷ involving vibrational perturbations of the ligand field Hamiltonian (H_{LF}):

$$\Delta Q_i = - \frac{\left\langle \psi_{elec}^e \left| \left(\frac{\partial H_{LF}}{\partial Q_i} \right)_0 \right| \psi_{elec}^e \right\rangle}{k_i} \quad (2-2.2)$$

Here ΔQ_i gives the excited state distortion along the vibrational mode Q_i , k_i is the force constant, and ψ_{elec}^e is the excited state wave function that spin-orbit couples into the ground state. The matrix element is evaluated at the ground state equilibrium geometry. The key utility of this expression lies in the application of group theory symmetry selection rules to the integral. The state symmetry of ψ_{elec}^e and Q_i (Γ_{elec} and Γ_{Q_i} , respectively) can be assigned through textbook techniques.²⁸ The ligand field Hamiltonian always has the totally symmetric irreducible representation in the molecular point group, so the derivative has the symmetry Γ_{Q_i} . Therefore, the symmetry of the integrand is given²⁷ by a direct triple product. For the integral to be nonzero, Equation 3a must contain the totally symmetric irreducible representation:

$$(\Gamma_{elec} \times \Gamma_{Q_i} \times \Gamma_{elec}) = a_1 + \dots \quad (2-2.3a)$$

Here a_1 in Equation 2-2.3a signifies the totally symmetric representation in the desired point group, and the excited state is group theoretically allowed to undergo distortion when the condition in Equation 3b is met:

$$[\Gamma_{elec} \times \Gamma_{elec}] = \Gamma_{Q_i} \quad (2-2.3b)$$

The square brackets in Equation 2-2.3b denote the symmetric direct product operation, appropriate for the product of Γ_{elec} with itself, and Γ_{Q_i} represents all mode symmetries that are allowed to

couple.^{27,29,30} This selection rule enables facile calculation of which vibrational symmetries will be able to exhibit linear spin-phonon coupling terms for a given coordination geometry and electronic structure. The coupling modes are those that are group theoretically allowed to undergo ligand field excited state distortions. For nondegenerate states, only the totally symmetric modes will couple, while other non-totally symmetric modes can couple for degenerate excited states. We note that this consideration is a more general basis for understanding forces in molecules (i.e., the Hellmann-Feynman force³¹), including those of relevance for transition metal photophysics^{32,33} and those predicted by the Jahn-Teller theorem to give rise to the instability of orbitally degenerate states.²⁹

To illustrate the power of this approach in understanding spin-phonon coupling contributions to decoherence in molecular qubits, we turn to a comparison between vanadyl phthalocyanine (VOPc) and copper phthalocyanine (CuPc) (Figure 2-2.1A).¹⁹ VOPc belongs to the non-centrosymmetric point group C_{4v} , while CuPc belongs to the centrosymmetric point group D_{4h} . The electronic ground state of VOPc has the state symbol 2B_2 (d_{xy}), which spin-orbit couples with the 2B_1 ($d_{x^2-y^2}$) excited state to introduce orbital angular momentum into g_z (Figure 2-2.1C). The situation is reversed in CuPc owing to the hole formalism, with a ${}^2B_{1g}$ ($d_{x^2-y^2}$) ground state and a ${}^2B_{2g}$ (d_{xy}) excited state (Figure 2-2.1C). The relevant lowest lying excited state for g_z is nondegenerate in both cases. Because the direct product of any nondegenerate irreducible representation with itself gives the totally symmetric irreducible representation, Equation 3b reduces to $a_1 = \Gamma_{Q_i}$ for VOPc in order for $\partial g_z / \partial Q_i \neq 0$. An identical analysis holds for CuPc, where a_{1g} is the totally symmetric representation in D_{4h} . Thus, the group theory model predicts that the strongest spin-phonon coupling for g_z should arise from totally symmetric vibrational modes. Indeed, previous computational studies have observed that a_{1g} or a_1 modes exhibit large coupling coefficients,^{22,24} with D_{2d} CuCl_4^{2-} possessing more spin-phonon coupling than D_{4h} CuCl_4^{2-} owing to a greater number of totally symmetric modes.²²

Though totally symmetric vibrational modes dominate g_z coupling for both VOPc and CuPc, the change in point group between C_{4v} and D_{4h} nonetheless has important consequences for spin-phonon coupling. CuPc displays a single a_{1g} mode below 400 cm^{-1} corresponding to the totally

symmetric Cu-N stretch (Figure 2-2.3A). Owing to the reduced number of irreducible representations in the C_{4v} point group, VOPc displays five total a_1 vibrational modes below 400 cm^{-1} , encompassing mixtures of both the symmetric stretch and metal out-of-plane motion (Figure 2-2.3B). The portion of the vibrational density of states which matters for spin-phonon coupling is thus very different: CuPc possesses a lone linear coupling mode at 262 cm^{-1} , while VOPc possesses five spin-phonon active modes below 400 cm^{-1} (Table 1). Calculation of the $\partial g_z/\partial Q_i$ coefficients for CuPc and VOPc via calibrated density functional theory (DFT)³⁴ according to a previous procedure²² (see also Supporting Information, Section 1) shows that the totally symmetric vibrations have the largest coefficients by orders of magnitude, confirming the group theory analysis (Figure 2-2.3C). The coefficient for CuPc is an order of magnitude larger than those for VOPc owing to the larger spin-orbit coupling constant of Cu(II) relative to V(IV).¹⁹ For both VOPc and CuPc, only a very small portion of the vibrational density of states contributes to spin-phonon coupling for g_z (Figure 2-2.3A,B)

Table 2-2.1. Linear g_z spin-phonon coupling modes for VOPc and CuPc. All modes have the totally symmetric representation.			
VOPc		CuPc	
E (cm^{-1})	$(\partial g_z/\partial Q)^2$	E (cm^{-1})	$(\partial g_z/\partial Q)^2$
42	5.5×10^{-8}	262	2.8×10^{-5}
178	1.5×10^{-6}		
262	6.3×10^{-7}		
317	2.9×10^{-6}		
395	1.9×10^{-6}		

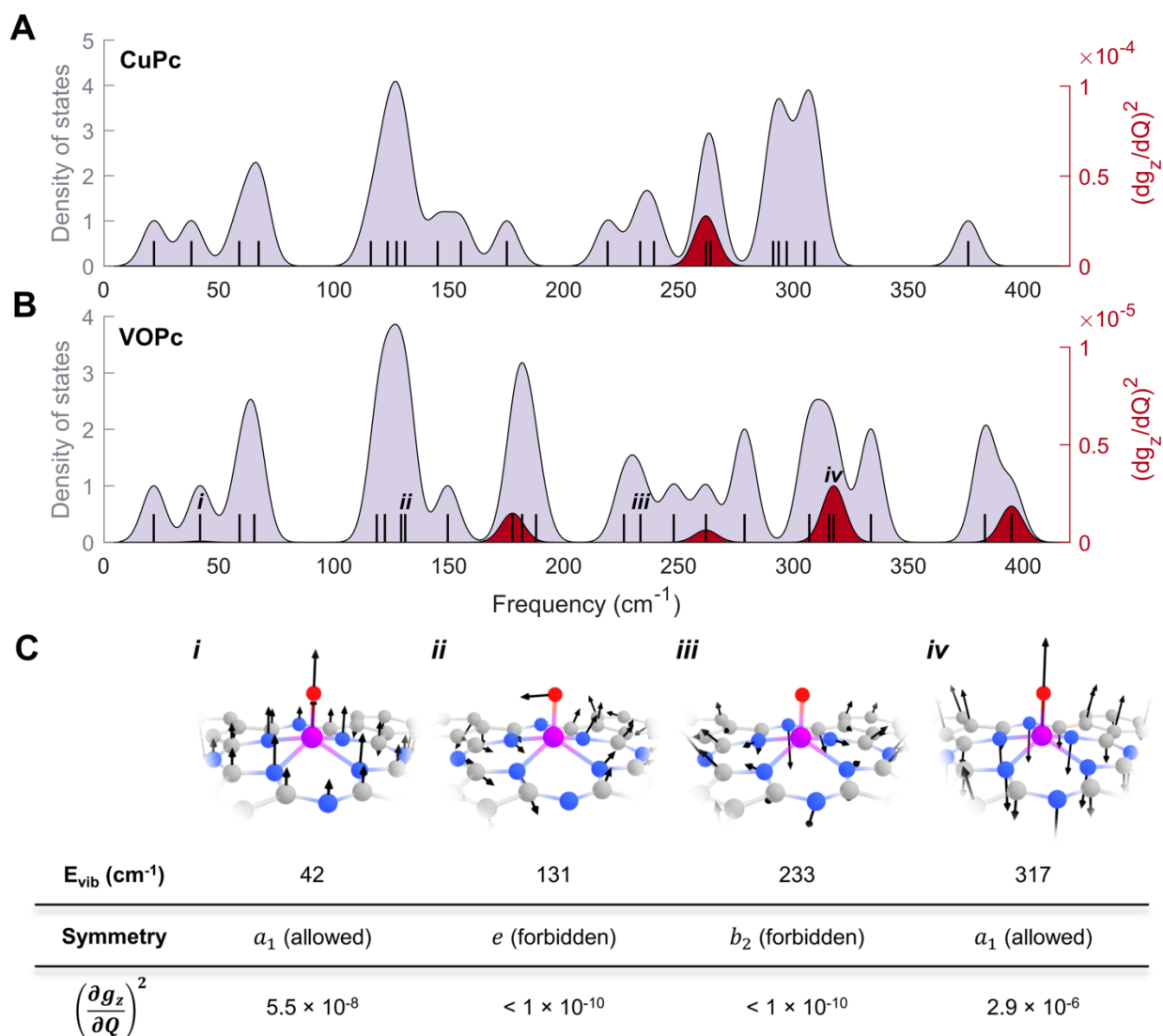


Figure 2-2.3. Impact of symmetry on spin-phonon coupling. (A) Normalized vibrational density of states (lavender, left y-axis) and spin-phonon coupling active vibrations (red, right y-axis) for CuPc. (B) Normalized vibrational density of states (lavender, left y-axis) and spin-phonon coupling active vibrations (red, right y-axis) for VOPc. (C) Analysis of selected modes for VOPc. Arrows indicate atomic displacements; additional pictures are provided in Tables 2-2.S3-2-2.S7. Symmetry selection rules are evaluated for the 2B_1 ($d_{x^2-y^2}$) excited state (g_z spin-phonon coupling) via Equation 2-2.3b. 1×10^{-10} constitutes the limit of numerical precision.

A similar analysis can be performed for $\partial g_x/\partial Q_i$. For both VOPc and CuPc, orbital angular momentum is introduced to g_x principally via spin-orbit coupling with the d_{xz}/d_{yz} excited states, which are orbitally doubly degenerate and have the representations 2E in C_{4v} and 2E_g in D_{4h} (Figure 2-2.1C). Evaluation of Equation 2-2.3b for VOPc now yields $(a_1 + b_1 + b_2) = \Gamma_{Q_i}$, showing that a_1 , b_1 , and b_2 vibrational modes are able to have $\partial g_x/\partial Q_i \neq 0$ by symmetry. (a_2 is produced by the antisymmetric direct product and is therefore discarded.)³⁰ Similarly, Equation 2-2.3b for CuPc yields $(a_{1g} + b_{1g} + b_{2g}) = \Gamma_{Q_i}$, showing that multiple nondegenerate *gerade* modes are able to couple for g_x . Note that the *gerade* selection rule would hold true even if the electronic state symmetry were *ungerade*, because Equation 2-2.3b contains the electronic symmetry twice. While group theory states which modes are allowed to couple by symmetry, as with any selection rule, this does not guarantee a large nonzero coefficient.²⁷

Comparison between the coupling modes for CuPc and $[\text{Cu}(\text{bdt})_2]^{2-}$ (bdt = 1,2-benzenedithiolate) illustrates the impact of descending in symmetry from D_{4h} to D_{2h} (Figure 2-2.4). Lower than 400 cm^{-1} , CuPc displays a single active mode with $\partial g_z/\partial Q_i$, the a_{1g} symmetric stretch. Two modes for CuPc display nonzero $\partial g_x/\partial Q_i$, including both the a_{1g} symmetric stretch and the b_{1g} antisymmetric stretching mode. The presence of the linearly coupling b_{1g} mode is enabled by the degeneracy of the 2E_g electronic state (Figure 2-2.1C). However, no degenerate irreducible representations exist in the D_{2h} point group, so the d_{xz} and d_{yz} orbitals are split into the B_{2g} and B_{3g} representations. All electronic states implicated in the g_x and g_y spin-phonon coupling are nondegenerate for $[\text{Cu}(\text{bdt})_2]^{2-}$, implying that only totally symmetric a_g vibrational modes will display linear coupling for all three canonical orientations. Indeed, examination of the spin-phonon coupling coefficients for $[\text{Cu}(\text{bdt})_2]^{2-}$ shows that the most prominent coupling modes are the same for both $\partial g_z/\partial Q_i$ and $\partial g_x/\partial Q_i$ and possess a_g symmetry as predicted (Figure 2-2.4). The coupling b_{1g} mode from CuPc correlates to a b_{1g} mode in $[\text{Cu}(\text{bdt})_2]^{2-}$, implying that the linear coupling of this antisymmetric stretch mode has been turned off by the descent in symmetry. Conversely, the b_{2g} in-plane scissoring mode in CuPc correlates to a_g symmetry for $[\text{Cu}(\text{bdt})_2]^{2-}$ and is activated for g_z coupling. Thus, descent in symmetry from D_{4h} to D_{2h} retains the total number of linear coupling

modes for g_x , but changes the identity of those modes (Figure 2-2.4). Similar behavior is observed for the C_{2v} qubit $[\text{VO}(\text{dmit})_2]^{2-}$, with many a_1 modes exhibiting coupling for both g_x and g_z . Global molecular symmetry can impact the spin-phonon coupling modes even for apparently similar coordination geometries, a surprising result elucidated by group theory. This result establishes control of degenerate electronic excited states as an important design consideration for controlling activation of spin-phonon coupling vibrational modes.

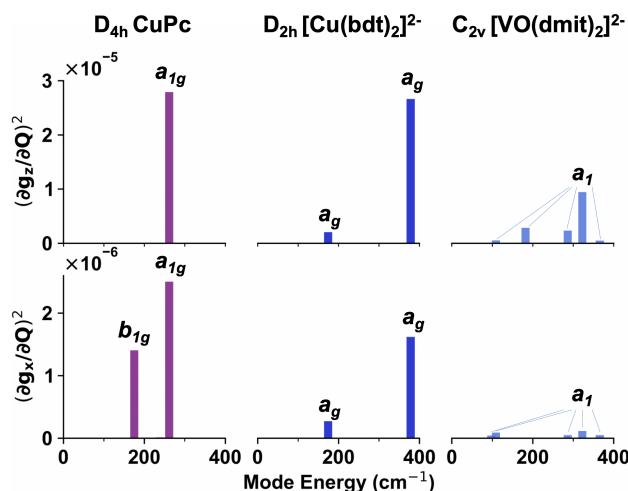


Figure 2-2.4. Orientation-dependent spin-phonon coupling coefficients for CuPc, $[\text{Cu}(\text{bdt})_2]^{2-}$, and $[\text{VO}(\text{dmit})_2]^{2-}$.

A previous study of two D_{4h} Cu(II) complexes empirically concluded that *gerade* modes exhibited the strongest coupling.²⁴ Our work differs in two important ways. First, the present approach provides a predictive group theory analysis not dependent on a centrosymmetric point group. In addition to the C_{nv} point groups considered in this work, this will also enable extension of spin-phonon coupling symmetry analysis to qubits with trigonal coordination environments.^{35,36} By analogy to *gerade/ungerade*, point groups containing the prime/double prime representations should see coupling only from the single-prime vibrational modes, as the double direct product of the electronic excited state in Equation 3b will yield a single-prime representation irrespective of the electronic representation, and the totally symmetric representation will always have a single-prime value. Furthermore, evaluation of Equation 3b for the D_{4h} point group reveals that the a_{2g} mode is

not predicted to exhibit linear coupling despite possessing *gerade* symmetry. This prediction is in agreement both with previous calculations²⁴ and our own.

Second, a point of variance with the previous study²⁴ arises over the role of the degenerate e_g vibrations, which are found to couple in that study, but not predicted to couple by the present group theory analysis. This is because the present analysis has considered the spin-phonon coupling coefficients corresponding to the canonical orientations of the g tensor; namely, g_x , g_y , and g_z . By contrast, Santanni et al. averaged all nine $\partial \mathbf{g} / \partial Q$ values for the non-diagonalized g tensor.²⁴ Nonzero off-diagonal derivatives correspond to dynamic rotation of the principal axes of the g tensor. Indeed, the R_x and R_y rotation operators transform as E_g in D_{4h} , and pictures of the e_g vibrational modes show that the first coordination sphere undergoes a rigid rotation out of the xy -plane (Table 2-2.S5). A minimal square-planar coordination environment such as D_{4h} CuCl_4^{2-} does not possess e_g normal modes,²² as these would correspond to pure rotational degrees of freedom. In CuPc , however, counterrotation of the phthalocyanine ligand framework enables e_g normal modes. As local rotation does not affect bonding in the first coordination sphere, e_g vibrational modes do not dynamically alter g_x , g_y , and g_z , in accordance with our group theory predictions. Similarly, the non-coupling a_{2g} modes transform as R_z .

Our choice to consider only the canonical g tensor derivatives ($\partial g_x / \partial Q$, $\partial g_y / \partial Q$, and $\partial g_z / \partial Q$) is supported by two independent lines of experimental evidence: orientation-dependent T_1 trends and temperature-dependent T_1 trends. Modes with canonical versus off-diagonal g tensor derivatives are predicted to have distinct patterns of orientation dependence. As shown in Figure 2-2.S18, modes with canonical g tensor derivatives are predicted to exhibit maximum and minimum coupling for molecules aligned along the principal tensor axes. By contrast, off-diagonal modes are predicted to exhibit maximum coupling at intermediate field positions in-between the canonical orientations. This provides an experimental test for whether canonical or off-diagonal modes dominate the observed T_1 behavior. Across a variety of systems, including D_{4h} Cu(II) coordination complexes,³⁷ C_{4v} nitridochromium(V) and oxochromium(V) complexes,^{38,39} and organic nitroxide spin labels,⁴⁰ the minimum and maximum values of T_1 are found to coincide with the canonical

orientations of the g tensor. These measurements encompass a range of temperatures from 50-130 K.⁴⁰ This experimental fact demonstrates that T_1 spin-lattice relaxation is driven not by rotational modes modulating the g tensor orientation, but by modes modulating the g_z and g_x , g_y principal values.^{37,38,40} Corroborating this, we obtain superior predictions of experimental temperature-dependent T_1 times by including only the on-diagonal elements (*vide infra*). We note that T_M often reaches minimum experimental values at intermediate-field positions and maximum values at canonical orientations of the g tensor.³⁸ This phenomenon is ascribed to the impact of librations in the context of glassy frozen solution measurements,³⁸ but the e_g modes in CuPc induce the same type of rotational motion. This evidence indicates that rotational modes can impact T_M , but do not generally dominate T_1 .

2-2.2.2. Thermally-weighted ligand field model of T_1 . Once the $\partial g/\partial Q$ values for molecular vibrations have been calculated,²² relative T_1 times can be predicted using a simplified model of the Raman spin-lattice relaxation process in molecular solids. A simple functional form for attributing Raman relaxation to molecular vibrations has been proposed on the basis of the two-phonon Green's function¹² and used to fit experimental T_1 data.^{24,41} We now employ this form to make comparative T_1 predictions informed by the preceding symmetry analysis:

$$\frac{1}{T_1} = A \sum_{i=1}^{3N-6} \left(\frac{\partial g}{\partial Q_i} \right)^2 \frac{\exp[E_i/k_B T]}{(\exp[E_i/k_B T] - 1)^2} \quad (2-2.4)$$

Here E_i is the energy of the lattice vibration, k_B is the Boltzmann constant, T is the lattice temperature, A is a proportionality constant to be determined by scaling to experimental data (Supporting Information, Section 2.2.5), and the sum is over all normal modes of vibration. A single scaling factor A is chosen for all molecules in each comparative T_1 prediction, ensuring that the relative T_1 ratios are unaltered by the scaling process. Modes without a first-derivative coupling term (Figure 2-2.2A) do not contribute to the sum. Owing to the exponentially vanishing thermal weighting factor, it is sufficient to consider only modes below 400 cm^{-1} . The prediction error due to

this cutoff is estimated to be no greater than 5-10% at 300 K for the complexes considered (Figure 2-2.S19), which has a negligible effect for a logarithmic scale. Here we present rate predictions using $\partial g_z / \partial Q_i$, while predictions using other elements of the Zeeman tensor are discussed in the Supporting Information Section 2-2.3 (Figures 2-2.S11-2-2.S17). Equations 3 and 4 together provide an analytical link between molecular vibrations and temperature dependent electron spin relaxation rates.

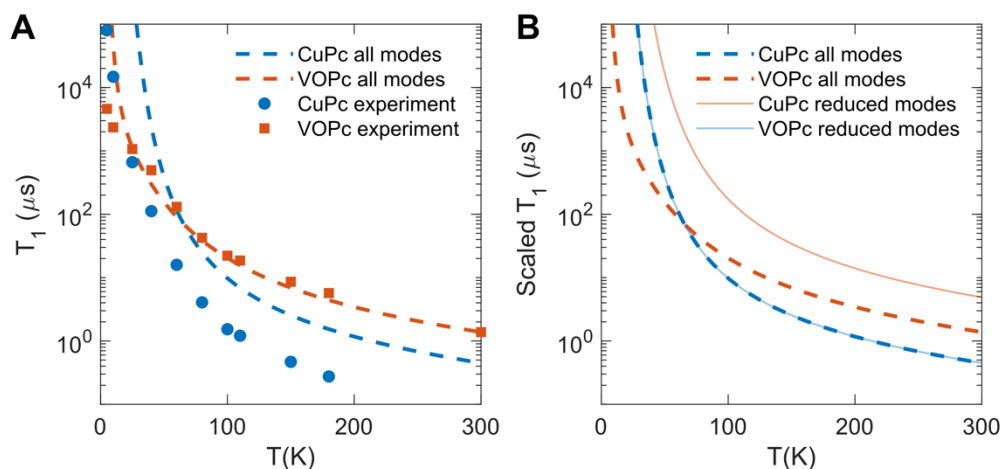


Figure 2-2.5. Thermally-weighted ligand field model for phthalocyanine qubits. (A) Comparison of T_1 model predictions (dashed lines) to experimental results from ref¹⁹ (solid circles and squares). (B) Comparison of T_1 model predictions employing all modes with T_1 model predictions using a reduced subset of the vibrational modes. Dashed lines: all spin-phonon active modes. Solid lines: only the two strongest modes at 317 cm^{-1} and 395 cm^{-1} for VOPc and the single strongest mode at 262 cm^{-1} for CuPc. All T_1 predictions are scaled by the same factor $A = 1.32 \times 10^5\ \mu\text{s}^{-1}$, chosen so the VOPc all-modes prediction matches the experimental data at 300 K.

Figure 2-2.5A shows the predicted temperature-dependent T_1 times for VOPc and CuPc, which are in good agreement with our previously obtained experimental data¹⁹ considering the simplicity of the model employed. Equation 2-2.4 correctly predicts that VOPc has a longer T_1 than CuPc at room temperature. Furthermore, Equation 2-2.4 correctly predicts the existence of a T_1 crossover point at lower temperatures, below which CuPc displays the longer T_1 time. Though observed in multiple systems in the molecular qubit literature,^{9,19} such crossover features have lacked

a clear interpretation and have been attributed to variations in the Raman exponent under a Debye model treatment or local mode terms.^{16,42,43}

We now show this phenomenon has a direct chemical interpretation in terms of molecular vibrations. As given in Table 2-2.1, VOPc possesses five linear coupling modes, while CuPc possesses only one. However, the magnitude of the spin-phonon coupling coefficient is significantly larger for the CuPc mode than for any of the VOPc modes, a fact explained by the difference in spin-orbit coupling coefficients between the two metals.^{19,22} Additionally, the lone CuPc mode sits higher in energy than three of the five VOPc modes. Thus, at the lowest temperatures modeled, the symmetric stretch of CuPc has negligible thermal population and minimal spin-phonon coupling. By contrast, VOPc possesses coupling modes as low as 42 cm⁻¹ (Figure 2-2.3, Table 2-2.1), which are thermally populated at low temperature and contribute to VOPc having a shorter T_1 than CuPc. As the temperature increases, higher energy vibrational modes of both VOPc and CuPc become thermally populated, but the spin-phonon coupling coefficient is largest for the CuPc symmetric stretch. This manifests in a larger T_1 slope for CuPc versus VOPc. When all modes are populated near room temperature, the larger $\partial g_z/\partial Q_i$ of CuPc takes over, and VOPc has the longer coherence time at room temperature. The high and low temperature behavior of T_1 thus relate to the magnitude of $\partial g_z/\partial Q_i$ and the relative energy of the coupling vibrational modes, respectively. For these two molecules, ligand field symmetry is most important for a longer T_1 at low temperatures, while chemical bonding properties^{6,19,22} contribute more strongly to a longer T_1 at high temperatures. The precise nature of this interplay will vary depending on the molecules analyzed.

The experimental T_1 crossover point is around 20K, while the modeled crossover point is around 65K (Figure 2-2.5, Table 2-2.S2). If $\partial g_x/\partial Q_i$ derivatives are used instead of $\partial g_z/\partial Q_i$, the modeled crossover point is around 35K. Thus, part of the uncertainty in the T_1 crossover temperature may arise from the choice of principal tensor derivative. Development of a model for anisotropic T_1 is called for to address this uncertainty. We note that the precise location of the crossover point likely also contains contributions from varying efficiencies of the direct process and Raman process operating on acoustic phonons. This may relate to effective acoustic phonon symmetry in the 1:1000 magnetic dilution data modeled here, as the 42 cm⁻¹ linear coupling mode in VOPc contains

displacements similar to an acoustic phonon (Figure 2-2.3C), and it has been suggested that acoustic phonons acquire spin-phonon coupling intensity through avoided crossings with low-lying optical phonons.²¹

The crossover behavior predicted in the model can be unambiguously assigned to the low-energy a_1 modes of VOPc by artificially manipulating the number of modes in the model. If only the two strongest-coupling modes of VOPc are considered (317 cm^{-1} and 395 cm^{-1}), no crossover is observed (solid orange line, Figure 2-2.5B). Indeed a crossover is barely observed upon simply deleting the a_1 mode at 42 cm^{-1} , indicating that low energy molecular vibrations produced by reduced symmetry can exert a large influence on the temperature-dependent T_1 times even when their spin-phonon coupling coefficients are small. The overall good agreement lends credence to the general use of this model to *a priori* predict the observation of room temperature coherence in any transition metal complex. Note that when modes of e_g and e symmetry (local rotations, *vide supra*) are included in the model through off-diagonal g tensor derivatives, they dominate the T_1 behavior for CuPc through thermal population owing to their low vibrational energy.²⁴ This eliminates the predicted T_1 crossover and fails to account for the power law exponents in the intermediate-temperature regime (50 – 125K; see Figures 2-2.S11 – 2-2.S17 and discussion), further motivating our choice to use only the canonical g value derivatives.

To demonstrate the broad applicability of the thermally-weighted ligand field model, we provide T_1 predictions for $[\text{V}(\text{bdt})_3]^{2-}$, $[\text{Cu}(\text{bdt})_2]^{2-}$, $[\text{V}(\text{bds})_3]^{2-}$, and $[\text{Cu}(\text{bds})_2]^{2-}$ (bds = 1,2-benzenediselenate). Figure 2-2.6 shows the model predicts the same order of experimental high temperature T_1 times observed previously:⁹ $[\text{Cu}(\text{bdt})_2]^{2-} > [\text{Cu}(\text{bds})_2]^{2-} > [\text{V}(\text{bdt})_3]^{2-} > [\text{V}(\text{bds})_3]^{2-}$. Interestingly, the model predicts a near T_1 crossover between $[\text{Cu}(\text{bds})_2]^{2-}$ and $[\text{V}(\text{bdt})_3]^{2-}$ around 100 K, as observed experimentally at 60 K. In the high temperature regime, $[\text{Cu}(\text{bds})_2]^{2-}$ is predicted to have a shallower slope than both $[\text{V}(\text{bdt})_3]^{2-}$ and $[\text{Cu}(\text{bdt})_2]^{2-}$, but a lower intercept than $[\text{Cu}(\text{bdt})_2]^{2-}$. Substitution of selenium for sulfur decreases the $\partial g_z / \partial Q_i$ value for the $[\text{Cu}(\text{bds})_2]^{2-}$ symmetric stretch relative to $[\text{Cu}(\text{bdt})_2]^{2-}$, but also lowers the energy of that vibrational mode. The onset of symmetric stretch spin-phonon coupling thus occurs at lower temperature in $[\text{Cu}(\text{bds})_2]^{2-}$ than $[\text{V}(\text{bdt})_3]^{2-}$, but the high temperature magnitude of spin phonon coupling is greater in $[\text{V}(\text{bdt})_3]^{2-}$ than

$[\text{Cu}(\text{bds})_2]^{2-}$ owing to the larger coefficients (Tables 2-2.S8 – 2-2.S9), leading to the near T_1 crossover.

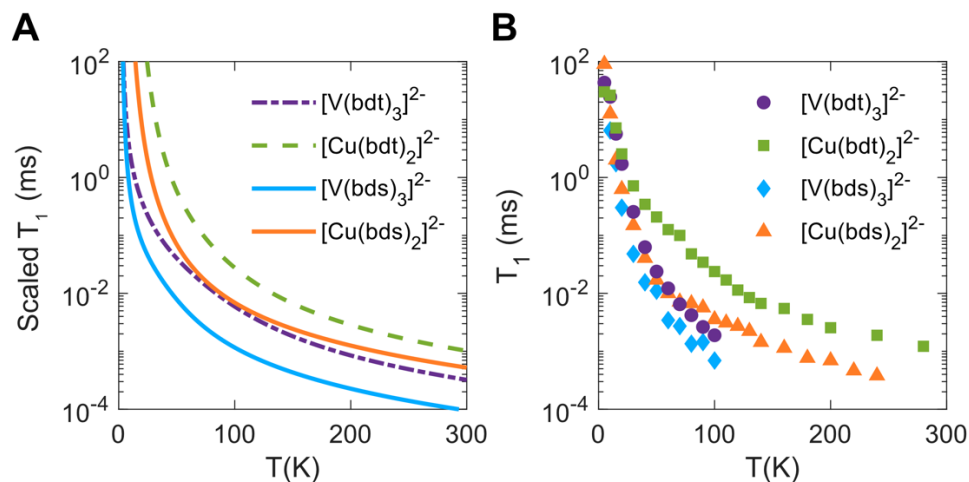


Figure 2-2.6. Thermally-weighted ligand field model for dithiolate and diselenate qubits. (A) T_1 predictions according to Equation 4. All T_1 predictions are scaled by the same factor $A = 1.01 \times 10^5 \mu\text{s}^{-1}$, chosen to match the experimental data for $[\text{Cu}(\text{bdt})_2]^{2-}$ at 280 K. (B) Comparison to experimental results from ref ⁹. Theoretical predictions and experimental results are overlaid in Figure S10.

2-2.3. Discussion

It has become commonplace to fit temperature-dependent spin-lattice relaxation data with a set of polynomial and exponential functions derived from the Debye model description of direct, Raman, Orbach, and local mode relaxation processes. These fits yield values such as the Debye frequency and the Raman exponent. However, recent literature has demonstrated that Debye model parameters have no unambiguous chemical interpretation for molecular solids, as the Debye model makes incompatible assumptions regarding the nature of crystalline vibrations.⁶ This hinders rational molecular design for quantum information science. A new molecular paradigm based on symmetry and vibrational principles is required.^{4,6,24}

We argue the present study provides a novel and attractive perspective for modeling T_1 on distinctly chemical grounds. Dynamic ligand field theory successfully predicts the magnitude²² and symmetry-based selection rules for the spin-phonon coupling coefficients. Coupled with thermal

weighting, this model successfully predicts relative T_1 trends and crossovers for a variety of structurally diverse molecular qubits. The group theory selection rules and functional forms employed for temperature-dependent T_1 times are explicitly grounded in physical quantities for molecular solids, unlike in the Debye model. Previous work has considered the role of bonding descriptors such as covalency, excited state energy, and the spin-orbit coupling constant in predicting the overall magnitudes of the spin-phonon coupling coefficients between different molecules.^{19,22,23} These insights can be integrated with the group theory and thermal weighting approaches described herein. Beyond the magnetically-dilute crystals considered in this work, this model will also describe intramolecular contributions to T_1 for frozen glass and solution phase systems, though spin-spin and motional contributions will be important considerations as well.⁶ We anticipate that the group theory methodology will yield insight into the molecular origins of T_1 times across a broad range of molecular electron spin qubits. Similar spin-orbit coupling expressions exist for organic radicals,^{44–46} such as nitroxide spin labels, and will likely enable an analogous theory of spin-phonon coupling.⁴⁰ Analysis of transition metal qubits in trigonal coordination environments will expand the range of symmetries considered,^{35,36} and applications to $S > 1/2$ optically addressable qubits may be enabled by applying group theory to zero-field splitting expressions.^{47,48}

The simplicity of the model in this study necessarily comes with approximations and limitations that should be clearly acknowledged. First, the direct process is entirely ignored, so the model will fail at very low temperatures ($<10 - 20$ K).¹² Second, the phonon dispersion across the Brillouin zone is not taken into account. Optical phonons are approximated by gas-phase calculations at the Γ point and acoustic phonons are ignored, implying the model will fail whenever the solid does not possess low-temperature molecular vibrations (i.e., non-molecular solids). These systematic errors likely accounts for much of the temperature offsets between predicted and observed quantities such as crossover points; however, experimental⁴⁰ and theoretical¹² analyses suggests that acoustic phonons are not important at temperatures much above the direct process regime. Third, the quantity $\partial \mathbf{g} / \partial Q$ is used as a proxy for $\partial^2 \mathbf{g} / \partial Q_i \partial Q_j$, the Raman coupling term predicted by Redfield theory.¹² As a result, it is challenging to convert the present model into an absolute rate prediction. However, the model can be accurately calibrated by comparison to molecular spin qubits with known

values of T_1 , and the magnitude of the two derivatives are expected to trend similarly.²⁰ The scaling constants used to match the data in Figures 2-2.5 and 2-2.6 agree to within 30%, suggesting that a scaling constant around $1 \times 10^5 \mu\text{s}^{-1}$ may be used to extend this model to complexes for which experimental data do not exist.

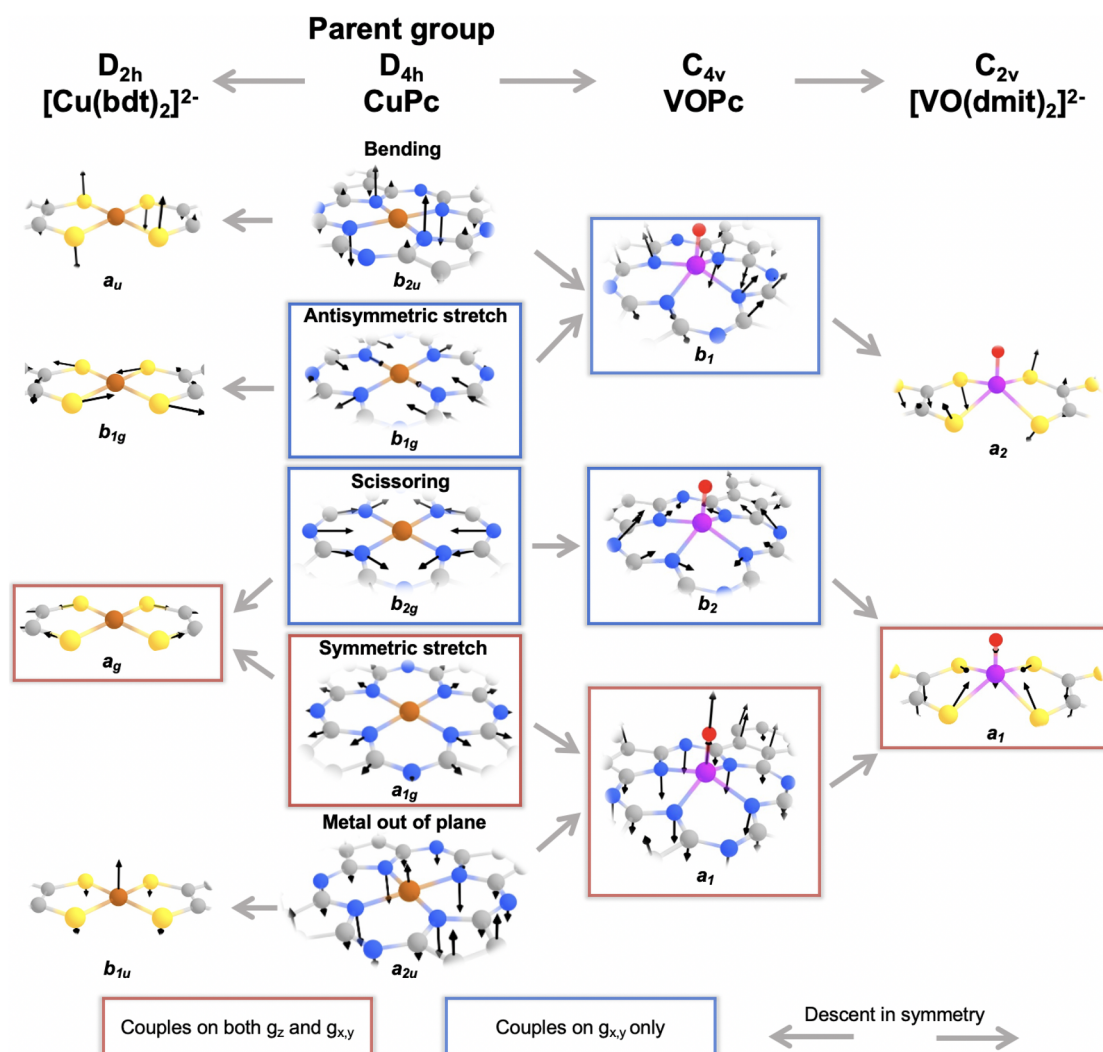


Figure 2-2.7. Symmetry flowchart of spin-phonon coupling coefficients. Convergent arrows indicate that vibrational modes mix under reduced-symmetry point groups, and boxes indicate the selection rules derived from Equation 2-2.3b.

In this study, we have analyzed archetypal qubits from four point groups: D_{4h} , D_{2h} , C_{4v} , and C_{2v} . Because D_{2h} , C_{4v} and C_{2v} are all subgroups of D_{4h} , the impact of symmetry on spin-phonon coupling can be viewed through the perspective of descent in symmetry on the CuPc structure (Figure 2-2.7). True D_{4h} complexes such as CuPc and D_{4h} CuCl_4^{2-} exhibit only a single g_z -active mode in the thermally accessible region, corresponding to the a_{1g} totally symmetric ligand-metal stretch (Table 2-2.S5). The b_{1g} antisymmetric ligand-metal stretch and the b_{2g} scissoring mode are also able to couple for g_x . Descent in symmetry to C_{4v} activates the a_{2u} (D_{4h}) out-of-plane modes, which transform as a_1 in C_{4v} . Phthalocyanine ligand scaffolds support many such low-energy a_{2u} modes, with CuPc possessing four a_{2u} modes below 400 cm^{-1} (Table 2-2.S5). These are activated for coupling in VOPc (Table 1, Table 2-2.S4), resulting in a smaller T_1 slope than CuPc and a characteristic crossover point. Descent in symmetry to D_{2d} is known to activate new modes for spin-phonon coupling, as the b_{2u} bending mode in D_{4h} transforms as a_1 in the distorted D_{2d} point group.²² Descent in symmetry to D_{2h} shuts down g_x spin-phonon coupling for the antisymmetric stretch b_{1g} mode while activating g_z coupling for the b_{2g} (D_{4h}) scissoring mode, which transforms as a_g in D_{2h} . The resulting a_g modes contain a mixture of symmetric stretch and scissoring character. This suggests that spin-phonon coupling could be decreased by selectively hindering scissoring and out-of-plane modes in lower symmetry point groups, a novel symmetry-based design strategy for molecular qubits.

In summary, we have developed a novel thermally-weighted dynamic ligand field model to describe and predict T_1 in molecular electron spin qubit candidates. The methodology has allowed for the determination of the specific vibrational modes that give rise to decoherence in the T_1 -limited regime, ultimately elucidating the critical spin-phonon coupling, chemical bonding, and symmetry factors leading to room temperature coherence. It can be employed to *a priori* predict new $S = 1/2$ transition metal complexes that may exhibit this phenomenon. Group theory prediction of anisotropic spin-phonon coupling coefficients may prove particularly important in the context of quantum sensing, where anisotropic g values provide a key motivation for employing transition metal complexes as spectrally addressable quantum sensors.

We believe future modeling work in the spin-phonon coupling field will profit from combining this molecular group theory approach with *ab initio* spin dynamics modeling employing Redfield theory.^{12,15,49,50} The strengths of these approaches complement each other: the former provides a direct connection to both chemical bonding parameters and analytical predictions of coupling terms, while the latter can simultaneously account for multiple relaxation mechanisms and predict the absolute relaxation rates without the need for a scaling parameter. Even when low symmetry molecules are considered *ab initio*, the descent in symmetry approach outlined in Figure 2-2.7 can provide a rational analysis of why coupling coefficients for different modes have the magnitudes that they do. A combined approach will have greater interpretability and predictive power than either taken in isolation.

Finally, we note that development of spin-phonon coupling models to date has suffered from a lack of experimental constraints. While the temperature-dependent relaxation times provide a single vector of data to reference, modeling this data demands calculation of coupling coefficients for dozens or hundreds of vibrational modes. There exists no way to independently verify the accuracy of the calculated coefficients, and many combinations of spin-phonon coupling parameters could in principle account for similar temperature-dependent relaxation behavior. While *ab initio* models have been steadily improving in both theoretical rigor and fidelity to existing data, we believe new spectroscopic techniques are called for to garner insight into spin-phonon coupling, including the direct experimental observation of spin-phonon coupling coefficients.

Acknowledgments

The authors thank Dr. Alec Follmer for helpful discussions. NPK acknowledges support by the National Science Foundation Graduate Research Fellowship under Grant No. DGE-1745301. This paper's computational modeling was supported in part by National Science Foundation MRI-grant 1726260 based at Calvin University in Grand Rapids, MI, USA. Financial support from Caltech and the Dow Next Generation Educator Fund is gratefully acknowledged.

References

- (1) Atzori, M.; Sessoli, R. The Second Quantum Revolution: Role and Challenges of Molecular Chemistry. *J. Am. Chem. Soc.* **2019**, *141* (29), 11339–11352. <https://doi.org/10.1021/jacs.9b00984>.
- (2) Wasielewski, M. R.; Forbes, M. D. E.; Frank, N. L.; Kowalski, K.; Scholes, G. D.; Yuen-Zhou, J.; Baldo, M. A.; Freedman, D. E.; Goldsmith, R. H.; Goodson, T.; Kirk, M. L.; McCusker, J. K.; Ogilvie, J. P.; Shultz, D. A.; Stoll, S.; Whaley, K. B. Exploiting Chemistry and Molecular Systems for Quantum Information Science. *Nat. Rev. Chem.* **2020**, *4* (9), 490–504. <https://doi.org/10.1038/s41570-020-0200-5>.
- (3) Graham, M. J.; Zadrozny, J. M.; Fataftah, M. S.; Freedman, D. E. Forging Solid-State Qubit Design Principles in a Molecular Furnace. *Chem. Mater.* **2017**, *29* (5), 1885–1897. <https://doi.org/10.1021/acs.chemmater.6b05433>.
- (4) Escalera-Moreno, L.; Baldoví, J. J.; Gaita-Ariño, A.; Coronado, E. Spin States, Vibrations and Spin Relaxation in Molecular Nanomagnets and Spin Qubits: A Critical Perspective. *Chem. Sci.* **2018**, *9* (13), 3265–3275. <https://doi.org/10.1039/C7SC05464E>.
- (5) Aromí, G.; Aguilà, D.; Gamez, P.; Luis, F.; Roubeau, O. Design of Magnetic Coordination Complexes for Quantum Computing. *Chem. Soc. Rev.* **2012**, *41* (2), 537–546. <https://doi.org/10.1039/C1CS15115K>.
- (6) Mirzoyan, R.; Kazmierczak, N. P.; Hadt, R. G. Deconvolving Contributions to Decoherence in Molecular Electron Spin Qubits: A Dynamic Ligand Field Approach. *Chem. – Eur. J.* **2021**, *27*, 9482–9494. <https://doi.org/10.1002/chem.202100845>.
- (7) Nielsen, M. A.; Chuang, I. L. *Quantum Computation and Quantum Information: 10th Anniversary Edition*, 1st edition.; Cambridge University Press: Cambridge ; New York, 2010.
- (8) Atzori, M.; Tesi, L.; Morra, E.; Chiesa, M.; Sorace, L.; Sessoli, R. Room-Temperature Quantum Coherence and Rabi Oscillations in Vanadyl Phthalocyanine: Toward Multifunctional Molecular Spin Qubits. *J. Am. Chem. Soc.* **2016**, *138* (7), 2154–2157. <https://doi.org/10.1021/jacs.5b13408>.
- (9) Fataftah, M. S.; Krzyaniak, M. D.; Vlaisavljevich, B.; Wasielewski, M. R.; Zadrozny, J. M.; Freedman, D. E. Metal–Ligand Covalency Enables Room Temperature Molecular Qubit Candidates. *Chem. Sci.* **2019**, *10* (27), 6707–6714. <https://doi.org/10.1039/C9SC00074G>.
- (10) Standley, K. J.; Vaughan, R. A. *Electron Spin Relaxation Phenomena in Solids*; Springer US: Boston, MA, 1969. <https://doi.org/10.1007/978-1-4899-6539-4>.
- (11) Bloch, F. Nuclear Induction. *Phys. Rev.* **1946**, *70* (7–8), 460–474. <https://doi.org/10.1103/PhysRev.70.460>.
- (12) Lunghi, A.; Sanvito, S. The Limit of Spin Lifetime in Solid-State Electronic Spins. *J. Phys. Chem. Lett.* **2020**, *11* (15), 6273–6278. <https://doi.org/10.1021/acs.jpcclett.0c01681>.
- (13) Van Vleck, J. H. Paramagnetic Relaxation Times for Titanium and Chrome Alum. *Phys. Rev.* **1940**, *57* (5), 426–447. <https://doi.org/10.1103/PhysRev.57.426>.
- (14) Orbach, R. Spin-Lattice Relaxation in Rare-Earth Salts. *Proc. R. Soc. Lond. A* **1961**, *264*, 458–484.

- (15) Lunghi, A.; Sanvito, S. How Do Phonons Relax Molecular Spins? *Sci. Adv.* **2019**, *5* (9), eaax7163. <https://doi.org/10.1126/sciadv.aax7163>.
- (16) Zhou, Y.; Bowler, B. E.; Eaton, G. R.; Eaton, S. S. Electron Spin Lattice Relaxation Rates for $S=1/2$ Molecular Species in Glassy Matrices or Magnetically Dilute Solids at Temperatures between 10 and 300 K. *J. Magn. Reson.* **1999**, *139*, 165–174.
- (17) Escalera-Moreno, L.; Suaud, N.; Gaita-Ariño, A.; Coronado, E. Determining Key Local Vibrations in the Relaxation of Molecular Spin Qubits and Single-Molecule Magnets. *J. Phys. Chem. Lett.* **2017**, *8* (7), 1695–1700. <https://doi.org/10.1021/acs.jpcclett.7b00479>.
- (18) Bader, K.; Winkler, M.; van Slageren, J. Tuning of Molecular Qubits: Very Long Coherence and Spin–Lattice Relaxation Times. *Chem. Commun.* **2016**, *52* (18), 3623–3626. <https://doi.org/10.1039/C6CC00300A>.
- (19) Follmer, A. H.; Ribson, R. D.; Oyala, P. H.; Chen, G. Y.; Hadt, R. G. Understanding Covalent versus Spin–Orbit Coupling Contributions to Temperature-Dependent Electron Spin Relaxation in Cupric and Vanadyl Phthalocyanines. *J. Phys. Chem. A* **2020**, *124* (44), 9252–9260. <https://doi.org/10.1021/acs.jpca.0c07860>.
- (20) Albino, A.; Benci, S.; Tesi, L.; Atzori, M.; Torre, R.; Sanvito, S.; Sessoli, R.; Lunghi, A. First-Principles Investigation of Spin–Phonon Coupling in Vanadium-Based Molecular Spin Quantum Bits. *Inorg. Chem.* **2019**, *58* (15), 10260–10268. <https://doi.org/10.1021/acs.inorgchem.9b01407>.
- (21) Garlatti, E.; Tesi, L.; Lunghi, A.; Atzori, M.; Voneshen, D. J.; Santini, P.; Sanvito, S.; Guidi, T.; Sessoli, R.; Carretta, S. Unveiling Phonons in a Molecular Qubit with Four-Dimensional Inelastic Neutron Scattering and Density Functional Theory. *Nat. Commun.* **2020**, *11* (1), 1751. <https://doi.org/10.1038/s41467-020-15475-7>.
- (22) Mirzoyan, R.; Hadt, R. G. The Dynamic Ligand Field of a Molecular Qubit: Decoherence through Spin–Phonon Coupling. *Phys. Chem. Chem. Phys.* **2020**, *22* (20), 11249–11265. <https://doi.org/10.1039/D0CP00852D>.
- (23) Lunghi, A. Ligand-Field Contributions to Spin-Phonon Coupling in a Family of Vanadium Molecular Qubits from Multi-Reference Electronic Structure Theory. *ArXiv191204545 Cond-Mat Physicsquant-Ph* **2019**.
- (24) Santanni, F.; Albino, A.; Atzori, M.; Ranieri, D.; Salvadori, E.; Chiesa, M.; Lunghi, A.; Bencini, A.; Sorace, L.; Totti, F.; Sessoli, R. Probing Vibrational Symmetry Effects and Nuclear Spin Economy Principles in Molecular Spin Qubits. *Inorg. Chem.* **2021**, *60* (1), 140–151. <https://doi.org/10.1021/acs.inorgchem.0c02573>.
- (25) Lunghi, A.; Totti, F.; Sessoli, R.; Sanvito, S. The Role of Anharmonic Phonons in Under-Barrier Spin Relaxation of Single Molecule Magnets. *Nat. Commun.* **2017**, *8* (1), 14620. <https://doi.org/10.1038/ncomms14620>.
- (26) Ballhausen, C. J. *Introduction to Ligand Field Theory*; McGraw-Hill, 1962.
- (27) Solomon, E. I. Inorganic Spectroscopy - An Overview. *Comments Inorg. Chem.* **1984**, *3*, 227–320.
- (28) Harris, D. C.; Bertolucci, M. D. *Symmetry and Spectroscopy: An Introduction to Vibrational and Electronic Spectroscopy*, New edition.; Dover Publications: New York, 1989.

- (29) Jahn, H. A.; Teller, E.; Donnan, F. G. Stability of Polyatomic Molecules in Degenerate Electronic States - I—Orbital Degeneracy. *Proc. R. Soc. Lond. Ser. - Math. Phys. Sci.* **1937**, *161* (905), 220–235. <https://doi.org/10.1098/rspa.1937.0142>.
- (30) Atkins, P. W.; Friedman, R. S. *Molecular Quantum Mechanics*, 5th edition.; Oxford University Press: Oxford ; New York, 2010.
- (31) Feynman, R. P. Forces in Molecules. *Phys. Rev.* **1939**, *56* (4), 340–343. <https://doi.org/10.1103/PhysRev.56.340>.
- (32) Wilson, R. B.; Solomon, E. I. Spectroscopic Studies of the Photoactive 4T_{2g} Excited State of Hexaamminechromium(III). *Inorg. Chem.* **1978**, *17* (7), 1729–1736. <https://doi.org/10.1021/ic50185a006>.
- (33) Wilson, R. B.; Solomon, E. I. Spectroscopic Studies of Photochemically Important Transition Metal Excited States. 2. The 1T_{1g}, 3T_{1g}, and 5T_{2g} Excited States of Hexaamminecobalt(III). *J. Am. Chem. Soc.* **1980**, *102* (12), 4085–4095. <https://doi.org/10.1021/ja00532a018>.
- (34) Szilagy, R. K.; Metz, M.; Solomon, E. I. Spectroscopic Calibration of Modern Density Functional Methods Using [CuCl₄]²⁻. *J. Phys. Chem. A* **2002**, *106* (12), 2994–3007. <https://doi.org/10.1021/jp014121c>.
- (35) Ariciu, A.-M.; Woen, D. H.; Huh, D. N.; Nodaraki, L. E.; Kostopoulos, A. K.; Goodwin, C. A. P.; Chilton, N. F.; McInnes, E. J. L.; Winpenny, R. E. P.; Evans, W. J.; Tuna, F. Engineering Electronic Structure to Prolong Relaxation Times in Molecular Qubits by Minimising Orbital Angular Momentum. *Nat. Commun.* **2019**, *10* (1), 3330. <https://doi.org/10.1038/s41467-019-11309-3>.
- (36) Fataftah, M. S.; Bayliss, S. L.; Laorenza, D. W.; Wang, X.; Phelan, B. T.; Wilson, C. B.; Mintun, P. J.; Kovos, B. D.; Wasielewski, M. R.; Han, S.; Sherwin, M. S.; Awschalom, D. D.; Freedman, D. E. Trigonal Bipyramidal V³⁺ Complex as an Optically Addressable Molecular Qubit Candidate. *J. Am. Chem. Soc.* **2020**, *142* (48), 20400–20408. <https://doi.org/10.1021/jacs.0c08986>.
- (37) Du, J.-L.; Eaton, G. R.; Eaton, S. S. Temperature and Orientation Dependence of Electron-Spin Relaxation Rates for Bis(Diethyldithiocarbamate)Copper(II). *J. Magn. Reson. A* **1995**, *117* (1), 67–72. <https://doi.org/10.1006/jmra.1995.9971>.
- (38) Konda, R.; Du, J.-L.; Eaton, S. S.; Eaton, G. R. Electron Spin Relaxation Rates for Nitridochromium(V) Tetratolylporphyrin and Nitridochromium(V) Octaethylporphyrin in Frozen Solution. *Appl. Magn. Reson.* **1994**, *7* (2), 185–193. <https://doi.org/10.1007/BF03162611>.
- (39) Du, J. L.; Eaton, G. R.; Eaton, S. S. Electron-Spin-Lattice Relaxation in Natural Abundance and Isotopically Enriched Oxo-Chromium(V)Bis (2-Hydroxy-2-Ethylbutyrate). *J. Magn. Reson. A* **1995**, *115* (2), 236–240. <https://doi.org/10.1006/jmra.1995.1172>.
- (40) Du, J. L.; Eaton, G. R.; Eaton, S. S. Temperature, Orientation, and Solvent Dependence of Electron Spin-Lattice Relaxation Rates for Nitroxyl Radicals in Glassy Solvents and Doped Solids. *J. Magn. Reson. A* **1995**, *115* (2), 213–221. <https://doi.org/10.1006/jmra.1995.1169>.
- (41) Camargo, L. C. de; Briganti, M.; Santana, F. S.; Stinghen, D.; Ribeiro, R. R.; Nunes, G. G.; Soares, J. F.; Salvadori, E.; Chiesa, M.; Benci, S.; Torre, R.; Sorace, L.; Totti, F.; Sessoli,

- R. Exploring the Organometallic Route to Molecular Spin Qubits: The [CpTi(Cot)] Case. *Angew. Chem.* **2021**, *133* (5), 2620–2625. <https://doi.org/10.1002/ange.202009634>.
- (42) Castle, J. G.; Feldman, D. W.; Klemens, P. G.; Weeks, R. A. Electron Spin-Lattice Relaxation at Defect Sites; E' Centers in Synthetic Quartz at 3 Kilo-Oersteds. *Phys. Rev.* **1963**, *130* (2), 577–588. <https://doi.org/10.1103/PhysRev.130.577>.
- (43) Castle, J. G.; Feldman, D. W. Resonance Modes at Defects in Crystalline Quartz. *Phys. Rev.* **1965**, *137* (2A), A671–A673. <https://doi.org/10.1103/PhysRev.137.A671>.
- (44) Stone, A. J. *G* Factors of Aromatic Free Radicals. *Mol. Phys.* **1963**, *6* (5), 509–515. <https://doi.org/10.1080/00268976300100571>.
- (45) Un, S.; Atta, M.; Fontecave, M.; Rutherford, A. W. G-Values as a Probe of the Local Protein Environment: High-Field EPR of Tyrosyl Radicals in Ribonucleotide Reductase and Photosystem II. *J. Am. Chem. Soc.* **1995**, *117* (43), 10713–10719. <https://doi.org/10.1021/ja00148a013>.
- (46) Sinnecker, S.; Rajendran, A.; Klamt, A.; Diedenhofen, M.; Neese, F. Calculation of Solvent Shifts on Electronic G-Tensors with the Conductor-Like Screening Model (COSMO) and Its Self-Consistent Generalization to Real Solvents (Direct COSMO-RS). *J. Phys. Chem. A* **2006**, *110* (6), 2235–2245. <https://doi.org/10.1021/jp056016z>.
- (47) Higdon, N. J.; Barth, A. T.; Kozlowski, P. T.; Hadt, R. G. Spin–Phonon Coupling and Dynamic Zero-Field Splitting Contributions to Spin Conversion Processes in Iron(II) Complexes. *J. Chem. Phys.* **2020**, *152* (20), 204306. <https://doi.org/10.1063/5.0006361>.
- (48) Bayliss, S. L.; Laorenza, D. W.; Mintun, P. J.; Kovos, B. D.; Freedman, D. E.; Awschalom, D. D. Optically Addressable Molecular Spins for Quantum Information Processing. *Science* **2020**, *370* (6522), 1309–1312. <https://doi.org/10.1126/science.abb9352>.
- (49) Briganti, M.; Santanni, F.; Tesi, L.; Totti, F.; Sessoli, R.; Lunghi, A. A Complete Ab Initio View of Orbach and Raman Spin–Lattice Relaxation in a Dysprosium Coordination Compound. *J. Am. Chem. Soc.* **2021**, *143* (34), 13633–13645. <https://doi.org/10.1021/jacs.1c05068>.
- (50) Reta, D.; Kragoskow, J. G. C.; Chilton, N. F. Ab Initio Prediction of High-Temperature Magnetic Relaxation Rates in Single-Molecule Magnets. *J. Am. Chem. Soc.* **2021**, *143* (15), 5943–5950. <https://doi.org/10.1021/jacs.1c01410>.

Supporting Information

Computational methods. All DFT spin-phonon coupling (SPC) calculations were performed in ORCA¹⁻³ 4.2.1 using the B3LYP functional.⁴⁻⁷ Vanadyl phthalocyanine (VOPc) and copper phthalocyanine (CuPc) were optimized in the gas phase prior to SPC calculations^{8,9} using the def2-TZVP basis set for all atoms in the first coordination sphere, the def2-SVP basis set for all remaining atoms, and the def2/J auxiliary basis set. [VO(dmit)₂]²⁻ was optimized in the gas phase prior to SPC calculations^{8,9} using the def2-TZVP basis set and the def2/J auxiliary basis set for all atoms. Frequency calculations were conducted using identical basis sets. Owing to non-negligible crystal packing distortions, geometries used for [V(bdt)₃]²⁻, [V(bds)₃]²⁻, [Cu(bdt)₂]²⁻, and [Cu(bds)₂]²⁻ were taken from literature crystal structures¹⁰ and H-atom optimized with the def2-TZVP basis set. SPC calculations were conducted using the ZORA relativistic correction in all cases, with the ZORA-def2-TZVP / ZORA-def2-SVP basis set partitioning for VOPc and CuPc as described above and the ZORA-def2-TZVP basis set for all other compounds, with an auxiliary basis set of SARC/J in all cases. DFT grid 7 and TightSCF convergence criteria were used throughout, giving a convergence tolerance of 10⁻⁸ Hartree. The % Hartree-Fock exchange (%HFX) included in the B3LYP functional was spectroscopically calibrated to experimental *g* values (Table 2-2.S1), in accordance with an established literature procedure.^{11,12} Smaller values of %HFX are required for accurate modeling of highly covalent complexes, including heavy-atom ligands and copper complexes. We did not consider a dependence of the molecular geometry on temperature. While bond lengths in VOPc crystal structures increase by 0.02 Å from 150K to 295K,^{13,14} this should have a negligible impact on $\partial g / \partial Q$ that is well within the inherent errors and approximations of the model. No symmetry constraints were imposed in ORCA at any point during the geometry optimizations, vibrational mode calculations, or spin-phonon coupling calculations. All irreducible representations in the text are based on manual assignment to the most appropriate point group.

Table 2-2.S1: Comparison of experimental and calculated g values used for %HFX DFT calibration.

Molecule	%HFX	g_z		g_y		g_x	
		Expt.	Calc.	Expt.	Calc.	Expt.	Calc.
CuPc	38	2.199	2.166	2.052	2.051	2.052	2.051
[Cu(bdt) ₂] ²⁻	20	2.085	2.047	2.019	2.015	2.019	2.016
[Cu(bds) ₂] ²⁻	20	2.082	2.089	2.018	2.053	2.018	2.031
VOPc	60	1.966	1.961	1.989	1.982	1.989	1.982
[V(bdt) ₃] ²⁻	60	1.988	1.963	1.970	1.947	1.970	1.947
[V(bds) ₃] ²⁻	20	1.950	1.945	1.955	1.939	1.960	1.935
[VO(dmit) ₂] ²⁻	60	1.970	1.951	1.988	1.980	1.986	1.978

Vibrational modes were defined according to the dimensionless normal coordinates^{1,2,15} given below¹⁶, which are directly comparable to previous studies.¹⁷

$$q_\alpha = \left(\frac{\omega_\alpha}{\hbar}\right)^{\frac{1}{2}} \sum_{k=1}^{3N} L_{k\alpha} \delta X_k \sqrt{M_k} \quad (2-2.S1)$$

These coordinates are implemented in ORCA 4.2.1 through the %mtr block, using the ddnc variable to control the scan step size. We conducted all vibrational scans using single point jobs rather than %mtr scans to afford greater control over the initial guess wavefunction. However, the vibrational steps used are identical to those produced by %mtr. Calculations of the g values were conducted over a dimensionless normal coordinate range from -0.15 to +0.15 in 0.05 step increments, with the exception of [V(bdt)₃]²⁻, where numerical noise required stepping from -0.75 to +0.75 in 0.25 increments. $\partial \mathbf{g} / \partial Q$ values were calculated by centered finite difference about the origin (for example, $\partial \mathbf{g} / \partial Q = (\mathbf{g}_{+0.05} - \mathbf{g}_{-0.05}) / (0.10)$). Principal tensor values are used for g_x , g_y , and g_z , while the non-diagonal g tensor was used in comparisons to alternative approaches (*vide infra*).¹⁷ Raw data from the normal coordinate scans is shown below in Figures 2-2.S1 – 2-2.S7.

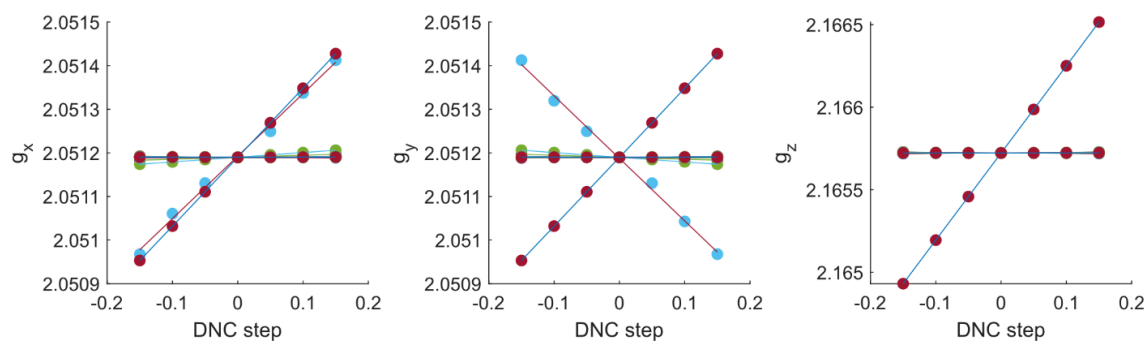


Figure 2-2.S1: CuPc g value scans and fits.

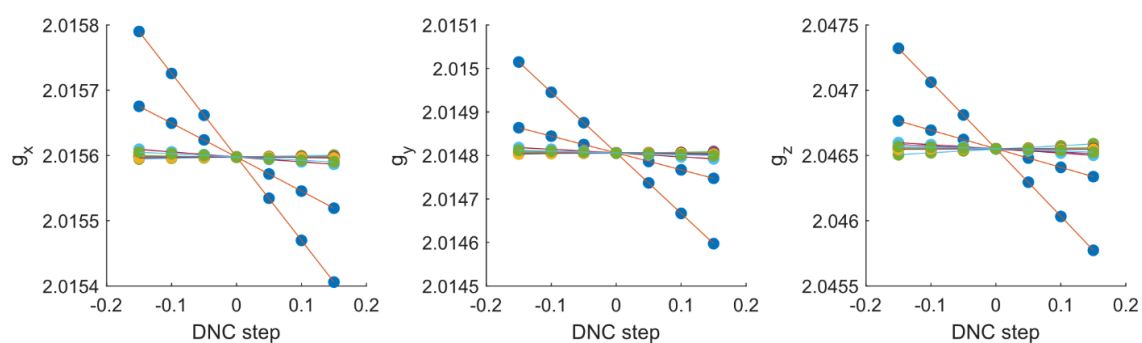


Figure 2-2.S2: $[\text{Cu}(\text{bdt})_2]^{2-}$ g value scans and fits.

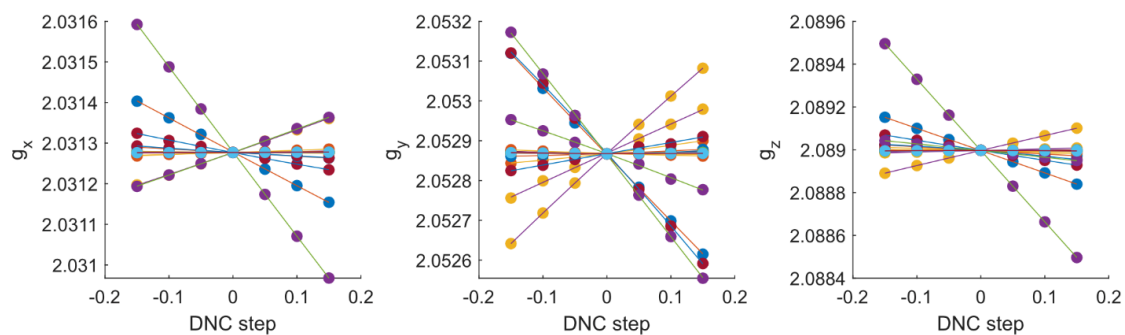


Figure 2-2.S3: $[\text{Cu}(\text{bds})_2]^{2-}$ g value scans and fits.

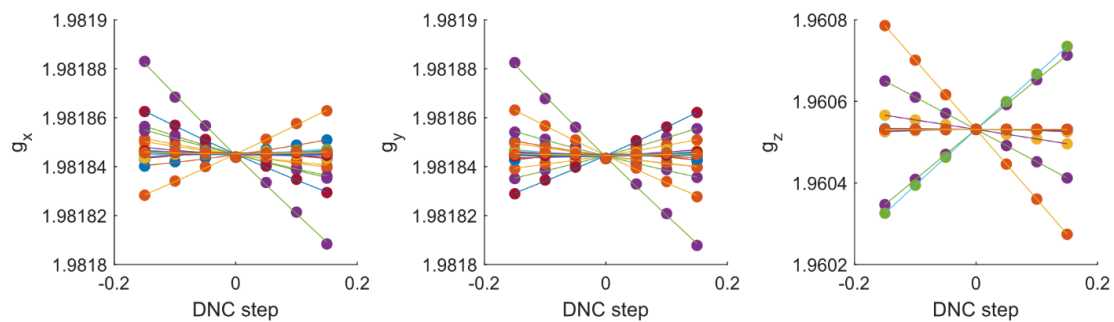


Figure 2-2.S4: VOPc g value scans and fits.

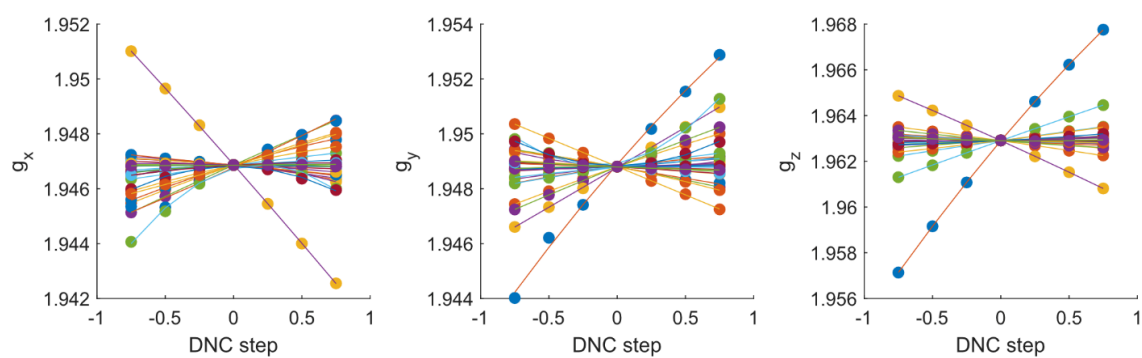


Figure 2-2.S5: $[V(bdt)_3]^2-$ g value scans and fits.

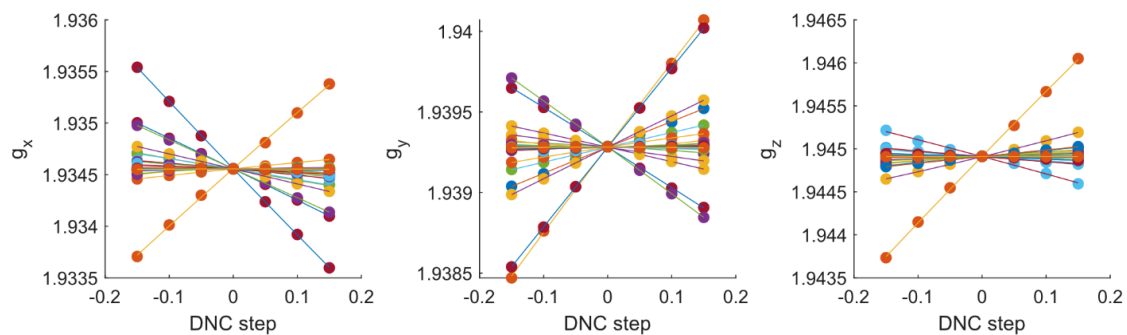


Figure 2-2.S6: $[V(bds)_3]^2-$ g value scans and fits.

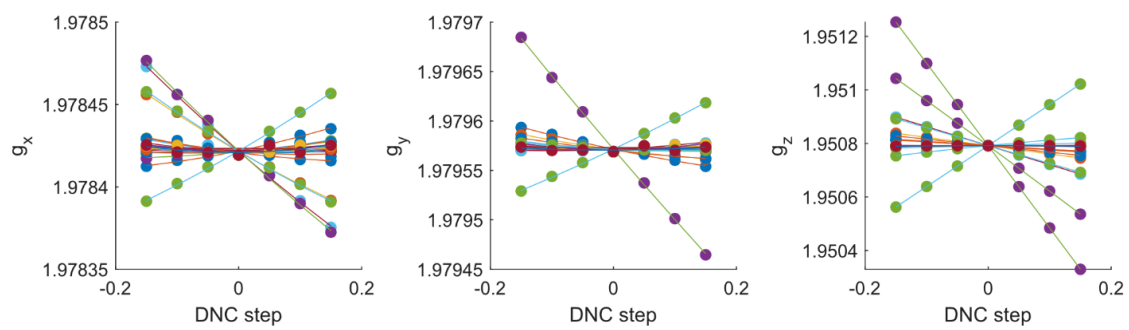


Figure 2-2.S7: $[\text{VO}(\text{dmit})_2]^{2-}$ g value scans and fits.

T1 model. H-atom optimized crystal structures of $[\text{V}(\text{bdt})_3]^{2-}$, $[\text{V}(\text{bds})_3]^{2-}$, $[\text{Cu}(\text{bdt})_2]^{2-}$, $[\text{Cu}(\text{bds})_2]^{2-}$, and $[\text{VO}(\text{dmit})_2]^{2-}$ were required to accurately describe molecular geometries for SPC coefficient calculations, as the square-planar Cu(II) complexes undergo tetrahedral distortion under gas-phase optimization and the six-coordinate V(IV) complexes exhibit substantial ligand field distortions from crystal packing. Consequently, $[\text{V}(\text{bds})_3]^{2-}$, $[\text{Cu}(\text{bdt})_2]^{2-}$, and $[\text{Cu}(\text{bds})_2]^{2-}$ possess negative energy vibrational modes in the gas phase frequency calculation. These modes are discarded to make the predictions in Figure 2-2.6. It is important to demonstrate that the predictions of the thermally-weighted T_1 model are insensitive to these modes. To accomplish this, we have made equivalent T_1 prediction plots in which all negative energy modes are assigned an arbitrary frequency of 20 cm^{-1} (Figure 2-2.S8). The results are qualitatively the same as in Figure 2-2.6 – the high-temperature ordering of all complexes is still preserved correctly, and $[\text{V}(\text{bdt})_3]^{2-}$ and $[\text{Cu}(\text{bds})_2]^{2-}$ undergo a nearly identical tangent crossover point under 100K.

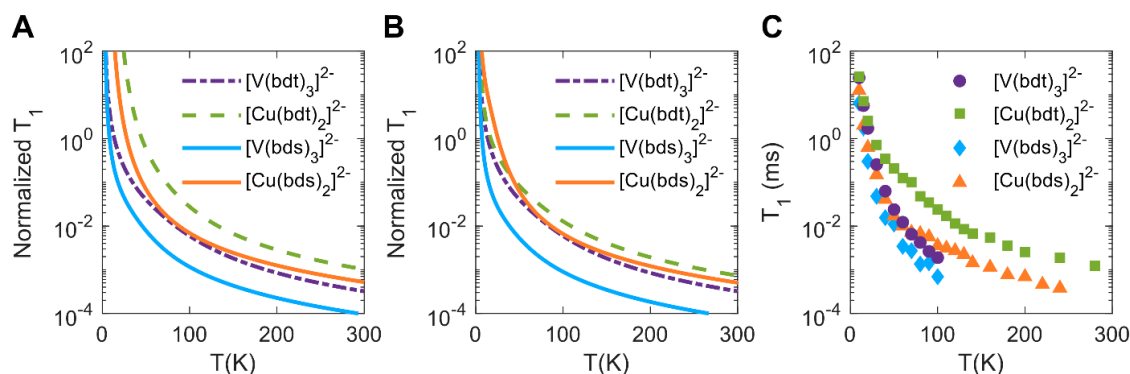


Figure 2-2.S8: Comparative effect of negative-frequency modes on T_1 predictions. (A) T_1 predictions produced by discarding negative-frequency modes. (B) T_1 predictions produced by setting all negative modes to an arbitrary frequency of 20 cm^{-1} and including their SPC coefficients in the thermal weighting. (C) Experimental data reproduced from Ref ¹⁰. Panels (A) and (C) present identical data as Figure 6 in the main text, but are reproduced here for comparison. All eight T_1 prediction curves in (A) and (B) are scaled by the same factor, chosen so that the $[\text{Cu}(\text{bdt})_2]^{2-}$ prediction in (A) matches the experimental $[\text{Cu}(\text{bdt})_2]^{2-}$ data at 280 K.

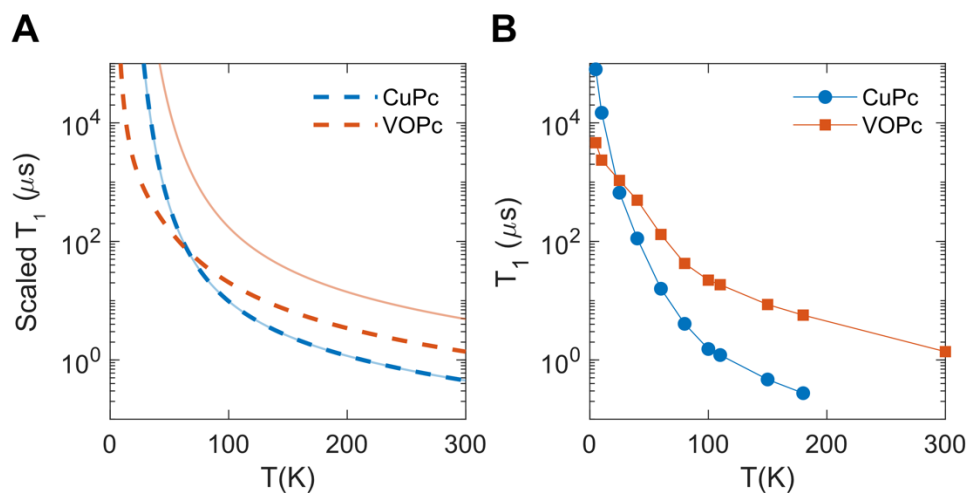


Figure 2-2.S9: Thermally-weighted ligand field model for phthalocyanine qubits (equivalent to Figure 5 in the main text, except plotting model predictions and experimental data points on separate panels A and B, respectively). All T_1 predictions are scaled by the same factor, chosen for the VOPc all-modes prediction to match the experimental data at 300 K.

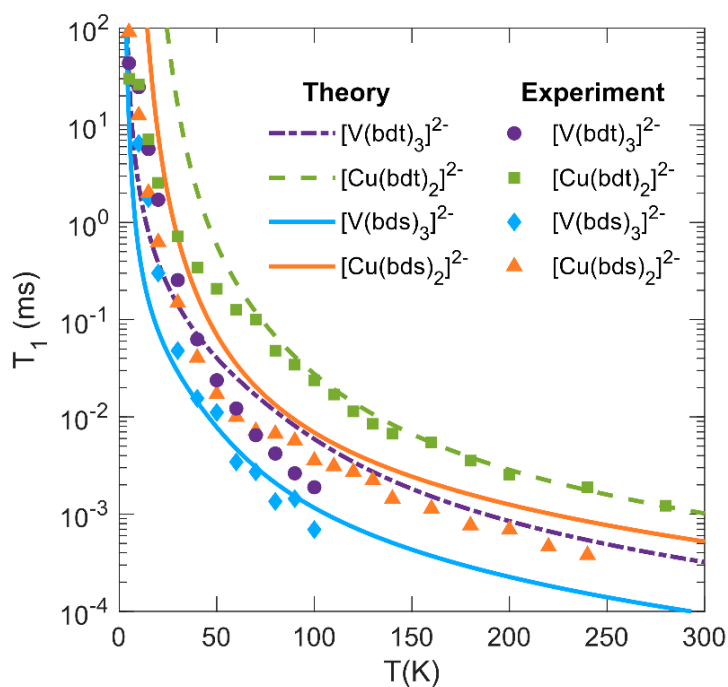


Figure 2-2.S10: Thermally-weighted ligand field model for dithiolate and diselenate qubits, plotted on the same graph (equivalent to Figure 2-2.6 in the main text). All T_1 predictions are scaled by the same factor, chosen for $[\text{Cu}(\text{bdt})_2]^{2-}$ to match the experimental data at 280 K.

Choice of spin-phonon coupling coefficients. In this study, we have chosen to employ only the principal g tensor values for analysis of spin-phonon coupling. Previous works have employed all nine g tensor values, thereby including not only orbital angular momentum modulation, but also rotation of the g tensor principal axes.¹⁷ Here we compare and contrast the two approaches. The principal g value derivatives for CuPc and VOPc are given in Figures 2-2.S11 – 2-2.S12. The full g tensor derivatives are given in Figures 2-2.S13 – 2-2.S14, while the summed off-diagonal components are given in Figure 2-2.S15.

Figures 2-2.S11 – 2-2.S18

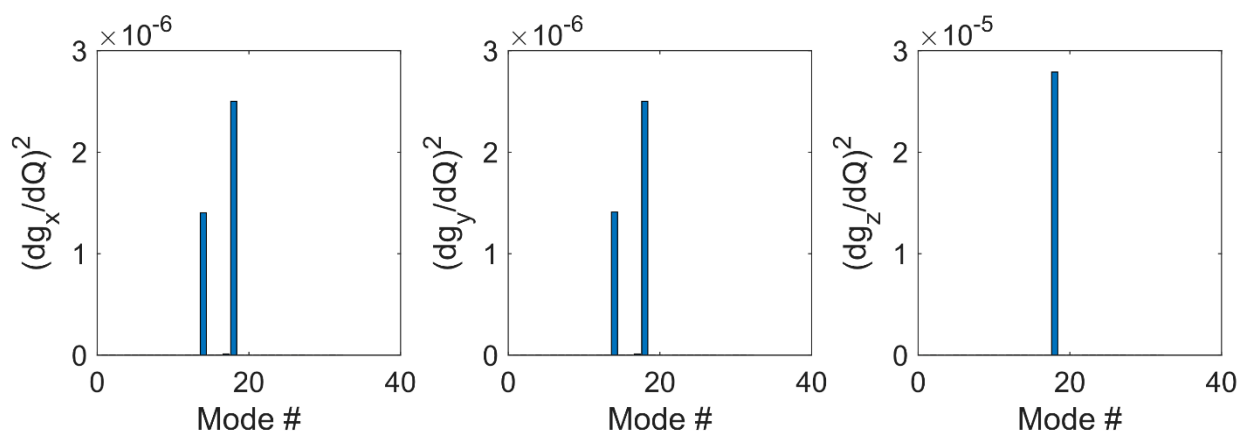


Figure 2-2.S11: CuPc principal g value derivatives.

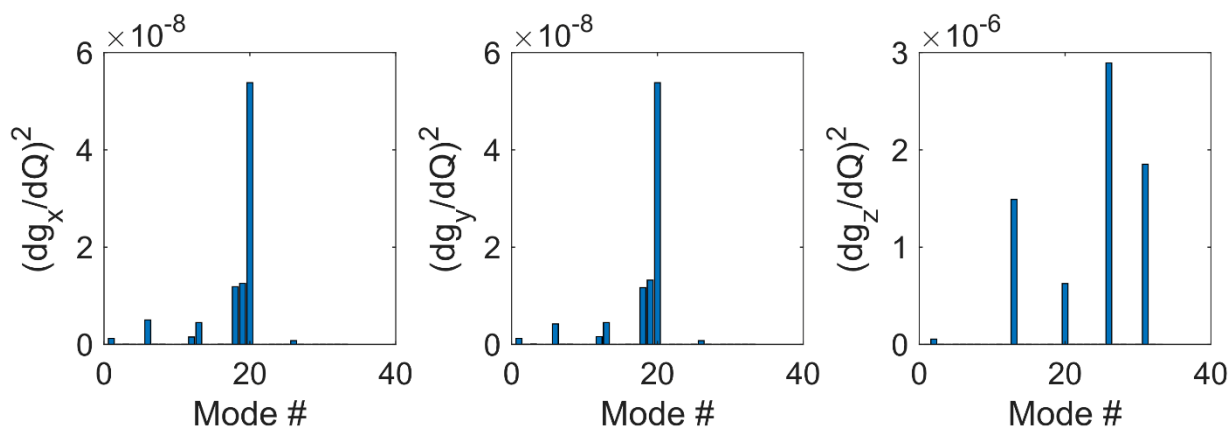


Figure 2-2.S12: VOPc principal g value derivatives.

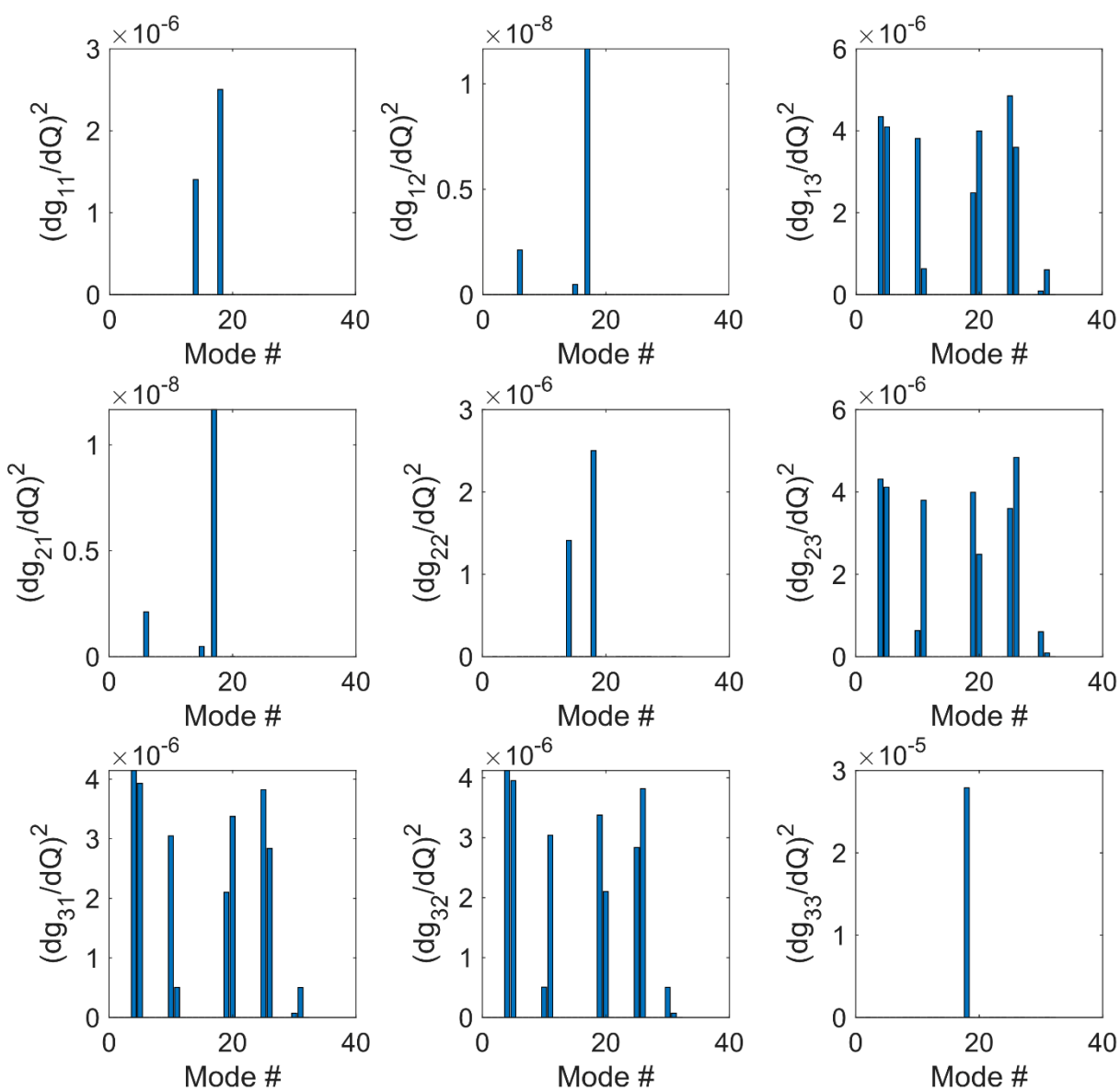


Figure 2-2.S13: CuPc full g tensor derivatives.

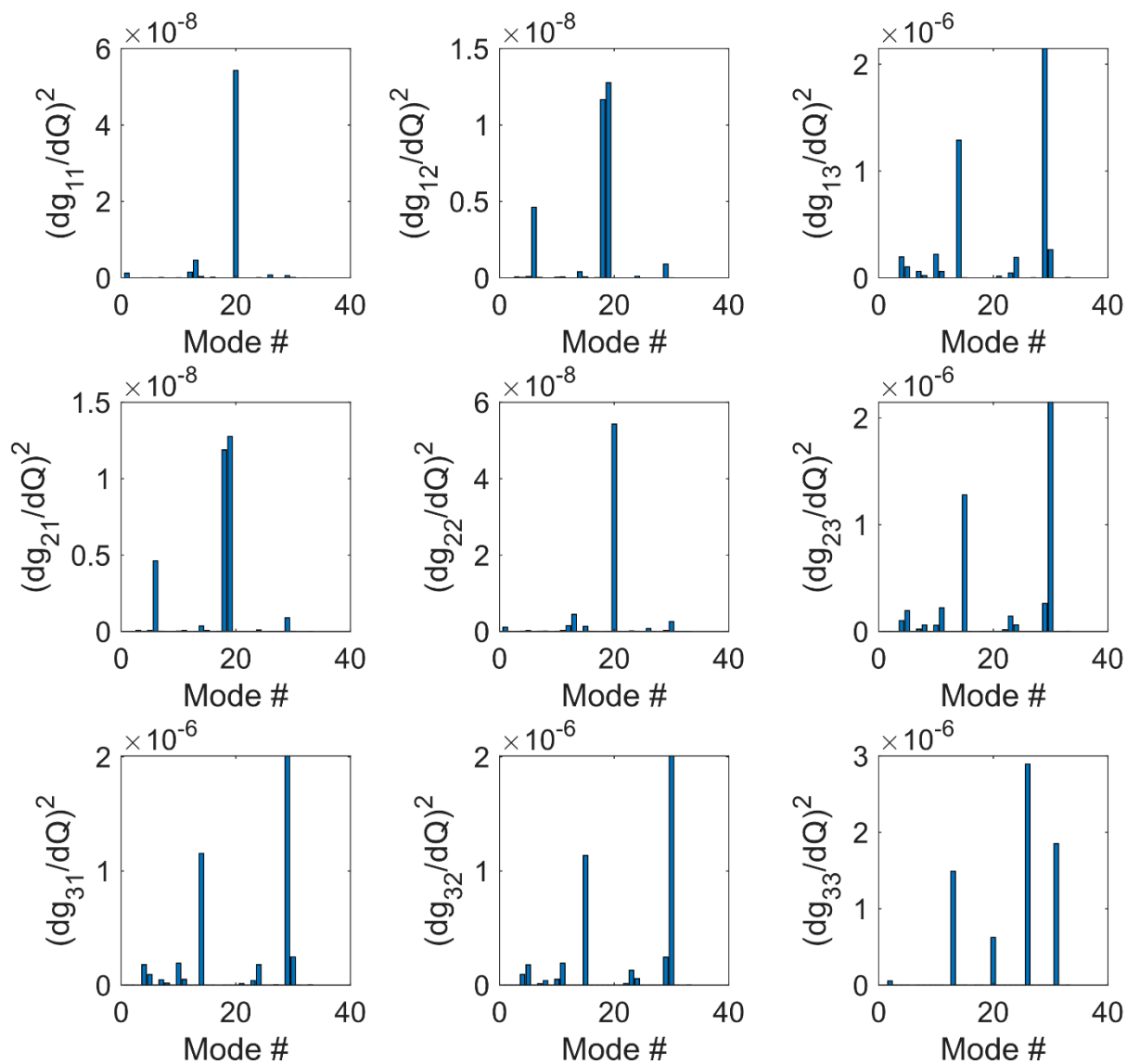


Figure 2-2.S14: VOPc full g tensor derivatives.

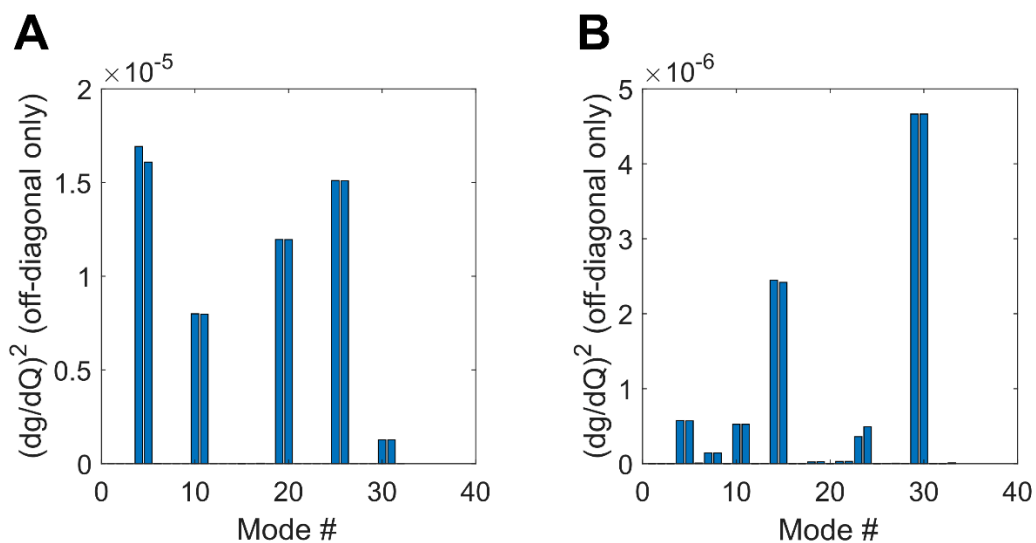
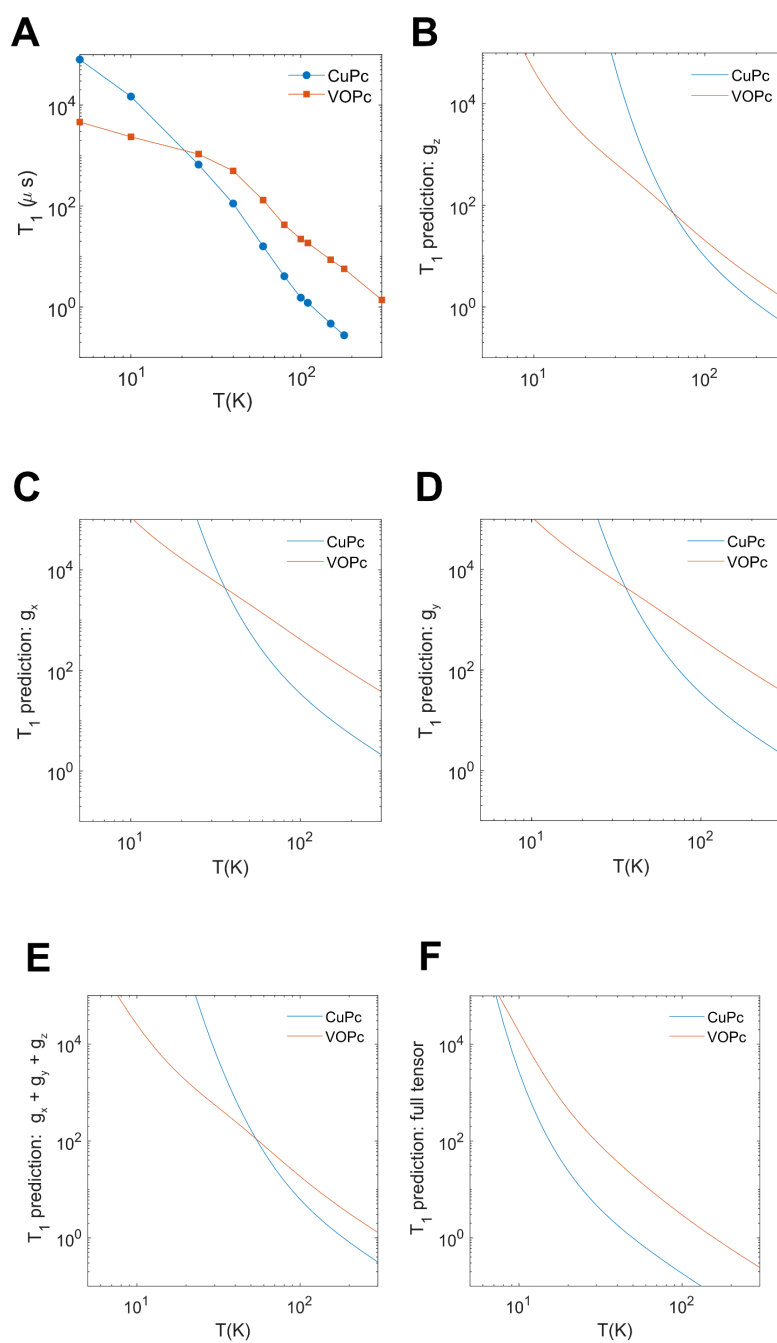


Figure 2-2.S15: Summed off-diagonal g tensor derivatives (elements 21, 31, 12, 32, 13, and 23). (A) CuPc. (B) VOPc.

Comparison between Figures 2-2.S11 – 2-2.S12 with Figures 2-2.S13 – 2-2.S14 shows that the principal value derivatives correspond closely to the on-diagonal g tensor derivatives for both VOPc and CuPc, as expected. Interpretation of the off-diagonal derivatives in Figures 2-2.S13 – 2-2.S14 is challenging, particularly as these derivatives appear to be associated with fundamentally different vibrational modes than the on-diagonal derivatives. However, the situation is clarified by summing over all the off-diagonal g tensor derivatives, as shown in Figure 2-2.S15. This analysis reveals that large off-diagonal derivatives occur exclusively in pairs for both VOPc and CuPc. Comparison to Tables 2-2.S4 – 2-2.S5 shows that these pairwise contributions correspond to vibrational modes with the irreducible representation e_g (CuPc) or e (VOPc). The rotation operators R_x and R_y transform as these representations in the D_{4h} and C_{4v} point groups.¹⁸ Such vibrations rotate the first coordination sphere and therefore the principal axes of the g tensor, rather than modulating the angular momentum content expressed in the principal g values g_x , g_y , and g_z . These vibrational modes do not exist in idealized D_{4h} and C_{4v} first coordination sphere geometries,¹¹ as they correspond to pure molecular rotations in that case. The presence of such modes is enabled by the extended phthalocyanine ligand scaffold.

Figure 2-2.S16 compares the results for various choices of the derivatives to include in the thermally-weighted T_1 model by plotting on a double-log scale.



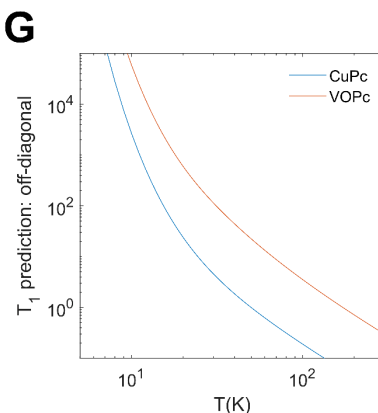


Figure 2-2.S16: Comparison of thermally-weighted T₁ prediction plots for CuPc and VOPc using different choices for the spin-phonon coupling coefficients. (A) Experimental data plotted on a double log scale (same data as in Figure 2-2.5B). (B) T₁ prediction using g_z derivatives (same data as in Figure 5A, dashed lines). (C) T₁ prediction using g_x derivatives. (D) T₁ prediction using g_y derivatives. (E) T₁ prediction using summed rate contributions from all three principal tensor derivatives (g_x, g_y, and g_z). (F) T₁ prediction using summed rate contributions from all nine g tensor derivatives. (G) T₁ prediction using only off-diagonal g tensor derivatives. Scaling factor is calculated so that the g_z T₁ prediction matches the experimental data at 300 K in panel (B), and all T₁ predictions in panels (B)-(G) are scaled according to the same factor $A = 1.32 \times 10^5 \mu\text{s}^{-1}$, which is the same scaling used in the main text for Figure 2-2.5.

Figure 2-2.S16A-E shows that all three principal g tensor values, in addition to their summed contribution, predict the same qualitative T₁ crossover behavior observed in the experimental data in the Raman temperature regime. However, inclusion of the off-diagonal elements into the model eliminates any crossover point above 10K, the approximate range of validity for this Raman process model (Figure 2-2.S16F-G).

A further point of comparison is furnished by examination of the slopes arising from a log-log plot of the relaxation data (that is, $\frac{\partial \log(1/T_1)}{\partial \log T}$). This metric corresponds to the exponent of a power law description for the relaxation process, a commonly-used metric for T₁.¹⁹ As shown in Figure S17, CuPc possesses a larger rate exponent than VOPc over the full range of experimental temperatures

tested. Use of the g_z principal tensor derivative correctly accounts for this trend, matching well the observed exponents above a temperature 70 K. Use of the full g tensor does not provide the correct trend, predicting a smaller exponent for CuPc than VOPc of most of the Raman process temperature range. This is consistent with strong contributions from the CuPc e_g modes at low energies in this model. Note that the decrease of the CuPc exponent at temperatures less than 70 K relative to the model is likely due to a combination of the direct process, higher-order coupling terms, and crystal distortions. In total, the principal value derivatives provide a superior match to the data and are therefore used in this study.

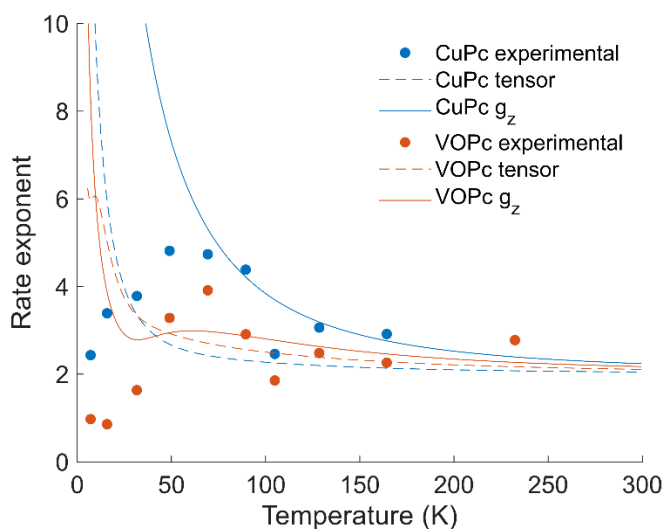


Figure2-2.S17: Rate exponents for CuPc and VOPc. Experimental values are computed by finite difference between adjacent points, with reported temperature values given as the geometric mean of the corresponding temperature values.

A final, independent line of evidence comes from consideration of orientation-dependent T_1 and T_M values. We first note that the Zeeman interaction is not governed by the entirety of the g tensor at any given instant, but only by those elements of the g tensor that are projected out by the field and spin orientations. We denote the projected g value as $g_{proj} = \vec{B} \cdot \mathbf{g} \cdot \vec{S}$. For simplicity, we model orientation-dependent spin-phonon coupling via $(\partial g_{proj} / \partial Q)^2$, and we consider $\vec{B} \parallel \vec{S}$ for all

orientations θ, φ with respect to the molecular z-axis. (For CuPc, the molecular z-axis is defined perpendicular to the plane of the molecule, so $g_{proj} = g_{\perp}$ for polar angle $\theta = 90^{\circ}$ and any value of the azimuthal angle φ .)

As noted previously, e_g vibrational modes modulate the g value by rotating the g tensor, while modes with canonical g tensor derivatives modulate the principal values of the g tensor. Numerical evaluation of $(\partial g_{proj}/\partial Q)^2$ shows that the e_g modes in CuPc lead to qualitatively different orientation dependence of spin-phonon coupling (Figure S18). For the e_g modes, $\partial g_{proj}/\partial Q$ goes to zero at both canonical orientations ($\theta = 0^{\circ}$ and $\theta = 90^{\circ}$). This result is geometrically intuitive, as any rotational mode must modulate g_{proj} symmetrically for +Q and -Q when aligned with a principal tensor value, and therefore linear coupling terms vanish and only second-order spin-phonon coupling is possible. Spin-phonon coupling from the e_g modes would thus be at a maximum for intermediate-field orientations. By contrast, the a_{1g} mode sees $(\partial g_{proj}/\partial Q)^2$ vary smoothly between $(\partial g_z/\partial Q)^2$ and $(\partial g_x/\partial Q)^2$, never reaching zero. This mode (and others like it that have nonzero derivatives of the canonical g values) will exhibit maximum spin-phonon coupling at one canonical orientation, minimum coupling at the other canonical orientation, and no special behavior at intermediate field positions. Experimental data for diverse systems exhibit the latter behavior over a range of temperatures.²⁰⁻²³ This suggests that spin-phonon coupling in molecular qubits is dominated by modulation of the canonical g values, supporting our decision to use those derivatives in our model. We note that square planar Cu(II) systems have been specifically shown to exhibit this behavior,²³ providing a direct comparison to CuPc studied in this work.

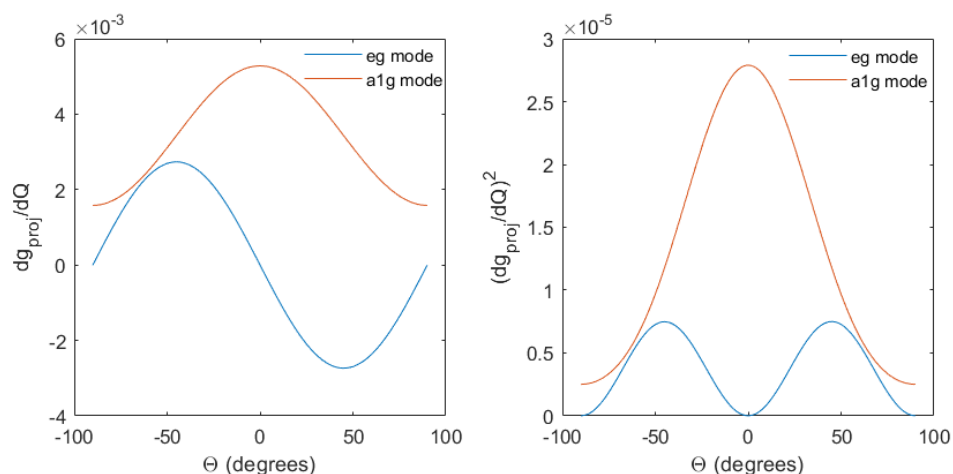


Figure 2-2.S18: Orientation dependence of spin-phonon coupling for rotational modes (example: CuPc e_g mode #25) versus modes with canonical g value derivatives (example: CuPc a_{1g} mode #18). A value of $\varphi = 45^\circ$ was chosen to maximize the e_g mode derivatives, as this mode rotates the first coordination sphere around the axis $x = -y$. The polar angle θ was swept to project out g_{\parallel} at $\theta = 0^\circ$ and g_{\perp} at $\theta = \pm 90^\circ$. Derivatives were evaluated via finite difference: $g_{\text{proj}} = \vec{\mathbf{B}} \cdot \mathbf{g} \cdot \vec{\mathbf{S}}$ was calculated for $Q = +0.1$ and $Q = -0.1$ for each orientation of the $\vec{\mathbf{B}} \parallel \vec{\mathbf{S}}$ vectors, and the difference was divided by 0.2. Left plot shows derivative prior to squaring, while right plot shows the squared spin-phonon coupling coefficient.

Choice of vibrational energy cutoff

In the text, spin-phonon coupling coefficients were not considered for vibrational modes with energy above 400 cm^{-1} , which corresponds roughly to $2kT$ at room temperature. Here, we directly demonstrate the appropriateness of this cutoff. Spin-phonon coupling coefficients were computed for all vibrational modes for $[\text{Cu}(\text{bdt})_2]^{2-}$ and $[\text{VO}(\text{dmit})_2]^{2-}$. The relative T_I predictions were compared with several potential values of the cutoff in Figure S19. In panels A and B, the deviation of the ratio from 1 corresponds to the relative error induced by the cutoff. We see the 400 cm^{-1} cutoff induces a maximum relative error of 5.8% at 300 K for $[\text{Cu}(\text{bdt})_2]^{2-}$ and a maximum relative error of 0.13% at 300 K for $[\text{VO}(\text{dmit})_2]^{2-}$. The error induced by the 400 cm^{-1} cutoff is the same as that induced by a 500 cm^{-1} cutoff in both cases, indicating that 400 cm^{-1} is an appropriate metric for capturing the most important metal-ligand bond vibrations. Based on these results, we estimate the maximum relative error due to the cutoff as 5-10% near room temperature. This error is visually unnoticeable on a logarithmic plot, as demonstrated in panels C and D.

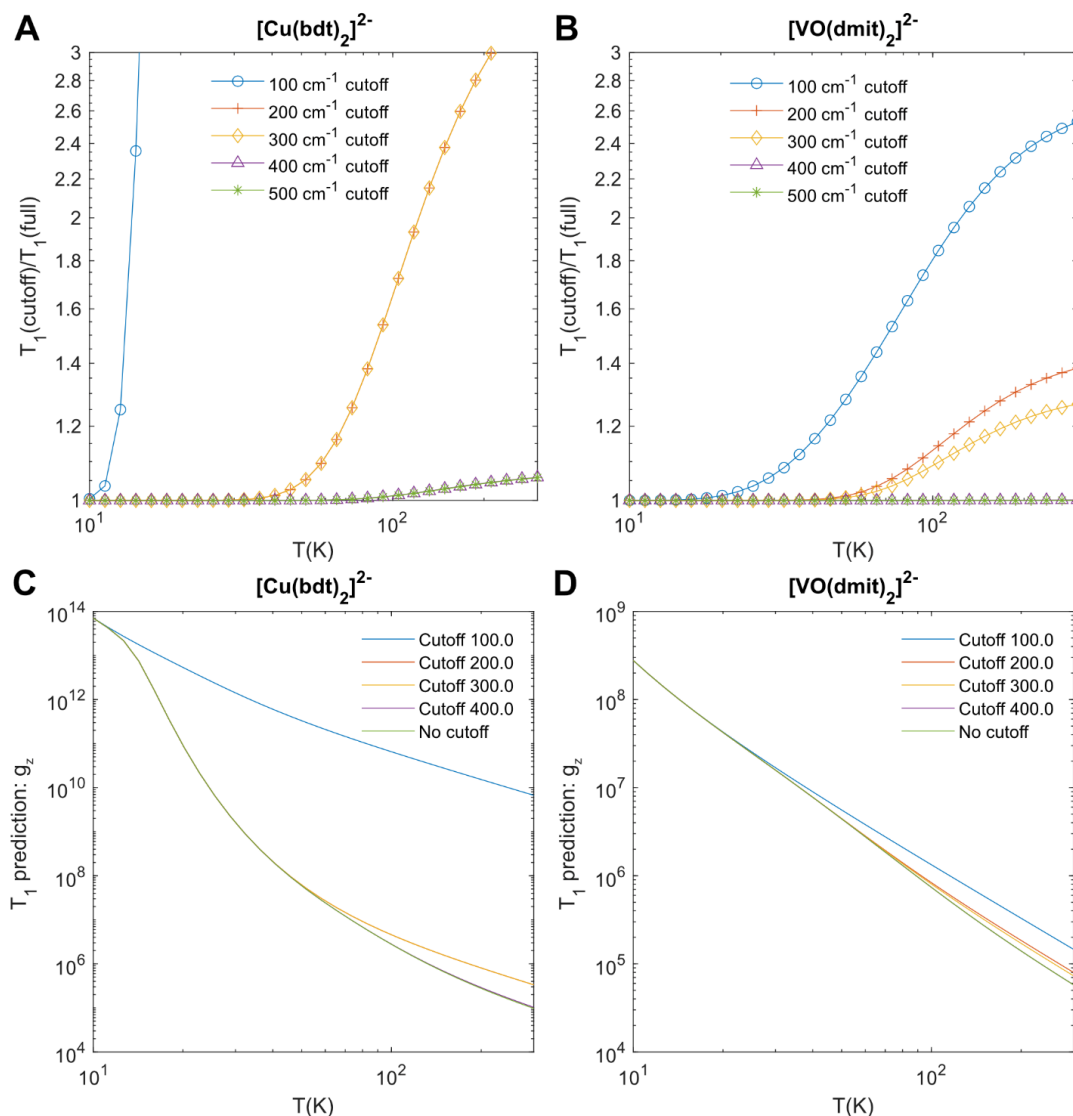


Figure 2-2.S19: Impact of wavenumber cutoff on the thermally-weighted ligand field model T_1 predictions. (A) Ratio of T_1 predictions between variable cutoffs and no cutoffs for $[\text{Cu}(\text{bdt})_2]^{2-}$. Ratios for 200 cm^{-1} cutoff and 300 cm^{-1} cutoff overlap, and ratios for 400 cm^{-1} cutoff and 500 cm^{-1} cutoff overlap. (B) Ratio of T_1 predictions between variable cutoffs and no cutoffs for $[\text{VO}(\text{dmit})_2]^{2-}$. Ratios for 400 cm^{-1} cutoff and 500 cm^{-1} cutoff overlap. (C) Unscaled T_1 predictions using variable wavenumber cutoffs for $[\text{Cu}(\text{bdt})_2]^{2-}$. Predictions for 200 cm^{-1} and 300 cm^{-1} cutoffs overlap, and predictions for 400 cm^{-1} cutoff and no cutoff overlap. (D) Unscaled T_1 predictions using variable wavenumber cutoffs for $[\text{VO}(\text{dmit})_2]^{2-}$. Predictions for 400 cm^{-1} cutoff and no cutoff overlap. All model predictions use the $\partial g_z / \partial Q$ coefficients as in the text. Compared to no cutoff, the 400 cm^{-1} cutoff displays a 5.8% relative error at 300 K for $[\text{Cu}(\text{bdt})_2]^{2-}$ and a 0.13% relative error at 300 K for $[\text{VO}(\text{dmit})_2]^{2-}$.

Scaling of T_1 model predictions

For increased clarity, we here describe the step-by-step process used to scale the T_1 model predictions produced by Equation 2-2.4. We use Figure 2-2.5 as an example. First, both the VOPc and CuPc T_1 predictions are computed according to Equation 2-2.4 in the text, with no scaling factor employed ($A = 1$). The temperature-dependent T_1 curves at this stage already have exactly the same shape and relative rates as displayed in the final Figure 2-2.5 (see Figure 2-2.S20 for the unscaled predictions). These trends are in very good agreement with experiment. However, these T_1 curves do not have units, as all quantities in Equation 4 are dimensionless. To endow the predicted T_1 values with units, we then multiply both the VOPc and CuPc unitless T_1 predictions *by the same scaling factor*. It is, of course, crucial to use the same scaling factor for each data series within a figure to avoid introducing artifacts into the relative T_1 predictions. For Figure 2-2.5, this scaling factor has the numerical value of ($A = 1.32 \times 10^5 \mu\text{s}^{-1}$) for both the VOPc model prediction and the CuPc prediction. After this two-step procedure, we have obtained the finalized temperature-dependent T_1 predictions to plot in Figure 2-2.5. An identical procedure is performed to yield Figure 6, in which the scaling constant used for *all four* datasets has the numerical value ($A = 1.01 \times 10^5 \mu\text{s}^{-1}$). The criteria for obtaining the scaling constants in Figure 2-2.5 and Figure 2-2.6 are given in the figure captions.

The similarity of the scaling constants employed for these different experimental comparisons suggests that a scaling constant of around $A = 1 \times 10^5 \mu\text{s}^{-1}$ may be used to make predictions where experimental data does not exist. We note this value is two orders of magnitude larger than Raman scaling factors reported in a previous study.¹⁷ This discrepancy likely arises from the different choice of g tensor derivatives employed in this work, as detailed in the main text at the end of Section 2-2.2.1. When seeking to make quantitative predictions of T_1 magnitudes, care should be taken to use a scaling factor derived for the elements of the g tensor being used.

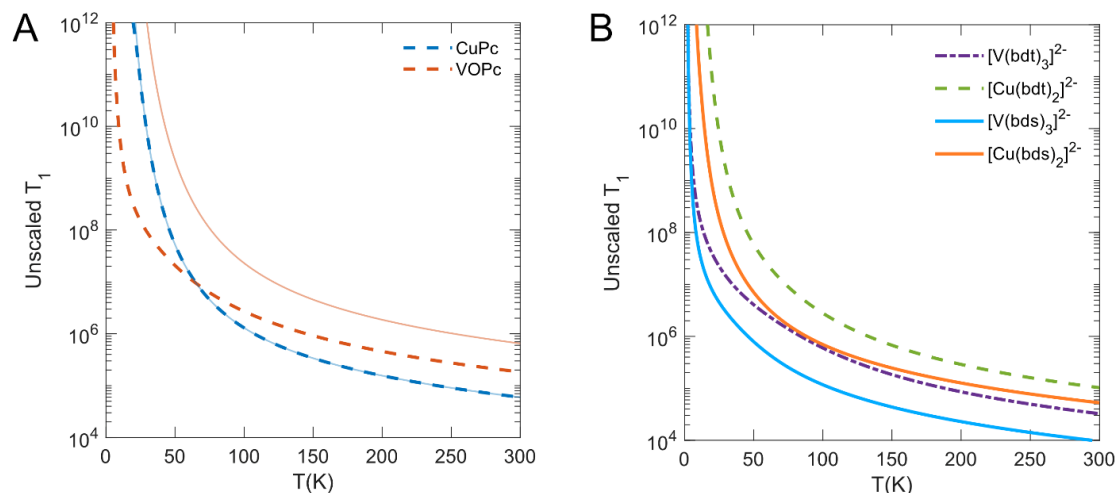


Figure 2-2.S20: Unscaled T_1 predictions corresponding to (A) Figure 2-2.5 in the main text and (B) Figure 2-2.6 in the main text. Plots generated from Equation 4 using g_z spin-phonon coupling coefficients and the trivial scaling factor $A = 1$ for all data series.

6. Tabulation of vibrational modes and spin-phonon coupling coefficients

Table 2-2.S2: Unscaled T_1 predictions for all six molecules in Figures 2-2.5 and 2-2.6, using the trivial scaling factor $A = 1$ in Equation 4.

T (K)	CuPc	VOPc	$[V(bdt)_3]^{2-}$	$[Cu(bdt)_2]^{2-}$	$[V(bds)_3]^{2-}$	$[Cu(bds)_2]^{2-}$
10	2.15E+13	6.05E+09	2.43E+08	7.07E+13	5.20E+07	2.55E+11
20	8.65E+11	2.96E+08	3.89E+07	9.08E+10	7.73E+06	7.92E+08
30	6.65E+09	8.90E+07	1.43E+07	1.60E+09	2.95E+06	7.07E+07
40	3.24E+08	3.97E+07	7.09E+06	2.08E+08	1.44E+06	1.79E+07
50	5.24E+07	2.08E+07	4.08E+06	5.91E+07	7.92E+05	7.05E+06
60	1.55E+07	1.21E+07	2.56E+06	2.42E+07	4.74E+05	3.54E+06
70	6.47E+06	7.62E+06	1.69E+06	1.21E+07	3.07E+05	2.07E+06
80	3.34E+06	5.14E+06	1.16E+06	6.84E+06	2.12E+05	1.35E+06
90	1.99E+06	3.65E+06	8.19E+05	4.23E+06	1.55E+05	9.44E+05
100	1.30E+06	2.71E+06	5.98E+05	2.80E+06	1.17E+05	6.98E+05
110	9.15E+05	2.08E+06	4.50E+05	1.95E+06	9.21E+04	5.38E+05
120	6.77E+05	1.64E+06	3.48E+05	1.43E+06	7.43E+04	4.28E+05
130	5.22E+05	1.33E+06	2.76E+05	1.08E+06	6.12E+04	3.49E+05
140	4.15E+05	1.10E+06	2.23E+05	8.43E+05	5.13E+04	2.91E+05
150	3.39E+05	9.20E+05	1.84E+05	6.75E+05	4.37E+04	2.46E+05
160	2.82E+05	7.83E+05	1.54E+05	5.52E+05	3.77E+04	2.11E+05
170	2.38E+05	6.74E+05	1.31E+05	4.60E+05	3.28E+04	1.83E+05

180	2.05E+05	5.87E+05	1.12E+05	3.89E+05	2.89E+04	1.61E+05
190	1.78E+05	5.16E+05	9.77E+04	3.33E+05	2.56E+04	1.42E+05
200	1.56E+05	4.57E+05	8.57E+04	2.89E+05	2.29E+04	1.27E+05
210	1.38E+05	4.08E+05	7.58E+04	2.53E+05	2.06E+04	1.14E+05
220	1.23E+05	3.66E+05	6.75E+04	2.23E+05	1.86E+04	1.03E+05
230	1.10E+05	3.31E+05	6.06E+04	1.99E+05	1.69E+04	9.32E+04
240	9.98E+04	3.01E+05	5.47E+04	1.78E+05	1.54E+04	8.50E+04
250	9.07E+04	2.74E+05	4.96E+04	1.61E+05	1.41E+04	7.78E+04
260	8.28E+04	2.51E+05	4.52E+04	1.46E+05	1.30E+04	7.16E+04
270	7.59E+04	2.31E+05	4.14E+04	1.33E+05	1.20E+04	6.60E+04
280	6.98E+04	2.13E+05	3.80E+04	1.21E+05	1.11E+04	6.11E+04
290	6.45E+04	1.98E+05	3.51E+04	1.12E+05	1.03E+04	5.67E+04
300	5.97E+04	1.84E+05	3.25E+04	1.03E+05	9.62E+03	5.28E+04

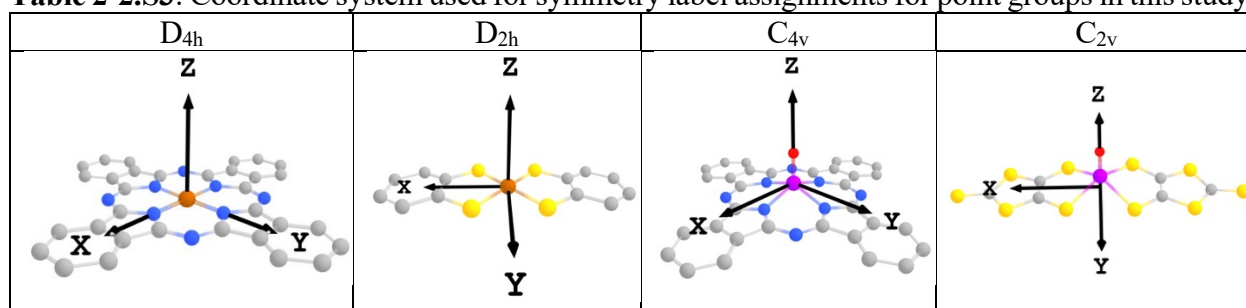
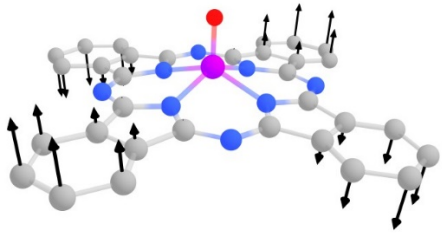
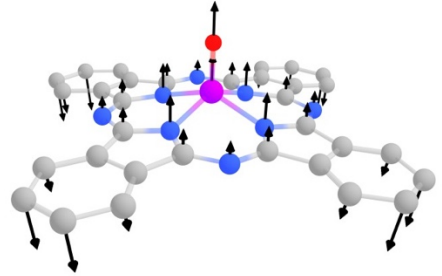
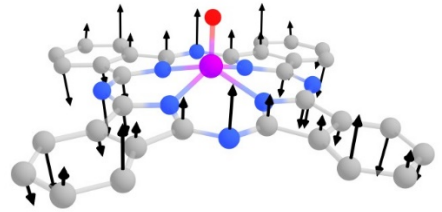
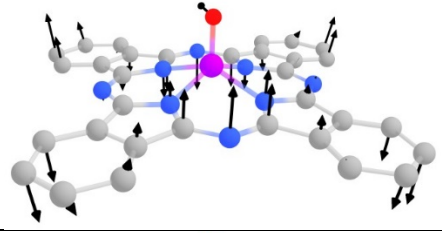
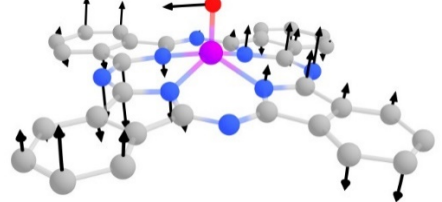
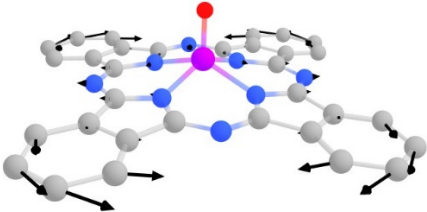
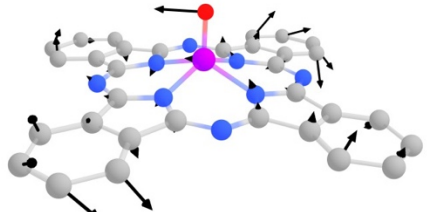
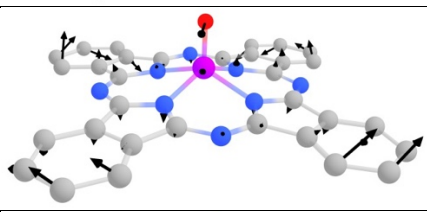
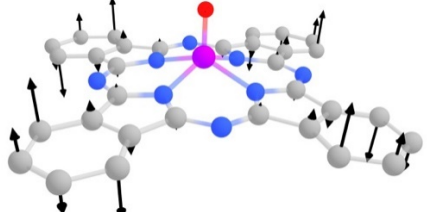
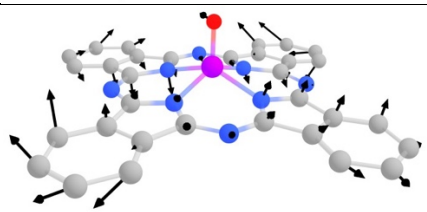
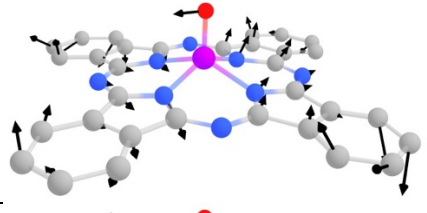
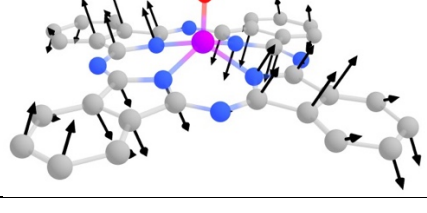
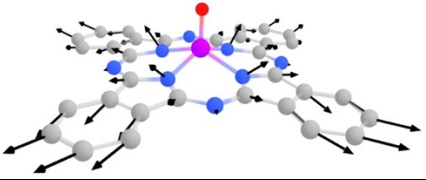
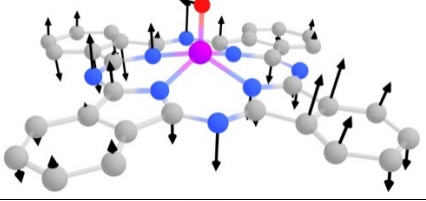
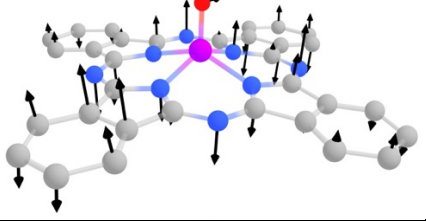
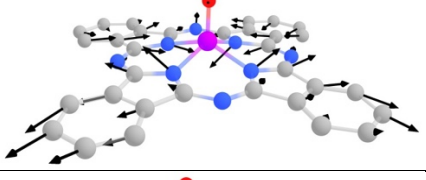
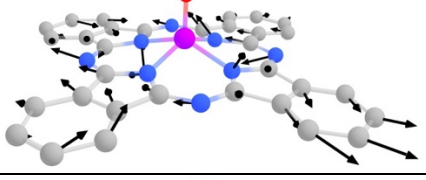
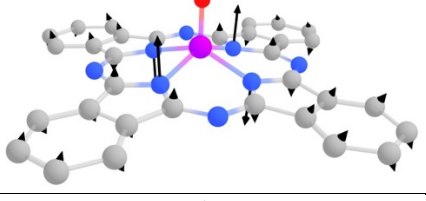
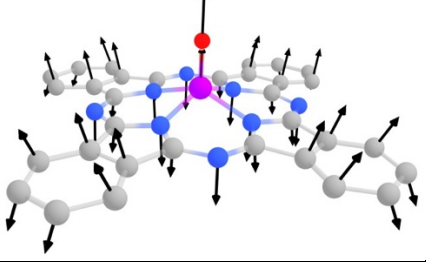
Table 2-2.S3: Coordinate system used for symmetry label assignments for point groups in this study.

Table 2-2.S4: Vibrational modes under 400 cm^{-1} , energies and symmetries of VOPc. Boxes are shaded red when g_z , g_x , and g_y each have symmetry-allowed spin-phonon coupling, and blue when only g_x and g_y have symmetry-allowed spin-phonon coupling, evaluated according to Equation 3b in the text.

Mode #	Displacement vectors	Energy (cm^{-1})	Sym. C_{4v}	$\left(\frac{\partial g_x}{\partial Q}\right)^2$	$\left(\frac{\partial g_y}{\partial Q}\right)^2$	$\left(\frac{\partial g_z}{\partial Q}\right)^2$
1		21.63	b_1	1.2E-09	1.2E-09	0.0E+0 0
2		41.77	a_1	4.0E-12	4.0E-12	5.5E-08
3		58.94	b_2	6.4E-11	1.0E-10	1.0E-12
4		65.34	e	1.0E-12	0.0E+0 0	0.0E+0 0
5		65.35	e	1.0E-12	0.0E+0 0	9.0E-12

6		118.6	b ₂	5.0E-09	4.2E-09	1.0E-12
7		122.14	e	2.5E-11	2.5E-11	1.0E-12
8		122.15	e	2.5E-11	3.6E-11	1.0E-12
9		129.21	a ₂	0.0E+0 0	0.0E+0 0	0.0E+0 0
10		130.96	e	0.0E+0 0	0.0E+0 0	0.0E+0 0
11		130.98	e	1.0E-12	0.0E+0 0	4.0E-12
12		149.5	b ₁	1.5E-09	1.6E-09	0.0E+0 0

13		177.63	a_1	4.5E-09	4.5E-09	1.5E-06
14		181.82	e	0.0E+0 0	0.0E+0 0	9.0E-12
15		181.85	e	0.0E+0 0	0.0E+0 0	2.5E-11
16		187.9	b_1	3.6E-11	1.6E-11	0.0E+0 0
17		226.1	a_2	9.0E-12	4.0E-12	0.0E+0 0
18		233.29	b_2	1.2E-08	1.2E-08	1.0E-12
19		247.76	b_2	1.3E-08	1.3E-08	0.0E+0 0

20		261.76	a_1	5.4E-08	5.4E-08	6.3E-07
21		278.55	e	0.0E+0 0	0.0E+0 0	1.0E-12
22		278.56	e	0.0E+0 0	1.0E-12	1.0E-12
23		306.72	e	1.0E-12	1.0E-12	1.0E-12
24		306.72	e	1.0E-12	0.0E+0 0	4.0E-12
25		315.28	b_1	1.0E-12	1.6E-11	2.5E-11
26		317.31	a_1	7.8E-10	7.8E-10	2.9E-06

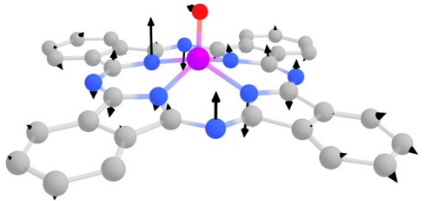
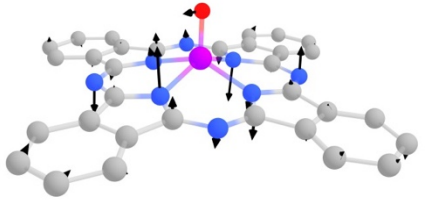
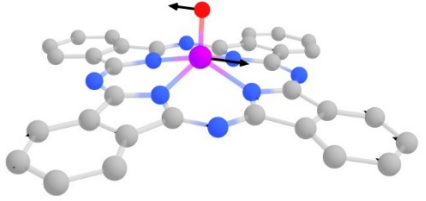
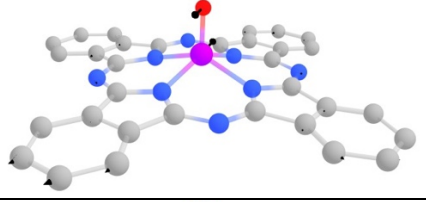
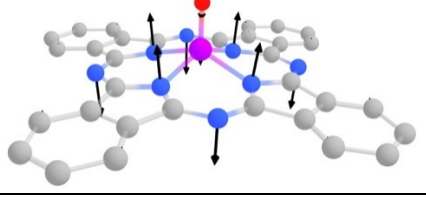
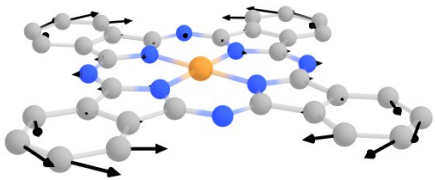
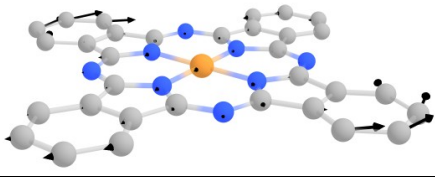
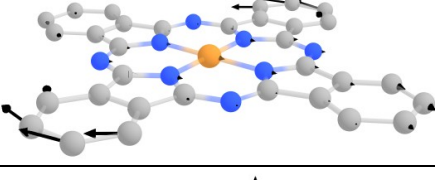
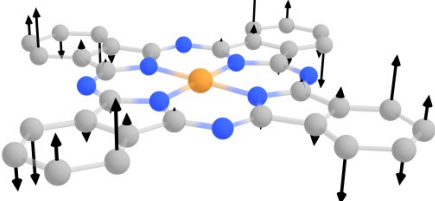
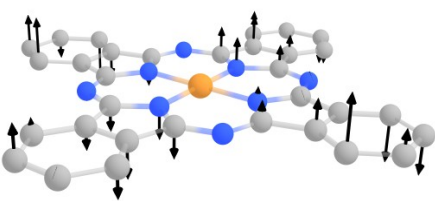
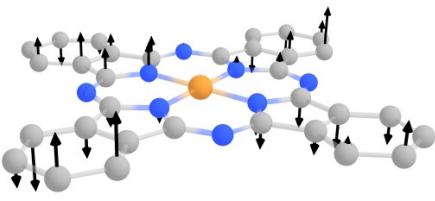
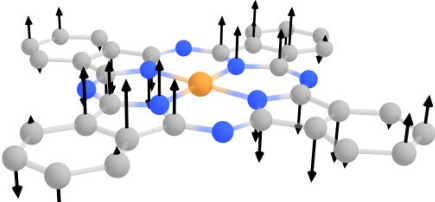
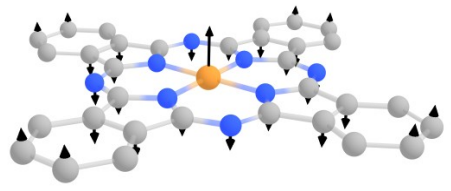
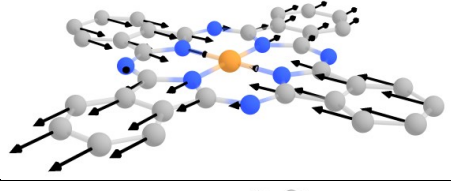
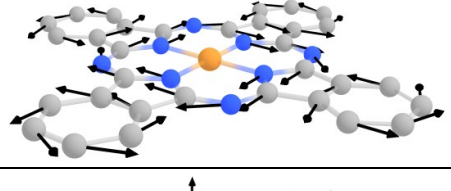
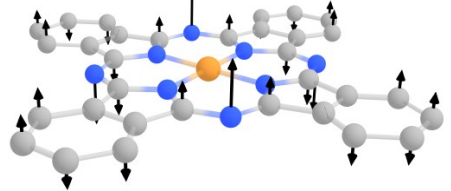
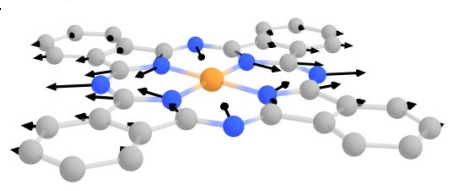
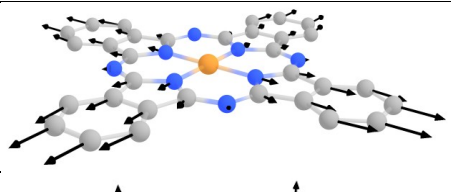
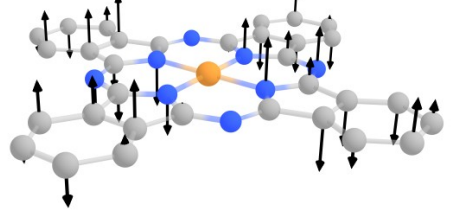
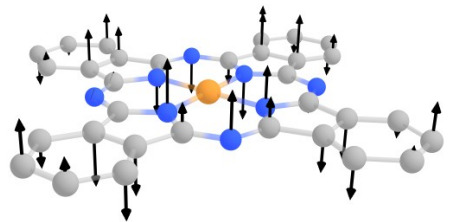
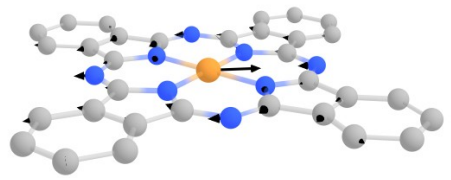
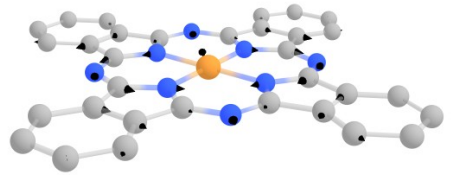
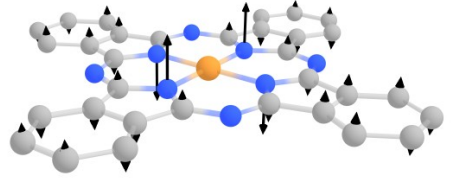
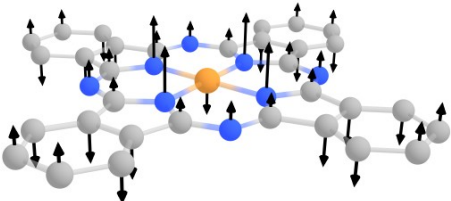
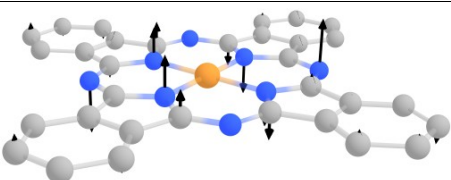
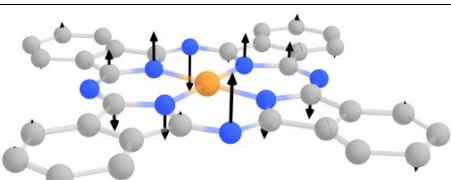
27		333.49	e	9.0E-12	1.6E-11	9.0E-12
28		333.51	e	0.0E+0 0	0.0E+0 0	2.6E-10
29		383.07	e	1.0E-12	1.0E-12	0.0E+0 0
30		383.09	e	1.0E-12	4.0E-12	4.0E-12
31		394.67	a ₁	1.0E-12	1.0E-12	1.9E-06

Table 2-2.S5: Vibrational modes under 400 cm^{-1} , energies and symmetries of CuPc. Boxes are shaded red when g_z , g_x , and g_y each have symmetry-allowed spin-phonon coupling, and blue when only g_x and g_y have symmetry-allowed spin-phonon coupling, evaluated according to Equation 3b in the text.

Mode #	Displacement vectors	Energy (cm^{-1})	Sym. D_{4h}	$\left(\frac{\partial g_x}{\partial Q}\right)^2$	$\left(\frac{\partial g_y}{\partial Q}\right)^2$	$\left(\frac{\partial g_z}{\partial Q}\right)^2$
1		21.73	b_{2u}	1.0E-12	0.0E+00	0.0E+00
2		37.99	a_{2u}	1.0E-12	1.0E-12	9.0E-12
3		58.78	b_{1u}	0.0E+00	0.0E+00	1.0E-12
4		67.23	e_g	1.0E-12	1.0E-12	1.0E-12
5		67.23	e_g	1.0E-12	0.0E+00	4.0E-12

6		116.03	b_{2g}	2.1E-09	1.9E-09	4.0E-12
7		123.31	e_u	1.0E-12	1.0E-12	1.0E-12
8		123.31	e_u	1.0E-12	1.0E-12	9.0E-12
9		127.25	a_{1u}	4.0E-12	4.0E-12	2.5E-11
10		130.91	e_g	4.0E-12	4.0E-12	3.6E-11
11		130.91	e_g	0.0E+00	0.0E+00	0.0E+00
12		145.07	b_{2u}	1.0E-12	1.0E-12	2.5E-11

13		155.18	a_{2u}	1.0E-12	4.0E-12	2.5E-11
14		175.18	b_{1g}	1.4E-06	1.4E-06	1.6E-11
15		219	a_{2g}	1.0E-12	1.0E-12	1.0E-12
16		233.18	b_{1u}	1.0E-12	1.0E-12	0.0E+00
17		239.17	b_{2g}	1.2E-08	1.1E-08	1.0E-12
18		261.73	a_{1g}	2.5E-06	2.5E-06	2.8E-05
19		263.78	e_g	0.0E+00	1.0E-12	1.0E-12

20		263.78	e_g	0.0E+00	0.0E+00	1.0E-12
21		290.98	e_u	0.0E+00	0.0E+00	0.0E+00
22		290.98	e_u	1.0E-12	1.0E-12	3.6E-11
23		293.37	b_{2u}	1.0E-12	1.0E-12	1.6E-11
24		296.91	a_{2u}	1.0E-12	1.0E-12	9.0E-12
25		305.09	e_g	0.0E+00	1.0E-12	4.0E-12
26		305.09	e_g	4.0E-12	4.0E-12	1.6E-11

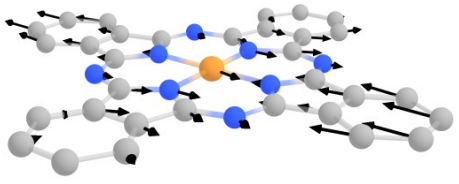
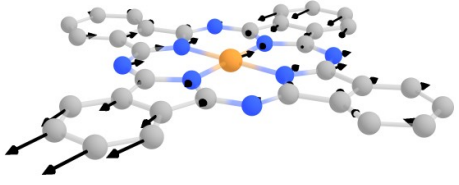
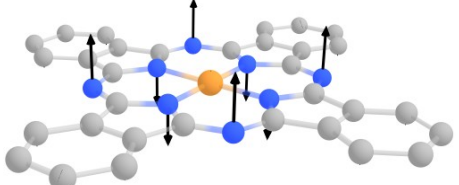
27		308.99	e_u	4.0E-12	1.0E-12	1.6E-11
28		308.99	e_u	0.0E+00	0.0E+00	0.0E+00
29		375.81	a_{2u}	0.0E+00	0.0E+00	1.0E-12

Table 2-2.S6: Vibrational modes under 400 cm^{-1} , energies and symmetries of $[\text{Cu}(\text{bdt})_2]^{2-}$. Boxes are shaded red when g_z , g_x , and g_y each have symmetry-allowed spin-phonon coupling, and blue when only g_x and g_y have symmetry-allowed spin-phonon coupling.

Mode #	Displacement vectors	Energy (cm^{-1})	Sym. D_{2h}	$\left(\frac{\partial g_x}{\partial Q}\right)^2$	$\left(\frac{\partial g_y}{\partial Q}\right)^2$	$\left(\frac{\partial g_z}{\partial Q}\right)^2$
1		-106.3	a_u	0.0E+00	0.0E+00	0.0E+00
2		-89.67	b_{2g}	6.4E-11	1.0E-09	3.2E-08
3		-63.04	b_{1u}	0.0E+00	0.0E+00	0.0E+00
4		30.85	b_{2u}	0.0E+00	0.0E+00	1.0E-12
5		72.88	a_u	0.0E+00	0.0E+00	0.0E+00
6		87.72	b_{1u}	0.0E+00	0.0E+00	1.0E-12
7		88.08	b_{3g}	2.5E-11	9.0E-12	1.6E-11
8		174.46	a_g	2.7E-07	1.5E-07	2.0E-06
9		192.23	b_{1g}	1.6E-11	0.0E+00	1.0E-12
10		199.14	b_{2g}	4.4E-10	1.4E-10	4.8E-08

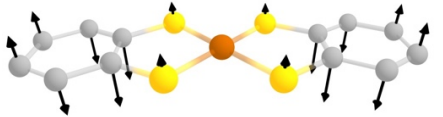
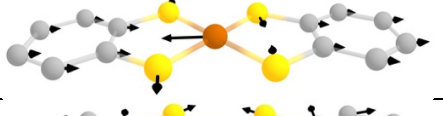
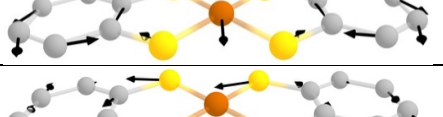
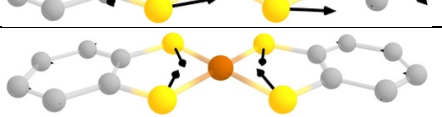

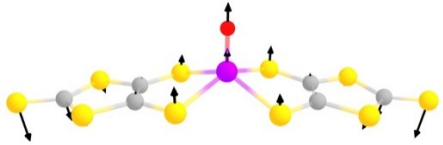
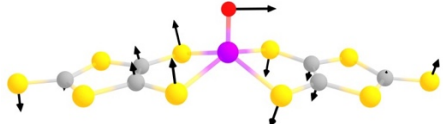

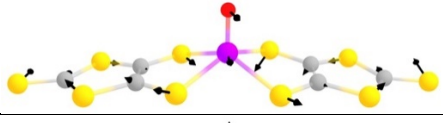
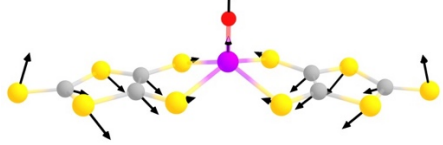
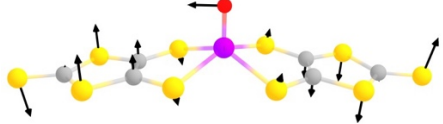
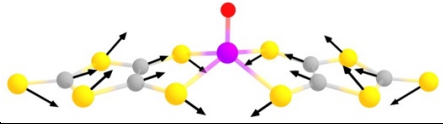
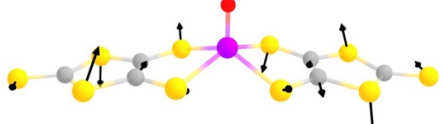
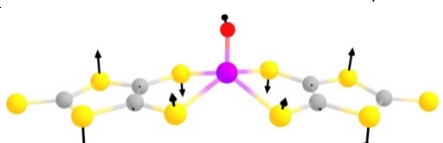
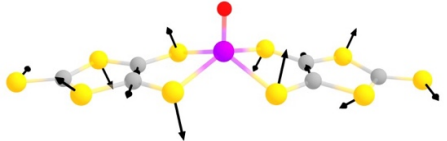
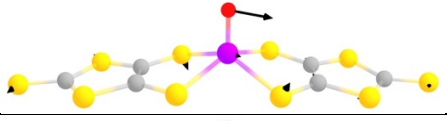
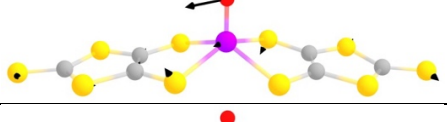
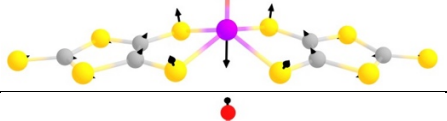
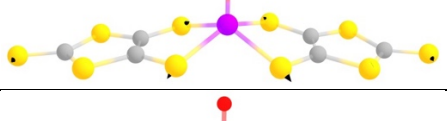
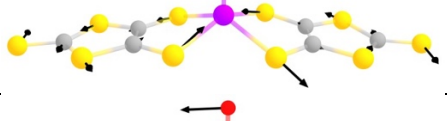
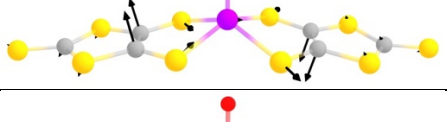
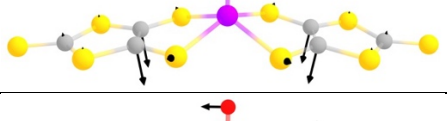
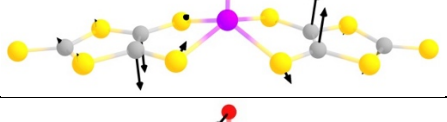
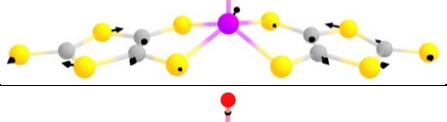
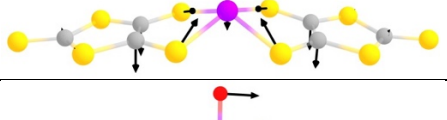
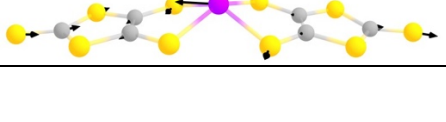
11		215.4	b_{1u}	0.0E+00	0.0E+00	1.0E-12
12		238.12	b_{3u}	0.0E+00	0.0E+00	0.0E+00
13		285.3	b_{2u}	0.0E+00	0.0E+00	1.0E-12
14		370.21	b_{1g}	5.8E-09	7.6E-09	1.0E-07
15		378.41	a_g	1.6E-06	1.9E-06	2.7E-05

Table 2-2.S7: Vibrational modes under 400 cm^{-1} , energies and symmetries of $[\text{VO}(\text{dmit})_2]^{2-}$. Boxes are shaded red when g_z , g_x , and g_y each have symmetry-allowed spin-phonon coupling, and blue when only g_x and g_y have symmetry-allowed spin-phonon coupling.

Mode #	Displacement vectors	Energy (cm^{-1})	Sym. C_{2v}	$\left(\frac{\partial g_x}{\partial Q}\right)^2$	$\left(\frac{\partial g_y}{\partial Q}\right)^2$	$\left(\frac{\partial g_z}{\partial Q}\right)^2$
1		16.88	a_1	6.7E-09	1.5E-08	2.5E-08
2		25.82	b_1	0.0E+00	1.0E-12	0.0E+00
3		32.04	a_2	7.3E-10	9.0E-10	5.0E-08
4		45.6	b_2	0.0E+00	0.0E+00	0.0E+00
5		96.39	a_1	4.1E-08	5.5E-09	9.4E-08
6		97.06	b_1	9.0E-12	9.0E-12	1.0E-12
7		107.73	a_1	8.9E-08	2.4E-09	5.0E-07
8		111.87	a_2	1.8E-09	1.7E-10	2.1E-08
9		120.78	b_2	9.0E-12	4.0E-12	1.0E-12

10		147.1	a_2	1.0E-10	1.2E-09	4.4E-09
11		172.52	$\sim b_1, b_2$	1.0E-12	1.0E-12	1.0E-12
12		178.11	$\sim b_1, b_2$	1.0E-12	0.0E+00	0.0E+00
13		181.82	a_1	1.4E-09	1.2E-10	2.8E-06
14		233.09	b_2	1.0E-12	1.0E-12	0.0E+00
15		238.81	a_2	2.9E-10	4.0E-12	2.0E-08
16		259.47	b_1	6.8E-10	7.3E-10	9.0E-12
17		285.56	a_1	4.7E-08	8.6E-08	2.3E-06
18		295.06	b_1	6.4E-11	6.4E-11	4.0E-12
19		312.9	b_2	0.0E+00	0.0E+00	0.0E+00
20		321.93	a_1	1.1E-07	5.2E-07	9.4E-06
21		325.12	b_1	1.8E-09	1.9E-09	4.0E-12

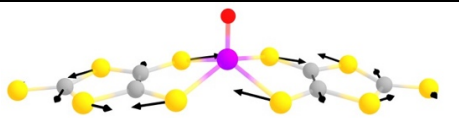
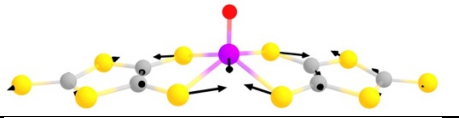
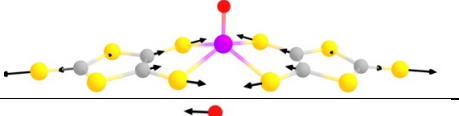
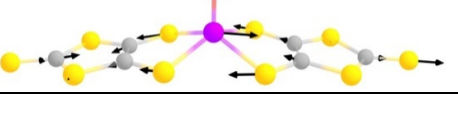
22		341.23	a ₂	1.5E-09	4.0E-09	5.8E-08
23		360.8	b ₂	0.0E+00	0.0E+00	0.0E+00
24		368.96	a ₁	4.8E-08	4.8E-10	4.4E-07
25		382.18	b ₁	1.8E-09	1.8E-09	1.6E-11

Table 2-2.S8: Spin-phonon coupling coefficients for $[\text{Cu}(\text{bds})_2]^{2-}$ for modes below 400 cm^{-1} .

Mode Frequency (cm^{-1})	$\left(\frac{\partial g_x}{\partial Q}\right)^2$	$\left(\frac{\partial g_y}{\partial Q}\right)^2$	$\left(\frac{\partial g_z}{\partial Q}\right)^2$
-61.74	1.0E-12	9.0E-12	0.0E+00
-35.05	2.9E-10	2.2E-06	5.5E-09
-29.63	0.0E+00	2.5E-11	1.0E-12
31.62	1.0E-12	3.6E-11	0.0E+00
57.97	1.5E-09	3.5E-08	1.0E-08
58.34	1.0E-12	1.0E-10	2.5E-11
97.75	4.0E-12	4.9E-11	2.5E-11
103.65	7.4E-07	2.6E-06	1.1E-06
107.54	3.1E-07	5.1E-07	4.8E-07
156.77	1.0E-12	9.0E-12	4.0E-12
187.04	8.5E-08	3.2E-06	2.2E-07
197.71	2.2E-10	2.3E-10	1.1E-09
199.3	4.4E-06	4.0E-06	1.1E-05
222.13	4.0E-12	1.0E-12	4.0E-12
244.77	8.8E-09	2.9E-09	2.8E-08
253.79	0.0E+00	4.0E-12	1.0E-12
281.76	4.0E-12	1.6E-11	1.0E-12
363.5	1.1E-08	1.0E-07	5.1E-08
373.47	2.5E-09	2.4E-09	6.8E-10
373.87	3.0E-07	2.9E-07	1.1E-07
375.71	1.6E-11	2.5E-11	9.0E-12

Table 2-2.S9: Spin-phonon coupling coefficients for $[\text{V}(\text{bdt})_3]^{2-}$ for modes below 400 cm^{-1} .

Mode Frequency (cm^{-1})	$\left(\frac{\partial g_x}{\partial Q}\right)^2$	$\left(\frac{\partial g_y}{\partial Q}\right)^2$	$\left(\frac{\partial g_z}{\partial Q}\right)^2$
16.49	2.6E-07	4.1E-07	2.9E-08
24.68	2.8E-07	2.3E-07	1.4E-08
39.29	5.0E-08	7.1E-10	2.6E-09
59.89	4.3E-08	8.4E-08	1.0E-10
66.72	2.9E-06	2.9E-06	1.4E-07
74.34	2.4E-09	8.3E-07	1.2E-07
115.62	1.6E-07	2.4E-08	8.3E-10
123.6	2.5E-06	8.1E-07	1.1E-07
136.51	9.8E-09	4.7E-08	5.8E-08
150.11	3.8E-07	5.2E-07	6.7E-07
152.4	3.0E-09	1.1E-08	3.9E-08
156.21	1.6E-07	9.4E-08	7.3E-07
181.22	5.0E-06	4.0E-06	5.4E-08
192.41	3.4E-08	2.4E-08	6.4E-08
195.58	2.4E-07	2.2E-08	1.9E-08
251.59	4.5E-08	3.1E-08	6.8E-09
255.2	2.6E-08	2.2E-07	5.5E-08
264.63	8.0E-08	2.8E-09	1.5E-08
284.49	1.2E-06	9.0E-07	5.7E-07
289.34	2.4E-08	8.3E-09	2.6E-07
301.33	1.1E-07	7.5E-08	7.0E-09
351.66	6.0E-06	3.1E-05	5.0E-05
354.97	3.3E-05	8.9E-06	7.3E-06
368.04	2.0E-06	6.6E-07	4.4E-06
391.87	5.1E-09	7.2E-10	1.0E-07
393.56	2.1E-06	4.2E-06	2.8E-08

Table 2-2.S10: Spin-phonon coupling coefficients for $[\text{V}(\text{bds})_3]^{2-}$ for modes below 400 cm^{-1} .

Mode Frequency (cm^{-1})	$\left(\frac{\partial g_x}{\partial Q}\right)^2$	$\left(\frac{\partial g_y}{\partial Q}\right)^2$	$\left(\frac{\partial g_z}{\partial Q}\right)^2$
-36.7	1.8E-09	1.2E-08	6.8E-10
-35.44	4.6E-09	7.4E-07	7.1E-08
-24.43	7.8E-10	4.9E-11	0.0E+00
-22.02	8.8E-06	6.8E-06	1.2E-07
-13.3	1.2E-09	3.1E-09	2.2E-10
21.11	1.3E-06	3.0E-08	3.3E-07
70.98	1.0E-10	6.3E-10	6.4E-11
74.21	5.0E-08	2.6E-06	3.6E-07
87.28	6.9E-09	8.5E-09	9.0E-10
89.16	1.1E-06	9.0E-07	2.4E-07
90.5	2.0E-10	0.0E+00	1.0E-10
97.97	3.2E-07	3.8E-07	2.2E-07
124.24	7.3E-06	8.1E-06	1.1E-08
127.34	3.3E-07	1.6E-09	3.8E-07
127.45	1.2E-08	2.9E-10	4.9E-09
175.32	4.4E-08	4.1E-07	2.9E-06
176.58	1.0E-12	6.4E-11	1.1E-09
190.18	3.6E-11	2.5E-11	9.0E-12
198.54	2.6E-05	2.4E-05	5.3E-05
202.4	2.1E-07	6.9E-09	9.7E-08
205.68	2.5E-11	6.4E-11	9.0E-12
232.2	4.0E-12	4.9E-11	4.9E-11
245.69	2.2E-06	3.8E-06	5.8E-07
246.65	3.6E-09	7.1E-09	1.0E-09
290.22	4.1E-05	2.4E-05	4.7E-07
304.1	1.0E-12	4.0E-12	9.0E-12
311.12	1.0E-12	9.0E-12	8.1E-11
367.11	3.6E-09	1.9E-07	2.6E-06
367.56	1.1E-09	7.2E-09	6.1E-07
367.65	1.4E-09	2.5E-11	1.5E-09
371.11	4.0E-12	1.4E-10	7.8E-10
374.73	1.5E-09	4.0E-09	7.0E-08
379.45	4.0E-12	1.0E-12	9.0E-12

Group theory tables

Table 2-2.S11: Correlation table for point groups pertaining to this study. Adapted from Atkins.²⁴

D_{4h}	$D_{2d} (C_2'' \rightarrow C_2')$	$D_{2h} (C_2'')$	C_{4v}	$C_{2v} (C_2, \sigma_d)$
A_{1g}	A_1	A_g	A_1	A_1
A_{2g}	A_2	B_{1g}	A_2	A_2
B_{1g}	B_2	B_{1g}	B_1	A_2
B_{2g}	B_1	A_g	B_2	A_1
E_g	E	$B_{2g} + B_{3g}$	E	$B_1 + B_2$
A_{1u}	B_1	A_u	A_2	A_2
A_{2u}	B_2	B_{1u}	A_1	A_1
B_1	A_2	B_{1u}	B_2	A_1
B_{2u}	A_1	A_u	B_1	A_2
E_u	E	$B_{2u} + B_{3u}$	E	$B_1 + B_2$

Table 2-2.S12: Direct products for groups D_4 , C_{4v} , D_{2d} (and $D_{4h} = D_4 + C_i$). Antisymmetric products are presented in square brackets []; otherwise, the products are symmetric.

	A_1	A_2	B_1	B_2	E
A_1	A_1	A_2	B_1	B_2	E
A_2		A_1	B_2	B_1	E
B_1			A_1	A_2	E
B_2				A_1	E
E					$A_1 + [A_2] + B_1 + B_2$

Table 2-2.S13: Character table and basis functions for the groups D_4 , C_{4v} , and D_{2d} .

	D_4	E	\bar{E}	$2C_4$	$2\bar{C}_4$	C_2 \bar{C}_2	$2C_2'$ $2\bar{C}_2'$	$2C_2''$ $2\bar{C}_2''$
	C_{4v}	E	\bar{E}	$2C_4$	$2\bar{C}_4$	C_2 \bar{C}_2	$2\sigma_v$ $2\bar{\sigma}_v$	$2\sigma_d$ $2\bar{\sigma}_d$
	D_{2d}	E	\bar{E}	$2S_4$	$2\bar{S}_4$	C_2 \bar{C}_2	$2C_2'$ $2\bar{C}_2'$	$2\sigma_d$ $2\bar{\sigma}_d$
A_1	Γ_1	1	1	1	1	1	1	1
A_2	Γ_2	1	1	1	1	1	-1	-1
B_1	Γ_3	1	1	-1	-1	1	1	-1
B_2	Γ_4	1	1	-1	-1	1	-1	1
E	Γ_5	2	2	0	0	-2	0	0
$S = 1/2$	Γ_6	2	-2	$\sqrt{2}$	$-\sqrt{2}$	0	0	0
	Γ_7	2	-2	$-\sqrt{2}$	$\sqrt{2}$	0	0	0

Table 2-2.S14: Multiplication table for the groups D_4 , C_{4v} and D_{2d} . Adapted from Koster, Dimmock, Wheeler and Statz.²⁵

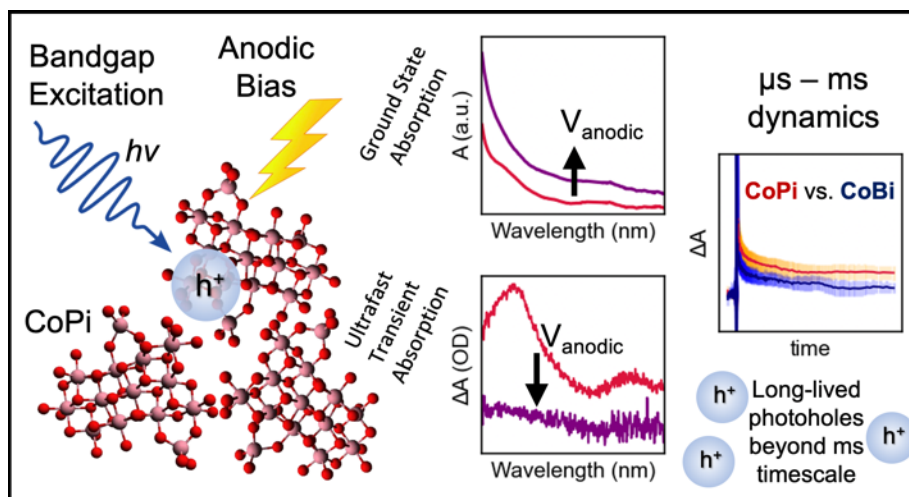
Γ_1	Γ_2	Γ_3	Γ_4	Γ_5	Γ_6	Γ_7	
Γ_1	Γ_2	Γ_3	Γ_4	Γ_5	Γ_6	Γ_7	Γ_1
	Γ_1	Γ_4	Γ_3	Γ_5	Γ_6	Γ_7	Γ_2
		Γ_1	Γ_2	Γ_5	Γ_7	Γ_6	Γ_3
			Γ_1	Γ_5	Γ_5	Γ_6	Γ_4
				$\Gamma_1 + \Gamma_2$ $+ \Gamma_3 + \Gamma_4$	$\Gamma_6 + \Gamma_7$	$\Gamma_6 + \Gamma_7$	Γ_5
					$\Gamma_1 + \Gamma_2$ $+ \Gamma_5$	$\Gamma_3 + \Gamma_4$ $+ \Gamma_5$	Γ_6
						$\Gamma_1 + \Gamma_2$ $+ \Gamma_5$	Γ_7

References

- (1) Neese, F. The ORCA Program System. *WIREs Comput. Mol. Sci.* **2012**, *2* (1), 73–78. <https://doi.org/10.1002/wcms.81>.
- (2) Neese, F. Software Update: The ORCA Program System, Version 4.0. *WIREs Comput. Mol. Sci.* **2018**, *8* (1), e1327. <https://doi.org/10.1002/wcms.1327>.
- (3) Neese, F. Prediction of Electron Paramagnetic Resonance g Values Using Coupled Perturbed Hartree–Fock and Kohn–Sham Theory. *J. Chem. Phys.* **2001**, *115* (24), 11080–11096. <https://doi.org/10.1063/1.1419058>.
- (4) Becke, A. D. A New Mixing of Hartree–Fock and Local Density-functional Theories. *J. Chem. Phys.* **1993**, *98* (2), 1372–1377. <https://doi.org/10.1063/1.464304>.
- (5) Lee, C.; Yang, W.; Parr, R. G. Development of the Colle-Salvetti Correlation-Energy Formula into a Functional of the Electron Density. *Phys. Rev. B* **1988**, *37* (2), 785–789. <https://doi.org/10.1103/PhysRevB.37.785>.
- (6) Vosko, S. H.; Wilk, L.; Nusair, M. Accurate Spin-Dependent Electron Liquid Correlation Energies for Local Spin Density Calculations: A Critical Analysis. *Can. J. Phys.* **2011**. <https://doi.org/10.1139/p80-159>.
- (7) Stephens, P. J.; Devlin, F. J.; Chabalowski, C. F.; Frisch, M. J. Ab Initio Calculation of Vibrational Absorption and Circular Dichroism Spectra Using Density Functional Force Fields. *J. Phys. Chem.* **1994**, *98* (45), 11623–11627. <https://doi.org/10.1021/j100096a001>.
- (8) Follmer, A. H.; Ribson, R. D.; Oyala, P. H.; Chen, G. Y.; Hadt, R. G. Understanding Covalent versus Spin–Orbit Coupling Contributions to Temperature-Dependent Electron Spin Relaxation in Cupric and Vanadyl Phthalocyanines. *J. Phys. Chem. A* **2020**, *124* (44), 9252–9260. <https://doi.org/10.1021/acs.jpca.0c07860>.
- (9) Atzori, M.; Morra, E.; Tesi, L.; Albino, A.; Chiesa, M.; Sorace, L.; Sessoli, R. Quantum Coherence Times Enhancement in Vanadium(IV)-Based Potential Molecular Qubits: The Key Role of the Vanadyl Moiety. *J Am Chem Soc* **2016**, *11*.
- (10) Fataftah, M. S.; Krzyaniak, M. D.; Vlaisavljevich, B.; Wasielewski, M. R.; Zadrozny, J. M.; Freedman, D. E. Metal–Ligand Covalency Enables Room Temperature Molecular Qubit Candidates. *Chem. Sci.* **2019**, *10* (27), 6707–6714. <https://doi.org/10.1039/C9SC00074G>.
- (11) Mirzoyan, R.; Hadt, R. G. The Dynamic Ligand Field of a Molecular Qubit: Decoherence through Spin–Phonon Coupling. *Phys. Chem. Chem. Phys.* **2020**, *22* (20), 11249–11265. <https://doi.org/10.1039/D0CP00852D>.
- (12) Szilagyi, R. K.; Metz, M.; Solomon, E. I. Spectroscopic Calibration of Modern Density Functional Methods Using [CuCl₄]²⁻. *J. Phys. Chem. A* **2002**, *106* (12), 2994–3007. <https://doi.org/10.1021/jp014121c>.
- (13) Ziolo, R. F.; Griffiths, C. H.; Troup, J. M. Crystal Structure of Vanadyl Phthalocyanine, Phase II. *J. Chem. Soc. Dalton Trans.* **1980**, No. 11, 2300. <https://doi.org/10.1039/dt9800002300>.
- (14) Ramadan, A. J.; Rochford, L. A.; Keeble, D. S.; Sullivan, P.; Ryan, M. P.; Jones, T. S.; Heutz, S. Exploring High Temperature Templating in Non-Planar Phthalocyanine/Copper Iodide (111) Bilayers. *J. Mater. Chem. C* **2014**, *3* (2), 461–465. <https://doi.org/10.1039/C4TC02116A>.

- (15) Jr, E. B. W.; Decius, J. C.; Cross, P. C. *Molecular Vibrations: The Theory of Infrared and Raman Vibrational Spectra*, Revised ed. edition.; Dover Publications: New York, 1980.
- (16) Neese, F.; Wennmohs, F. ORCA Manual Version 4.2.1. 2019.
- (17) Santanni, F.; Albino, A.; Atzori, M.; Ranieri, D.; Salvadori, E.; Chiesa, M.; Lunghi, A.; Bencini, A.; Sorace, L.; Totti, F.; Sessoli, R. Probing Vibrational Symmetry Effects and Nuclear Spin Economy Principles in Molecular Spin Qubits. *Inorg. Chem.* **2021**, *60* (1), 140–151. <https://doi.org/10.1021/acs.inorgchem.0c02573>.
- (18) Harris, D. C.; Bertolucci, M. D. *Symmetry and Spectroscopy: An Introduction to Vibrational and Electronic Spectroscopy*, New edition.; Dover Publications: New York, 1989.
- (19) Standley, K. J.; Vaughan, R. A. *Electron Spin Relaxation Phenomena in Solids*; Springer US: Boston, MA, 1969. <https://doi.org/10.1007/978-1-4899-6539-4>.
- (20) Du, J. L.; Eaton, G. R.; Eaton, S. S. Temperature, Orientation, and Solvent Dependence of Electron Spin-Lattice Relaxation Rates for Nitroxyl Radicals in Glassy Solvents and Doped Solids. *J. Magn. Reson. A* **1995**, *115* (2), 213–221. <https://doi.org/10.1006/jmra.1995.1169>.
- (21) Konda, R.; Du, J.-L.; Eaton, S. S.; Eaton, G. R. Electron Spin Relaxation Rates for Nitridochromium(V) Tetratolylporphyrin and Nitridochromium(V) Octaethylporphyrin in Frozen Solution. *Appl. Magn. Reson.* **1994**, *7* (2–3), 185–193. <https://doi.org/10.1007/BF03162611>.
- (22) Du, J. L.; Eaton, G. R.; Eaton, S. S. Electron-Spin-Lattice Relaxation in Natural Abundance and Isotopically Enriched Oxo-Chromium(V)Bis (2-Hydroxy-2-Ethylbutyrate). *J. Magn. Reson. A* **1995**, *115* (2), 236–240. <https://doi.org/10.1006/jmra.1995.1172>.
- (23) Du, J.-L.; Eaton, G. R.; Eaton, S. S. Temperature and Orientation Dependence of Electron-Spin Relaxation Rates for Bis(Diethyldithiocarbamate)Copper(II). *J. Magn. Reson. A* **1995**, *117* (1), 67–72. <https://doi.org/10.1006/jmra.1995.9971>.
- (24) Atkins, P. W.; Child, M. S.; Phillips, C. S. G. *Tables for Group Theory*; Oxford University Press: Oxford, 1970; Vol. 6.
- (25) Koster, G. F.; Dimmock, J. O.; Wheeler, R. G.; Statz, H. *Properties of the Thirty Two Point Groups (Research Monograph)*; The MIT Press, 1963.

STEADY-STATE AND ULTRAFAST SPECTROELECTROCHEMICAL INVESTIGATIONS OF AMORPHOUS OXYGEN-EVOLVING COBALT OXIDE FILMS



Adapted with permission from:

Mirzoyan, R.; Follmer, A. H.; Hadt, R. G. Observing Long-Lived Photogenerated Holes in Cobalt Oxyhydroxide Oxygen Evolution Catalysts. *ACS Appl. Energy Mater.* **2024**, 7 (7), 2837–2846. <https://doi.org/10.1021/acsaem.3c03269>.

Copyright 2024 American Chemical Society.

Abstract

Steady state and time-resolved spectroelectrochemical optical absorption techniques were used to investigate photoexcited states of amorphous cobalt-phosphate oxyhydroxide (CoPi) and cobalt-borate oxyhydroxide (CoBi) oxygen evolution catalysts. These materials revealed concurrent spectroelectrochemical intensity changes in their ground-state and photoexcited visible spectra, providing insights into the dynamics of defect states attributable to trapped holes. Notably, long-lived photoexcited states, assignable to hole-based defects persisting beyond 10 ms in H₂O, were observed in CoPi and CoBi for the first time. With ~380 nm bandgap excitation and delays shorter than 10 ps, excited-state decay for CoPi was markedly faster than CoBi, despite the ultimately longer-lived signal of CoPi beyond the ms timescale. The distinct kinetic profiles highlight the films' differences in structural and electronic properties despite strong similarities in absorption spectral profiles. These results provide further insight into the differences between the electronic properties and dynamics of CoPi and CoBi, which have been challenging to structurally and electronically characterize due to their amorphous nature.

Introduction

Materials and devices that harvest photon energy and convert H₂O into fuel in the form of H₂ provide a promising avenue to an alternative renewable energy infrastructure.¹⁻³ The oxygen evolution reaction (OER) is a key bottleneck to the water-splitting process, with many historically successful catalysts being comprised of expensive, non-earth-abundant metals.⁴ Amorphous cobalt-phosphate oxyhydroxide (CoPi) is a self-healing oxygen-evolving catalyst with a low overpotential at neutral pH.^{5,6} It has been integrated with a variety of semiconductor-based light-harvesting materials⁷⁻¹⁴ and is a key component of the ‘Artificial Leaf,’ a triple-junction amorphous silicon photovoltaic with a ternary alloy and CoPi interfaced on either side for the hydrogen and oxygen evolution half-reactions, respectively.⁷ This device proved to be extremely robust, operating in natural water conditions for days with no decline in activity.

Until recently, the photophysical properties of CoPi have not been considered in detail. Sprague-Klein et al. demonstrated direct photochemical effects on the OER through wavelength-dependent electrochemical responses with either 415 nm or 623 nm LED irradiation.¹⁵ With 415 nm excitation, the overpotential increased, while the opposite effect was observed for 623 nm excitation. These effects were attributed to photoinduced redistributions of electron density within Co–O bonds, with shifts toward oxygen improving the surface oxo reactivity previously implicated in the mechanism of O–O bond formation.^{6,16-19}

In addition to CoPi, electrodeposited thin films from borate buffer (CoBi) have provided comparative insights into thin film formation and stability.²⁰ Cyclic voltammograms of thin films in their respective buffers show Co(II)/Co(III) quasi-reversible redox features at 1.05 V vs. NHE (CoPi) and 0.88 V vs. NHE (CoBi) (Figure 3.1).²¹ There also exists a Co(III)/Co(IV) redox feature near the onset of the OER catalytic wave, with Co(IV) formation representing a mechanistic prerequisite for catalysis. Interestingly, Costentin et al. have also correlated the presence of high valent Co(IV) to a semiconductor-type charge transport in the thin film. Relatedly, it was further observed that the proton-electron conductivity increases with applied anodic potential and is higher for CoBi than CoPi.²¹

These electrochemical and conductivity differences have been related to the distinct morphologies of CoPi and CoBi.^{16,21,22} Co K-edge extended X-ray absorption fine structure (EXAFS) data suggested both films are comprised of edge-sharing MO₆ clusters of molecular dimensions.^{19,23,24} Pair distribution function (PDF) analysis further revealed that the intermediate-range structure differs substantially between CoPi and CoBi: CoBi is more structurally coherent, resembling a layered structure similar to CoO(OH) with 3 – 4 nm clusters making up coherent domains, while CoPi consists of smaller clusters that are not coherently stacked.²² A combination of X-ray spectroscopies and model compounds have also been used to propose that CoPi is comprised of 44% O_h Co(III), 39% O_h Co(II) and 17% T_d Co(II), while CoBi is comprised of 65% O_h Co(III) and 35% O_h Co(II).²⁵ The T_d Co(II) uniquely present in CoPi was proposed to exist at edge atom sites (Figure 3.1).²⁵ Along with the established morphological differences, the presence of distinct coordination sites may play important roles for charge transport and catalysis.

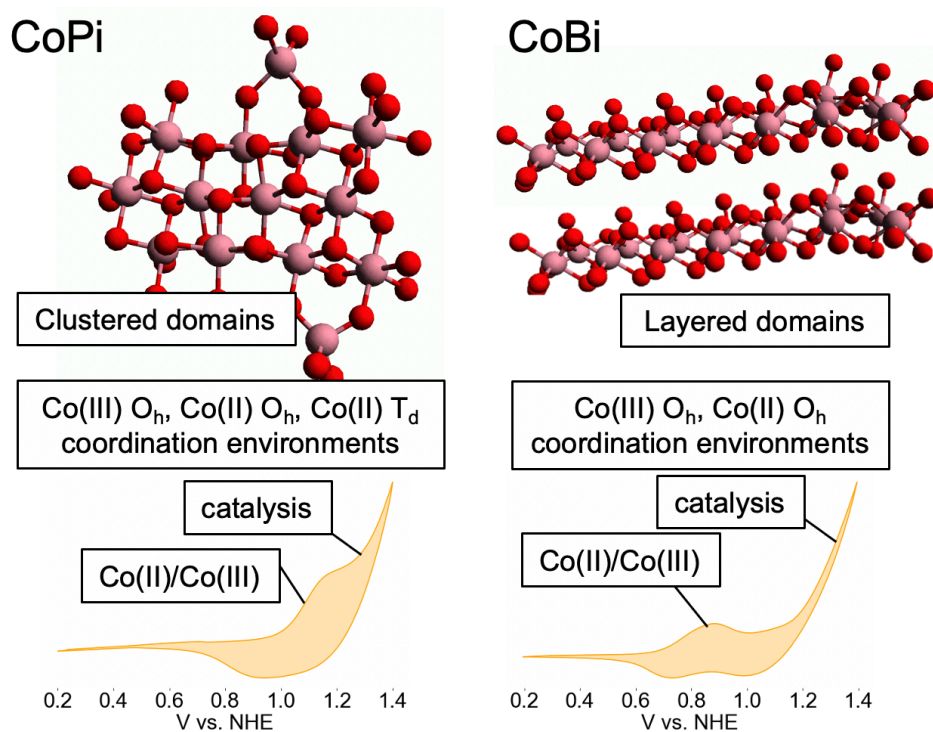


Figure 3.2. Graphical qualitative depictions of CoPi and CoBi domains with an overview of morphological and voltametric differences under pH 7.0 and pH 9.2 buffered conditions, respectively.

To gain further fundamental insight into the structural and electronic differences between CoPi and CoBi, and to explore their photophysical properties, we carried out steady state and time-resolved optical spectroscopic studies of the two thin films. Upon 380 nm excitation, we observed, for the first time, distinct differences in photophysical behavior between the two materials, along with relaxation processes attributable to hole-based defect sites that persist beyond 10 ms. Ground- and excited-state spectroelectrochemistry further revealed insights about the band structure of CoPi and CoBi. Thus, this study provides new spectroscopic signatures that may be related to their differences in charge transport and oxygen evolution reactivity.

3.2. Results

3.2.1. Steady-state and ultrafast transient absorption spectra of CoPi and CoBi films

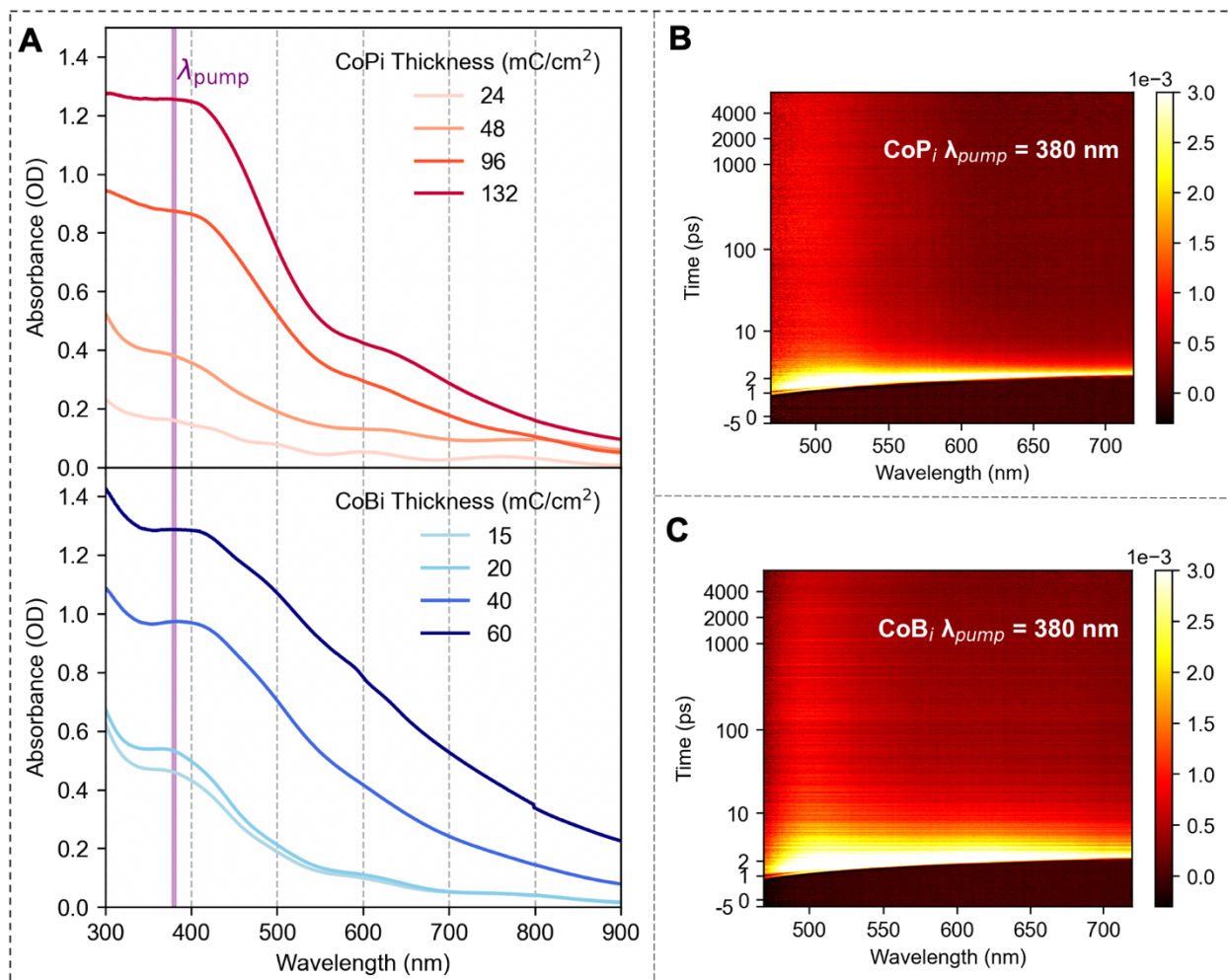


Figure 3.2. Steady state and time-resolved electronic absorption spectra of CoPi and CoBi thin films. (A) Background-subtracted (FTO + buffer) UV-vis absorption spectra of CoPi and CoBi films of varying thickness. Apparent oscillations can occur in the frequency domain for thinner films due to incomplete removal of thin film interference of the underlying FTO substrate. Two-dimensional transient absorption spectra of 96 mC/cm² CoPi (B) and 48 mC/cm² CoBi (C) thin films collected with 380 nm pump excitation in their respective buffers. The transient absorption spectra in this figure are not chirp corrected.

Thin films of CoPi and CoBi electrodeposited on fluorine-doped tin oxide (FTO) both exhibit a relatively intense electronic absorption band at ~ 400 nm, with lower intensity absorption at wavelengths > 500 nm (Figure 3.2A), the latter of which are more intense for CoBi films. The background FTO absorption spectrum exhibits oscillations due to thin film interference (Figure 3.S1). However, interference contributions are minimized with increasing CoPi/CoBi film thickness, which is proportional to the amount of charge passed during electrodeposition (mC/cm^2). Films were between ~ 100 nm and ~ 1 μm , as determined separately through profilometry (Table 3.S1). Band energies do not change with film thickness. As expected, thicker films are visibly darker (Figure 3.S2).

In addition to ground-state spectra, transient absorption measurements were carried out to probe the excited-state dynamics and to gain additional insight into the electronic structural differences between CoPi and CoBi. Optical transient absorption spectra of CoPi (Figure 3.2B) and CoBi (Figure 3.2C) in H_2O excited with a 380 nm, ~ 120 fs pump pulse exhibit broad excited state absorption (ESA) features that appear immediately after excitation. Power titrations ensured pump pulse energies were within the linear response regime (Figures 3.S3-3.S5). Also, film thickness affects the overall excited-state population, but not the corresponding kinetics or spectral profiles (Figure 3.S6). Spectral traces at characteristic time points reveal an ESA at ~ 500 nm, along with a broad, less intense ESA at $\sim 600 - 720$ nm (Figure 3.3). ESA band energies are similar between CoPi and CoBi, suggesting excited-state spectra do not reflect changes in intermediate-range structure or film morphology. While there is some variability in the relative intensity of the $600 - 720$ nm region between films (Figures 3.S7, 3.S8), in all cases the ~ 500 nm feature blue shifts with time, while the lower energy region red shifts. The early time dynamics differ significantly between CoPi and CoBi. At time delays of 1 ns and below, the CoPi excited state signal decays much faster than CoBi (Figure 3.4, top panel). Pump wavelength dependence ranging from 380 nm to 620 nm showed similar profiles, albeit the more visible pump wavelength energies did not have sufficient pump energy at the pump powers to measure signal beyond noise (Figure 3.S9). To discern possible differences in dynamics, a 10 Hz repetition laser with larger attainable pulse energies within the linear response regime was used, with the results being detailed in the following section.

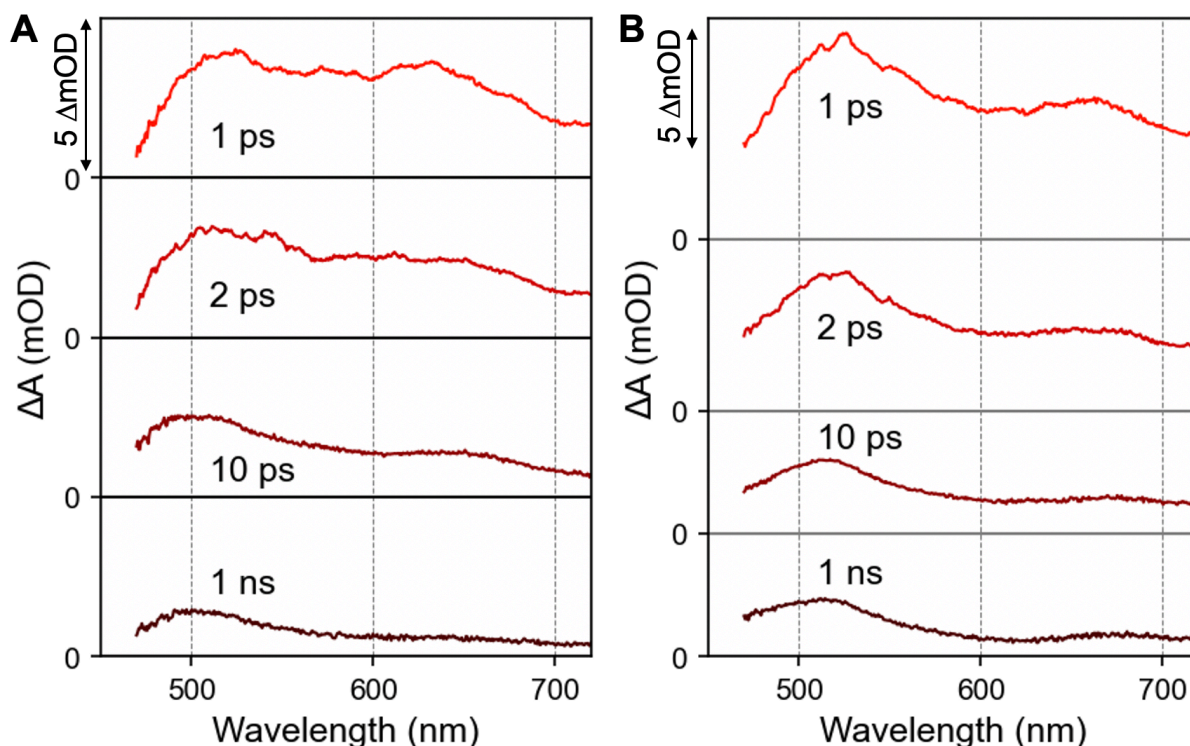


Figure 3.3. Spectral traces of (A) 96 mC/cm² CoPi and (B) 48 mC/cm² CoBi in H₂O at characteristic time delays.

3.2.2. μ s and ms timescale excited-state dynamics of CoPi and CoBi thin films

Using a tunable Nd:YAG laser, 380 nm pump, single wavelength probe (500 nm) measurements were used to quantify excited-state dynamics on longer, μ s and ms time scales. A 10 ns pulse width excitation relative to ~ 120 fs (*vide supra*) increases the pulse energy by three orders of magnitude while maintaining a similar average power, allowing for the collection of weaker transient absorption signals out to significantly longer times. Indeed, ESA signals for CoPi and CoBi films in water persisted beyond 10 ms, with comparative traces for a 500 nm probe across multiple time regimes given in Figure 3.4. Despite relaxing more rapidly on the ultrafast time scale (Figure 3.4, top panel), the overall CoPi transient absorption signal decays more slowly than CoBi (Figure 3.4, middle and bottom panels). The markedly faster CoPi decay in the first 10 ps and the crossover point at 1 ns represent a distinct observable difference in ultrafast dynamics that will be considered in the

Discussion section. Note higher pulse energies as a result of the 10 Hz laser resulted in a rapid photodissolution of the thin film, limiting the number of usable laser shots before the excited portion of the film became optically transparent (Figures 3.S10, 3.S11). Despite this, there were no apparent changes in decay kinetics as the films dissolved upon irradiation. Nevertheless, the thickness of the film was not conserved over the course of a measurement. It was further shown that this long-lived ESA is not solely due to heating, as temperature-dependent steady state absorption spectra give rise to a distinct difference signal relative to the observed ESA (Figure 3.S12). It should be noted, however, that the thermal difference spectra for CoPi and CoBi do differ qualitatively. CoBi ground state absorption intensity decreases with increased temperature, while the CoPi absorption intensity increases. The thermal spectrum overlaps with parts of the ESA, which suggests there may be a contribution from heating. However, as described below, quenching experiments support that the ESA is not primarily a result of heating effects.

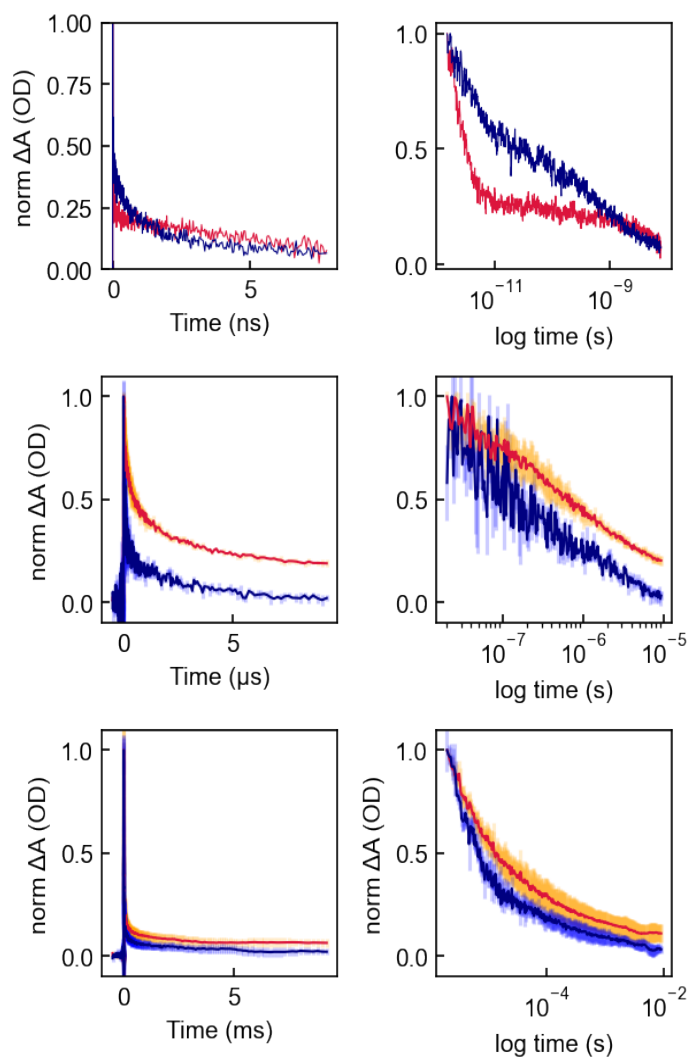


Figure 3.4. Comparative decay traces (380 nm pump, 500 nm probe) of CoPi (red) and CoBi (blue) in H₂O spanning nearly 10 orders of magnitude of time decay from sub-ps to 10 ms. Top row: 7 ns range decay with an ~120 fs pulse width ultrafast laser. Second and third rows correspond to time ranges of 10 μ s and 10 ms, respectively, with a 10 ns pulse width Nd:YAG laser. Traces correspond to the average normalized decay of multiple films; error bars correspond to the standard deviation.

The long-lived excited-state decay was investigated in the presence of various solvents to determine whether hydrogen bonding, polarity, and/or electron/hole scavenging influenced the dynamics. Only MeOH, a hole scavenger, had a substantial effect (Figure 3.S13). Averaged decay

curves obtained for both CoPi and CoBi in H₂O vs MeOH probed at 500 nm are shown in Figure 3.5, while individual constituent decay curves are shown in Figures 3.S14 – 3.S20.

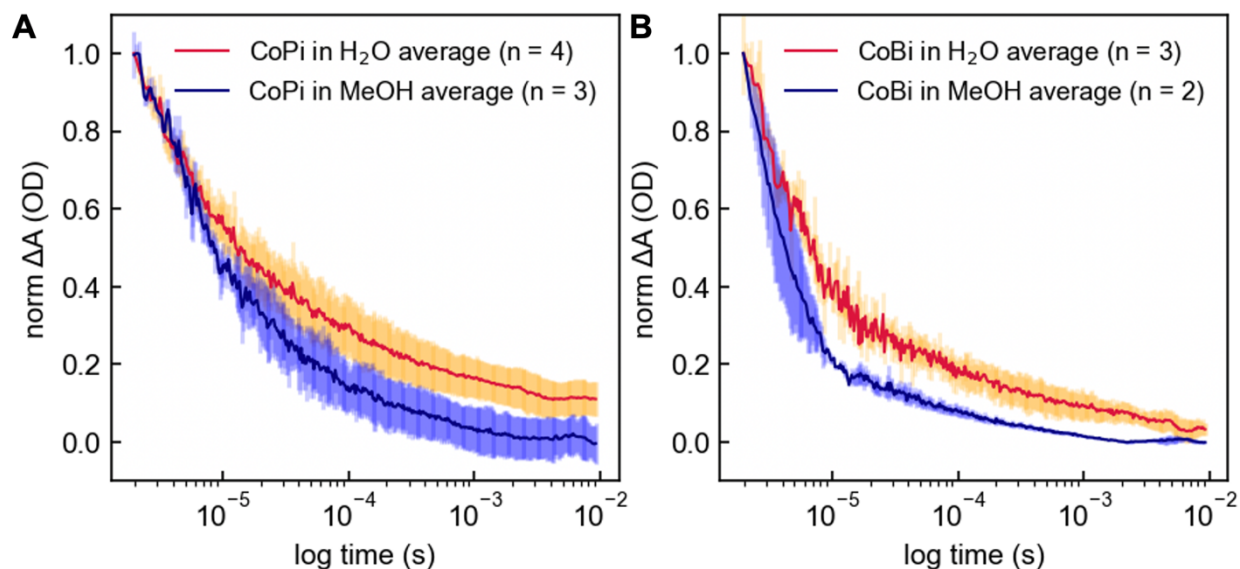


Figure 3.5. Comparison between the excited-state decay of (A) CoPi films immersed in neat H₂O vs MeOH and (B) CoBi films immersed in neat H₂O vs MeOH. Error bars represent standard deviations.

The dependence of the observed dynamics on both the pump and probe wavelengths were investigated. For CoPi, 380 nm excitation resulted in a longer-lived excited state than that for 600 nm, 650 nm, or 700 nm pump wavelengths, which resulted in similar kinetic profiles (Figure 3.S21). This difference in kinetics may be attributable to the UV excitation accessing distinct and longer-lived trap states that are unattainable for visible wavelength excitation. For CoBi, the difference between UV and visible pump is less dramatic. Furthermore, the excited-state decays for CoPi showed little change with different visible probe wavelengths when pumped at 380 nm (Figure 3.S22), suggesting that the trap states themselves have a broad absorption over the visible range. Comparable data for CoBi was complicated by a weaker ESA signal at visible wavelengths, so a direct comparison between probe wavelengths was not obtained.

3.2.3. Spectroelectrochemistry in the ground- and photo-excited states

Distinct steady state and time-resolved spectral changes are observed for CoPi and CoBi thin films upon application of an electrochemical potential (Figure 3.6). When the potential is scanned anodically from the open circuit potential (OCP), the ground-state absorption intensity increases over the whole spectral range for both CoPi and CoBi (Figures 3.6A and 3.6B, respectively). It was confirmed that the absorption intensity of FTO itself was unaffected by the applied potentials (Figure 3.S23). This spectral intensity change is reversible to a certain extent for both thin films when a reducing potential is applied to the oxidized films. Without actively reducing the films, they remain in a more oxidized state, possibly due to an electrochemically induced phase transition. A film initially measured at OCP has only been exposed to a relatively mild deposition potential. Cyclic voltammograms (Figure 3.S24) provide a context for the applied potentials mentioned here relative to the irreversible OER wave. Further anodic bias appears to change the composition of the material as indicated by an increase in OCP after oxidation experiments. This observation suggests a change in the Fermi level of the material, which is reversible upon application of a cathodic bias as seen by the decrease back to initial OCP intensity in (Figures 3.6A, 3.6B). A similar argument could explain the differences in intensity and frequency shifts between OCP spectral traces and their externally biased return to similar potentials. The increase in visible absorption is evident even upon visual inspection of two films, one of which has been held under anodic bias (Figure 3.S25). Note there is some variability in the shapes of the difference spectra (Figures 3.S26, 3.S27), likely due to the oxidation history of the film as described above. However, the general observation is that for both CoPi and CoBi films, the change in spectral intensity is nearly uniform across the UV-vis region, with greater change occurring in the UV region.

To compare ground-state spectroelectrochemical changes to dynamics in the excited state, we further carried out spectroelectrochemical optical transient absorption spectroscopy (Figure 3.6C, 3.6D). In contrast to the increase in ground-state absorption intensity with anodic bias, the ESA intensity decreased with anodic bias for all time delays up to 7 ns (Figures 3.S28, 3.S29).

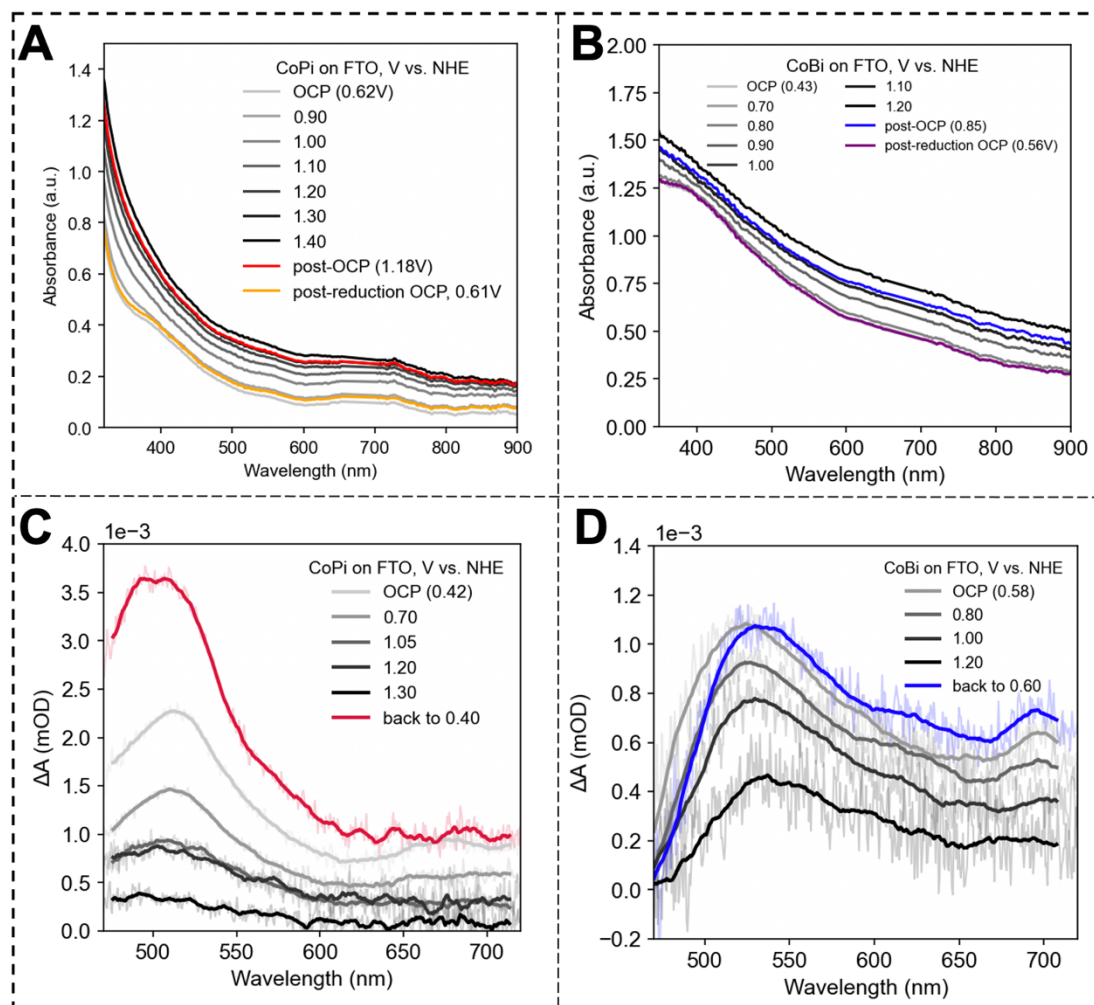


Figure 3.6. Steady state absorption spectra of (A) 96 mC/cm² CoPi and (B) 48 mC/cm² CoBi at varying applied potentials. After applying oxidizing potentials, the absorbance profile remains at larger values, and the OCP potential (post-OCP) differs from that of the initial value of the as-deposited film. A reducing potential (post-reduction OCP) brings the spectral profile back to initial OCP values. Corresponding transient absorption spectral traces (time delay of 1.0 ns) of (C) 96 mC/cm² CoPi and (D) 48 mC/cm² CoBi are shown. For panels (C) and (D), a linear averaging function over 15 adjacent points was applied for visual separation of the spectral traces. The open circuit potential (OCP) excited state spectra are taken with no applied potentials, while all other potentials listed are actively applied.

In order to gain further experimental insight into the origin of the observed spectroelectrochemical absorption changes, similar experiments were carried out in acetonitrile with 0.1 M TBAPF₆ supporting electrolyte. The same trends of increasing ground-state intensity and

decreasing excited-state intensity were observed with increased oxidizing potential. No substantial difference in absorption intensity changes were observed when titrating in buffered H₂O (Figure 3.S27), despite an increase in current as apparent through cyclic voltammograms (Figure 3.S30).

3.3 Discussion

3.3.1 Nature of photoexcited states in amorphous cobalt oxide films

Through the measurements described above, there are three complementary experimental observations to suggest the long-lived photoexcited states in CoPi and CoBi films are attributable to trapped holes. These will be detailed below and consist of the following: 1) the increase in ground-state electronic absorption intensity with anodic bias, 2) the decrease of ESA intensity when excited at 380 nm and monitored spectroelectrochemically under anodic bias, and 3) the quenching of decay kinetics in the presence of MeOH.

3.3.1.1 Ground-state absorption intensity increases under applied anodic bias

The ground-state absorption spectra of CoPi and CoBi exhibit higher intensity in the UV region. This spectral intensity can be attributed to ligand-to-metal charge transfer (LMCT) transitions, while the moderate intensity in the lower-energy range can be attributed to ligand field (d-d) transitions and intervalence charge transfer (IVCT) bands. Similar band assignments have been made for Co₃O₄.²⁶ The broad rising absorption profile complicates the picture of a straightforward band structure as observed in many undoped crystalline metal oxides, in which the onset of absorption appears clearly at the energy of the band gap.²⁷ The increasing ground-state absorption intensity with anodic bias is observed both in aqueous buffers and in acetonitrile with 0.1 M TBAPF₆ (Figure 3.6). The spectral shape in both the ground state and photoexcited states does not change appreciably in acetonitrile relative to native buffers (Figure 3.S31). As would be expected for water oxidation, the current response is significantly less when oxidation occurs in acetonitrile as opposed to aqueous buffer (Figure 3.S30). However, the non-negligible presence of faradaic current in acetonitrile suggests that oxidation events are taking place on the film, likely largely due to the conversion of

Co(II) to Co(III). Similar behavior of the spectroelectrochemical difference spectrum in the UV-vis region of CoPi had been observed previously and attributed to increasing Co(III) character by Durrant and coworkers.¹²

3.3.1.2 The photoexcited state absorption intensity decreases under applied anodic bias

The ESA profile upon 380 nm excitation is similar to that of other metal oxides that host trapped hole or electron states upon photoexcitation. Similar UV-pumped excited-state spectra were observed for anatase TiO₂ nanoparticles (10 – 15 nm diameter)²⁸ and nitrogen-doped anatase TiO₂ powder.²⁹ In hematite, a μs – ms long-lived ESA band at 580 nm was attributed to hole absorption, whereas the long-lived ESA band in our study appears closer to 510 nm, with lifetimes in a comparable range (on the order of μs , with a generous stretching parameter in the case of stretched exponential fits as shown in Table 3.1).^{30,31} The photoinduced holes in hematite were quenched by MeOH, as was observed in the case of CoPi and CoBi and detailed in the following section. Similar assignments in the visible probe region were made for several other systems, including 1) Cu₂O (transient absorption maxima at > 475 nm, quenched by Na₂SO₃),³² 2) WO₃ (transient absorption maxima at 430 – 500 nm, quenched by methanol),^{33–37} and 3) colloidal CdS (transient absorption maxima at 470 – 500 nm, quenched by NaI and thiophenol).^{38–42} The use of exogenous electron donors and the resulting quenching effects supported the assignment of the transient absorption to photoinduced holes. The long-lived ESA observed here for CoPi and CoBi is, thus, consistent with photoinduced trapped holes.⁴³ As the film gets oxidized, the ground-state intensity increases from the increased number of holes in the form of Co(III) in the material. Consequently, the ESA intensity decreases as the trapped holes are filled with increasing applied potential, resulting in fewer holes to be generated by photoexcitation.

3.3.1.3 Photoexcited state decay kinetics are quenched in the presence of MeOH

When considering the band structure formalism, both the steady state and transient absorption spectra are consistent with the abundance of mid-gap states in amorphous cobalt oxide films. Similar to other metal oxides, such defect states can host either trapped holes or trapped electrons. To further

characterize the nature of the trapped state, both electron and hole scavengers were added to monitor which quenches the excited state.⁴³ Both CoPi and CoBi excited states were found to be quenched in the presence of MeOH, a known hole scavenger (Figure 3.5).⁴³ A CoPi film was tested in the presence of H₂O, D₂O, phosphate buffer, MeOH (hole scavenger), 1.0 M Na₂SO₃ (electron scavenger), 1.0 M AgNO₃ (electron scavenger), and acetonitrile (Figure 3.S13). Only MeOH resulted in a quenching effect, further suggesting the long-lived excited state is a trapped hole state. A similar quenching effect in the presence of MeOH was observed in microcrystalline hematite films.³⁰ We note that while the differences in excited-state decay were evident by the 10 Hz laser with delay times up to 10 ms, ultrafast transient absorption spectra did not resolve discernable differences in decay kinetics as the delay times were only limited to 7 ns (Figure 3.S32).

3.3.2. Differences between the photoexcited spectra and the spectroelectrochemical difference spectra

As shown in Figure 3.7, the electrochemical difference spectra representing the additional intensity from injected holes under applied anodic bias and the transient absorption excited-state spectrum at long time intervals do not overlay or show much similarity, other than covering a broad region. The differences in the spectra observed in amorphous cobalt oxide upon photoexcitation versus electrochemical oxidation can be attributed to several factors rooted in the material's electronic structure and the nature of the excitation processes. Photoexcitation excites electrons across the bandgap, creating electron-hole pairs. The specific excitation energies involved can selectively populate certain trap states, leading to distinct spectral features. Electrochemical oxidation, on the other hand, alters the Fermi level leading to a broader range of accessible electronic transitions, including those involving defect states or surface states that are not directly accessed by photon absorption. The spectrum under pulsed laser excitation is influenced by the dynamics of electron-hole pairs and their interaction with intraband trap states.

Such differences were considered previously in microcrystalline hematite by Durrant and coworkers.³⁰ Under anodic bias, these trapped states become oxidized (electron-depleted), affecting how electrons and holes recombine and thus altering the spectral features. The lifetime of the

photoexcited trapped holes was extended up the order of seconds under applied anodic bias, while the amplitude of the long-lived signal decreased.³⁰ In contrast to nanocrystalline hematite, amorphous materials typically have a more disordered structure than crystalline materials, leading to a higher density and different distribution of trap states. In CoPi and CoBi, we similarly observe a decrease in the amplitude of the excited-state signal upon application of anodic bias. We did not observe significant changes to the decay rate at a ps – ns timescale under applied anodic bias, though this does not rule out an effect on the μs – ms timescale. As such, it remains unclear whether there is a long-time component of the excited state decay that is sensitive to anodic bias. The trapped hole feature observed at ~ 510 nm for bandgap excitation of CoPi and CoBi suggests the presence of specific trap states that are effectively participating in hole trapping under photoexcitation conditions. Electrochemical oxidation of the ground state results in a broad, featureless increase in intensity, indicating a more uniform distribution of trap states or a lack of specific spectral features associated with these states. In contrast to hematite, where specific trap states below the conduction band play a significant role, the behavior in CoPi and CoBi suggests a different mechanism or a more homogenous distribution of states within the bandgap. This is consistent with the disparities observed for the transient absorption spectra and spectroelectrochemical difference spectra profiles of CoPi and CoBi films.

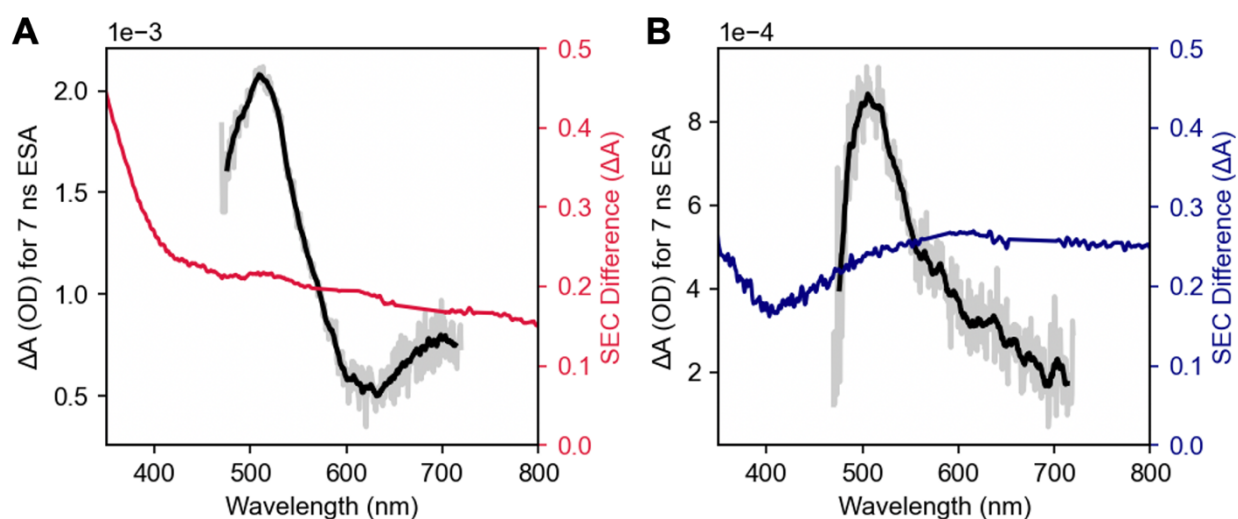


Figure 3.7. Comparisons between photoexcited ESA spectra with 7 ns pump-probe delay and the electrochemical difference spectra for CoPi (**A**) and CoBi (**B**) films in their respective buffered solutions. The spectroelectrochemical difference spectrum is the subtraction between the 1.4 V vs. NHE (OER overpotential of 0.58 V) spectrum and the open-circuit potential spectrum for CoPi, and the subtraction between 1.2 V vs. NHE (OER overpotential of 0.51 V) with the open-circuit potential spectrum for CoBi. Regions around 585 nm and 690 nm of the SEC difference spectrum have been omitted and replaced with a connecting straight line as the spectrometer lamp exhibited saturating artifacts at those wavelengths.

3.3.3 Implications of long-lived excited states for the oxygen evolution reaction (OER)

The excited-state spectral shapes and decay kinetics of CoPi and CoBi films were not significantly affected by solvent conditions, except for MeOH (Figure 3.S13). This suggests that the long-lived excited states would more likely correspond to deep traps in the middle of the band gap, rather than shallow traps, which would be shorter-lived and more sensitive to external perturbations.⁴⁵ Furthermore, it has been postulated that deep hole trapping should be common to amorphous oxides and has been observed in materials such as a-SiO₂, a-Al₂O₃ and a-TiO₂.⁴⁶ Applied bias does not have a marked effect on any of the decay features (Figure 3.S28). This is unlike observations for hematite photoanodes, where applied bias was found to have a significant retarding effect on the electron-hole recombination rates.⁴⁴ Furthermore, the observation of similar change in absorption intensity upon applying anodic bias without the presence of H₂O suggests that H₂O itself is not necessary to stabilize the trap states. Therefore, there is nothing to suggest that the long-lived trapped hole states play a role in the OER. Nevertheless, the trapped hole states may still play a role in charge transport through the film and highlight the complicated electronic structural nature of the catalytic films. Future photoconductivity measurements may elucidate the potential role of these trapped states in charge transport.

3.3.4 Hole trap decay kinetics in CoPi and CoBi films

While the intermediate-range structure of the two films are known to differ, both the steady-state and time-resolved optical spectra of the films in the UV-vis do not show dramatic differences. In addition, the double layer capacitance in CoPi vs. CoBi films were found to be similar (Figure 3.S4). Therefore, the differences in decay kinetics can be potentially tied to differences in the films'

properties that would otherwise be undetectable from steady state methods. Due to the complicated electronic structure and amorphous nature of the materials, it is unsurprising that the kinetics of CoPi and CoBi films could not be fit to a simple multi-exponential model (Figures 3.S34, 3.S35). Instead, both CoPi and CoBi decays are best fit by a sum of two stretched exponentials of the form $\Delta A = a_1(e^{-k_1})^{\beta_1} + a_2(e^{-k_2})^{\beta_2}$ (Figure 3.S36). Stretched exponentials are commonly used to fit relaxation processes in disordered materials and semiconductor trap states, where the stretching term can be used as a metric for disorder within the films.⁴⁷⁻⁴⁹ The fitted parameters are presented in Table 3.1. The low β_1 and β_2 values may reflect the amorphous nature of the films. The long-lived excited-state decays of CoPi and CoBi are characterized here for the first time, with CoPi ultimately having a longer lifetime than CoBi despite CoPi having a much faster decay in the first 10 ps (Figure 3.4). It is important to emphasize that the fitting parameters are for comparing the long-lived excited-state dynamics between CoPi and CoBi and do not have a mechanistic origin. In fact, due to the 10 ns pulse width of the laser used to probe the long time delays, the initial rapid ultrafast decay in the first 10 ps is not captured by the ns timescale decay traces. As a result, the remnant excited state signal at 10 ns is overestimated compared to the early time maximum of the ESA. This is supported by Figure 3.S37, where there is no intensity before time zero with 1 kHz ultrafast pumping; any remnant intensity is below the discernable signal-to-noise limit.

Table 3.1. Average fitted values for a phenomenological stretched biexponential model of decay.

	CoPi	CoBi
Normalized a_1 coefficient (%)	80%	29%
k_1	$2.0 \times 10^7 \text{ s}^{-1}$	$1.9 \times 10^6 \text{ s}^{-1}$
$\tau_1 = 1/k_1$	50 ns	0.5 μs
β_1	0.23	0.13
Normalized a_2 coefficient (%)	20%	71%
k_2	$6.1 \times 10^5 \text{ s}^{-1}$	$1.7 \times 10^6 \text{ s}^{-1}$
$\tau_2 = 1/k_2$	1.6 μs	0.6 μs
β_2	0.11	0.47

The distinct ultrafast decay dynamics and long-lived excited-state behaviors observed between CoPi and CoBi may stem from their inherent structural and electronic differences. For CoPi, the rapid decay within the first 10 ps could be attributed to the presence of a higher density of accessible trap states due to its disordered intermediate-range structure. These sites, possibly located at edges of the smaller, less coherently stacked clusters, may provide pathways for faster non-radiative relaxation processes, rapidly quenching the excited states. Conversely, the persisting ESA intensity of trapped holes in CoPi beyond the ms timescale suggests that while its structure may allow for faster energy dissipation, it also allows for the formation of localized states that stabilize the trapped holes, possibly due to a greater heterogeneity in the electronic environment created by disordered clusters. In contrast, CoBi's more structurally coherent domains may facilitate charge migration, reducing the likelihood of hole trapping, leading to shorter excited-state lifetimes. We emphasize that the intermediate-range structures have only thus far been indirectly determined from fitting of X-ray scattering data; therefore, explanations concerning differences in structure, non-radiative decay pathways and trap sites are speculative. In addition to structural considerations, we note that the phosphate and borate capping groups are electron donating and electron withdrawing, respectively. Some of the additional stabilization of the longer-lived trapped holes in CoPi could be due to the electron donating nature of the phosphate groups. As of now, the contributions of electronic vs. structural stabilization to the differences in trap lifetimes are unclear. The difference in the relative amounts of Co(III) and Co(II) between the two materials may also play a role, with the higher proportion of O_h Co(III) in CoBi potentially contributing to a more ordered electronic landscape that disfavors the same level of trapping as observed in CoPi. While mechanistic differences between the excited-state decay pathways are currently unclear, their starkly different dynamics are likely related to catalytically relevant structural and electronic differences that arise from the mechanism of film growth and relative cobalt speciation changes when using different buffers (i.e., phosphate vs. borate).

3.4 Conclusion

Dynamics from sub-picosecond to millisecond timescales were probed for the first time in CoPi and CoBi thin films using transient absorption spectroscopy, revealing structurally distinct photophysics and long-lived relaxation dynamics persisting beyond 10 ms. By applying spectroelectrochemistry in the ground- and photo-excited states, along with the observed excited-state quenching by a hole scavenger, these relaxation dynamics can be attributed to deep hole traps reminiscent of other metal oxides. Based on solvent-dependent transient absorption measurements, it is unclear whether the optically probed trap states are important for the OER. However, they could potentially play a role in charge transport and offer new electronic structural insights into the amorphous films.

Acknowledgements

RM acknowledges NSERC PGSD3-557779-2021 funding. Parts of this work were supported by NIH grant 1S10OD032151-01 for the purchase of a High-Energy Tunable Nanosecond-Pulsed Laser in the Beckman Institute Laser Resource Center. Financial support from Caltech and the Dow Next Generation Educator Fund is gratefully acknowledged.

References

- (1) Service, R. F. Hydrogen Economy? Let Sunlight Do the Work. *Science* **2007**, *315* (5813), 789–789. <https://doi.org/10.1126/science.315.5813.789>.
- (2) Barber, J. Photosynthetic Energy Conversion: Natural and Artificial. *Chem. Soc. Rev.* **2008**, *38* (1), 185–196. <https://doi.org/10.1039/B802262N>.
- (3) Tachibana, Y.; Vayssieres, L.; Durrant, J. R. Artificial Photosynthesis for Solar Water-Splitting. *Nat. Photonics* **2012**, *6* (8), 511–518. <https://doi.org/10.1038/nphoton.2012.175>.
- (4) Doyle, R. L.; Lyons, M. E. G. The Oxygen Evolution Reaction: Mechanistic Concepts and Catalyst Design. In *Photoelectrochemical Solar Fuel Production: From Basic Principles to Advanced Devices*; Giménez, S., Bisquert, J., Eds.; Springer International Publishing: Cham, 2016; pp 41–104. https://doi.org/10.1007/978-3-319-29641-8_2.
- (5) Kanan, M. W.; Nocera, D. G. In Situ Formation of an Oxygen-Evolving Catalyst in Neutral Water Containing Phosphate and Co^{2+} . *Science* **2008**, *321* (5892), 1072–1075. <https://doi.org/10.1126/science.1162018>.
- (6) Surendranath, Y.; Kanan, M. W.; Nocera, D. G. Mechanistic Studies of the Oxygen Evolution Reaction by a Cobalt-Phosphate Catalyst at Neutral pH. *J. Am. Chem. Soc.* **2010**, *132* (46), 16501–16509. <https://doi.org/10.1021/ja106102b>.
- (7) Nocera, D. G. The Artificial Leaf. *Acc. Chem. Res.* **2012**, *45* (5), 767–776. <https://doi.org/10.1021/ar2003013>.
- (8) Reece, S. Y.; Hamel, J. A.; Sung, K.; Jarvi, T. D.; Esswein, A. J.; Pijpers, J. J. H.; Nocera, D. G. Wireless Solar Water Splitting Using Silicon-Based Semiconductors and Earth-Abundant Catalysts. *Science* **2011**, *334* (6056), 645–648. <https://doi.org/10.1126/science.1209816>.
- (9) Khnayzer, R. S.; Mara, M. W.; Huang, J.; Shelby, M. L.; Chen, L. X.; Castellano, F. N. Structure and Activity of Photochemically Deposited “CoPi” Oxygen Evolving Catalyst on Titania. *ACS Catal.* **2012**, *2* (10), 2150–2160. <https://doi.org/10.1021/cs3005192>.
- (10) Zhong, D. K.; Cornuz, M.; Sivula, K.; Grätzel, M.; Gamelin, D. R. Photo-Assisted Electrodeposition of Cobalt–Phosphate (Co–Pi) Catalyst on Hematite Photoanodes for Solar Water Oxidation. *Energy Environ. Sci.* **2011**, *4* (5), 1759–1764. <https://doi.org/10.1039/C1EE01034D>.
- (11) Steinmiller, E. M. P.; Choi, K.-S. Photochemical Deposition of Cobalt-Based Oxygen Evolving Catalyst on a Semiconductor Photoanode for Solar Oxygen Production. *Proc. Natl. Acad. Sci.* **2009**, *106* (49), 20633–20636. <https://doi.org/10.1073/pnas.0910203106>.
- (12) Ma, Y.; Kafizas, A.; Pendlebury, S. R.; Le Formal, F.; Durrant, J. R. Photoinduced Absorption Spectroscopy of CoPi on BiVO_4 : The Function of CoPi during Water Oxidation. *Adv. Funct. Mater.* **2016**, *26* (27), 4951–4960. <https://doi.org/10.1002/adfm.201600711>.
- (13) Jeon, T. H.; Choi, W.; Park, H. Cobalt–Phosphate Complexes Catalyze the Photoelectrochemical Water Oxidation of BiVO_4 Electrodes. *Phys. Chem. Chem. Phys.* **2011**, *13* (48), 21392–21401. <https://doi.org/10.1039/C1CP23135A>.
- (14) Zhang, J.; Jiang, D.; Wang, P.; Zhong, J.; Sun, G.; Yao, Y.; Luo, W.; Zou, Z. A High-Voltage Solar Rechargeable Device Based on a CoPi/ BiVO_4 Faradaic Junction. *J. Mater. Chem. A* **2022**, *10* (4), 1802–1807. <https://doi.org/10.1039/D1TA08949H>.

- (15) Sprague-Klein, E. A.; He, X.; Mara, M. W.; Reinhart, B. J.; Lee, S.; Utschig, L. M.; Mulfort, K. L.; Chen, L. X.; Tiede, D. M. Photo-Electrochemical Effect in the Amorphous Cobalt Oxide Water Oxidation Catalyst Cobalt–Phosphate (CoPi). *ACS Energy Lett.* **2022**, *7* (9), 3129–3138. <https://doi.org/10.1021/acscenergylett.2c01560>.
- (16) Ullman, A. M.; Brodsky, C. N.; Li, N.; Zheng, S.-L.; Nocera, D. G. Probing Edge Site Reactivity of Oxidic Cobalt Water Oxidation Catalysts. *J. Am. Chem. Soc.* **2016**, *138* (12), 4229–4236. <https://doi.org/10.1021/jacs.6b00762>.
- (17) Hadt, R. G.; Hayes, D.; Brodsky, C. N.; Ullman, A. M.; Casa, D. M.; Upton, M. H.; Nocera, D. G.; Chen, L. X. X-Ray Spectroscopic Characterization of Co(IV) and Metal–Metal Interactions in Co₄O₄: Electronic Structure Contributions to the Formation of High-Valent States Relevant to the Oxygen Evolution Reaction. *J. Am. Chem. Soc.* **2016**, *138* (34), 11017–11030. <https://doi.org/10.1021/jacs.6b04663>.
- (18) Brodsky, C. N.; Hadt, R. G.; Hayes, D.; Reinhart, B. J.; Li, N.; Chen, L. X.; Nocera, D. G. In Situ Characterization of Cofacial Co(IV) Centers in Co₄O₄ Cubane: Modeling the High-Valent Active Site in Oxygen-Evolving Catalysts. *Proc. Natl. Acad. Sci.* **2017**, *114* (15), 3855–3860. <https://doi.org/10.1073/pnas.1701816114>.
- (19) Kanan, M. W.; Yano, J.; Surendranath, Y.; Dincă, M.; Yachandra, V. K.; Nocera, D. G. Structure and Valency of a Cobalt–Phosphate Water Oxidation Catalyst Determined by in Situ X-Ray Spectroscopy. *J. Am. Chem. Soc.* **2010**, *132* (39), 13692–13701. <https://doi.org/10.1021/ja1023767>.
- (20) Surendranath, Y.; Lutterman, D. A.; Liu, Y.; Nocera, D. G. Nucleation, Growth, and Repair of a Cobalt-Based Oxygen Evolving Catalyst. *J. Am. Chem. Soc.* **2012**, *134* (14), 6326–6336. <https://doi.org/10.1021/ja3000084>.
- (21) Brodsky, C. N.; Bediako, D. K.; Shi, C.; Keane, T. P.; Costentin, C.; Billinge, S. J. L.; Nocera, D. G. Proton–Electron Conductivity in Thin Films of a Cobalt–Oxygen Evolving Catalyst. *ACS Appl. Energy Mater.* **2019**, *2* (1), 3–12. <https://doi.org/10.1021/acsaem.8b00785>.
- (22) Farrow, C. L.; Bediako, D. K.; Surendranath, Y.; Nocera, D. G.; Billinge, S. J. L. Intermediate-Range Structure of Self-Assembled Cobalt-Based Oxygen-Evolving Catalyst. *J. Am. Chem. Soc.* **2013**, *135* (17), 6403–6406. <https://doi.org/10.1021/ja401276f>.
- (23) Risch, M.; Khare, V.; Zaharieva, I.; Gerencser, L.; Chernev, P.; Dau, H. Cobalt–Oxo Core of a Water-Oxidizing Catalyst Film. *J. Am. Chem. Soc.* **2009**, *131* (20), 6936–6937. <https://doi.org/10.1021/ja902121f>.
- (24) Risch, M.; Klingan, K.; Ringleb, F.; Chernev, P.; Zaharieva, I.; Fischer, A.; Dau, H. Water Oxidation by Electrodeposited Cobalt Oxides—Role of Anions and Redox-Inert Cations in Structure and Function of the Amorphous Catalyst. *ChemSusChem* **2012**, *5* (3), 542–549. <https://doi.org/10.1002/cssc.201100574>.
- (25) Kwon, G.; Jang, H.; Lee, J.-S.; Mane, A.; Mandia, D. J.; Soltau, S. R.; Utschig, L. M.; Martinson, A. B. F.; Tiede, D. M.; Kim, H.; Kim, J. Resolution of Electronic and Structural Factors Underlying Oxygen-Evolving Performance in Amorphous Cobalt Oxide Catalysts. *J. Am. Chem. Soc.* **2018**, *140* (34), 10710–10720. <https://doi.org/10.1021/jacs.8b02719>.

- (26) Qiao, L.; Xiao, H. Y.; Meyer, H. M.; Sun, J. N.; Rouleau, C. M.; Puzos, A. A.; Geohegan, D. B.; Ivanov, I. N.; Yoon, M.; Weber, W. J.; Bieganski, M. D. Nature of the Band Gap and Origin of the Electro-/Photo-Activity of Co_3O_4 . *J. Mater. Chem. C* **2013**, *1* (31), 4628–4633. <https://doi.org/10.1039/C3TC30861H>.
- (27) Makula, P.; Pacia, M.; Macyk, W. How To Correctly Determine the Band Gap Energy of Modified Semiconductor Photocatalysts Based on UV–Vis Spectra. *J. Phys. Chem. Lett.* **2018**, *9* (23), 6814–6817. <https://doi.org/10.1021/acs.jpcclett.8b02892>.
- (28) Yoshihara, T.; Katoh, R.; Furube, A.; Tamaki, Y.; Murai, M.; Hara, K.; Murata, S.; Arakawa, H.; Tachiya, M. Identification of Reactive Species in Photoexcited Nanocrystalline TiO_2 Films by Wide-Wavelength-Range (400–2500 Nm) Transient Absorption Spectroscopy. *J. Phys. Chem. B* **2004**, *108* (12), 3817–3823. <https://doi.org/10.1021/jp031305d>.
- (29) Yamanaka, K.; Morikawa, T. Charge-Carrier Dynamics in Nitrogen-Doped TiO_2 Powder Studied by Femtosecond Time-Resolved Diffuse Reflectance Spectroscopy. *J. Phys. Chem. C* **2012**, *116* (1), 1286–1292. <https://doi.org/10.1021/jp209210u>.
- (30) Pendlebury, S. R.; Barroso, M.; Cowan, A. J.; Sivula, K.; Tang, J.; Grätzel, M.; Klug, D.; Durrant, J. R. Dynamics of Photogenerated Holes in Nanocrystalline $\alpha\text{-Fe}_2\text{O}_3$ Electrodes for Water Oxidation Probed by Transient Absorption Spectroscopy. *Chem. Commun.* **2010**, *47* (2), 716–718. <https://doi.org/10.1039/C0CC03627G>.
- (31) Huang, Z.; Lin, Y.; Xiang, X.; Rodríguez-Córdoba, W.; McDonald, K. J.; Hagen, K. S.; Choi, K.-S.; Brunshwig, B. S.; Musaev, D. G.; Hill, C. L.; Wang, D.; Lian, T. In Situ Probe of Photocarrier Dynamics in Water-Splitting Hematite ($\alpha\text{-Fe}_2\text{O}_3$) Electrodes. *Energy Environ. Sci.* **2012**, *5* (10), 8923–8926. <https://doi.org/10.1039/C2EE22681B>.
- (32) Pastor, E.; Pesci, F. M.; Reynal, A.; Handoko, A. D.; Guo, M.; An, X.; Cowan, A. J.; Klug, D. R.; Durrant, J. R.; Tang, J. Interfacial Charge Separation in $\text{Cu}_2\text{O}/\text{RuOx}$ as a Visible Light Driven CO_2 Reduction Catalyst. *Phys. Chem. Chem. Phys.* **2014**, *16* (13), 5922–5926. <https://doi.org/10.1039/C4CP00102H>.
- (33) Cristino, V.; Marinello, S.; Molinari, A.; Caramori, S.; Carli, S.; Boaretto, R.; Argazzi, R.; Meda, L.; Bignozzi, C. A. Some Aspects of the Charge Transfer Dynamics in Nanostructured WO_3 Films. *J. Mater. Chem. A* **2016**, *4* (8), 2995–3006. <https://doi.org/10.1039/C5TA06887H>.
- (34) Kim, W.; Tachikawa, T.; Monllor-Satoca, D.; Kim, H.; Majima, T.; Choi, W. Promoting Water Photooxidation on Transparent WO_3 Thin Films Using an Alumina Overlayer. *Energy Environ. Sci.* **2013**, *6* (12), 3732–3739. <https://doi.org/10.1039/C3EE42151A>.
- (35) Zhai, X.-P.; Gao, L.-F.; Zhang, H.; Peng, Y.; Zhang, X.-D.; Wang, Q.; Zhang, H.-L. Defect Engineering of Ultrathin WO_3 Nanosheets: Implications for Nonlinear Optoelectronic Devices. *ACS Appl. Nano Mater.* **2022**, *5* (1), 1169–1177. <https://doi.org/10.1021/acsanm.1c03791>.
- (36) Sachs, M.; Park, J.-S.; Pastor, E.; Kafizas, A.; Wilson, A. A.; Francàs, L.; Gul, S.; Ling, M.; Blackman, C.; Yano, J.; Walsh, A.; Durrant, J. R. Effect of Oxygen Deficiency on the Excited State Kinetics of WO_3 and Implications for Photocatalysis. *Chem. Sci.* **2019**, *10* (22), 5667–5677. <https://doi.org/10.1039/C9SC00693A>.

- (37) Pesci, F. M.; Cowan, A. J.; Alexander, B. D.; Durrant, J. R.; Klug, D. R. Charge Carrier Dynamics on Mesoporous WO₃ during Water Splitting. *J. Phys. Chem. Lett.* **2011**, *2* (15), 1900–1903. <https://doi.org/10.1021/jz200839n>.
- (38) Kamat, P. V.; Dimitrijevic, N. M.; Fessenden, R. W. Photoelectrochemistry in Particulate Systems. 6. Electron-Transfer Reactions of Small Cadmium Sulfide Colloids in Acetonitrile. *J. Phys. Chem.* **1987**, *91* (2), 396–401. <https://doi.org/10.1021/j100286a029>.
- (39) Kamat, P. V.; Ebbesen, T. W.; Dimitrijević, N. M.; Nozik, A. J. Primary Photochemical Events in CdS Semiconductor Colloids as Probed by Picosecond Laser Flash Photolysis. *Chem. Phys. Lett.* **1989**, *157* (5), 384–389. [https://doi.org/10.1016/0009-2614\(89\)87267-7](https://doi.org/10.1016/0009-2614(89)87267-7).
- (40) Uchihara, T.; Fox, M. A. Nanosecond Laser Flash Photolysis of Thiophenolate-Capped Cadmium Sulfide Particles in Acetonitrile. *Inorganica Chim. Acta* **1996**, *242* (1), 253–259. [https://doi.org/10.1016/0020-1693\(96\)04875-X](https://doi.org/10.1016/0020-1693(96)04875-X).
- (41) Uchihara, T.; Oshiro, H.; Kinjo, A. Subpicosecond Studies of Primary Photochemical Events of CdS Particles with Surface Modified by Various Capping Agents. *J. Photochem. Photobiol. Chem.* **1998**, *114* (3), 227–234. [https://doi.org/10.1016/S1010-6030\(98\)00225-1](https://doi.org/10.1016/S1010-6030(98)00225-1).
- (42) Wang, W.; Tao, Y.; Fan, J.; Yan, Z.; Shang, H.; Phillips, D. L.; Chen, M.; Li, G. Fullerene–Graphene Acceptor Drives Ultrafast Carrier Dynamics for Sustainable CdS Photocatalytic Hydrogen Evolution. *Adv. Funct. Mater.* **2022**, *32* (23), 2201357. <https://doi.org/10.1002/adfm.202201357>.
- (43) Schneider, J.; Curti, M. Spectroscopic and Kinetic Characterization of Photogenerated Charge Carriers in Photocatalysts. *Photochem. Photobiol. Sci.* **2022**. <https://doi.org/10.1007/s43630-022-00297-x>.
- (44) Pendlebury, S. R.; Wang, X.; Le Formal, F.; Cornuz, M.; Kafizas, A.; Tilley, S. D.; Grätzel, M.; Durrant, J. R. Ultrafast Charge Carrier Recombination and Trapping in Hematite Photoanodes under Applied Bias. *J. Am. Chem. Soc.* **2014**, *136* (28), 9854–9857. <https://doi.org/10.1021/ja504473e>.
- (45) Viswanath, A. K. Chapter 3 - Surface and Interfacial Recombination in Semiconductors. In *Handbook of Surfaces and Interfaces of Materials*; Nalwa, H. S., Ed.; Academic Press: Burlington, 2001; pp 217–284. <https://doi.org/10.1016/B978-012513910-6/50010-4>.
- (46) Strand, J.; Kaviani, M.; Gao, D.; El-Sayed, A.-M.; Afanas'ev, V. V.; Shluger, A. L. Intrinsic Charge Trapping in Amorphous Oxide Films: Status and Challenges. *J. Phys. Condens. Matter* **2018**, *30* (23), 233001. <https://doi.org/10.1088/1361-648X/aac005>.
- (47) Zatryb, G.; Podhorodecki, A.; Misiewicz, J.; Cardin, J.; Gourbilleau, F. On the Nature of the Stretched Exponential Photoluminescence Decay for Silicon Nanocrystals. *Nanoscale Res. Lett.* **2011**, *6* (1), 106. <https://doi.org/10.1186/1556-276X-6-106>.
- (48) Van de Walle, C. G. Stretched-Exponential Relaxation Modeled without Invoking Statistical Distributions. *Phys. Rev. B* **1996**, *53* (17), 11292–11295. <https://doi.org/10.1103/PhysRevB.53.11292>.
- (49) Cui, B.; Milkus, R.; Zaccone, A. The Relation between Stretched-Exponential Relaxation and the Vibrational Density of States in Glassy Disordered Systems. *Phys. Lett. A* **2017**, *381* (5), 446–451. <https://doi.org/10.1016/j.physleta.2016.12.003>.

Supporting Information

Observing Long-lived Photogenerated Holes in Cobalt Oxyhydroxide Oxygen Evolution Catalysts

Materials. $\text{Co}(\text{NO}_3)_2$ 99.999%, K_2HPO_4 99.99%, H_3BO_3 99.999%, KOH 99.99% were used as received from Millipore Sigma. All electrolyte solutions were prepared with MilliPore filtered water with 18.20 $\text{M}\Omega\text{-cm}$ resistivity. All experiments used fluorine-tin-oxide (FTO; TEC-7) coated glass slides that were purchased as pre-cut 1 cm \times 2.5 cm glass piece from MSE Supplies.

Electrochemical Methods. Aqueous electrochemical measurements were conducted using a BioLogic VSP-300 Potentiostat, a Ag/AgCl reference electrode with saturated KCl from BASi and a high surface area Pt-mesh counter electrode. Aqueous experiments were performed using a three-electrode electrochemical cell consisting of 25 mL of electrolyte solution. Experiments were performed at ambient temperature (21 °C) and electrode potentials were converted to the NHE scale using $E(\text{NHE}) = E(\text{Ag}/\text{AgCl}) + 0.199 \text{ V}$. Phosphate (Pi) buffers were made to contain 0.1 M phosphate and were adjusted to pH 7.00. Borate (Bi) buffers were made to contain 0.1 M borate and were adjusted to pH 9.20. Non-aqueous electrochemical measurements were conducted in 0.1 M TBAPF₆ in acetonitrile. A non-aqueous reference electrode containing a silver wire and a CoralPor® tip from BASi was used and filled with 0.010 M AgPF₆ (Millipore Sigma) and 0.1 M TBAPF₆ (Millipore Sigma) acetonitrile solution. Pt-mesh was used as the counter electrode. Acetonitrile was dried prior to use, however, the experiments were conducted in ambient conditions and trace amounts of water are expected to be present. Cyclic voltammograms and absorbance spectra from water titration experiments were done by starting from acetonitrile, rinsing, cleaning, and drying the electrochemical cell container (a 1.0 cm pathlength cuvette), and filling with a prepared acetonitrile solution of known aqueous buffer content (1%, 2% and 5%). Phosphate buffer was used for CoPi, while borate buffer was used for CoBi.

Film Preparation. Catalyst films of CoPi (CoBi) were prepared via chronoamperometry of Pi (Bi) electrolyte solutions containing 0.5 mM $\text{Co}(\text{NO}_3)_2$. FTO-coated glass pieces were used as the working and electrode and rinsed with acetone and water prior to use. A piece of Scotch tape was affixed to the electrode such that 1.0 cm^2 area was exposed to the electrolyte solution. At a potential of 1.05 V vs. NHE, chronoamperometry is carried out and the charge passed in mC/cm^2 is used as a proxy for the thickness of the catalyst film. A typical steady-state deposition current density is 6 $\text{mA}\cdot\text{h}/\text{s}$.

Steady State UV-Vis Absorption and Spectroelectrochemistry. Absorption spectra were recorded with a StellarNet BLACK-Comet UV-VIS Spectrometer, with two separate light sources (SL1 Tungsten Halogen Lamp and SL3 UV Deuterium Source). The FTO-coated glass pieces with deposited catalyst were placed vertically in a 1.0 cm pathlength quartz cuvette with the catalyst-coated side in contact with the corresponding native Co^{2+} -free buffer. The potentiostat was connected to the electrodes in the cuvette and spectra were recorded after 60 seconds of exposure to each applied potential. Heating of the sample was achieved by a Unisoku USP-203 cryostat sample holder.

Ultrafast Transient Absorption (TA) and TA Spectroelectrochemistry. The 800 nm output of a 5 W, 1 kHz pulsed Ti:sapphire amplifier (Coherent Astrella) was split with a 50:50 beamsplitter. One half was fed into an OPerA Solo optical parametric amplifier tuned to a 380 nm output, which was used as the excitation pump and routed through a femtosecond HELIOS FIRE transient absorption spectrometer (Ultrafast Systems). The other half was used to generate broadband probe light of the visible wavelength region. The resulting pulse-width at the sample was 120 fs, as measured from fitting of the instrument response function on various samples. Samples were measured in a 1.0 cm pathlength quartz cuvette in their native Co^{2+} -free buffers. In the case of applied anodic bias, the 1.0 cm cuvette served as a three-electrode cell. Transient absorption spectra were collected as the sample was held at various externally applied potentials.

Nanosecond/ Microsecond/ Millisecond TA. A tunable 10 Hz OPOTEK laser was used to generate a pump pulse of 10 ns pulse-width, while a Xenon arc lamp was used to generate the probe light. A monochromator set to isolate a specific probe wavelength was used. A photomultiplier tube with 10^4 V/A gain was used and the signal was digitized (with full bandwidth in the case of ≤ 100 μ s time range, and 1 MHz bandwidth in the case of 10 MHz time range) to generate the resulting ΔA signal.

Profilometry. Profilometry measurements were taken with a DektakXT Stylus Profilometer with a 2 μ m stylus tip diameter. Software leveling was implemented with the “Terms Removal (F-Operator)” method. Multiple measurements were made at varying lateral cross-sections for each film, and the average thickness and standard deviation was computed by scanning from the FTO surface to the cobalt oxide film over the span of a few mm and taking the data where the height of the film levels off after the initial height step (which tended to have remnants of adhesive and seeming more film deposition near the edge).

Fitting of Kinetic Traces. All ultrafast (1000 Hz) spectral cuts shown were chirp corrected to a 3rd order polynomial and time-zero corrected.

To fit the excited state decays as collected from the 10 Hz laser up to time delays of 10 ms, several trial functions were tested. The initial maximum intensity value of the data was taken as time zero. The trial functions comprised of the following:

“Biexponential”:

$$\Delta OD = a_1 \exp(-k_1 t) + a_2 \exp(-k_2 t)$$

“Triexponential”:

$$\Delta OD = a_1 \exp(-k_1 t) + a_2 \exp(-k_2 t) + a_3 \exp(-k_3 t)$$

“Two exponentials, one stretched exponential”:

$$\Delta OD = a_1 \exp(-k_1 t) + a_2 \exp(-k_2 t) + a_3 \exp((-k_3 t)^\beta)$$

“Two stretched exponentials”:

$$\Delta OD = a_1 \exp((-k_1 t)^\beta) + a_2 \exp((-k_2 t)^\beta).$$

A non-linear least squares method was used with a function tolerance of 1e-7, optimality tolerance of 1e-7, step tolerance of 1e-7, maximum iterations of 1e-4 and maximum function evaluations of 5e3. These fits are implicated and detailed in Figures 3.S34-3.S36 and Tables 3.S2-3.S4.

Figures

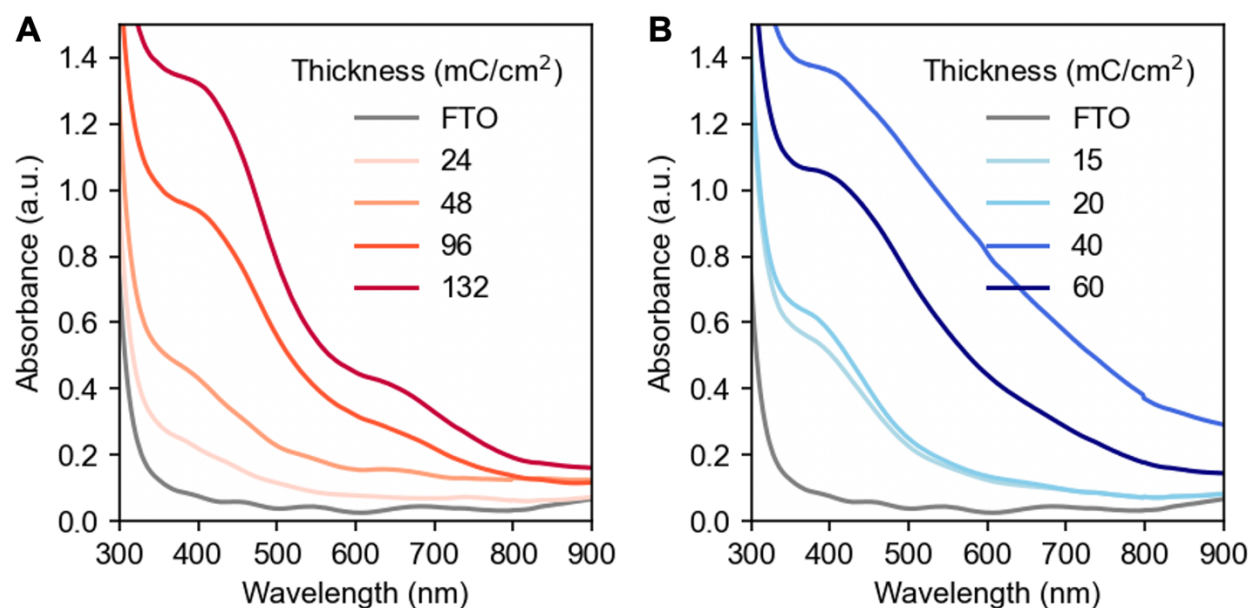


Figure 3.S1: Absorption spectra of CoPi (A) and CoBi (B) films of various thicknesses in their native buffers. The reference spectrum was a piece of FTO immersed in the native buffer without any deposited material. Thin film interference results in oscillations in the frequency domain superimposed on the absorptive features.

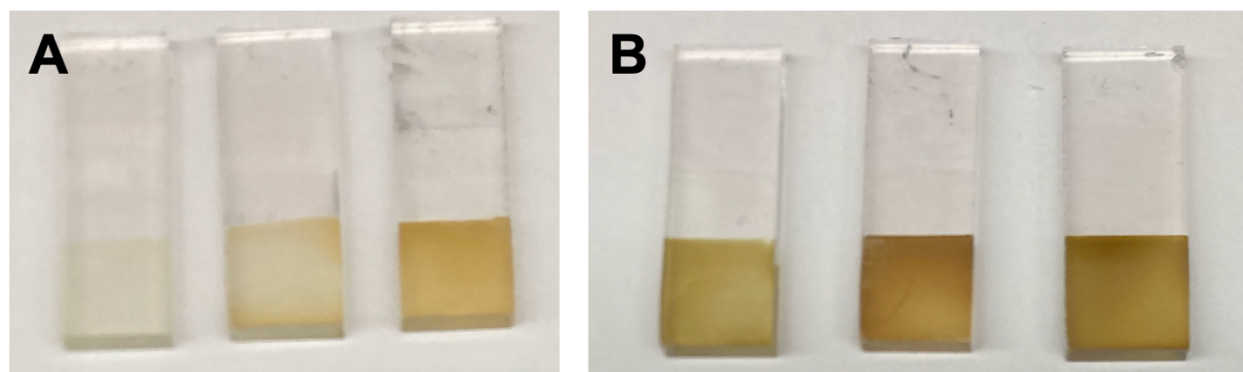


Figure 3.S2. A) CoPi films of 10 mC/cm², 20 mC/cm² and 40 mC/cm² thickness. **B)** CoPi films of 24 mC/cm², 48 mC/cm² and 96 mC/cm² thickness.

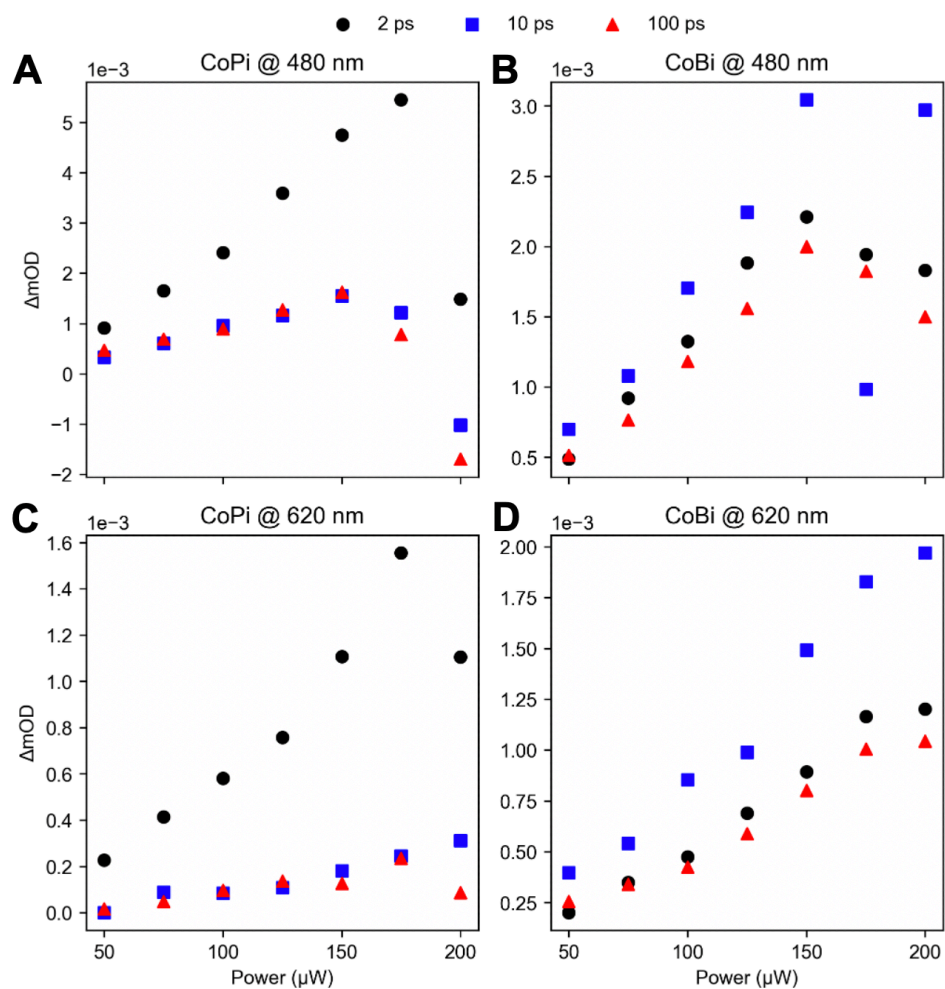


Figure 3.S3. Power dependence of ultrafast 120 fs pulse-width 380 nm pump TA signal for 48 mC/cm^2 CoPi (A, C) and 20 mC/cm^2 CoBi (B, D). A pump power of 100 μW was used for all transient absorption studies as it is well within the linear regime.

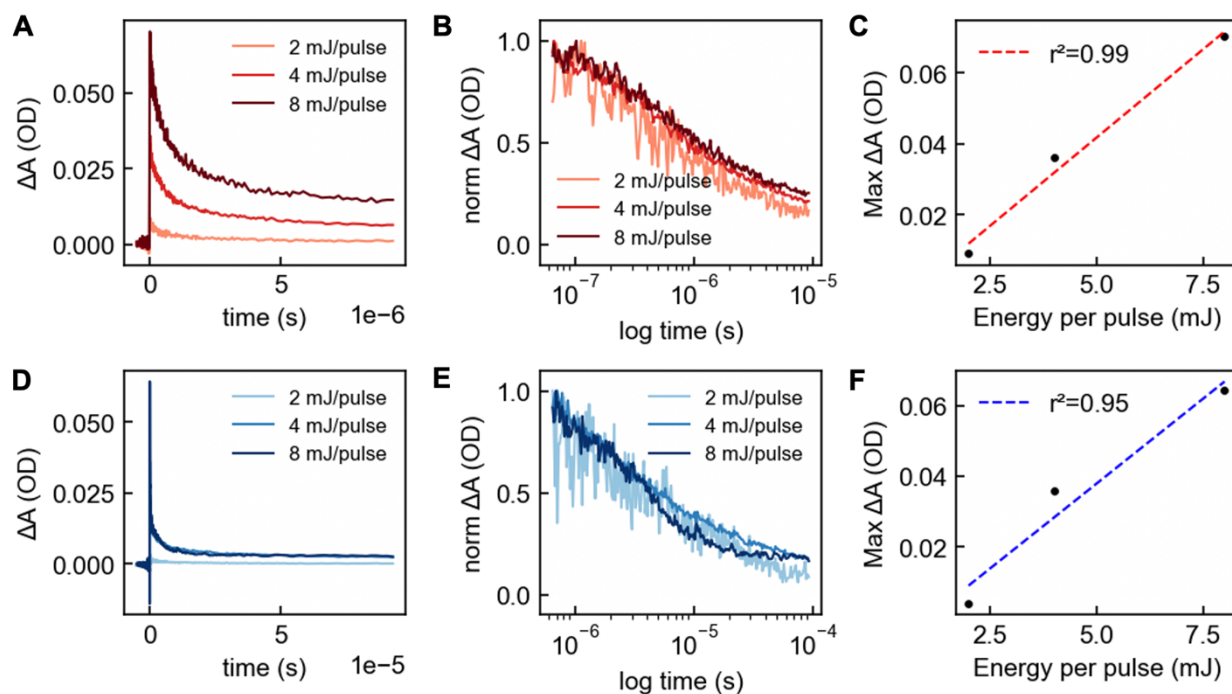


Figure 3.S4. Power dependence of 380 nm pump with 10 ns pulse-width laser transient absorption signal for CoPi (A, B, C) and CoBi (D, E, F) immersed in H₂O. Pulse energies below 8 mJ/pulse were used for all experiments. The spot size diameter is on the order of 1 cm.

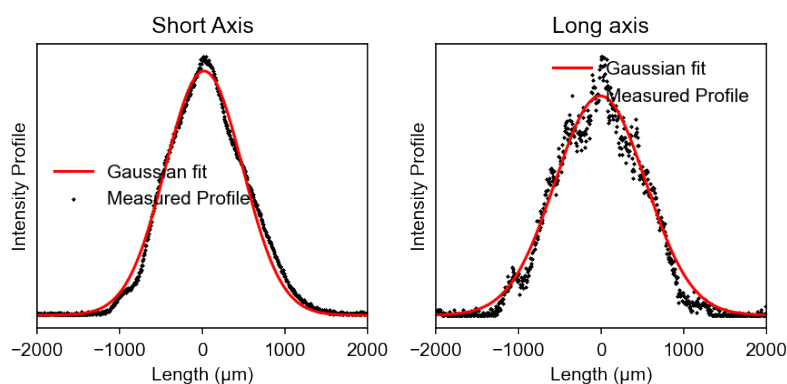


Figure 3.S5. Intensity profiles of the 380 nm ultrafast pump beam at the sample position (FWHM: 1100 μm for short axis, 1200 μm for long axis).

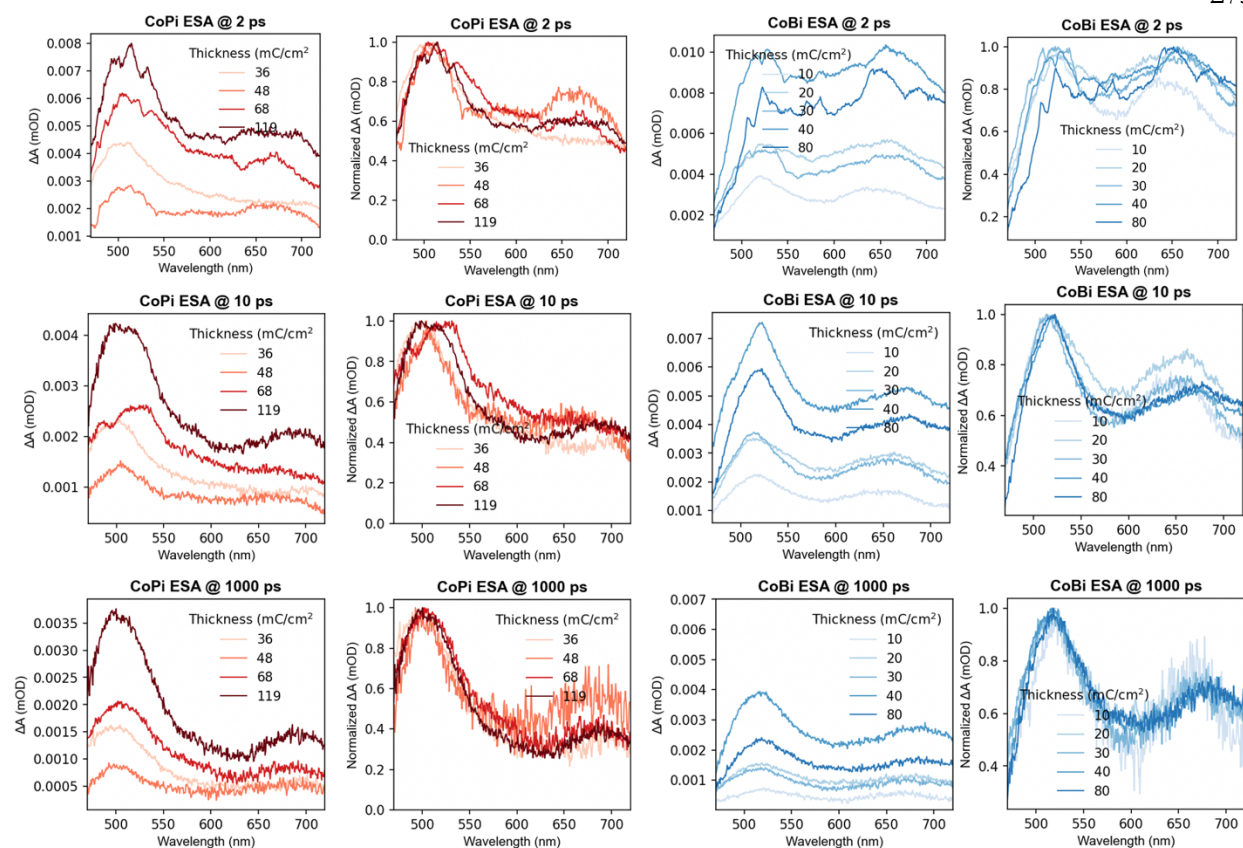


Figure 3.S6. Thickness dependence of transient absorption spectral traces of CoPi and CoBi films at characteristic time delays. Overlaid normalized spectra are shown next to the unnormalized spectra.

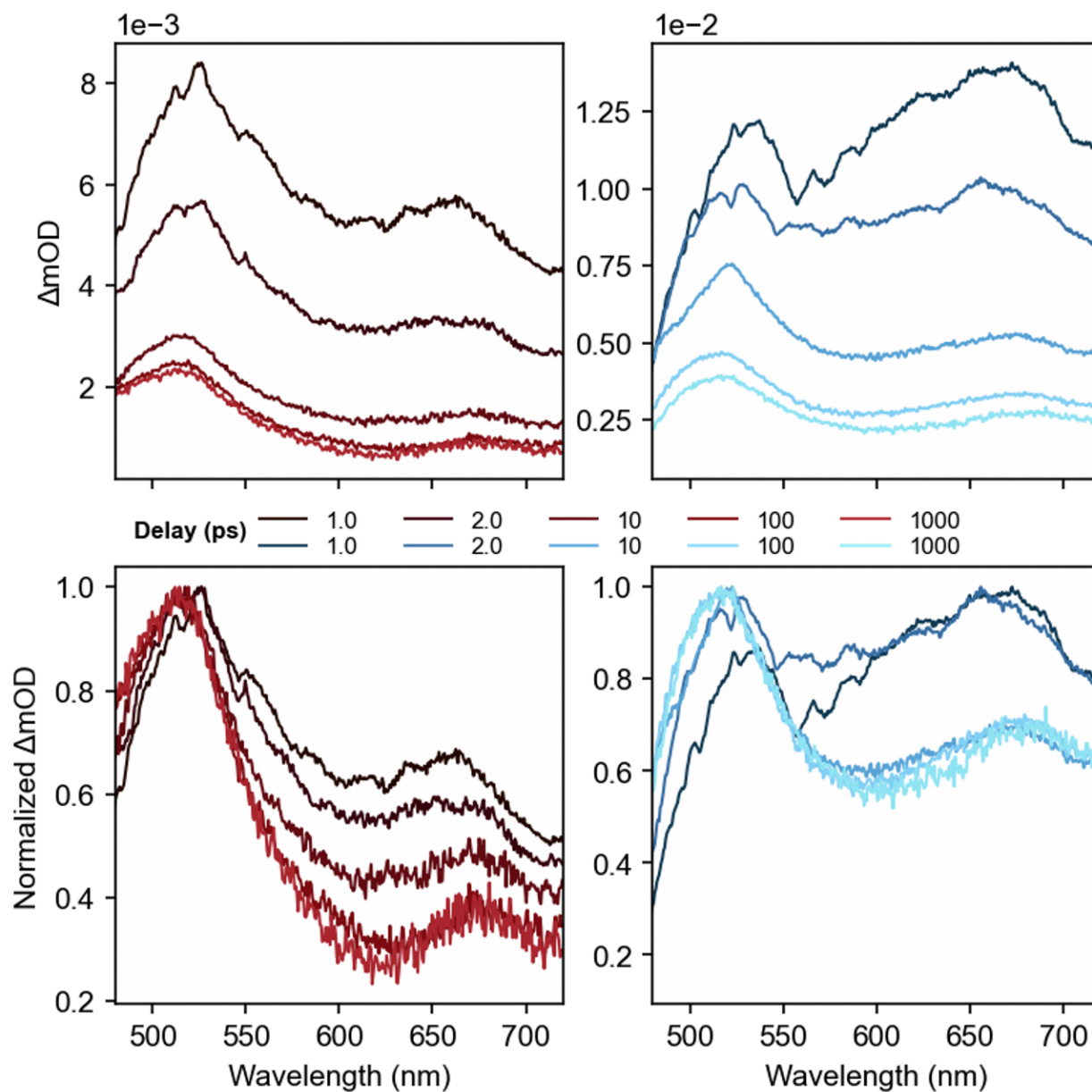


Figure 3.S7. Transient absorption spectral traces at time delays of 2 ps, 10 ps and 1000 ps with applied bias of 96 mC/cm² CoPi (A, C, E) and 48 mC/cm² CoBi (B, D, F) films in their respective native buffers. Samples were pumped at 380 nm with a 120 fs pulse-width ultrafast laser.

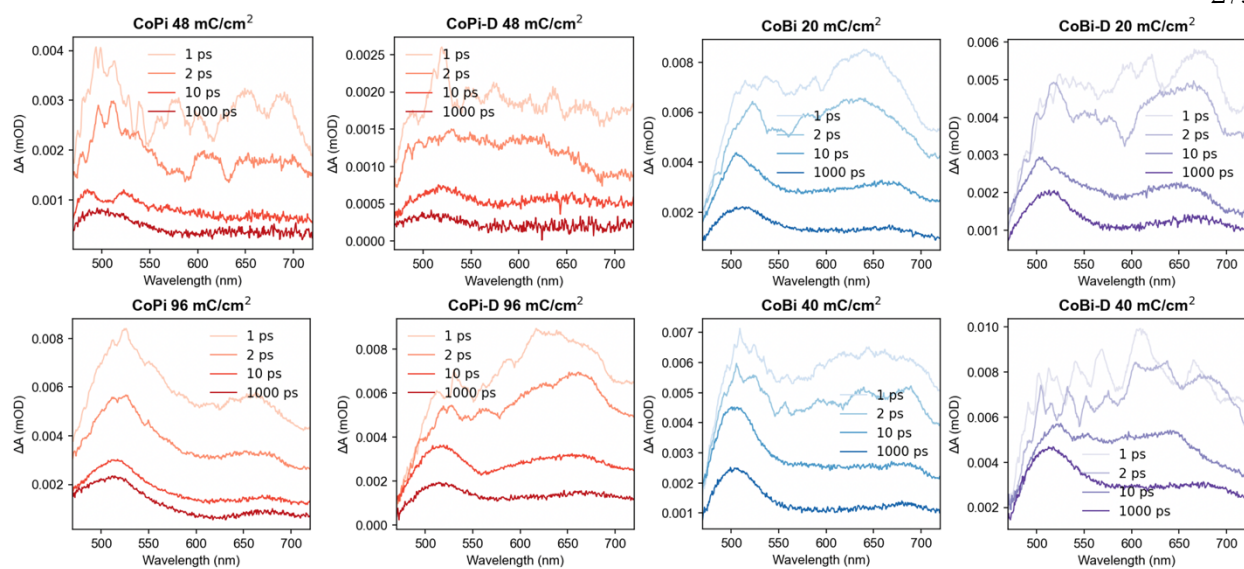


Figure 3.S8. Transient absorption spectral traces for CoPi and CoBi in their respective buffers, both deuterated and non-deuterated. Samples were pumped at 380 nm with a 120 fs pulse-width ultrafast laser.

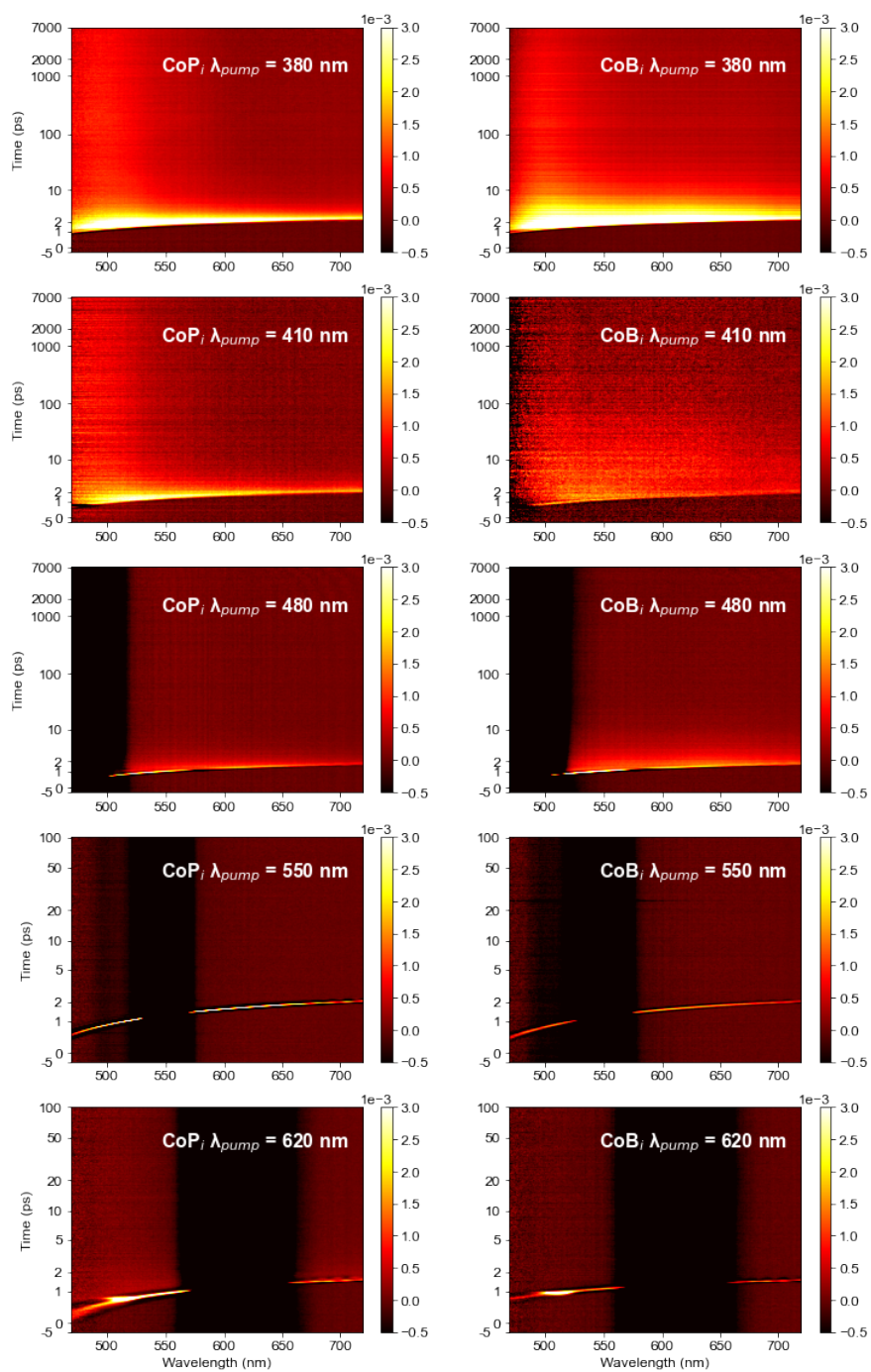


Figure 3.S9. Pump wavelength dependence of ultrafast transient absorption spectra of films taken in their respective buffer solutions with 120 fs pulse-width ultrafast laser.

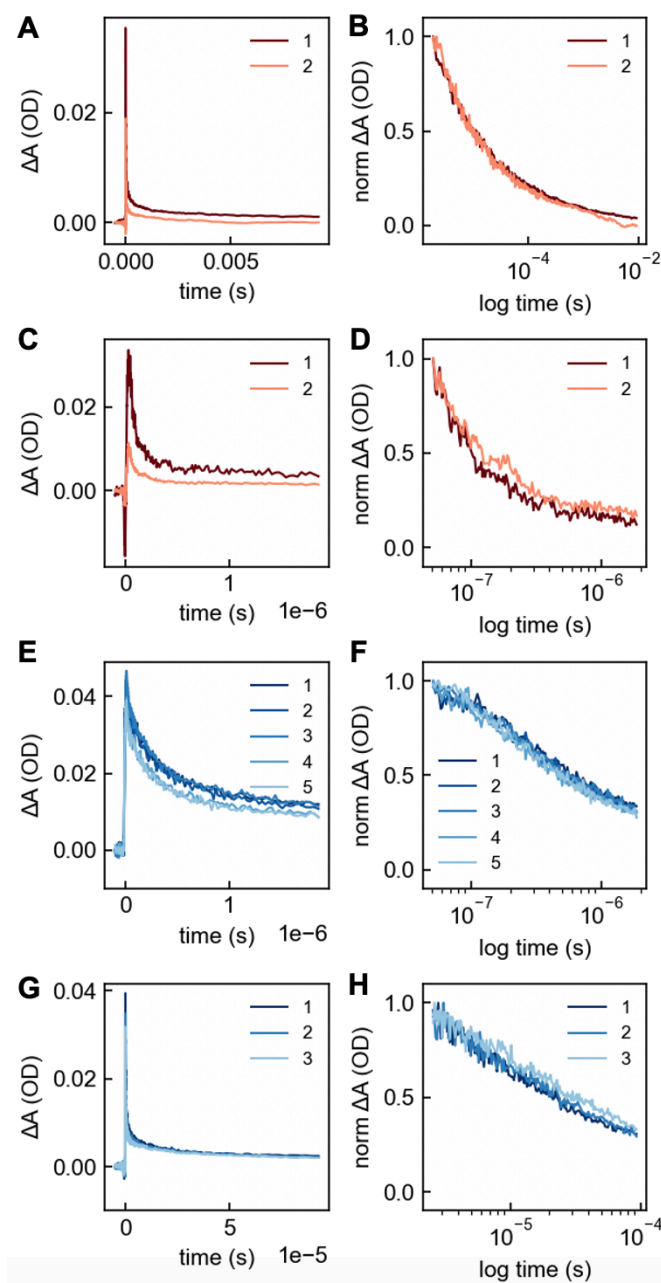


Figure 3.S10. Successive shots of 380 nm pump of 10 ns pulse-width laser showing film dissolution effects for CoPi (**A, B, C, D**) and CoBi (**E, F, G, H**) in H₂O.

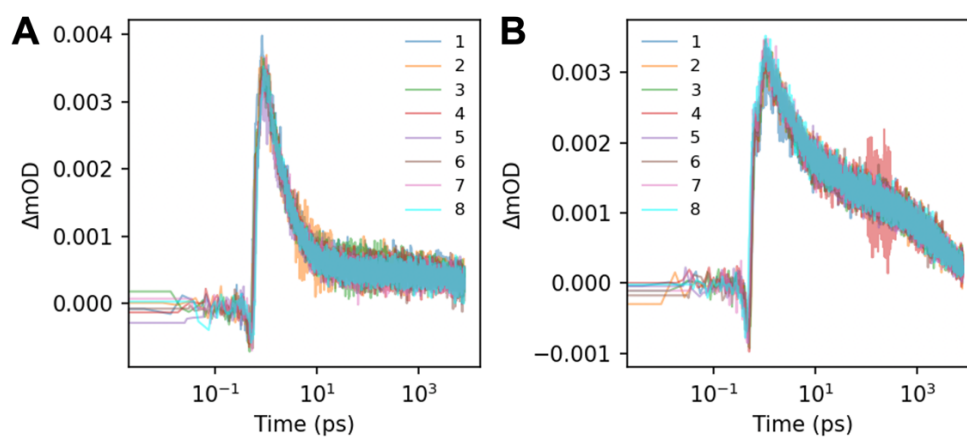


Figure 3.S11. Successive ultrafast TA scans at a pump wavelength of 380 nm and 0.1 μJ pulse energy with a 10 ns pulse-width laser, suggesting no film dissolution or decomposition upon continued irradiation at the corresponding fluence.

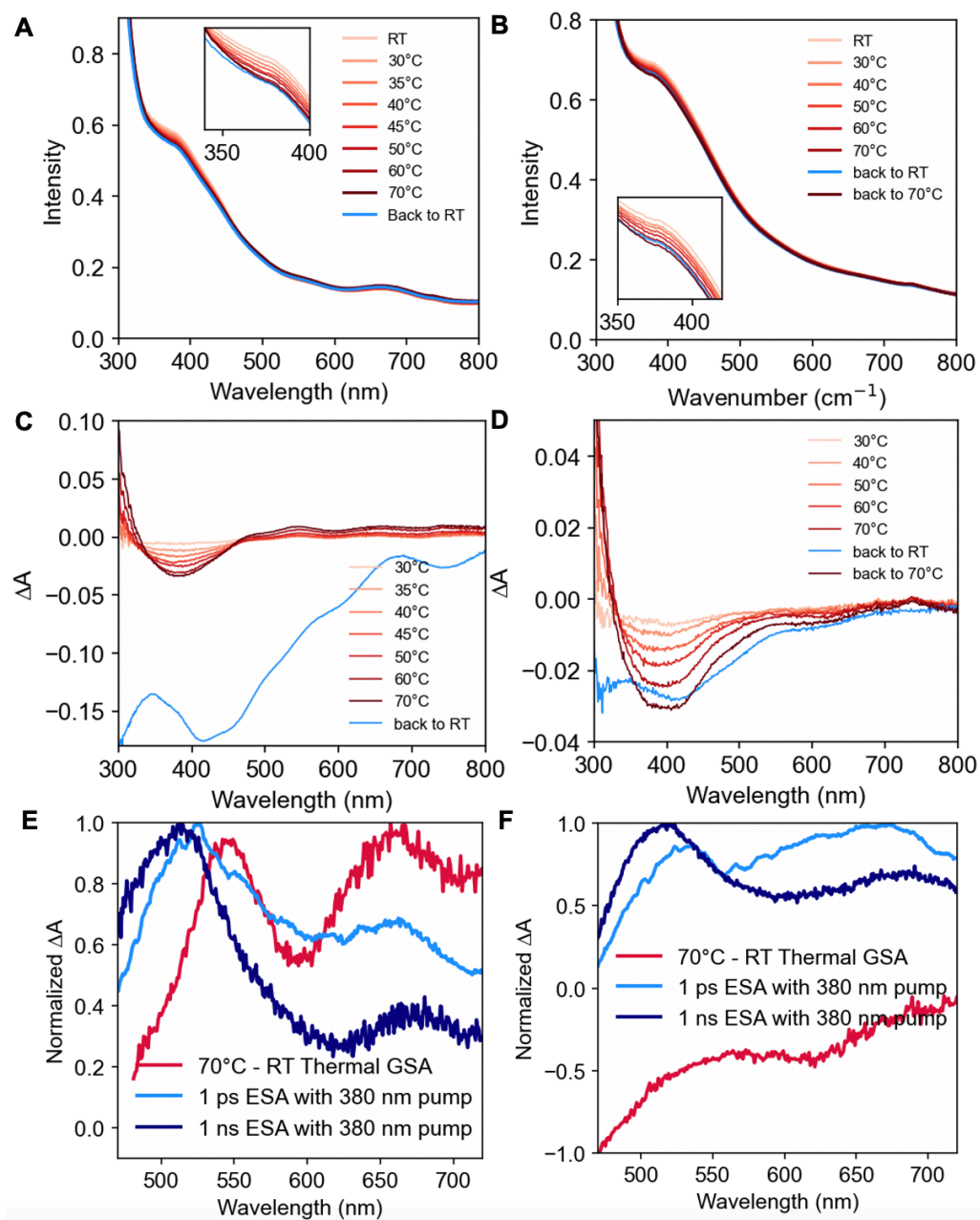


Figure 3.S12. Effects of increased temperature on the absorption spectra of CoPi (A) and CoBi (B) films, with respective difference spectra (C, D) taken in their respective buffer solutions. Comparisons between the thermal difference spectra and excited state absorption spectra at representative time delays of 1 ps and 1 ns are shown for CoPi (E) and CoBi (F).

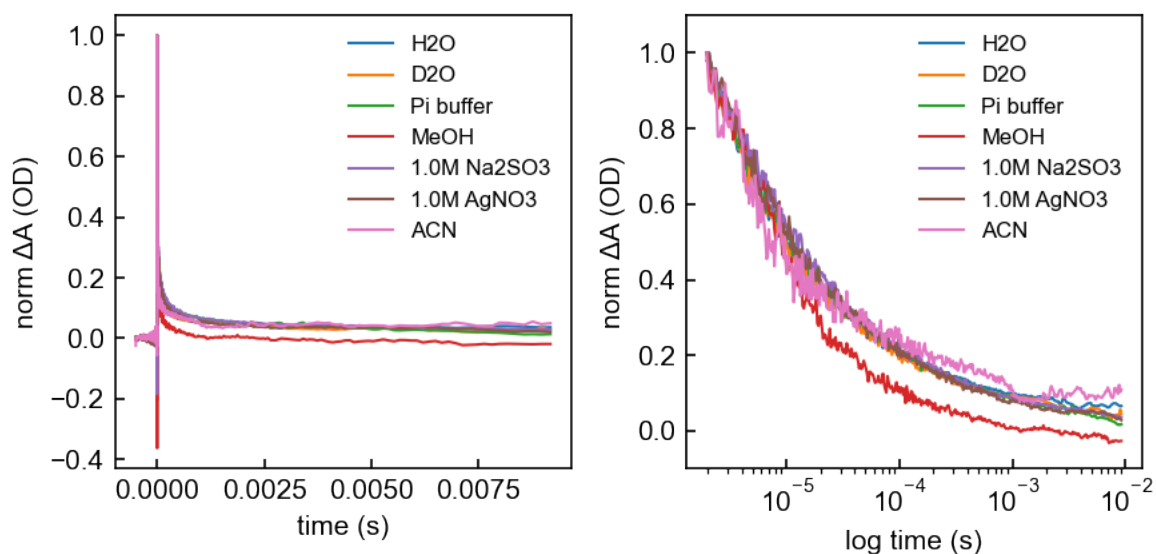


Figure 3.S13. A comparison of 10 ms time range decays of a CoPi film in various media. The sample was translated between measurements in different solvents, such that the pump and probe were hitting a new non-photodegraded spot on the film for each measurement. A quenching effect is observed with MeOH.

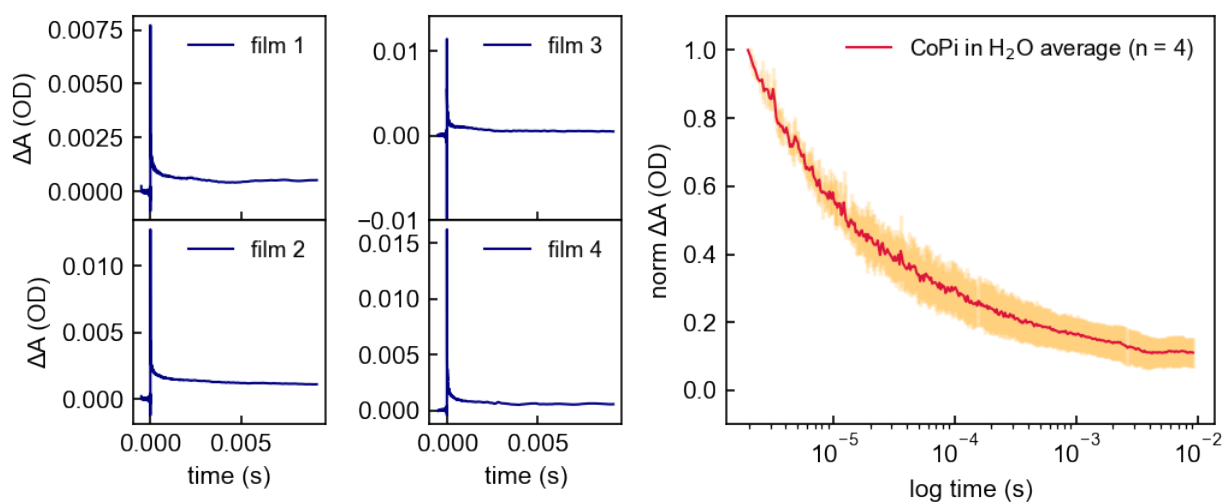


Figure 3.S14. 10 ms time range decays of various CoPi films in H₂O, with average decay curve displayed.

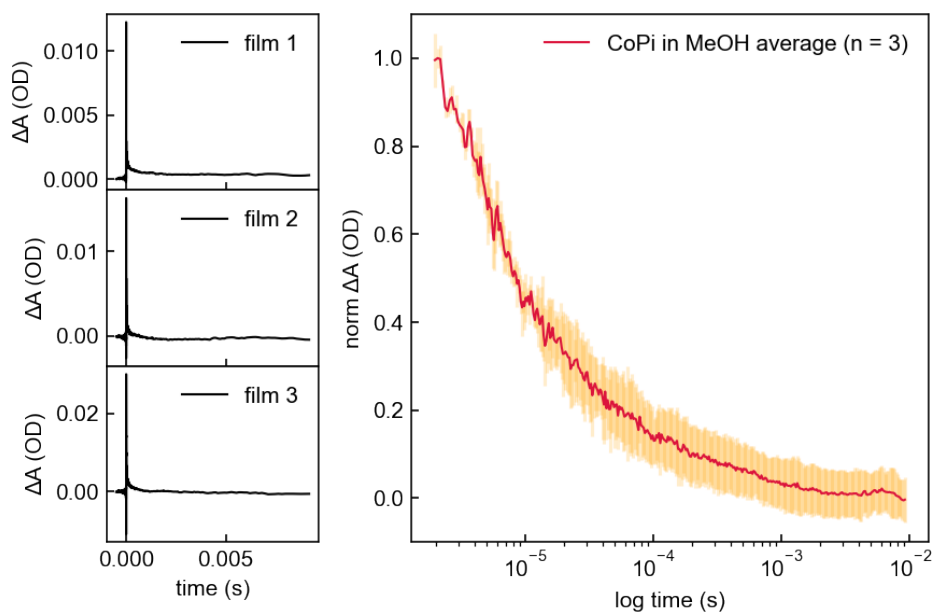


Figure 3.S15. 10 ms time range decays of various CoPi films in MeOH, with average decay curve displayed.

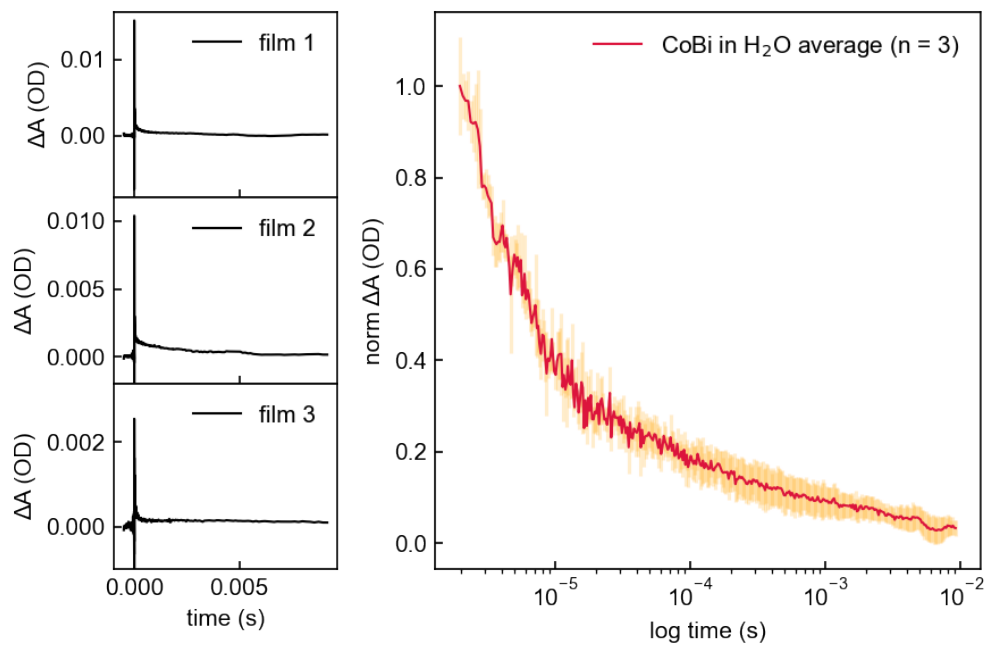


Figure 3.S16. 10 ms time range decays of various CoBi films in H₂O, with average decay curve displayed.

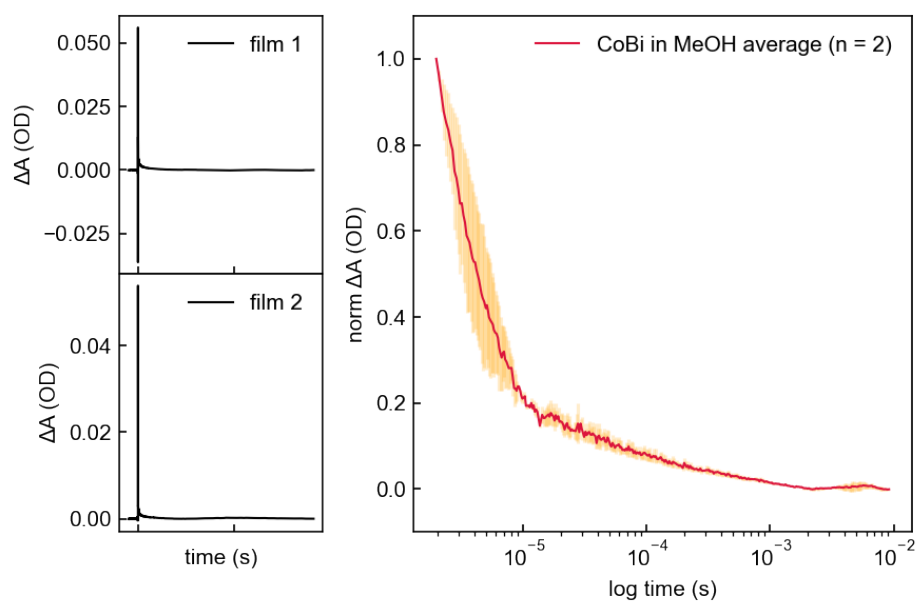


Figure 3.S17. 10 ms time range decays of various CoBi films in MeOH, with average decay curve displayed.

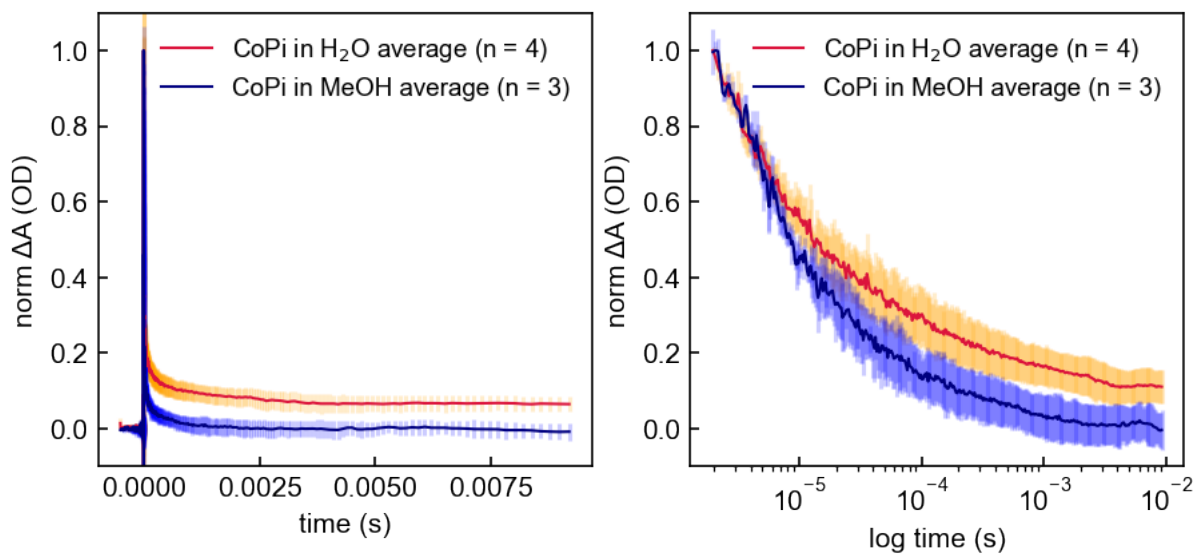


Figure 3.S18. A comparison of average 10 ms time range decays of CoPi films in H₂O compared to CoPi films in MeOH.

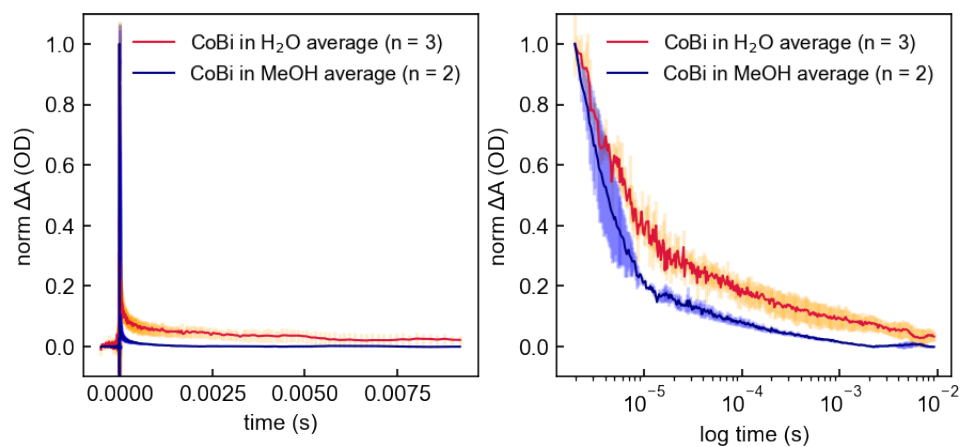


Figure 3.S19. A comparison of average 10 ms time range decays of CoBi films in H₂O compared to CoBi films in MeOH.

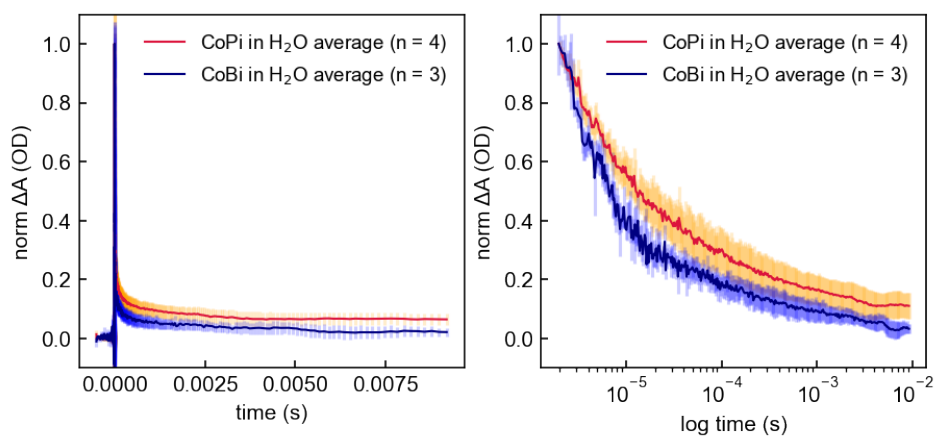


Figure 3.S20. A comparison of average 10 ms time range decays of CoPi films in H₂O compared to CoBi films in H₂O.

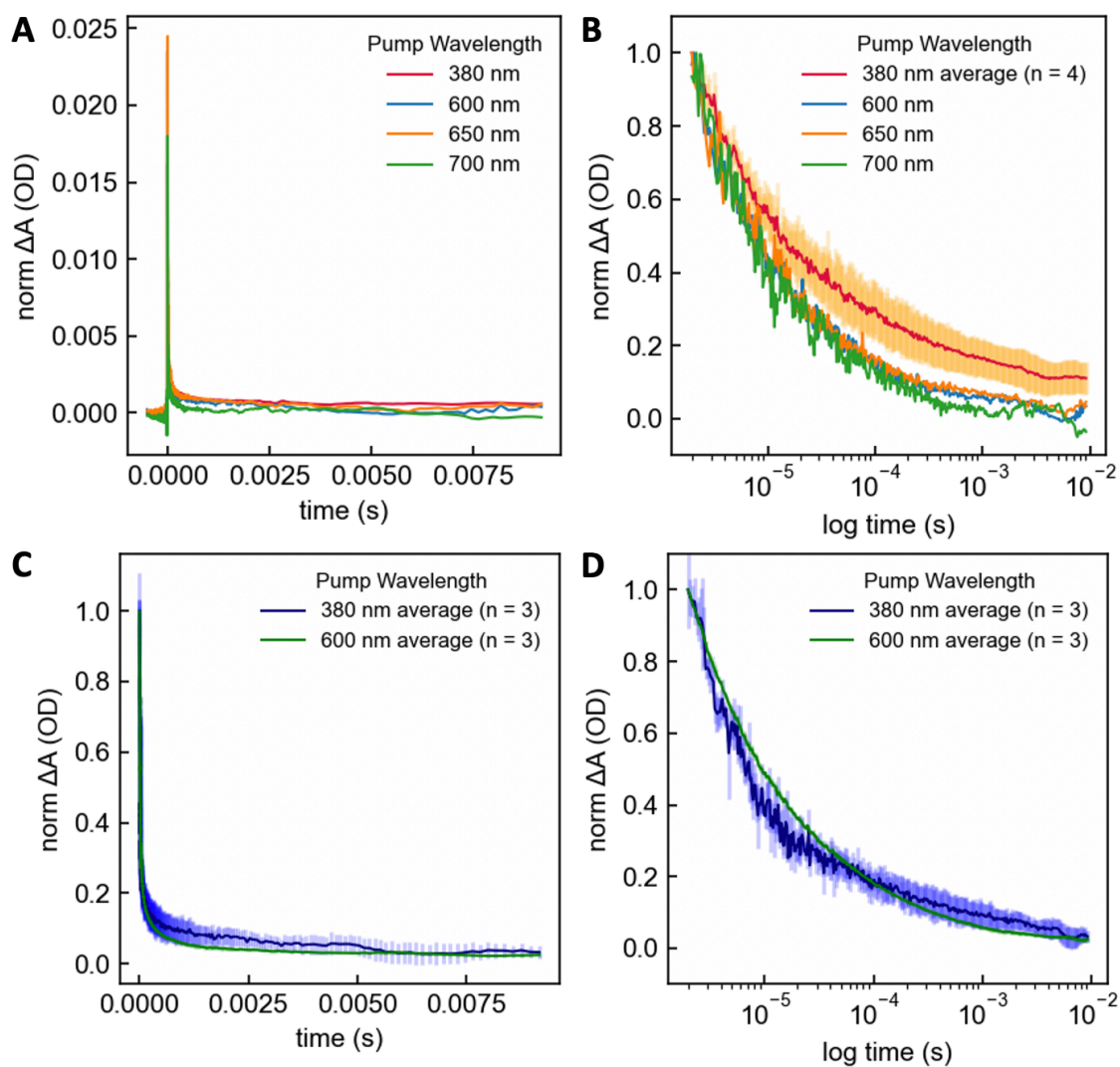


Figure 3.S21. Pump wavelength dependent decay traces taken with 10 ns pulse-width laser probed at 500 nm. CoPi 4 mJ/pulse traces at varying pump wavelengths on a linear (A) and logarithmic (B) time scale. CoBi 4mJ/pulse traces at varying pump wavelengths on a linear (C) and logarithmic (D) time scale.

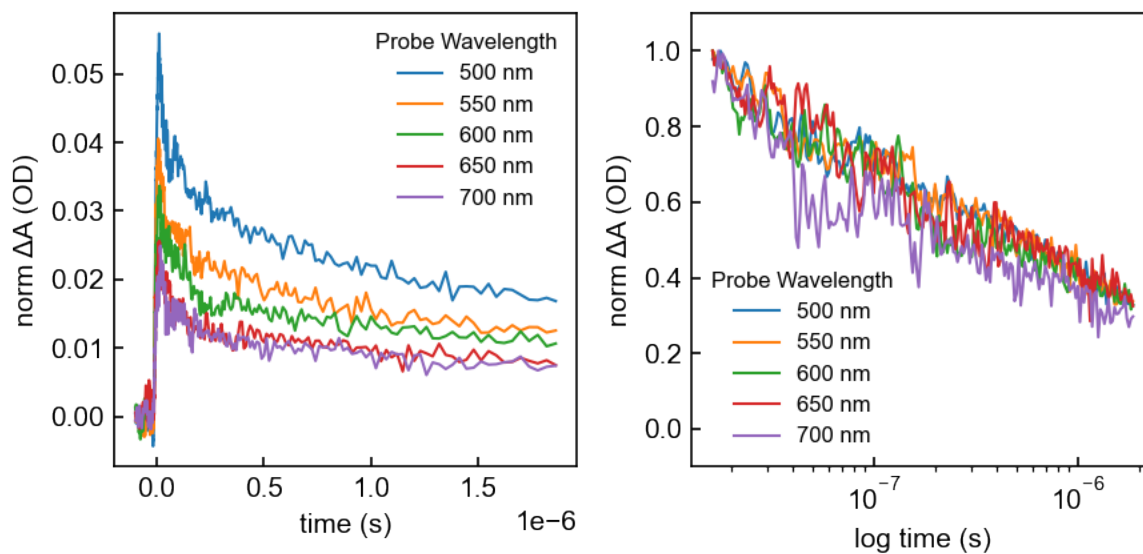


Figure 3.S22. Decays of a CoPi film at various probe wavelengths, translating the film between scans to avoid dissolution effects and maintaining a constant detector gain for the transient absorption signal.

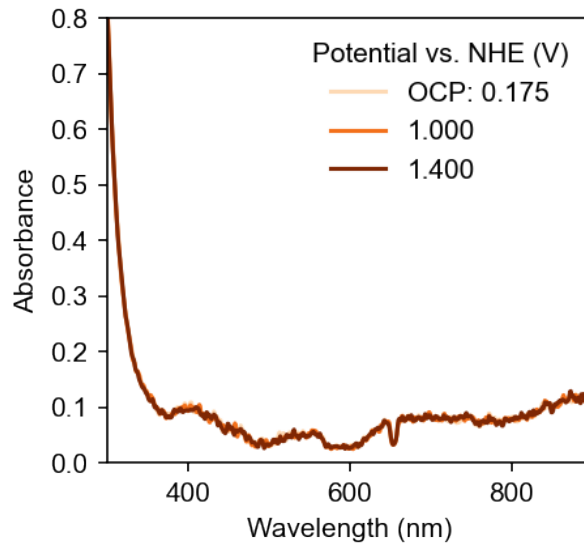


Figure 3.S23: Unchanging spectral intensity with applied potential for an FTO film in phosphate buffer solution without the electrodeposited catalyst.

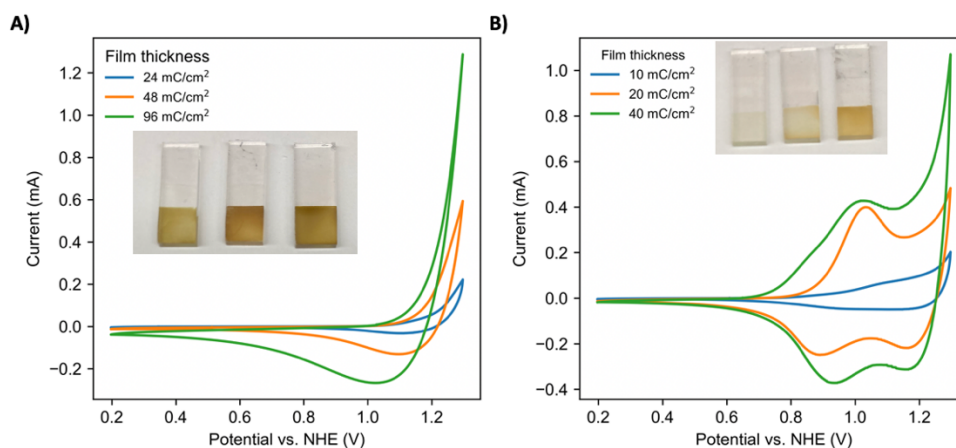


Figure 3.S24: Cyclic voltammograms (first cycles) of 24, 48, and 96 mC/cm² CoPi (A) and 10, 20, 40 mC/cm² CoBi (B) films in their native buffers (pH 7.0 phosphate buffer for CoPi, pH 9.2 borate buffer for CoBi). Scan rates are 100 mV/s.

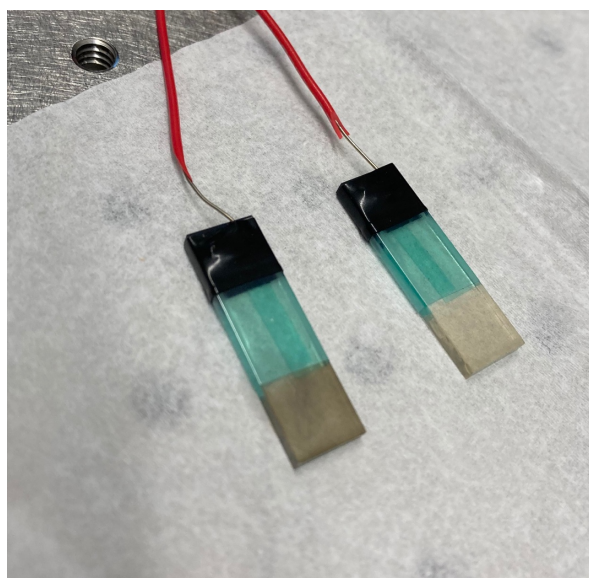


Figure 3.S25. Pictures of two 10 mC/cm² CoPi films. On the left, the film has been under anodic bias for several hours. On the right, the film has only seen the anodic bias corresponding to the electrodeposition potential. The difference in visible absorption is apparent and quantified spectroelectrochemically.

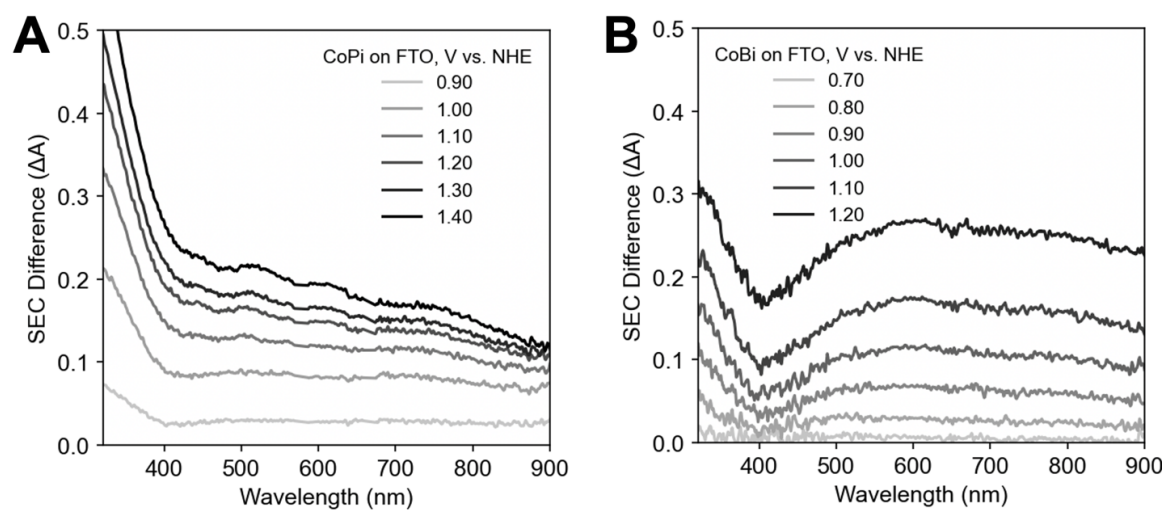


Figure 3.S26. Spectroelectrochemical difference spectra (vs. NHE) of CoPi in pH 7.0 phosphate buffer (**A**) and CoBi in pH 9.2 borate buffer (**B**).

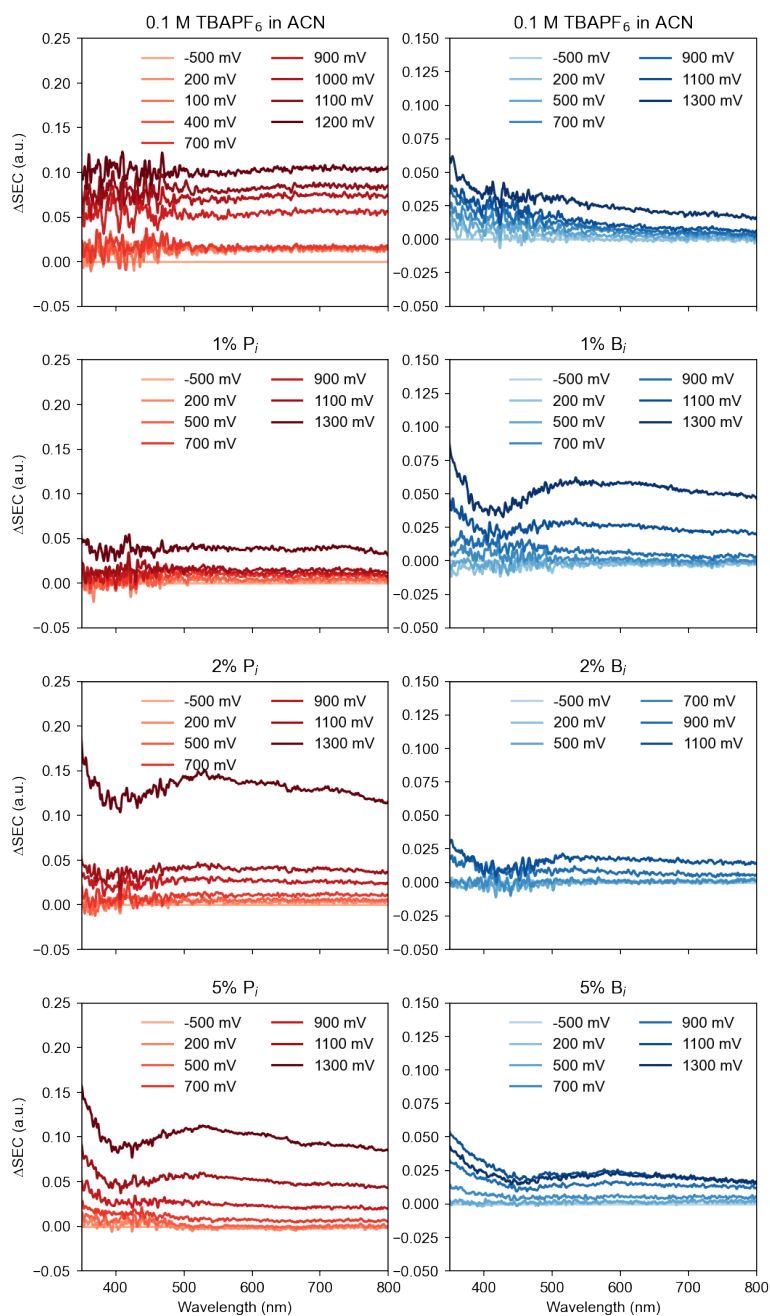


Figure 3.S27. Spectroelectrochemical difference spectra (vs. 10 mM Ag/AgPF₆) of CoPi (left) and CoBi (right) in dry acetonitrile with 0.1 M TBAPF₆ with increasing amounts of aqueous buffer titrated in.

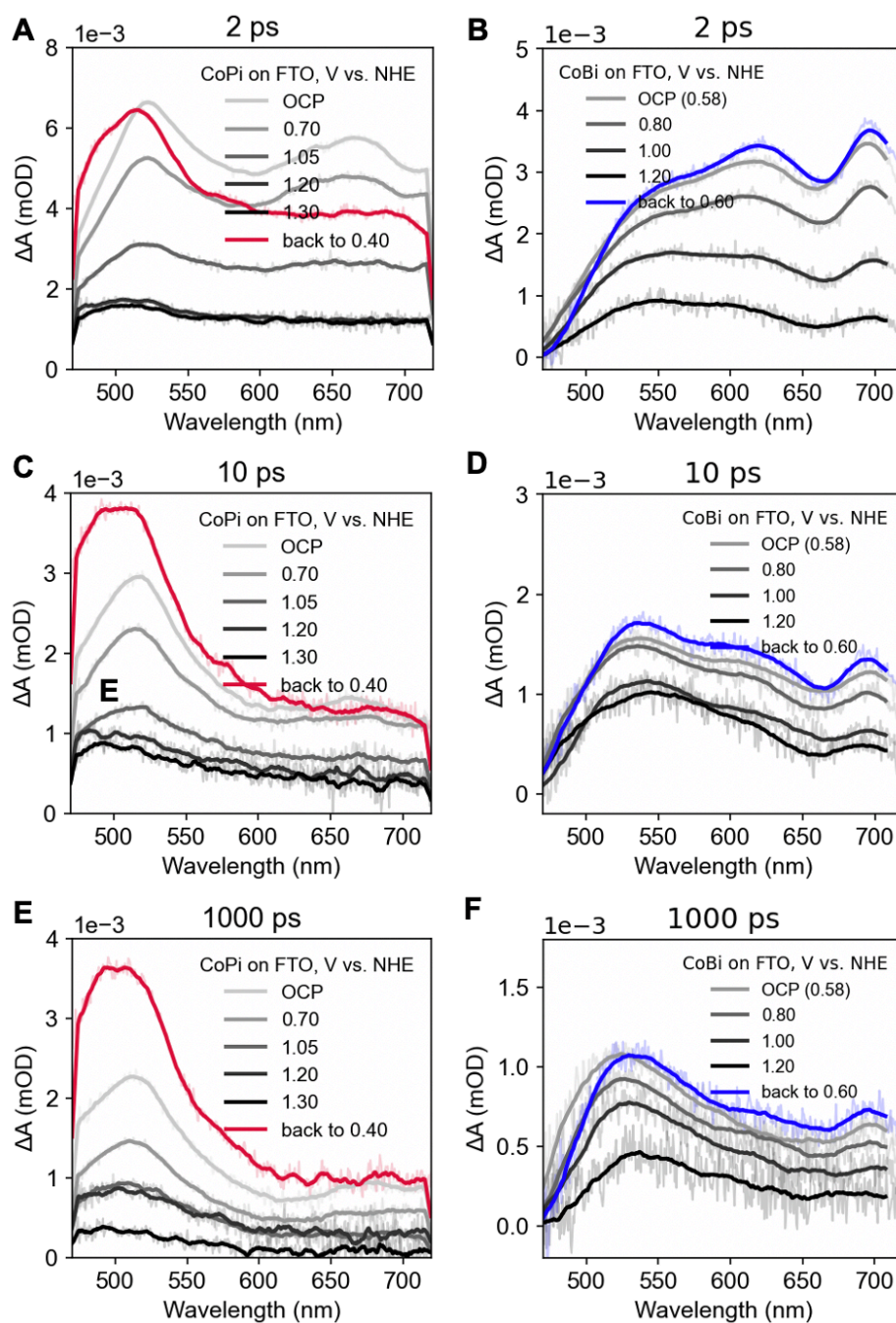


Figure 3.S28. Transient absorption spectral traces at time delays of 2 ps, 10 ps and 1000 ps with applied bias of 96 mC/cm² CoPi (A, C, E) and 48 mC/cm² CoBi (B, D, F) films in their respective native buffers. Samples were pumped at 380 nm with a 120 fs pulse-width ultrafast laser.

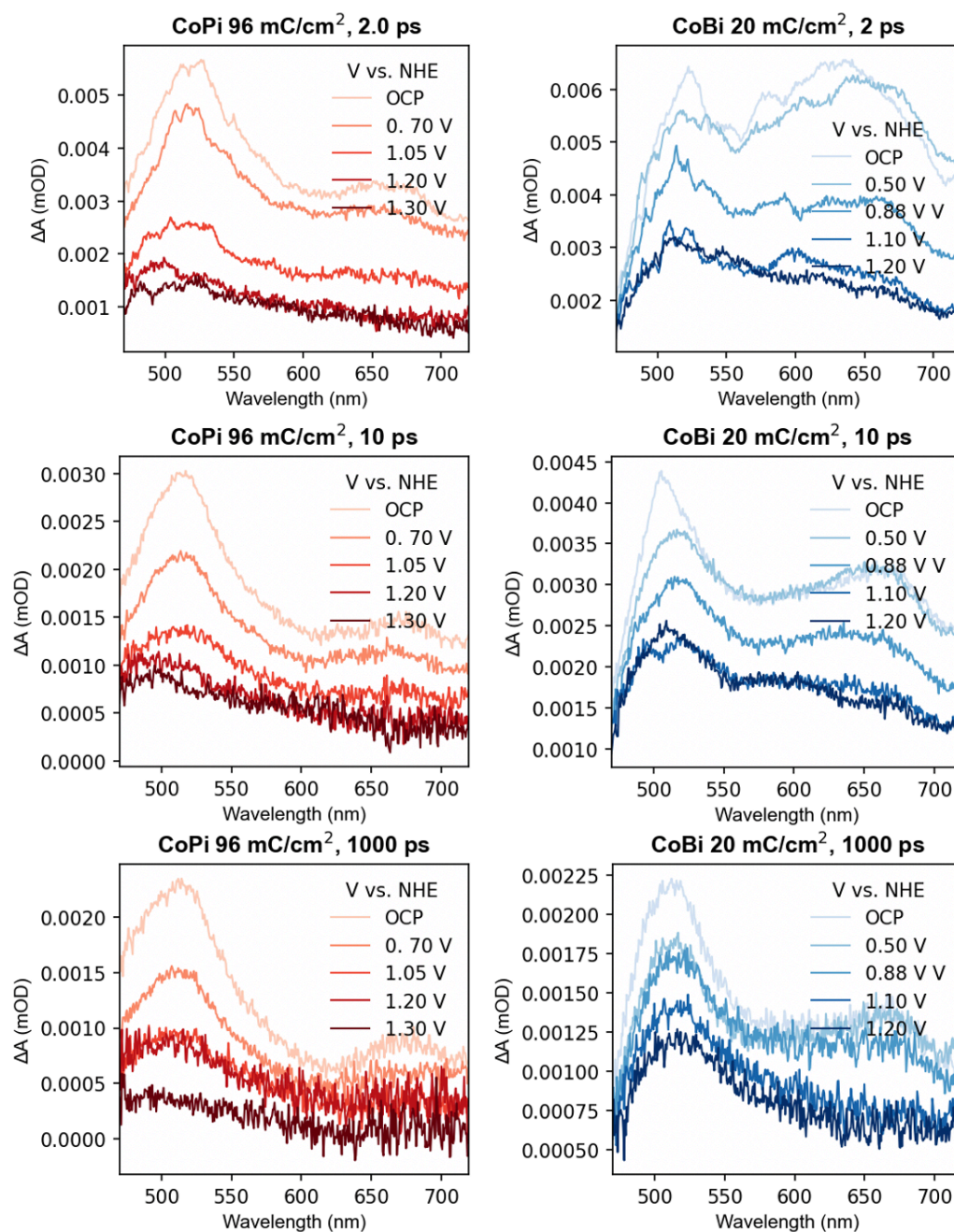


Figure 3.S29. Transient absorption spectral traces at time delays of 2 ps, 10 ps and 1000 ps with applied bias of 96 mC/cm² CoPi and 20 mC/cm² CoBi films in their respective native buffers. Samples were pumped at 380 nm with a 120 fs pulse-width ultrafast laser.

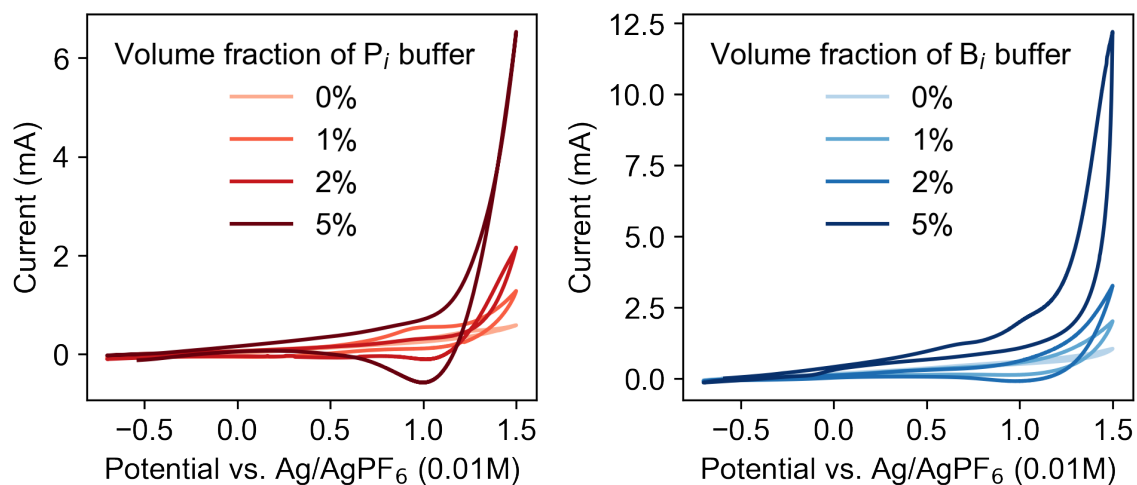


Figure 3.S30. Cyclic voltammogram of CoPi (A) and CoBi (B) in dry acetonitrile with 0.1 M TBAPF₆ and corresponding amounts of respective aqueous buffer solutions added.

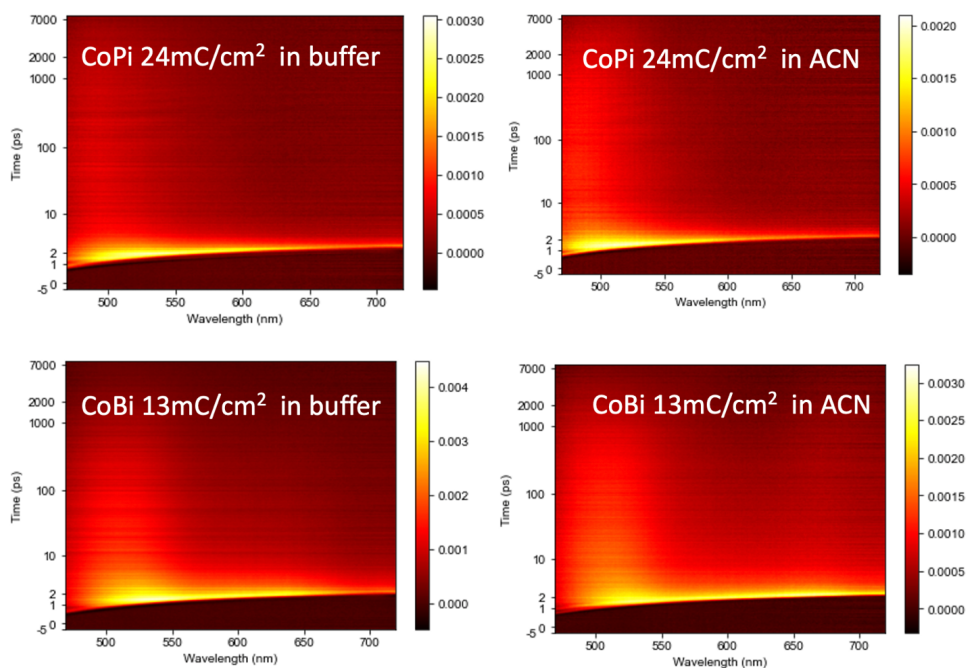


Figure 3.S31. 2D transient absorption spectra of 24 mC/cm² CoPi and 13 mC/cm² CoBi films immersed in buffer and in acetonitrile.

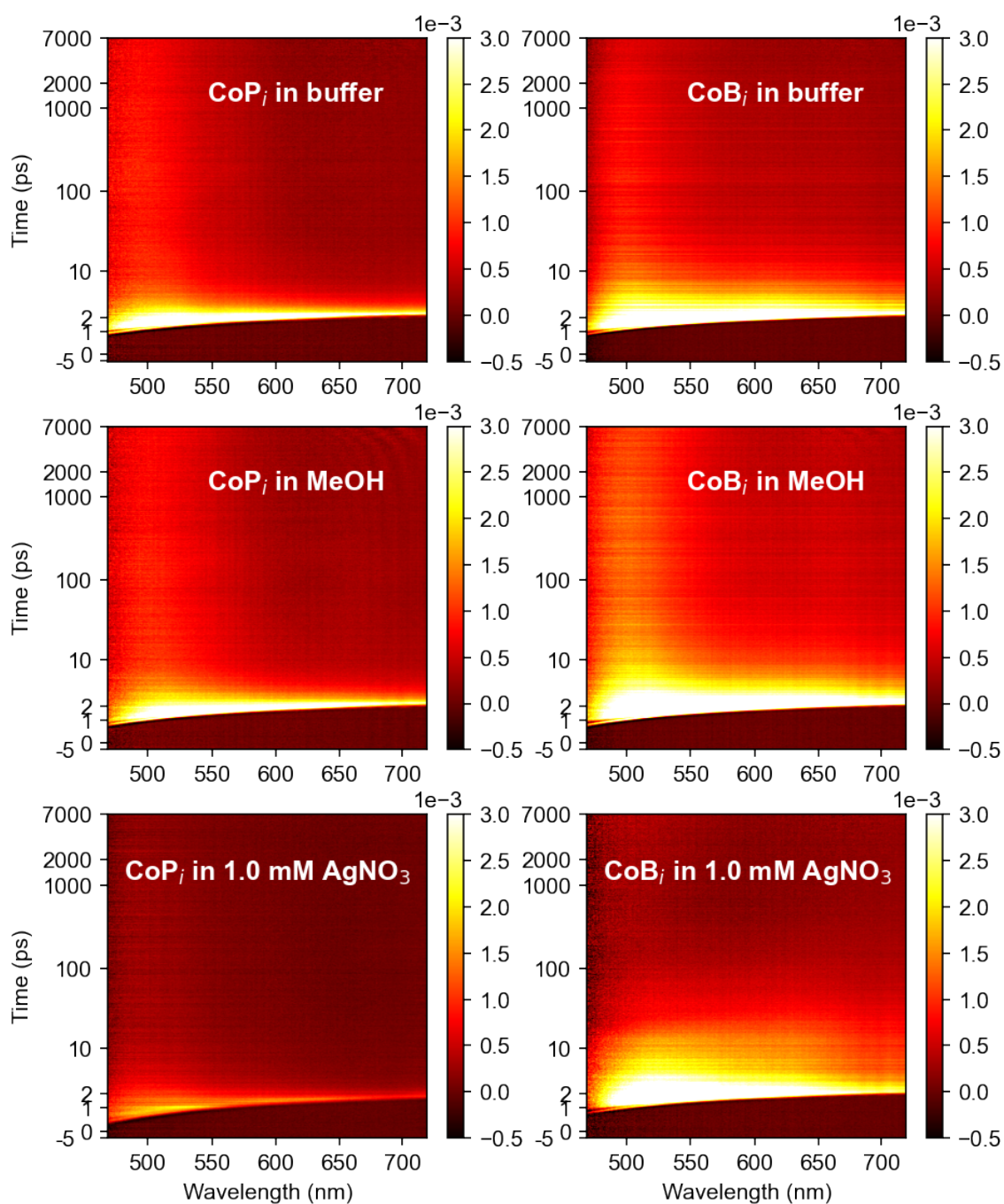


Figure 3.S32. 2D transient absorption spectra of 48 mC/cm² CoPi and 20 mC/cm² CoBi films immersed in buffer, MeOH (hole scavenger) and aqueous AgNO₃ (electron scavenger) solutions.

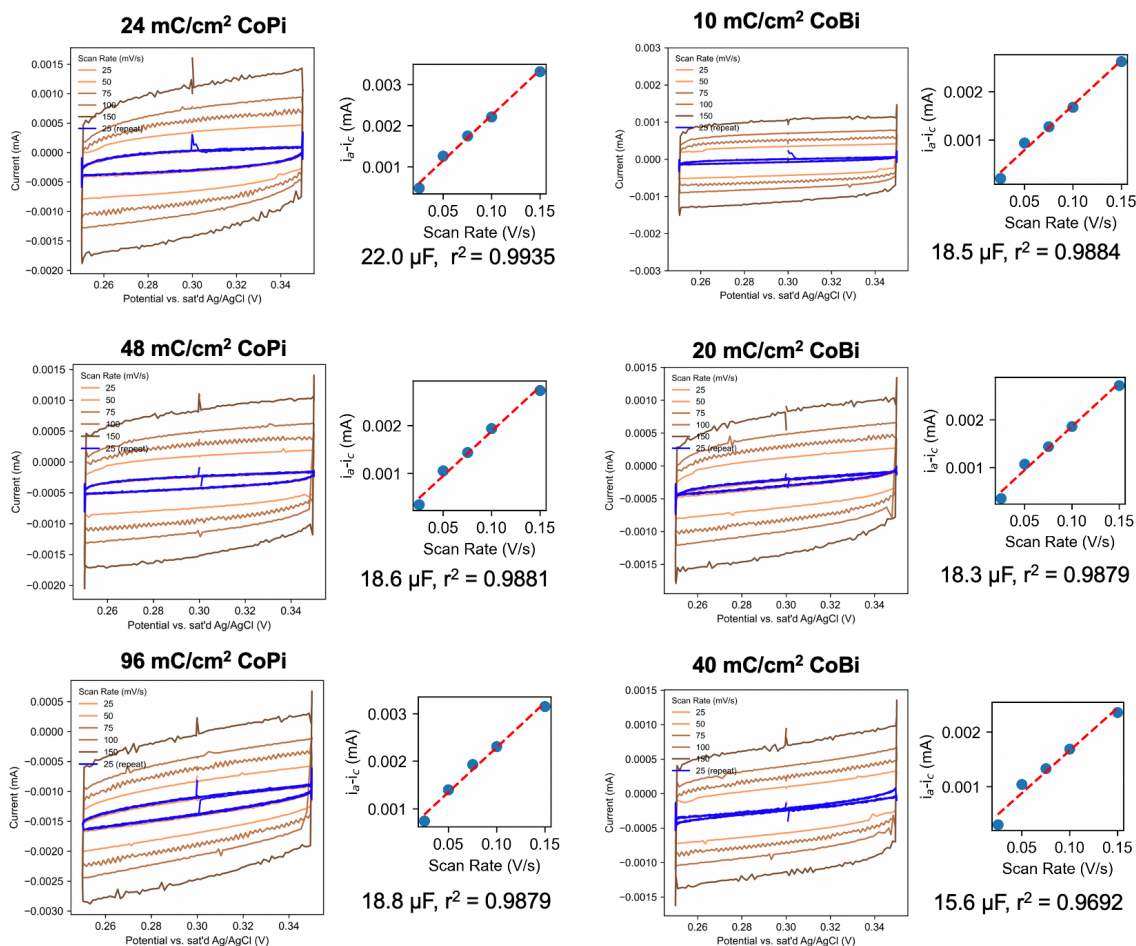


Figure 3.S33: Scan rate dependence on non-faradaic regions of CVs of various film types and thicknesses in their native buffer solutions. The line of best fit yields a slope proportional to double layer capacitance, which is similar for the different film types and thicknesses. We note that the 75 mV/s scan rate data appears to have rapid oscillations in all cases due to an artefact with the data collection under the employed potentiostat settings. The “averaged” data are in line with the other measurements and therefore is still deemed reliable for this purpose.

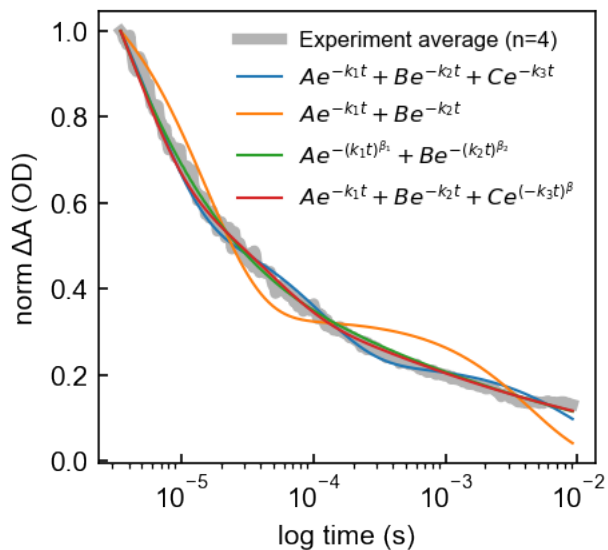


Figure 3.S34. CoPi 10 ms time range average decay with various fitting models.

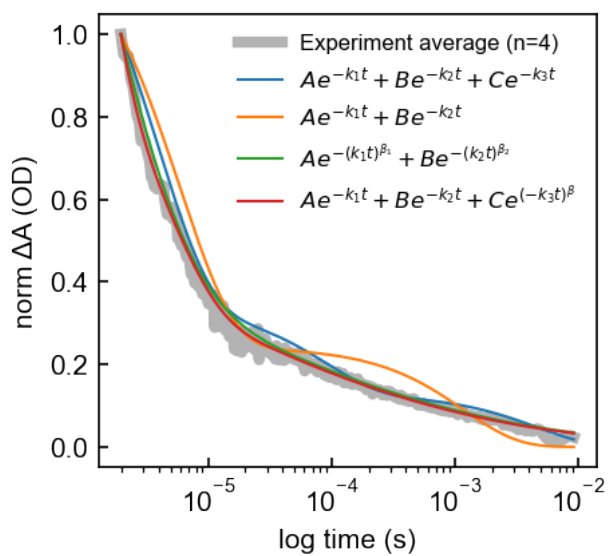


Figure 3.S35. CoBi 10 ms time range average decay with various fitting models.

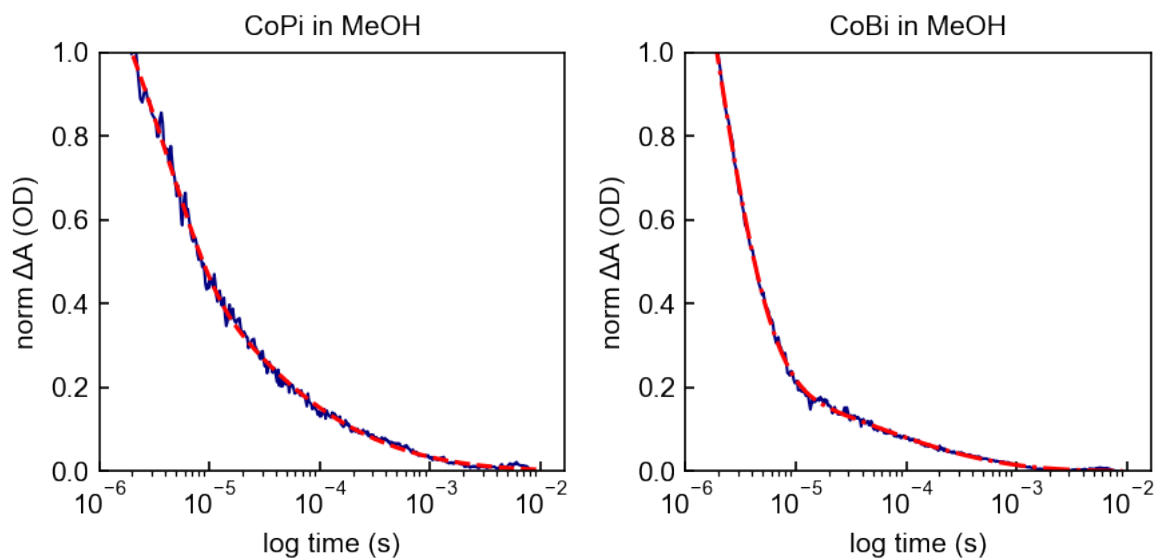


Figure 3.S36. Normalized average 10 ms decays of CoPi ($n = 3$) and CoBi ($n = 2$) fit to two stretched exponentials. Details of fit given in Table S4.

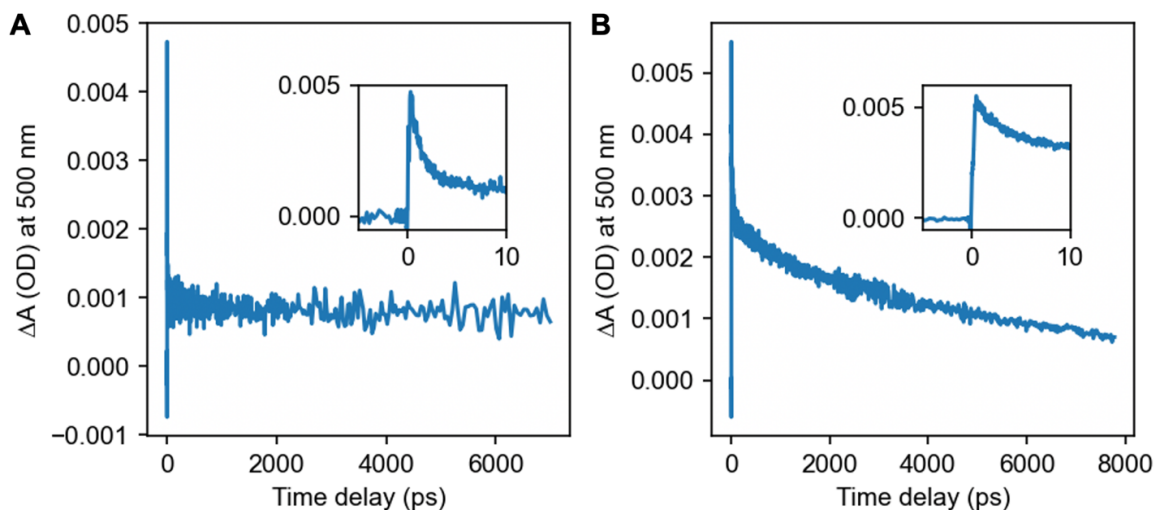


Figure 3.S37. Ultrafast decay traces at 380 nm pump wavelength and 500 nm probe wavelength of 96 mC/cm^2 CoPi (**A**) and 40 mC/cm^2 CoBi (**B**). The insets show the decay before around time zero. The flat zero intensity line before time zero suggests that the 1 kHz repetition rate is appropriate for any measurable excited state population from the previous pump pulse to have decayed.

Tables

Table 3.S1: Thickness data from profilometry.

Film	Charge passed (mC/cm²)	Thickness profilometry (nm)	Standard deviation (nm)
CoP _i	24	86	29 (n = 2)
CoP _i	48	473	73 (n = 2)
CoP _i	96	774	53 (n = 4)
CoB _i	10	108	10 (n = 4)
CoB _i	20	476	41 (n = 3)
CoB _i	40	1109	34 (n = 4)

Table 3.S2: Fitting parameters for CoPi in H₂O: 10 ms time range kinetics.

	Triexponential
A	0.70
B	0.27
C	0.18
k ₁	184428
k ₂	8862
k ₃	91.0

	Two stretched exponentials
A	5.30
B	1.31
k_1	1.96e+07
k_2	6.06e+05
β_1	0.233
β_2	0.113

	Biexponential
A	0.66
B	0.26
k_1	65440
k_2	226.5

	Two exponentials, one stretched exponential
A	0.14
B	0.58
C	1.61
k_1	21440

k_2	256400
k_3	3.83e+06
β	0.099

Table 3.S3: Fitting parameters for CoBi in H₂O: 10 ms time range kinetics

	Triexponential
A	0.98
B	0.19
C	0.11
k_1	260675
k_2	11164
k_3	213.7

	Two stretched exponentials
A	3.19
B	1.30
k_1	1.70e+06
k_2	1.91e+06

β_1	0.468
β_2	0.134

Biexponential	
A	0.88
B	0.20
k_1	169553
k_2	841

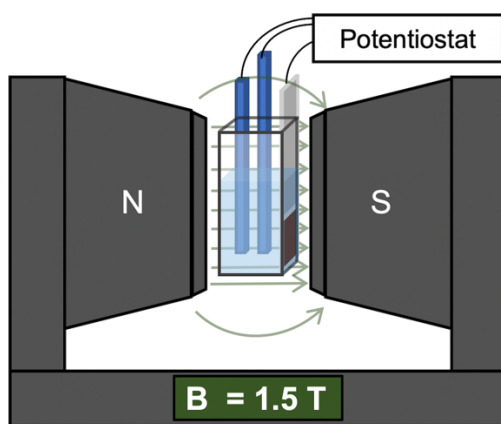
Two exponentials, one stretched exponential	
A	0.61
B	3.01
C	1.68
k_1	226045
k_2	1.46e+06
k_3	7.73e+06
β	0.123

Table 3.S4: Fits of two stretched exponentials to the normalized average decay of CoPi in MeOH and CoBi in MeOH.

	CoPi
A	0.40
B	3.87
k_1	2.00e+05
k_2	1.25e+07
β_1	1.20
β_2	0.16

	CoBi
A	2.76
B	0.36
k_1	7.39e+05
k_2	3.48e+04
β_1	0.72
β_2	0.33

MAGNETIC FIELD EFFECTS ON ELECTROCATALYTIC OXYGEN EVOLUTION BY AMORPHOUS COBALT OXIDE FILMS



30-40% magneto-enhancement of water oxidation with CoPi electrocatalytic films

Adapted from:

Mirzoyan, R.; Barrientos, H. K.-H.; Hwang, K. H.; Hadt, R. Magnetic Field Effect on the Electrocatalytic Activity of Cobalt-Phosphate Oxyhydroxide Oxygen Evolving Thin Films. *ChemRxiv* August 23, 2024. <https://doi.org/10.26434/chemrxiv-2024-k3x2k>.

[This chapter is temporarily embargoed.]

*Appendix A*ELUCIDATING TOTALLY SYMMETRIC VIBRATIONAL MODE CONTRIBUTIONS OF
S = 1/2 MOLECULAR QUBIT CANDIDATES THROUGH RESONANCE RAMAN
SPECTROSCOPY

[This section is temporarily embargoed.]